LBNL-39789
UC-814

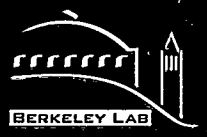

ERNEST ORLANDO LAWRENCE
BERKELEY NATIONAL LABORATORY

Forecast of Thermal-Hydrological Conditions and Air Injection Test Results of the Single Heater Test at Yucca Mountain

J.T. Birkholzer and Y.W. Tsang
Earth Sciences Division

December 1996

LBNL-39789
UC-814

Forecast of Thermal-Hydrological Conditions and Air Injection Test Results of the Single Heater Test at Yucca Mountain

J. T. Birkholzer and Y. W. Tsang
December 1996

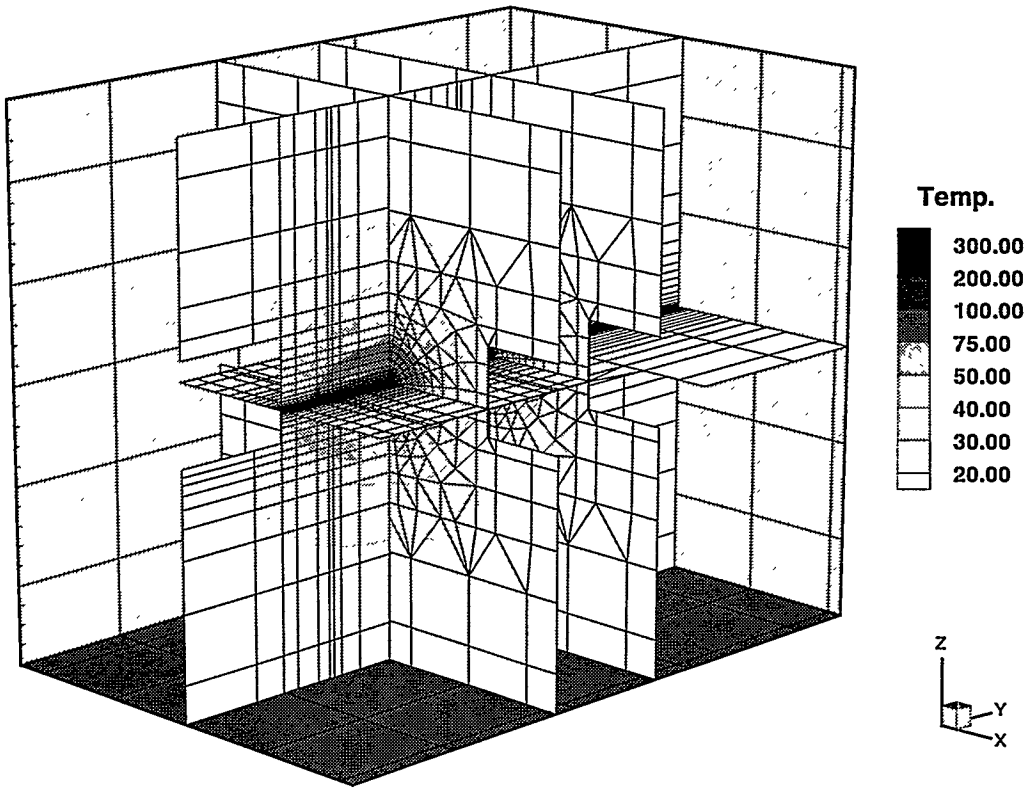

ERNEST ORLANDO LAWRENCE
BERKELEY NATIONAL LABORATORY
ONE CYCLOTRON ROAD,
BERKELEY, CALIFORNIA 94720

This work was prepared under the Office of Civilian Radioactive Waste Management, U.S. Department of Energy Contract No. DE-AC03-76SF00098.

Table of Contents

Forecast of Thermal-Hydrological Conditions and Air Injection Test Results of the Single Heater Test

Level 4 Milestone SP918M4

J. T. Birkholzer and Y.W. Tsang
Earth Sciences Division, LBNL
1 Cyclotron Road, Mailstop: 90-1116
Berkeley CA 94720

1 Introduction

The heater in the Single Heater Test (SHT) in alcove 5 of the Exploratory Studies Facility (ESF) was turned on August 26, 1996. A large number of sensors are installed in the various instrumented boreholes to monitor the coupled thermal-hydrological-mechanical-chemical responses of the rock mass to the heat generated in the single heater. In this report we present the results of the modeling of both the heating and cooling phases of the Single Heater Test (SHT), with focus on the thermal-hydrological aspect of the coupled processes. Also in this report we shall present simulations of air injection tests which will be performed at different stages of the heating and cooling phase of the SHT.

The most prominent thermal-hydrological response of the rock mass to the heater power output is the initial drying of the rock mass surrounding the heater, the carrying away of moisture in the form of vapor from the heated area, and the subsequent condensation of the vapor in the cooler regions of the rock mass farther away from the single heater. As the power output of the single heater is turned off during the cooling phase, rewetting occurs as water moves back to the vicinity of the heater under the driving force of the capillary suction. These vaporization, drying, condensation and rewetting processes are reflected in the spatial variation and temporal evolution of the liquid saturation in the rock mass, which in turn affect the spatial and time dependence of the air permeability values. In each of the two hydrology holes 16 and 18 in the SHT block, four inflatable high-temperature packers have been installed and pressure and humidity sensors are placed behind each packer. The above instrumentation allows air injection tests to be performed in different zones in each borehole. The pressure response in each of the eight monitoring sensors to air injection in different zones in both holes 16 and 18 measures the integrated air permeability between the injection zone and the pressure monitoring zone. In this report we present simulations of air injection tests at different stages of the heating and cooling phase of the Single Heater Test. These simulations are intended to capture how the pressure response of the different zones

in holes 16 and 18 may be utilized to reveal the thermal-hydrological evolution of the SHT environment.

The numerical simulations presented in this report are performed in three dimensions with the multi-component, multi-phase flow simulator TOUGH2 (Pruess, 1987 and 1991). The configuration, parameters, initial and boundary conditions of our numerical model are designed to resemble the actual Single Heater Test as closely as possible. Furthermore, all site specific characterization data such as laboratory measurements of thermal and hydrological properties of cores from the SHT block, fracture mapping of the drifts in the thermomechanical alcove, in-situ air permeability characterization, and borehole video logs are incorporated into our conceptual model for the numerical simulations of the Single Heater Test. Even so, due to the complexity of the multiple physical processes, and uncertainty in key input parameters such as fracture properties, it is to be expected that the simulated results from any one conceptual model will deviate from actual data. Therefore we also include in this report a number of sensitivity studies carried out in both two dimensions and three dimensions. These will provide insight as to how individual processes and input parameters affect the thermal-hydrological performance, and will aid us to later refine and calibrate the conceptual model against real data.

Thermal-hydrological numerical simulations of the Single Heater Test will be presented for heating phases of both nine months and one year. These will serve as input to help the Thermal Testing Team to determine the actual period of heating to be implemented in the Single Heater Test.

2 QA Status of Work

The work performed in this study is documented in Yucca Mountain Project Scientific Notebook YMP-LBNL-JBH-1. For input to this study, LBNL has used data collected under an approved YMP Quality Assurance Program whenever possible. The software packages used during this study include standard spreadsheets and visualization and plotting programs. Such programs are not subject to QA requirements under QARD Rev. 5. The software used to simulate thermal-hydrological conditions in the Single Heater Test is the TOUGH2 code (Pruess, 1987 and 1991). This program has been qualified under an approved YMP QAP (Pruess et al., 1996).

Table 2-1 presents a summary of the Q data used in this study. The table presents a description of the data, the collecting organization, Q status, and data tracking number (DTN) used to identify the data for the YMP.

Table 2-1 Study data summary and Q status

Data Type, Organization	Q - Status	DTN
Fracture permeability, density, porosity, water content field and lab experiments in SHT area, LBNL, Y. Tsang	Y	LB960500834244.001
Core analysis for density, porosity borehole UE-25 UZ#16, USGS, L. Flint	Y	GS940508312231.006
Physical properties, water potential of core borehole USW NRG-6, USGS, L. Flint	Y	GS950608312231.007
Physical properties, water potential of core borehole USW SD-9, USGS, L. Flint	Y	GS950308312231.004
Physical properties, water potential of core borehole USW UZ-14, USGS, L. Flint	Y	GS950608312231.005
Physical properties, water content, water potential borehole USW SD-7, USGS, L. Flint	Y	GS951108312231.009
Physical properties, water content, water potential borehole USW UZ-7a, USGS, L. Flint	Y	GS951108312231.011
Physical properties, water content borehole USW NRG-7/7A, USGS, L. Flint	Y	GS951108312231.010
Lab measurements of density, porosity, water content borehole USW UZ-7a, USGS, L. Flint	Y	GS951108312231.011
Lab measurements of thermal conductivity four tuff samples from SHT block, SNL, S.R. Sobolik	Y	SNL22080196002.002
Lab measurements of heat capacity samples from Tptpmn, SNL, S.R. Sobolik	Y	SNL01C12159302.002
Borehole videos LANL, A. Mitchell	Y	NA See reference in Section 7.
Y = Yes, NA = not available, N = No		

The main conclusions of this report are based on qualified data and qualified software. However, it was necessary to use some data sets containing Thermal Test Facility site-specific data which were still in review and not qualified at the time the report was written (e.g. fracture mapping, test block geometry). They are expected to become officially qualified records soon. Other data, in particular the fracture van Genuchten parameters, were estimated from different sources (see Section 3.3), and are not qualified. Currently, qualified fracture van Genuchten parameters are being developed at LBNL based on fracture data collected by the USGS during FY96. As all these data become qualified, this study can be extended to provide fully qualified results.

3 Problem Definition

3.1 Single Heater Test Configuration

Figure 3.1.1 shows the layout and borehole arrangement in the Single Heater Test. Figure 3.1-2 shows the configuration of the Single Heater Test with dimensions. The test block is surrounded by the Access/Observation Drift to the north, the Thermomechanical Alcove to the west, and the Thermomechanical Alcove Extension to the south. A 4-KW heater of 5 m length has been placed in the horizontal borehole 1 collared on the west wall. The near end of the heater is located approximately 2 m into the rock from the wall. The three rock surfaces exposed to the alcoves and drift are covered with a 15.2 cm thick layer of insulation material with plastic backing. The same insulation material is used to backfill the first 2 m of the heater hole 1. No insulation is used for the ceiling and the floor of the alcoves.

All coordinates in this report are given relative to the location of the heater hole 1. The origin of the coordinate system is at the collar of the heater hole. The positive X - axis points horizontally and approximately south (perpendicular to the heater); the positive Y - axis points horizontally and along the heater axis approximately east; and the positive Z - direction points vertically upward from the origin. The heater collar is located 1.52 m from the floor of the Thermo-mechanical Alcove; the distance to the north wall of the test block is 6.59 m, and the distance to the south wall of the test block is 6.26 m. The Thermomechanical Alcove Extension extends 9.5 m along the south wall of the block.

Air injection tests are to be performed in the hydrology holes 16 and 18 throughout the heating and cooling phases of the Single Heater Test. Boreholes 16 and 18 are collared on the south wall of the test block in the Thermomechanical Alcove extension. Both holes are parallel to and are at approximately the same distance from the west wall: about 4.25 m for 18 and 4.27 m for 16. Hole 18 is almost horizontal with a length of 4.66 m. Hole 16 has a slightly positive slope with a length of 5.10 m. The diameter of the boreholes is 7.57 cm. The collar height above floor for holes 16 and 18 is 1.56 m and 1.30 m, respectively.

The hydrology holes 16 and 18 are each installed with four high-temperature packers, labeled as P_1, P_2, P_3, and P_4 in Figure 3.1-3. Each packer measures 63.5 cm, and the spacing between two packers is 6.35 cm. Behind each packer and in the center of the 6.35 cm interval are housed a high-temperature pressure transducer and a humicap which measure both the relative humidity and the temperature. The positions of these sensors are labeled as 18-1, 18-2, 18-3, 18-4, 16-1, 16-2, 16-3 and 16-4, respectively. The top of the first packer P_1 is located at a distance of 29 cm

and 38 cm respectively from the collar of the holes 16 and 18. Table 3.1-1 gives the coordinates of the sensors with respect to the heater hole collar.

Table 3.1-1 Sensor locations in hydrology holes 16 and 18 given with respect to the heater hole collar

Sensor ID	X - coordinate (m)	Y - coordinate (m)	Z - coordinate (m)
16-1	5.233	4.271	0.191
16-2	4.540	4.274	0.283
16-3	3.848	4.277	0.375
16-4	3.155	4.280	0.467
18-1	5.120	4.255	-0.205
18-2	4.422	4.254	-0.215
18-3	3.723	4.252	-0.224
18-4	3.025	4.250	-0.234

An air injection line is associated with each packer so that air can be injected behind each packer. By selectively deflating different packers, various injection zones for each hydrology hole are formed. The three injection test configurations included in our simulations are: (1) deflate packer P_2 and use the air injection line for P_1, (2) deflate packer P_3 and use the air injection line for P_2, (3) inflate all four packers and use the air injection line for P_4. These three configurations are denoted by Zone 1, Zone 2 and Zone 3, respectively in Figure 3.1-3. It should be noted that all four packers in the monitoring hole are always inflated so that pressure response can be monitored in each of the four sensors.

3.2 Conceptual Model

The Single Heater Test block is located in the Topopah Springs Middle Non-Lithophysal unit at Yucca Mountain (Tptpmn). For model input we rely on the measured data from the Tptpmn unit, and, where ever possible, site specific data from the Thermomechanical Alcove in the ESF is incorporated in the numerical model.

The welded Topopah Springs tuff formation in which the Single Heater Test block resides is known to be densely fractured. Fracture maps of the alcove drift walls reveal that there are two subvertical joints sets three to four meters in extent (Characterization of the ESF Thermal Test Area, CRWMS M&O Document No. B00000000-01717-5705-00047 Rev 01, September 1996; Tsang et al., 1996). These subvertical joints sets were very much in evidence in the borehole video logs of the 27 instrumented boreholes in the SHT block (Mitchell, 1996).

For our thermal-hydrological simulations, the welded formation is conceptualized as composed of both the matrix continuum with very low permeability, and the fracture continuum with permeability orders of magnitude higher than that of the matrix continuum. Different capillary pressure and relative permeability characteristic curves will be assigned to the matrix and fracture continuum. For the 3D simulations, the matrix and fracture continua are assumed to be in thermodynamic equilibrium, that is, the matrix and fracture are characterized by the same temperature and pressure at all times (Effective Continuum Model: ECM, Pruess et al., 1990; Bodvarsson & Bandurraga, 1996). Under such an assumption, the combined effective continuum phase permeability k_b of phase b is the sum of the fracture and matrix continuum phase permeabilities, given as

$$k_b = k_m k_{r,m} + k_f k_{r,f} \tag{3.2.1}$$

and the combined effective continuum phase saturation S_b is given as

$$S_b = \frac{S_{b,m}\phi_m + S_{b,f}\phi_f}{\phi_m + \phi_f} \tag{3.2.2}$$

where k_m (k_f) is the saturated continuum permeability of the matrix (fractures), $k_{r,m}$ ($k_{r,f}$) is the relative permeability to phase b in the matrix (fractures), $S_{b,m}$ ($S_{b,f}$) is saturation of phase b in the matrix (fractures), and ϕ_m (ϕ_f) is porosity of the matrix (fractures). In one of the sensitivity studies in 2D, the effective continuum assumption is relaxed and a dual permeability model is implemented (see Section 6.4).

Ambient (pre-heat) characterization of the SHT Area by air injection tests has shown that the local air permeability for the boreholes tested ranges from 5.0×10^{-15} m^2 to 5.2×10^{-12} m^2 as shown in Figure 3.2-1. In addition to air injection tests for the entire borehole, some boreholes were also packed off in shorter sections (0.635 m to 3 m), and their local air permeability tested (Characterization of the ESF Thermal Test Area, CRWMS M&O Document No. B00000000-01717-5705-00047 Rev 01, September 1996; Tsang et al., 1996).

The air permeability values for all boreholes and straddled sections tested are shown in Figure 3.2-2. The two lowest values of 10^{-16} m^2 are not actual permeability values but in fact represent measurements that show practically impermeable behavior. The median for all the air permeability values shown in Figure 3.2-2 is 5.85×10^{-14} m^2. In that same report on characterization of the ESF Thermal Test Area it is also shown that in those boreholes with large permeability values, a few discrete fracture zones within the borehole account for all the air flow from the entire borehole.

A further study of the cross hole interference pressure response of the air injection tests performed prior to turning on the heat reveals the presence of a direct flow path from borehole 11 to boreholes 7, 13, and 12. In other words, an almost identical steady state pressure response is observed in boreholes 7, 13, and 12 as that in borehole 11 when air is injected in borehole 11. While boreholes 11 and 12 both originate from the west face of the test block, boreholes 7 and 13 are collared on the south face of the test block. On the other hand, boreholes 28, 29, 30, and 31 (which are collared also on the west face, and which are situated between boreholes 11 and 12 in very close proximity to borehole 11) register little pressure increase in response to air injection in hole 11, indicating that they hardly communicate with borehole 11.

An examination of the borehole video logs for holes 11, 7, 13 and 12 show discrete zones of open unfilled fractures in these four holes lying in a common vertical plane and having a strike azimuth of 40° (the angle is defined so that north is 18°, and the positive X-axis in Figure 3.1-2 is 198°). Fracture mapping in the thermal alcove (Characterization of the ESF Thermal Test Area, CRWMS M&O Document No. B00000000-01717-5705-00047 Rev 01, September 1996) shows that there is indeed one subvertical joint set with the strike azimuth angle 40 ° and having a spatial extent of three to four meters. Hence the presence of a vertical high-permeability feature with strike azimuth 40° extending 4 meters and starting from just below the boreholes 8 and 10 is consistent with the pressure interference data in the Single Heater Test block. Such a high-permeability feature can account for the fast pressure response in holes 7, 13 and 12, the much weaker response in 8 and 10, and the non-response of the pressure data in boreholes 28, 29, 30 and 31, since these holes are too short to intersect this vertical fracture.

Figure 3.2-3 shows the steady state pressure response in all instrumented boreholes to the air injection in hole 11, performed at pre-heat conditions. The pressure increase in each borehole is normalized to that in hole 11 and coded in rainbow colors, with red denoting the largest pressure increase. In the figure is also shown a vertical plane intersecting boreholes 11, 7, 13, and 12, representing the high-permeability feature which accounts for the large pressure responses in the air injection tests described above.

In the 3D simulations presented here a conceptual model is used for the fracture continuum which is consistent with the interference air injection data. A high-permeability feature with a permeability value of $5.2 \times 10^{-12} m^2$ is superposed on the homogeneous background which is given a lower permeability of $5.85 \times 10^{-14} m^2$. In addition to this so-called "Base Case", a homogeneous model is studied with the uniform background permeability value assigned to the fracture continuum throughout the entire test block.

The significance of certain physical processes in affecting the thermal-hydrological performance of the Single Heater Test is evaluated in sensitivity studies. One is the effect of enhanced vapor

diffusion. The diffusion coefficient D_{va} for the vapor-air mixture in a porous medium is given by (Vargaftik, 1975; Walker et al., 1981)

$$D_{va} = \tau\phi S_g D^{o}_{va} \frac{P_o}{P}\left[\frac{T}{T_o}\right]^{\theta} = \beta D^{o}_{va} \frac{P_o}{P}\left[\frac{T}{T_o}\right]^{\theta} \qquad (3.2.3)$$

Here, D^{o}_{va} is the free-space diffusion coefficient, θ is a factor for temperature dependence, ϕ is the porosity, S_g is the gas saturation, τ is the tortuosity factor, and T_o and P_o are standard conditions of 273.15 K and 1 bar. The parameter group $\beta = \tau\phi S_g$ represents the reduction of diffusion strength in a porous medium and is usually on the order of 0.01. However, experimental evidence in the soil science literature indicates that vapor diffusion may be greatly enhanced due to pore level phase change effects so that the parameter group β is typically in the range of 1 to 3.5 for a variety of partially saturated porous media (Jury & Letey, 1979, and references in Tsang & Pruess, 1990). It is not known whether the same phenomenon is also present in the welded tuff. If present, it has the effect of providing a more efficient mechanism for moving vapor away from the heater. In our study, ordinary binary diffusion is assumed for the simulations in 3D, and the effect of enhanced vapor diffusion is studied in 2D in the sensitivity simulations.

3.3 Input Parameters

As stated earlier, for model input we rely on the measured data from the Tptpmn unit, and, when possible, site specific data from the Thermomechanical Alcove in the ESF is incorporated. Most of the input data are qualified. However, it was necessary to use some data sets containing Thermal Test Facility site-specific data which were still in review and not qualified at the time the report was written. Some data, such as fracture van Genuchten parameters or vapor diffusion θ and τ, are non qualified. We shall discuss the input parameters item by item as follows, marking the value chosen for the "Base Case" in bold:

Matrix Liquid Saturation

The initial matrix liquid saturation in the SHT block prior to the turning on of heat is taken to be **0.92**. This is the value given for borehole SD9 (Flint, 1996). This high matrix saturation is consistent with the laboratory data from grab samples obtained directly from the Thermomechanical Alcove (Characterization of the ESF Thermal Test Area, CRWMS M&O Document No. B00000000-01717-5705-00047 Rev 01, September 1996; Tsang et al., 1996) where values ranging from 0.805 to 0.99 are reported.

Matrix Porosity

The mean value of all boreholes in the Tptpmn is reported to be **0.11** (Flint, 1996).

Matrix Permeability

The value of **4.0 x 10^{-18} m^2** as given in Flint (1996) is assumed for our 3D simulations. Matrix permeability measurements are available only for boreholes SD9 and UZ16. However, because of the low apparatus threshold of 10^{-20} m^2, many of the permeability measurements are biased. If all the small permeability values below the threshold are removed, one is left with one measured value for SD9 and 10 measured values for UZ16, giving the above average of 4.0 x 10^{-18} m^2 as reported by Flint (1996). If the small values were not removed, an average of 1.56 x 10^{-20} m^2 would result. This small value is used in the pretest design calculations for the Single Heater Test by Sandia (Sobolik et al., 1996).

Matrix van Genuchten Parameters

The capillary suction and the relative permeability ***for liquid*** have the following functional form

$$P_{cap} = -\frac{1}{\alpha}\left\{\left(S_{l,eff}\right)^{-\frac{1}{m}} - 1\right\}^{\frac{1}{\beta}}$$
$$k_{rl} = \left(S_{l,eff}\right)^{\frac{1}{2}}\left\{1-\left(1-\left(S_{l,eff}\right)^{\frac{1}{m}}\right)^{m}\right\}^{2} \qquad (3.3.1)$$

where P_{cap} is capillary pressure, $k_{r,l}$ is liquid relative permeability, $S_{l,eff}$ is liquid effective saturation, $1/\alpha$ is a capillary scaling factor (air entry pressure), β is pore size distribution coefficient, and m is equal to $(1-1/\beta)$. Matrix van Genuchten parameters have been measured in three samples from UZ16. Values as given in Flint (1996) are **6.4 x 10^{-7} Pa^{-1}** for α ($1/\alpha$ =1.5625 MPa) and **1.47** for β (i.e. m = 0.32). The residual liquid saturation is **0.18**. These are the same values that have been used in the pretest design calculations for the Single Heater Test by Sandia (Sobolik et al., 1996).

In this study, the relative permeability ***for gas*** is derived from the Brooks-Corey formulation as follows

$$k_{r,g} = \left(1-S_{l,eff}\right)^{2}\left(1-S_{l,eff}^{\left(\frac{2+\lambda}{\lambda}\right)}\right) \qquad (3.3.2)$$

with λ chosen to 2. Often, the gas relative permeability is calculated as $(1 - k_{r,l})$, where $k_{r,l}$ is the liquid relative permeability. This, however, gives large gas relative permeability values even for very small gas saturations because the liquid relative permeability decreases very fast with saturation.

Matrix Grain Density

The value of **2540 kg/m^3** is derived from laboratory measurements of cores from the Single Heater Test area (Characterization of the ESF Thermal Test Area, CRWMS M&O Document No. B00000000-01717-5705-00047 Rev 01, September 1996).

Rock Mass Thermal Properties

Laboratory measurements of cores from the Single Heater Test Area give an average value of thermal conductivity of **1.67 W/(m °K)**. No effort was made in the experiments to distinguish between "dry" and "wet" thermal conductivity. Thus, we assume a constant value for all conditions. The heat capacity is taken to be the average from the Tptpmn unit, **928.0 J/ (kg °K)**, which was also used in the pretest calculations by Sandia (Sobolik et al., 1996).

Heater Output

Average power of **3.861 kW** is assumed for the 5 m heater. This value is the actual average of the heater output in the Single Heater Test during the month of September 1996.

Vapor Diffusion Parameters

Reasonable numbers for the vapor diffusion coefficient are $D^{\circ}_{va} = 2.14 \times 10^{-5}$ **m^2/s**, and $\theta = 2.334$ for temperature dependence, after Pruess & Tsang (1994). A reasonable number for the tortuosity of the path followed during the gas diffusion process is $\tau = 0.2$.

Fracture Porosity

We use the value of **0.000243** as given by the LBNL UZ Site-Scale model (Bodvarsson and Bandurraga, 1996) for the Tptpmn layer. Values ranging from 0.000132 to 0.00146 were used in the pretest analysis of the SHT by Sandia (Sobolik et al., 1996).

Fracture Permeabilities

These values are taken from the air permeability measurements of the Single Heater Test (Characterization of the ESF Thermal Test Area, CRWMS M&O Document No. B00000000-01717-5705-00047 Rev 01, September 1996; Tsang et al. 1996) as discussed in the previous Section 3.2.

Fracture van Genuchten parameters

The capillary suction and the relative permeability for liquid as well as gas in fractures have the same functional form as given by Equations 3.3.1 and 3.3.2 for the matrix. No measurements exist for the functional parameters. Calibrated values from the UZ site scale model of α range from 1.22×10^{-4} Pa^{-1} to 1.37×10^{-3} Pa^{-1}. Values of 1.2×10^{-4} Pa^{-1} to 1.3×10^{-3} Pa^{-1} are used in the pretest analysis of the SHT by Sandia (Sobolik et al., 1996). In our model we shall assume an air entry value of 1000 Pa (i.e. $\alpha = 1.0 \times 10^{-3}$ **Pa^{-1}**). The van Genuchten β is chosen to **1.47**, a value similar to the respective matrix parameter. This is lower than the value of 3.0 used in the pretest

analysis by Sandia (Sobolik et al., 1996). By choosing a smaller value for β we account for the aperture variation in natural fractures, giving rise to a less rigid draining/wetting behavior than in fractures idealized as parallel plates. In the latter case fractures would be either totally dry or completely saturated, which can be modeled by prescribing higher β values (such as the value of 3.0). Residual liquid saturation for the fracture continuum is chosen to be **0.01** for the simulations presented in this report, which is in the range of values used in previous studies.

Fracture Liquid Saturation

The underlying assumption in the Effective Continuum Model is that there is thermodynamic equilibrium between the matrix and fracture continua at all times. Therefore the initial fracture liquid saturation in the SHT block can be derived from the given matrix initial saturation value, using the above given van Genuchten relationships and parameters for matrix and fractures. For the assumed matrix saturation of 0.92, the fracture initial saturation is **0.052**. (In some studies the effective continuum concept has been used by applying a somewhat arbitrarily chosen threshold saturation value lower than 100 %. Water is only allowed to enter the fractures when the matrix saturation exceeds this threshold value (Bodvarsson & Bandurraga, 1996). In our study no such threshold saturation is implemented.)

Table 3.3-1 lists all the hydrological and thermal input values used for the SHT analyses, and also indicates parameter variations considered in a sensitivity study. Figures 3.3-1 and 3.3-2 show the van Genuchten relationships for capillary pressure and liquid relative permeability for both matrix and fractures with the parameters given above.

Since the capillary suction in the matrix is much stronger than the capillary suction in the fracture, local equilibrium implies that the liquid saturation in the fractures will remain near zero until the matrix saturation approaches 100 %. Therefore, liquid flow in fractures will only become significant for matrix saturations very close to 1. This is exemplified in Table 3.3-2 which presents equilibrated matrix and fracture saturations for different capillary pressures and provides respective liquid phase continuum permeabilities for fractures and matrix. In the last two columns of the table are shown the percentage of flow in the fracture and matrix continua, respectively. It is clear from the table that fracture flow is negligible in most of the range given; it becomes relevant only when the matrix saturation is higher than 99.95 %. At full saturation, however, fracture flow exceeds matrix flow by orders of magnitude. In light of the sensitivity of fracture flow to liquid saturation, caution is needed in the interpretation of the simulated fracture liquid flow rates, given the fact that no measurements exist for the fracture van Genuchten parameters. Furthermore, it has been suggested recently that, although the bulk of the fractures will be drained at matrix saturations close but smaller than 100 %, a thin film of liquid remains present on the walls of drained fractures, and may actually account for significant liquid flow (Tokunaga & Wan, 1996). This film flow mechanism has not been incorporated into our conceptual model for the simulations presented in this report.

Table 3.3-1 Hydrological and thermal input values

Parameter	Value	Parameter Variation
Initial Matrix Liquid Saturation	0.92	0.98
Matrix Porosity	0.11	
Matrix Permeability	4.0×10^{-18} m^2	4.0×10^{-20} m^2
Matrix VG α	6.4×10^{-7} Pa^{-1}	
Matrix VG β	1.47	
Matrix Residual Liquid Saturation	0.18	
Matrix Grain Density	2540.0 kg/m^3	
Initial Fracture Liquid Saturation	0.052	0.08
Fracture Porosity	0.000243	
Fracture Permeability (homogeneous background)	5.85×10^{-14} m^2	5.2×10^{-12} m^2
Fracture Permeability (high-permeability feature)	5.2×10^{-12} m^2	
Fracture VG α	1.0×10^{-3} Pa^{-1}	
Fracture VG β	1.47	
Fracture Residual Liquid Saturation	0.01	
Rock Mass Thermal Conductivity	1.67 W/(m °K)	
Rock Mass Heat Capacity	928.0 J/(kg °K)	
Heater Power	3861 W	
Vapor Diffusion Coefficient Factor for Temperature Dependence Parameter Group β	2.14×10^{-5} m^2/s 2.334 from $\beta = (\tau\phi S_g)$, $\tau = 0.2$	 $\beta = 1.0$

Table 3.3-2 Liquid saturation, permeability, and percentage of liquid flow in the matrix and fracture continua in the Effective Continuum Model.

P_{cap}	$S_{l,m}$	$(k_m k_{r,m})$	$S_{l,f}$	$(k_f k_{r,f})$	Matrix Flow in %	Fract. Flow in %
8.07E+05	0.9200	4.36E-19	0.0524	3.50E-24	100.00	0.001
6.38E+05	0.9400	5.91E-19	0.0574	7.37E-24	100.00	0.001
4.67E+05	0.9600	8.30E-19	0.0659	1.99E-23	100.00	0.002
2.81E+05	0.9800	1.26E-18	0.0797	9.98E-23	99.99	0.008
1.72E+05	0.9900	1.68E-18	0.0977	4.71E-22	99.97	0.028
1.07E+05	0.9950	2.06E-18	0.1199	2.16E-21	99.90	0.105
9.15E+04	0.9960	2.18E-18	0.1282	3.52E-21	99.84	0.162
7.51E+04	0.9970	2.31E-18	0.1396	6.59E-21	99.72	0.284
5.69E+04	0.9980	2.49E-18	0.1577	1.59E-20	99.37	0.632
3.55E+04	0.9990	2.77E-18	0.1944	7.11E-20	97.50	2.505
2.21E+04	0.9995	2.99E-18	0.2398	3.16E-19	90.45	9.547
1.56E+04	0.9997	3.14E-18	0.2801	9.44E-19	76.87	23.130
7.40E+03	0.9999	3.38E-18	0.3898	9.64E-18	25.97	74.030
0.00E+00	1.0000	4.00E-18	1.0000	5.85E-14	0.007	99.993

4 Three-Dimensional Thermal-Hydrological Simulation

Three-dimensional thermal-hydrological simulations of the Single Heater Test are performed with the multi-component, multi-phase code TOUGH2. The effective continuum approach (ECM) is applied to account for the combined effect of the matrix and the fracture continua. The simulations were performed under the following assumptions:

- The thermal-hydrologic calculations presented in this section provide input for the simulation of air injection tests which are performed at different stages of the heating and cooling phase of the Single Heater Test (see Section 5). In the simulation runs, we assume that injection tests are performed at 77 days, 6 months, 9 months and 12 months after the heater has been turned on. (The first time of 77 days was originally chosen to coincide with the date of the first planned field test in hydrology holes 16 and 18. Unfortunately, instrument problems were encountered and the actual measurements were not obtained until three months after the heater was turned on.) In the cooling phase, injection tests will be performed at three-month intervals.
- In the Base Case, the heater is assumed to operate at 3.861 kW for one year. The simulations cover this heating period plus a 12 month cooling period after the heater is turned off. In addition, the impact of a shorter 9 month heating phase is studied.
- In the Base Case, the permeability values assigned to the fracture continuum account for a local high-permeability feature which is superposed on a lower background permeability. All other hydrologic properties of fractures and matrix are uniform throughout the test block. The values of hydrologic properties are given in Section 3.3. In addition to the heterogeneous Base Case, we also study a completely homogeneous test domain.
- Liquid saturation is assumed to be initially uniform throughout the test block. In the Base Case, the initial matrix saturation is 0.92. An additional case with a higher initial matrix saturation of 0.98 is studied.
- All the four 3D runs described here - the Base Case, the cases with the shorter heating period, homogeneous model domain, and higher initial saturation - will be used in the 3D air permeability studies presented in Section 5.
- More thermal-hydrological simulations were performed in 2D to study the sensitivity of individual processes and input parameters.
- Isotropy is assumed for all thermal-hydrologic properties.
- Except for the backfill in the heater hole, we assume rock properties for all the boreholes, thus making the implicit assumption that wiring, grouting, and instrumentation in the test block does not affect the thermal-hydrological behavior.

4.1 Grid Design, Boundary and Initial Conditions

The computational domain for the thermal-hydrological simulations includes the entire test block plus significant rock volumes added in all directions to guarantee a proper definition of boundary conditions.

Figure 4.1-1 shows a XZ - cross section of the discretization grid. The origin of the computation coordinates is at the collar of the heater hole 1. Fine gridding and radial symmetry is maintained around the heater hole up to a radius of 2.8 m, at which distance the grid is converted gradually to cartesian in order to better represent the boundaries of the drift and alcove walls. The size of the grid blocks increases with distance to minimize the number of computational elements. The radial increments start as small as 2.2 cm at the heater hole (Radius 4.8 cm) and increase up to 40 cm at a distance of 2.8 m.

The top and bottom boundaries of the test block are 14 m each from the heater hole; they are sufficiently far from the heater that they can safely represent infinity conditions (i.e., constant primary variables). The north and south boundaries are each extended to the outer walls of the alcoves, with the alcove geometry being explicitly modeled by eliminating grid blocks. The distance from the heater centerline to the south boundary is 10.76 m, which is defined by the 6.26 m distance from the heater to the alcove inner wall plus the 4.5 m alcove width. The north boundary is at 11.59 m, defined by the 6.59 m distance to the Access/Observation Drift wall and the 5.0 m drift width. Both north and south boundaries are modeled as no-flow boundaries for heat, liquid and gas. The floor and the ceiling of the alcoves are not insulated; thus they represent boundaries with constant primary variables.

The alcove walls facing the test block are insulated with a very low thermal conductivity material. This insulation is explicitly modeled, it is 15.2 cm thick, has a 0.0447 Watt/(m^2 K) thermal conductivity, a density of 32 kg/m^3, and a heat capacity of 835 J/(kg K) (values provided by N. Francis, Sandia National Laboratories, personal communication, 1996, to be qualified by Sandia). However, the surfaces are assumed to be open for moisture to escape from the test block in the form of both liquid water and vapor.

Nineteen element layers have been discretized in the Y - direction (along the heater axis, perpendicular to the XZ - cross section shown above). Figure 4.1-2 shows a vertical cross section (i.e. YZ - plane) of the discretization at X = 0.0 m, and Figure 4.1-3 shows a horizontal cross section (i.e. XY - plane) of the discretization grid at Z = 0.0. A three-dimensional view of the model grid is depicted in Figure 4.1-4, it consists of 9016 grid blocks. (Note that the displayed grids in Figures 4.1-2 to 4.1-4 do not show the actual interfaces between grid blocks in the finite difference discretization. The post-processing software automatically designs a mesh by connecting the center nodes of each finite difference grid. These post-processed meshes are depicted here.)

Starting from the Thermomechanical Alcove wall at Y = -5.5 m, the first two element layers represent the rock volume above and below the alcove (-5.5 m < Y < 0.0 m), the next five layers represent the 2 m standoff between the west wall and the heater (0.0 m < Y < 2.0 m), the next six elements represent the 5 m heater extension (2.0 m < Y < 7.0 m), and the last 6 elements extend behind the heater up to a no-flow boundary at Y = 17.0 m. The front boundary at Y = -5.5 m is also modeled with a no-flow condition. Similar to the other alcoves in the XZ - cross section, the floor and ceiling of the Thermomechanical Alcove have been assigned a constant primary variable boundary, while the insulation on the wall is explicitly modeled with the above given parameters. The same insulation material is used to backfill the first 2 m of the heater hole. Each of the 19 layers has a similar discretization in the XZ - plane, except for the first two and the last two layers which are slightly different to account for the alcove geometry.

Figure 4.1-3 also indicates the location of the localized subvertical fracture zone with higher permeability (compare to Figure 3.2-3). The 40° strike azimuth feature is represented by extending the fracture zone over three different element layers in the XY - plane. In the Z - direction, the high-permeability zone extends from -2.8 m to 1.2 m.

The initial conditions for the model domain are chosen as 87.0 kPa for the gas pressure, 25 °C for temperature, and 0.92 for the matrix saturation. The corresponding fracture saturation is 0.052. Then, the effective continuum liquid saturation derived from Equation 3.2.2 is 0.918. This value is very close to the matrix saturation since the majority of the pore space in the rock mass is provided by the matrix pores. No geothermal gradient is assigned because of the small vertical extension of the model. A typical geothermal gradient of 0.02 °C/m would only give a temperature difference of 0.56 degrees between the top and the bottom boundary, which is negligibly small compared to the temperature perturbation enforced by the heater.

The above given initial values for gas pressure, saturation and temperature are also used to define the infinity (constant primary variable) boundaries at the top/bottom of the model domain, and at the alcove walls. Note that the alcove walls are open for liquid and gas to escape from the model domain; however, no liquid or gas is allowed to enter the model domain from the alcoves.

4.2 Simulation Results for the Base Case

Contour plots of the predicted thermodynamic behavior for the Base Case are presented in Figures 4.2-1 to 4.2-18. Two XZ - cross sections are shown: one is located at Y = 4.25 m in the plane of boreholes 16 and 18, the other is located at Y = 6.0 m at the center of the high-permeability fracture zone. Note that the location of the test holes 16 and 18 is indicated in the respective figures for the XZ - cross section at Y = 4.25 m. Also a YZ - cross section is chosen intersecting the heater element (i.e. X = 0.0 m).

Figures 4.2-1 to 4.2-3 show the temperature response 1 year after the heater is turned on. The maximum temperature at the heater is about 300 °C. The 100 °C line is approximately at a 90 cm distance from the source, the 50 °C line at about 3.70 m. The temperature distributions near the heat source are symmetrical with respect to heater center line, indicating that the energy transport is conduction dominated. However, in all three cross sections it is evident, that at some distance from the heater the temperatures are influenced by the insulated alcove walls. The results for the Y = 4.25 m and the Y = 6.0 m cross section are very similar. The fracture heterogeneity has little effect on the temperature distribution.

Figures 4.2-4 to 4.2-6 depict the effective continuum liquid saturation at 1 year (which is essentially identical to the matrix saturation), showing significant differences from the initially uniform distribution. An approximately 1 m wide dry-out zone has developed around the heater. Moisture is carried away from the heated area in the form of vapor, mainly in the fractures because of the low matrix conductivity, and driven by the gas pressure gradient. In cooler regions the vapor condenses at the fracture walls, giving rise to an increase in liquid saturation in both fractures and matrix. Subsequently, the liquid, driven by capillary forces, migrates away from the condensation zone; the majority of it towards the boiling region, and smaller amounts outward. Because of the low matrix permeability, radial outflow of vapor exceeds radial inflow of liquid, giving rise to the drying around the heater. As can be clearly seen in Figure 4.2-5 for the XZ - cross section at Y = 6.0 m, the moisture distribution is non-symmetrical as a result of the enhanced vapor transport in the high-permeability fracture zone. This effect can also be seen in the other XZ - cross section at Y = 4.25 m; however, since this cross section does not intersect the high-permeability zone, it is less apparent.

Figures 4.2-7 to 4.2-9 present the liquid saturation in the fractures after one year. The condensation of vapor gives only a slight increase in the fracture saturation since most of the liquid is immediately drawn into the matrix by capillary suction. (Note that the *transient* behavior of this fracture-matrix interaction cannot be modeled with an ECM formulation, since local equilibrium is assumed at all times.) The very slight saturation increase implies that the saturation in the fractures remains close to residual, therefore the liquid in the fractures is essentially immobile. The liquid flow in the matrix is also slow because of the low matrix permeability. Therefore, gravity driven liquid flow is not apparent in the moisture distributions.

Figures 4.2-10 to 4.2-18 show a similar sequence of temperature and saturation distribution after 15 months, which is 3 months after the heater is turned off. The rock mass has cooled substantially; the maximum temperatures at this time are slightly over 40 °C. Now, in the absence of vaporization and condensation processes, the dominant mode of fluid movement is water flow through the matrix toward the heater under the driving force of capillary suction to rewet the dry-out region. However, the rewetting is much slower than the cooling because of the low matrix permeability.

As we are most interested in the impact of moisture redistribution on the air permeability values of the rock mass, we shall study the thermal-hydrologic conditions in the vicinity of the test holes 16 and 18 in more detail. Figures 4.2-19 to 4.2-26 show thermal-hydrologic properties along a horizontal sampling line in the test hole plane at Y = 4.25 m, extending from the heater hole at X = 0.0 m, Z = 0.0 m to the wall of the Thermomechanical Alcove Extension at X = 6.26 m, Z = 0.0 m. Results are presented at 77 days, 6 , 9, 12, 15, 18, 21 and 24 months. The heating period is 1 year. Temperature, liquid saturation in the matrix and liquid saturation in the fracture are plotted in each figure as a function of distance from the heater. The location of the sensors (pressure transducers, humicaps) and the bottom of test hole 18 is also labeled to give a better orientation. Air permeability tests are performed with injection zones extending from sensor 18-1 to 18-2 (Zone 1 in Figure 3.1-3), 18-2 to 18-3 (Zone 2 in Figure 3.1-3), and from 18-4 all the way to the end of the hole (Zone 3 in Figure 3.1-3). Hole 16 has a similar setup of packers and sensors as hole 18 with respect to their horizontal coordinates along the sampling line. The X - coordinates of 16-1, 16-2, 16-3, 16-4 are within 0.13 m of the corresponding sensors in hole 18 (see Table 3.1-1).

The temperature distributions show a distinct heat pipe region throughout the heating period. This region of liquid and vapor counter-flow is evidenced by the plateau in the temperature curve near 100 °C. The end of the heat pipe region coincides with the starting point of the condensation area where matrix and fracture saturations build-up. With time, the spatial pattern of dry-out, heat-pipe and condensation zones migrates radially outward, indicating that the vapor flux outflow rate is larger than the respective liquid counter-flow. However, comparing the results at 9 and 12 months indicates that the migration has already slowed down; the temperature and saturation distributions of the two time steps are similar. This indicates that a heating period of 9 months might be sufficiently long to yield meaningful test results.

During the entire heating period, boreholes 16 and 18 remain entirely in a wet environment; therefore all the relative humidity sensors are expected to register 100 % readings. Similarly, since gas pressure build-up due to heating occurs in the dry-out region (with a strong pressure decline in the adjacent heat pipe zone), and since the dry-out zone does not extend to the bottom of the boreholes, the pressure sensors in holes 16 and 18 are not expected to register readings much different from that of the ambient value of 87.0 kPa during passive monitoring either. During active testing by air injection, the readings in the pressure transducers are impacted by the moisture distribution. The strongest effect of moisture redistribution on the air permeability tests is expected for injection between sensor 18-4/16-4 and the bottom of the holes, because these zones coincide with the condensation area. Less impact is expected for injection in Zones 1 and 2 (compare to Figure 3.1-3) which are closer to the collar.

When the heater is turned off, the temperatures decrease rapidly, while the rewetting of the dried out areas is very slow. After a cooling period of one year, liquid saturations in the matrix remain

as low as 20 % close to the heater. However, the saturation peak which is observed in the condensation zone during heating flattens out faster. Thus we should expect significant differences in results for injection tests performed during heating and cooling.

In Figure 4.2-27 we compare simulation results after 3 months of cooling following heating periods of 9 and 12 months, respectively. Hollow symbols and dashed lines represent results for 9 month heating, solid symbols and lines denote results for 12 month heating (as shown before in Figure 4.2-23). Only minor differences are evident, and it can be expected that air permeability tests performed after 9 or 12 month heating will give comparable results.

4.3 Sensitivity to Fracture Continuum Conceptualization

In the Base Case the fracture medium consists of a high-permeability feature superposed on a low permeability fracture continuum. In this section, a homogeneous model domain is considered, with the fracture permeabilities set to 5.85×10^{-14} m^2 throughout the domain. The simulated moisture distributions are symmetrical now with respect to the heater center line, as is demonstrated in Figures 4.3-1 and 4.3-2 for the XZ - cross section at Y = 4.25 m. Temperature distributions in this cross section are identical to the Base Case, and are not shown here.

Figure 4.3-3 compares the Base Case and the homogeneous case with respect to temperatures and saturations along the X - axis at Y = 4.25 m and Z = 0.0 m at 1 year. As this sample line is outside the heterogeneous region, the differences between the homogeneous runs and the Base Case are very small. However, results for another horizontal sample line, which actually intersects the heterogeneous zone at Y = 6.0 m, show some differences. The heat pipe effect is less distinct in the homogeneous case because less vapor is driven away from the boiling area (Figure 4.3-4). Consequently, the matrix and fracture saturations in the condensation zone are smaller, because vapor condenses at a lower rate.

4.4 Sensitivity to Initial Saturation

In this section we assume a higher initial saturation in the rock mass. The matrix initial saturation is set to 98 %, which gives a fracture initial saturation of 8 %. Under this assumption, we expect higher saturations in the condensation zone around the heater, possibly resulting in (1) finite liquid mobility in the fractures, and (2) stronger pressure response to air injection tests.

Figures 4.4-1 to 4.4-3 depict temperature and saturation distributions for the XZ - cross section at Y = 4.25 m after 1 year of heating. The temperatures appear to be similar to the Base Case, with the apparent symmetry indicating mainly conductive heat transport. However, the maximum temperature close to the heater is only 280 °C compared to 300 °C in the Base Case. The saturation distributions show a more distinct vertical asymmetry than in the Base Case, with

higher saturations below the heater than above. This phenomenon might partially be due to gravity driven liquid flux in fractures; the main reason, however, is the asymmetric extension of the high-permeability fracture zone located behind the depicted cross section.

In Figure 4.4-4, we present temperatures and saturations along the X - axis for both the Base Case and for high initial saturation. The heat pipe effect is more distinct in the latter case because (1) initially more water is available to vaporize in the boiling zone, and (2) more liquid flows back from the condensation zone towards the heater. This results in a less extensive dry-out region and in slightly lower temperatures in the boiling zone as more heat is transported away from the heater by convection. Outside the dry-out zone, the saturation values in both fractures and matrix are significantly higher than in the Base Case. Temperatures, however, are almost identical outside the dry-out zone.

5 Air Injection Tests in Hydrology Holes 16 and 18

The field air injection tests in the hydrology holes 16 and 18 are intended to capture the spatial variation and temporal evolution of the liquid saturation in the rock mass as a result of vaporization, condensation, drying and rewetting during the heater test. In Figures 4.2-4 and 4.2-13 we have shown the effective continuum liquid saturation contours in the plane of the hydrology holes 16 and 18 as a function of time during the heating and cooling phase of the SHT. Furthermore, in Figures 4.2-7 and 4.2-16 we have also shown the liquid saturation in the fracture continuum at various stages of the test. It is clear from these liquid saturation contours that the pressure response to air injection in different zones will evolve with time.

For the following discussion we refer the reader to the geometry and instrument configuration of holes 16 and 18 as shown in Figure 3.1-3. The three alternative zones for air injection in each hole are (1) Zone 1 between packers P_1 and P_3, (2) Zone 2 between P_2 and P_4 and (3) Zone 3 between packer P_4 and the bottom of the borehole. It should be noted that all four packers in the monitoring hole are always inflated so that pressure response can be monitored in each of the four sensors. We do not simulate tests where injection is performed behind each packer when all four packers are inflated. This is because the small spacing of 6.35 cm between two consecutive inflated packers will incur very large local pressure build-up with even very little injected air, and unless these small zones directly intersect a high-permeability feature, a small amount of air injected is not useful for getting meaningful pressure responses from monitoring sensors that are farther away.

The single hole permeability values for holes 16 and 18 are respectively 8.3×10^{-15} m^2 and 8.8×10^{-14} m^2 (Tsang et al., 1996), which are on the lower end of the range of values found for the Single Heater Test block, and there is no indication of any high-permeability feature intersecting these holes. That very little air can be injected without incurring very high local pressure response in these short sections between two consecutive packers was indeed observed during field air injection tests for these two hydrology holes prior to the heater turn on.

A typical field test consists of injecting with a constant flow rate into a selected injected zone and monitoring the pressure response in all eight pressure transducers. Since a steady state pressure response is usually attained fairly rapidly, the constant flow rate injection never needs to last longer than half an hour before the injection can be stopped and the pressure decay monitored. The steady state pressure response from each sensor gives an estimate of the integrated air permeability between the injection zone and the monitoring sensor. For all results shown below, we simulate constant flow rate injection for one hour to insure that steady state pressure response in all sensors is reached.

The air injection simulation runs are performed in three dimensions with the simulator TOUGH2, using the Effective Continuum Model, which assumes a thermodynamic equilibrium between fractures and matrix at all times. In air injection tests we expect a very rapid pressure response in the fractures, and a slightly retarded response in the matrix, due to its low permeability. As this effect cannot be captured with the ECM approach, the simulation results might overestimate the response times in the fractures, while underestimating the response times in the matrix. However, as shown in Bodvarsson & Bandurraga (1996), this effect is minor, as the fracture/matrix interaction for gas is much faster than for liquid. Furthermore, for deriving air permeabilities from injection tests, we are mainly interested in the steady-state pressure response which is correctly simulated with the ECM.

5.1 Grid Design, Boundary and Initial Conditions

The 3D numerical grids shown in Figures 4.1-1 through 4.1-4 were designed to model the thermal-hydrological evolution of the Single Heater Test. In that case, a radial symmetry and fine gridding around the 5 m long heater is essential. On the other hand, for the air injection tests, it is crucial that the injection zones in boreholes 16 and 18 are explicitly gridded, and their actual volumes preserved. Just as important is the need for fine gridding around these two holes in order to simulate the pressure response to the air injection and the reading in the monitoring sensors properly.

Figures 5.1-1 and 5.1-2 show the numerical grid designed for the injection runs in a XZ - cross section in the plane of the boreholes. In the first figure, the entire grid is presented, the second figure shows a detailed view of the refined gridding in the vicinity of the hydrology holes. The test hole and the packer geometry are explicitly represented. Compared to the thermal-hydrological simulation in Section 4, the grid extension here is substantially smaller, since the pressure response to the air injection is not transmitted over long distances. The air injection grid extends in X - direction from the Access/Observation Drift wall on one side to the Thermomechanical Alcove Extension on the other side, and in Z - direction from -7.0 m to +7.0 m.

Fourteen identical layers have been composed in Y - direction to build the three-dimensional discretization which consists of 9940 grid blocks. The central layer in the test hole plane at Y = 4.25 m has a small width of 8 cm, chosen such that the actual hole volume is correctly represented. The adjacent layers are assigned widths of 7 cm, 18 cm, 46 cm, 1.50 m, and 2.25 m toward the direction of the Thermomechanical alcove, and 7 cm, 18 cm, 46 cm, 67 cm, 67 cm, 67 cm, 1.75 m, 3.0 m in the opposite (backward) direction. The different increments designed for the two directions are needed for two reasons, (1) because of the high-permeability feature behind the test hole plane, and (2) because the boundary conditions are set at different distances from the test hole plane. The front boundary is given by the wall of the Thermomechanical Alcove at Y = 0.0 m, while the back boundary is set at Y = 11.30 m, i.e. 7.0 m away from the

central layer. All boundaries are Dirichlet-type, i.e. they have constant thermal-hydrological properties throughout the injection period.

The simulations of the air injection tests are carried out as follows. Thermal-hydrological calculations using the numerical grids shown in Figures 4.1-1 through 4.1-4 are stopped at specific intervals, namely 77 days, 6 months, 9 months and 12 months after heating; and 3 months, 6 months, 9 months, and 12 months after cooling. The initial conditions for the air injection runs are taken from the results of the thermal-hydrological simulations presented in Section 4. Simulated values of pressure, liquid saturation and temperature are mapped from the thermal-hydrological 3D grid of Figure 4.1-1 through 4.1-4 to the air injection 3D grid shown in Figures 5.1-1 and 5.1-2. The mapping from one grid to the other might involve numerical inaccuracies which could give rise to unwanted perturbation because the simulations would start with slightly inaccurate initial conditions. Therefore we performed initial runs prior to actual air injection. The initial simulations were run for a time period of 1 hour, without injecting air, but using the air injection grid and the mapped primary variables as initial condition. We assume that possible inaccuracies have leveled out after 1 hour. In a second step, the actual air injection simulations are performed, using the results of the initial run as initial condition.

The actual test configuration for each test is numerically simulated as follows: Inflated packers which form the boundary of an injection zone are modeled by assigning very low permeabilities to the respective grid elements. Injection zones are represented by high-permeability grid elements in order to allow for immediate pressure response along the open hole. The parameters of the monitoring hole and the remaining parts of the injection hole are not changed, i.e. they are assigned the properties of the rock mass. The above modeling steps are designed to avoid numerical problems, and to ensure a proper reading at the sensor grid elements.

5.2 Air Injection Test Results for the Base Case

A study of the time evolution of the liquid saturation contours such as Figures 4.2-4, 4.2-7, 4.2-13, 4.2-16 from Section 4.2 clearly shows that the majority of the drying and rewetting from the heating and cooling of the SHT occurs within one meter of the heater. Both holes 16 and 18 are too short to sample this region of vigorous boiling, drying and rewetting. However, the increase of liquid saturation due to condensation does occur in the region of the two hydrology holes, and again the effect is more prominent the closer it is to the heater. Therefore the air injection tests carried out in Zone 3 behind packer P_4 would be of most interest in revealing the dominant thermal-hydrological phenomena in the test block.

In Figures 5.2-1 through 5.2-9 we show an entire time sequence of the contours of steady state pressure (units of Pa) in the XZ - plane of the hydrology holes after an hour of air injection into Zone 3 of hole 18 at a constant flow rate of 10^{-2} m^3 per minute. Only a part of the entire grid is

shown, namely, a section extending from the heater center line to the alcove wall. The figures are respectively for the nine specific times: pre-heat, 77 days, 6 months, 9 months, 1 year, 15 months, 18 months, 21 months, and 24 months where the heating period is one year.

The ambient pressure before heating is 87.0 kPa, and in Figure 5.2-1 before turning on heat in the SHT, the pressure build-up around the injection Zone 3 is due entirely to the injection in hole 18. In Figure 5.2-2, the higher pressure build-up arises from two sources. Contours of radial symmetry around the origin (0,0) arise from the heating, and ellipsoidal contours around injection Zone 3 behind P_4 are response to the injection in hole 18. We note that the build-up of pressure around Zone 3 of hole 18 increases as heating time increases, reflecting the lowering of air permeability from the increase in liquid saturation. In Figure 5.2-6, at 3 months after turning off heat, the radial pressure build-up due to heating has disappeared and only the pressure rise in response to the air injection remains. Figures 5.2-7 through 5.2-9 for air injection tests at 6, 9 and 12 months after turning off heat are similar to Figure 5.2-6.

In Figures 5.2-10 and 5.2-11 we present the actual transient pressure response during a typical injection test. Figure 5.2-10 is for pre-test conditions, and Figure 5.2-11 is for the test carried out at one year after heating. We note that steady state pressure is reached in a relatively short time. The magnitude of the steady state pressure responses from all the sensors are consistent with that of a continuum, that is, the pressure response varies inversely as the distance between the monitoring sensor and the injected zone. To the injection in Zone 3 (sensor 18-4), the sensors in descending order of the magnitude of the pressure response are 16-4, 18-3, 16-3, 18-2, 16-2, 18-1, and 16-1. Since the injection flow rate is kept constant for all the tests, one may interpret the higher pressure response at one year after heating to lower gas phase permeability because of increased liquid saturation caused by condensation.

Since the eight different pressure transducers fall into different regions of the pressure contour plots of Figure 5.2-1 through Figure 5.2-9, they will register different steady state pressure readings. This information is contained in Figures 5.2-12, where we show the steady-state pressure response to the air injection in Zone 3 of hole 18 for all eight pressure sensors, at different test times. As expected, the air permeability decreases steadily with heating, but rises dramatically within three months of cooling, indicating that the liquid saturation in the condensation zone returns to pre-heat conditions in relatively short time after the heater is turned off. At 1 year after cooling, the pressure response in all sensors are almost at their initial values.

In Figures 5.2-13 and 5.2-14 we present similar curves of the steady state pressure response at different test times for injection into Zone 1 and Zone 2 of hole 18. As anticipated, these zones are farther away from the heater; therefore the condensation effect is less, and the pressure change during different times is less prominent than that observed in Figure 5.2-12 for Zone 3. Otherwise, the trend of increasing pressure response during heating, and decreasing pressure

response during cooling is similar to that observed in Figure 5.2-12. Prior to turning on the heat, the pressure response observed here is higher than that for injection into Zone 3, due to the shorter length of injection Zones 1 and 2.

In Figures 5.2-15 and 5.2-16 we show the pressure contours for injection in Zone 2 with packer P_3 deflated for pre-heat condition as well as after 1 year of heating. It is clear from the contour maps that sensors 18-2 and 18-3 should register the same pressure in the injection zone. The sensors in descending order of the magnitude of steady state pressure change are 16-3, 16-2, 18-1, 18-4, 16-4, 16-1, as is to be expected from the continuum representation of the fractures.

The test results for injecting air into hole 16 are very similar to those already discussed in terms of injection into hole 18. In Figures 5.2-17 and 5.2-18 we show the steady state pressure contours for pre-heat conditions and after one year of heating, for injecting into Zone 3 of hole 16. In Figures 5.2-19, 5.2-20, 5.2-21 are shown the steady-state pressure response at different test times for injection into Zones 1, 2, and 3 respectively. Note again that the largest variation in pressure response is for injection into Zone 3, the closest zone to the single heater.

Since the heating period of the SHT can be 9 months or 1 year, we examine the sensitivity of the air injection tests to the duration of the heating period. In Figure 5.2-22 we show the transient pressure response to an air injection test carried out at 1 year, 3 months after the cooling, when the heating is 9 months. On the same figure we superpose the results for an air injection test carried out at 15 months, at 3 months after the cooling when the heating period is 1 year. Note that the results are almost identical.

5.3 Sensitivity to Fracture Continuum Conceptualization

Our conceptual model of the fracture medium consists of a high-permeability feature superposed on a low permeability fracture continuum. In this section, we study the effect of the high-permeability feature on the air injection tests. Figure 5.3-1 shows the pressure response in the eight sensors for air injection into Zone 3 of hole 18, for a model where the high-permeability feature is absent in the fracture medium. That is, the fracture medium is represented by a continuum of uniform permeability $5.85 \times 10^{-14}\ m^2$. On the same figure is also shown the pressure response of sensor 18-4 if the high-permeability feature were included, labeled as Base Case. We note a slightly higher pressure response with the homogeneous model of the fracture medium. Our interpretation is that the high-permeability feature serves as an efficient pathway for injected air to be carried away so that less pressure is built up. However, since the high-permeability feature is not directly in the plane of holes 16 and 18, the difference of pressure response between this and the Base Case is not very great. Also the impact of the high-permeability feature is somewhat canceled by the overall higher liquid saturation in the condensation zone of this feature.

5.4 Sensitivity to Initial Saturation

Since the pressure response is sensitive to the liquid saturation of the rock, and since the laboratory analyses of the liquid saturation of samples from the Thermal-Mechanical Alcove (Tsang et al., 1996) indicated a range of values from 0.81 to 0.99, a complete suite of air injection test runs during one year of heating is carried out for the case where the initial liquid saturation for the matrix continuum is 0.98 instead of 0.92.

In Figure 5.4-1 we show the transient pressure response for air injection into Zone 3 of borehole 18 after one year of heating. In the same figure we superpose the pressure response of sensor 18 4 with the original liquid saturation of 0.92 labeled as Base Case and shown previously in Figure 5.2-11. The pressure response is higher here than in the Base Case because of the higher liquid saturation. Furthermore, the pressure response differs from that of the Base Case in that there is a slight decay right after the initial fast rise which seems to arise from some liquid being displaced by the injected air.

The steady state pressure response to the injection in Zone 3 of hole 18 is shown for different test times in Figure 5.4-2. In this figure we also include the curve labeled as Base Case, which is the response of sensor 18-4 for injection of air into Zone 3 with the initial liquid saturation of 0.92, as previously shown in Figure 5.2-12. Indeed, with a higher initial liquid saturation, the effect on the pressure response in the formation is more pronounced.

5.5 Sensitivity to Gas Relative Permeability Formulation

In Figure 5.5-1 we show the transient pressure response of an air injection test for Zone 3 of hole 18 at 1 year of heating, calculating the gas relative permeability as $(1 - k_{r,l})$ rather than using the Brooks-Corey formulation as given in Equation 3.3.2. This former equation effectively registers a higher value for gas relative permeability at small gas saturation, or high liquid saturation, which is the condition around Zone 3 of hole 18 at this stage of heating. As expected, the pressure response in Zone 3 of hole 18 is considerably lower than that of the Base Case.

5.6 Summary

The simulated results presented in this section show that interference air injection tests carried out throughout the heater test can be very useful for monitoring the most dominant thermal-hydrological processes of vaporization, drying, condensation, and rewetting. While the qualitative features of the test results do not change with various input parameters, the sensitivity studies show that different parameter input can affect the test results quantitatively. For example, in our thermal-hydrological simulations, holes 16 and 18 are located in a fracture continuum with a uniform fracture continuum permeability of 5.85×10^{-14} m^2. However, the local permeabilities

of holes 16 and 18 have been determined to be 8.3 x 10^{-15} m^2 and 8.8 x 10^{-14} m^2 (Tsang et al., 1996). This implies that a real field air injection test carried out in hole 16 will probably measure a higher pressure response than that simulated. Furthermore, the pre-test air injection tests carried out in the field also indicate that the local permeabilities of Zones 1 and 2 in both holes 16 and 18 are higher than that of Zone 3. Since the simulations in our forecast do not account for the variation of local permeability in the hydrology holes, the field pressure response again can be quantitatively different than simulated one. However, the objective of the simulations presented here is to provide a good understanding of the factors affecting the test results, so that more site specific data may be included later to refine and calibrate this baseline numerical model.

It is regretful that the hydrology holes 16 and 18 are not longer. The present geometry of holes 16 and 18 allows the monitoring of the evolution of the condensation zone, but not the dry-out zone. The configuration of the hydrology holes in the Drift Scale Test have a far superior geometry since they include all zones of interest. We foresee that interference air injection tests carried out in the 12 hydrology holes during different heating and cooling stages of the Drift Scale Test can be extremely valuable in unraveling the thermal-hydrological conditions.

6 Sensitivity Study for Thermal-Hydrological Conditions

The thermal-hydrological response of the rock mass to the heater power involves multiple physical processes of great complexity. At the same time, many model input parameters are unknown or uncertain. Therefore, in this section we study how individual processes and input parameters affect the thermal-hydrological behavior. Our sensitivity study includes modeling concepts as well as key input data. In order to reduce the numerical effort, we restrict the study to two dimensions, with the modeling domain chosen perpendicular to the heater center line. We are fully aware of the fact that 2D results can not quantitatively represent the actual three-dimensional behavior of the rock mass. However, 2D simulations in a sensitivity study still have considerable merit to help us better understand the relative importance of parameters and processes in a qualitative manner. This will aid us to refine and improve the three-dimensional model.

The numerical simulations are again performed with the simulator TOUGH2. The 2D grid is identical to the XZ - cross section grid shown in Figure 4.1-1. The heater power in 2D is 772.0 W/m, corresponding to a total heater power of 3.86 kW for a 5 m long heater element. Unless we specify otherwise, the conceptual model, input data, boundary and initial conditions are identical to the Base Case modeled in Section 4, using the parameters introduced in Section 3.3. However, as the third dimension is not included, we can not incorporate the high-permeability fracture zone. Thus, the 2D model domain is homogeneous.

In the following, we shall introduce the 2D Base Case results, then study sensitivities to the conceptual model (boundary conditions, enhanced vapor diffusion, dual permeability), and finally study sensitivities to certain key input parameters (fracture permeability, matrix permeability). Note that the impact of a higher initial saturation has already been studied in Section 4. For the sensitivity study on fracture and matrix permeability, we concentrate on the range of values with the strongest impact on the liquid saturation in the condensation zone. In fact, we are mostly interested in parameter variations which give rise to an increase in saturation compared to the Base Case to evaluate the possibility and impact of liquid becoming mobile in fractures.

Generally, only one model concept or parameter is varied at the time, all others remain fixed to the Base Case. All results presented below are at 1 year, at the end of a 1 year heating period.

6.1 Base Case Results

Figures 6.1-1 through 6.1-3 show contours of temperature, equivalent continuum liquid saturation (which is essentially identical to the matrix saturation), and fracture liquid saturation. Figure 6.1-4 gives the same thermal-hydrological properties along a horizontal sampling line extending from the heater to the right alcove wall at Z = 0.0 m. This sampling line is in close vicinity to the hydrology test holes 16 and 18. Approximate locations for the pressure sensors and the bottom of hole 18 are indicated in the figure.

The basic features of the temperature and moisture perturbation are similar to the 3D results. However, the response of the rock mass to the heater is much more pronounced here. Maximum temperature at the heater is about 330 °C, the 100 °C "heat pipe" plateau extends from about 1.20 m to about 2.80 m distance from the heater, and the 50 °C line is very close to the alcove wall boundary. We also note a much larger dry-out zone around the heater and a more extended condensation zone, the latter with higher matrix and fracture saturations. Basically, the entire spatial pattern of dry-out zone, heat pipe zone and condensation zone has significantly shifted outwards compared to the 3D results, while temperature and saturation build-up are more pronounced. Removal of the third dimension, in which heat transfer can effectively occur, overestimates the impact of heat introduced into the system. This demonstrates the importance of 3D modeling to more realistically capture the system response. As the 2D results "overestimate" the actual 3D behavior, the sensitivities identified in our study are "overestimated" as well. Therefore, in interpreting the results of this sensitivity study, one has to keep in mind that the impact of certain model concept/parameter changes might be reduced in magnitude in 3D.

6.2 Alcove Boundary Condition

Alcove walls facing the test block are insulated with a low thermal conductivity material of 15.2 cm thickness, which is explicitly being modeled in the Base Case. However, in the Base Case we do allow liquid and gas to escape from the test block into the alcoves, postulating that the thermal insulation with plastic backing is not a perfect liquid/vapor barrier. In this section, we modify the alcove boundary condition such that (1) the alcove walls are *closed* for heat, liquid, and gas (perfect insulation), and (2) the alcove walls are *open* for heat, liquid, and gas (no insulation).

Figures 6.2-1 through 6.2-3 show temperature and liquid saturation contours for the "perfect insulation" case. In Figure 6.2-4 we present temperatures and saturations along the X - axis at Z = 0.0. In the same figure we superpose the results of the Base Case, as previously shown in Figure 6.1-4, here indicated by hollow symbols and dashed lines. We note significant differences between the two types of boundary condition, in particular for the fracture liquid saturations in

the condensation zone. As this zone coincides with the region where air injection tests are performed we can expect higher pressure responses to air injection. Additional analysis may be needed to assess the performance of the alcove wall insulation; however, we should keep in mind that the effect of the changed boundary condition may be significantly less in 3D.

Less impact can be seen in Figures 6.2-5 through 6.2-8, showing the simulation results for the "no insulation" case. Here, the only difference to the Base Case is the absence of the thermal insulation, giving lower temperatures in the region close to the alcove walls. The lower temperatures result in somewhat higher saturation values.

6.3 Enhanced Vapor Diffusion

Thermally enhanced vapor diffusion might be a significant mechanism in moisture redistribution as it moves vapor away from the heater by forces other than the gas pressure gradient. The potential importance of this phenomenon is studied by setting the vapor diffusion enhancement factor β to 1. Results are shown in Figures 6.3-1 through 6.3-4. Compared to the Base Case with ordinary vapor diffusion, the simulation with enhanced vapor diffusion shows some significant differences:

1. The dry-out region is much wider as more vapor is driven away from the heater; it actually propagates beyond the nominal boiling point.

2. The temperature distribution does not show the "heat pipe" plateau at 100 °C observed in the Base Case. Apparently, the vapor diffusion mechanism overcomes the effect of vapor-liquid counter-flow.

3. The contour plots show a strong impact of the alcove boundary condition with respect to liquid saturation. Saturation values in horizontal direction are much lower than in vertical direction. Note that this effect only occurs for the Base Case boundary condition, with insulation for heat, but open walls for liquid and gas to escape (not to reenter). No such effect is observed for any one of the other boundary conditions introduced in Section 6.2.

6.4 Dual Permeability

In this section we apply a dual permeability formulation for the rock mass as opposed to the ECM model used in the Base Case. A dual permeability model is able to capture the transient response in the matrix to perturbations of temperature, pressure or saturation in the fractures. In other words, fracture and matrix continua do not need to be in thermodynamic equilibrium at all times, as assumed with the ECM. The matrix is represented by *one* continuum, i.e., a "dual" permeability formulation rather than a "MINC" (Multiple Interacting Continua, after Pruess &

Narasimhan, 1985) formulation is applied. This means that the fracture/matrix interaction is proportional to the primary variable difference between the two continua. Several studies have shown that this approach, which is often referred to as "quasi-steady", somewhat underestimates the exchange rates between fractures and matrix, mainly because it cannot accurately account for the early time behavior in matrix blocks with steep gradients at the block surfaces.

Dual permeability models require some additional information regarding the geometry of the fractured rock, i.e. the interface area between fractures and matrix, and the size of a representative matrix block. Both can be estimated from the fracture density, here assumed to be 7.6 fractures/m^3 as is used in the Sandia pre-test analysis (Sobolik et al., 1996). Our simulations are performed with an interface area of 15.2 m^2/m^3, and a representative block size of 13.2 cm, which represents the block thickness between neighboring fractures for one set of plane, infinite fractures.

Contour plots of the simulation results for the dual permeability case are presented in Figures 6.4-1 through 6.4-3. As the temperatures in fractures and the matrix are almost identical, we only show the matrix temperatures in Figure 6.4-1. The most prominent difference from the ECM simulations is the apparent presence of gravity driven liquid flux. Both the matrix and fracture saturations show a much stronger saturation build-up below the heater than above. This is even more obvious in Figure 6.4-4 which depicts temperature and saturation values along a vertical sampling line at X = 0.0 m. Apparently, vapor which is driven away from the heater in the fractures condenses faster than it is drawn into the matrix by capillary suction. This gives rise to a sufficiently large saturation build-up in the fractures to achieve liquid mobility. However, the symmetry of the temperature perturbation is not affected by these gravity effects. Also we note from the contour plots that the saturation perturbation in fractures migrates much further than in the matrix, due to the slow response time in the low permeability rock. In fact, the perturbation in the fracture continuum approaches the top and the bottom of the model area, jeopardizing the validity of the constant primary variable boundary condition.

Figure 6.4-5 directly compares results from the dual permeability model and the ECM. Clearly, the dual permeability results feature a larger dry-out region than the ECM results. Also the heat pipe effect is less distinct. Our interpretation is that in the dual permeability calculation significant amounts of liquid are carried away from the condensation zone by gravity effects, leaving less liquid available to be drawn back by capillary suction toward the heat source.

Our results indicate the importance of model conceptualization. However, we expect the real system behavior to be bounded somewhere between the two extreme cases of ECM and dual permeability. The former conceptual model underestimates matrix response times because of the equilibrium assumption, the latter overestimates because of calculating the fracture/matrix interaction with a "steady-state" approach. The latter can be improved by analysis using MINC.

6.5 Fracture Permeability

In this section we change the fracture continuum permeability from 5.85 x 10^{-14} m^2 to 5.2 x 10^{-12} m^2 which is at the high end of the permeability values estimated from air injection tests at ambient conditions (Tsang et al., 1996). Other than that, the model concept and input parameters are identical to the Base Case. This means in particular that ECM is used to model the combined effect of fractures and matrix.

Contour plots of temperature and saturation show some obvious differences to the Base Case (Figure 6.5-1 to 6.5-3). As in the previous section, gravity driven liquid flow is apparent in the moisture distributions of fractures and matrix, indicated by the asymmetry of saturation in vertical direction (Figure 6.5-4). In fact, if such asymmetry occurs, air injection tests performed in holes 16 and 18 would miss the areas with the strongest thermodynamic response. Buoyant gas phase convection seems to impact the temperature distribution which appears slightly non-symmetric in the vertical direction.

Liquid in the fractures appears to become mobile because of the higher rate of vapor migrating radially outward from the heater in the highly permeable fractures. While more vapor condenses, the saturations in fractures and matrix build up because the amount of liquid counter-flow in the matrix remains basically unchanged, limited by the low matrix permeability. A direct comparison between the Base Case and the high fracture permeability results is given in Figure 6.5-5. We note that the dry-out region around the heater propagates slightly further for the high-permeability case, due to the higher rate of vapor flowing away from the heat source.

6.6 Matrix Permeability

In this section we present results for simulations when the matrix permeability is lowered by a 2 orders of magnitude. It is apparent from Figures 6.6-1 through 6.6-5 that the simulated system response is similar to the results shown in the previous section. Gravity driven liquid flow is apparent. The saturation build-up in the condensation zone is more pronounced than in the Base Case because less liquid is carried away from that zone in the matrix, due to its lower permeability. For the same reason, the dry-out region is more extended since the rate of liquid back-flow in the matrix towards the heat source is smaller.

As a result of both this section and the preceding section we note that the larger the difference in fracture/matrix permeabilities, the more pronounced is the saturation build-up in the condensation zone, and the more likely is the presence of liquid mobility in the fractures.

7 Summary

We have presented simulations in 3D to forecast the thermal-hydrological conditions of the Single Heater Test during both the heating and cooling phases. The dominant thermal-hydrological response of the welded fractured tuff to the heater power output is the temperature rise, boiling, vaporization, drying, condensation, and rewetting of the dry-out zones. The manifestation of the above coupled physical processes is the spatial variation and temporal evolution of the liquid saturation in the rock mass. Therefore, these thermal-hydrological processes may be captured by interference air injection tests, provided the air injection and pressure monitoring zones bracket regions in the rock mass where there is significant liquid saturation changes as the Single Heater Test progresses.

The configuration of hydrology holes 16 and 18 are such they allow the monitoring of the condensation zone, but regrettably not the drying zone close to the heater. Since both the gas pressure build-up as well as relative humidity decrease occur in the dry-out region close to the heater, all the relative humidity sensors at 16-1, 16-2, 16-3, 16-4, 18-1, 18-2, 18-3, 18-4 are expected to register approximately 100 % reading, and all the eight pressure transducers will remain practically at ambient pressure conditions during passive testing throughout the heating and cooling period. The only parameter monitored by the sensors in holes 16 and 18 that will show changes during the heater test is temperature. The highest temperature registered by the sensors is a little over 60 ^{o}C for sensors 16-4 and 18-4 at 1 year of heating.

Simulations in 3D were performed for air injection tests in holes 16 and 18 for nine specific times: pre-heat, 77 days, 6 months, 9 months, 1 year, 15 months, 18 months, 21 months, and 24 months where the heating period is one year. Our results indicate that the pressure response to air injection is indeed affected by condensation processes due to heating, and the pressure build-up will be different at different heating and cooling stages of the SHT. Hence, these tests can be very useful to capture the thermal-hydrological evolution of the SHT environment. Additional calculations were carried out for an alternative heating period of 9 months. Our simulated results indicate that the change in the thermal-hydrological parameters between 9 months and 1 year of heating is small, and that the thermal-hydrological conditions reflected in the air injection tests at 3 months after the heater is turned off, whether at 9 months or at 1 year, is very similar. These results suggest that as far as thermal-hydrological performance of the Single Heater Test is concerned, it is probably sufficient to heat for only the shorter period of 9 months without sacrificing valuable information.

Because of the uncertainty related to both the complexity of multiple processes, and to various key parameters, simulations in 3D were carried out for several plausible conceptual models. For

example, though our choice of the matrix liquid saturation is 0.92 for the Base Case simulations, it is equally plausible to choose a higher value based on the laboratory analyses of core samples from the Single Heater Test area. A higher liquid saturation will definitely give rise to large changes in the air injection test results at different times of the heater test.

Several other processes and parameters also affect the moisture redistribution in the test block due to vaporization and condensation, and can in turn give rise to different air injection results. The sensitivity of the thermal-hydrological conditions to several parameters and model conceptualizations were studied in 2D simulations. The processes and parameters isolated out were boundary conditions at the alcove wall, mode of vapor diffusion transport, fracture and matrix permeability values, and dual continuum conceptualization of the fractured welded tuff. This rather extensive numerical modeling effort as reported in the previous chapters has placed us in an excellent position to further analyze the Single Heater Test data. Since we understand how individual process parameters affect the simulated results, we shall be able to better understand the sources for possible discrepancies between the forecast results and the real data. And indeed, in zeroing in on the discrepancy between forecast results and the data, we may actually constrain the uncertainty related to the key parameters or conceptualization.

Acknowledgment

We thank Stefan Finsterle and Chris Doughty for their review of the manuscript and comments for improvement. This work was supported by the Director, Office of Civilian Radioactive Waste Management, through a Memorandum Purchase Order EA9013MC5X between TRW Environmental Safety Systems, Inc. and E.O. Lawrence Berkeley National Laboratory. The support is provided to E. O. Lawrence Berkeley National Laboratory through the U. S. Department of Energy Contract No. DE-AC03-76SF00098.

References

Bodvarsson, G.S., T.M. Bandurraga (eds.). Development and calibration of the three-dimensional site scale unsaturated zone model of Yucca mountain, Nevada, Lawrence Berkeley National Laboratory report, Berkeley, CA, 1996.
DTN: LB960800831229.001

CRWMS M&O Report B00000000-01717-5705-00047, Characterization of the ESF Thermal Test Area, September 1996.

Flint, L.E. Matrix properties of hydrogeologic units at Yucca Mountain, Nevada, U.S.G.S. Water - Resources Investigation Report, 1996, (in print).

Jury, W.A., J. Letey. Water vapor movement in soil: Reconciliation of theory and experiment, Jour. Soil Sci. Am., 43(5), 823-827, 1979.

Mitchell, A., Memorandum. Borehole Videos from the Exploratory Studies Facility Thermal Testing Facility (TTF) - Thermomechanical Alcove (TMA), LA-EES-13-LV-05-96-021, dated May 21 1996. LBNL has copy # 4 of Quality Assurance "lifetime record copy of the borehole videos".

Pruess, K., T.N. Narasimhan. A practical method for modeling fluid and heat flow in fractured porous media, Soc. Pet. Eng. J., 25, 1, 14-26, 1985.
ACCN: NNA.19890522.0235

Pruess, K. TOUGH user's guide, Lawrence Berkeley National Laboratory report LBL-20700, Berkeley, CA, 1987.
ACCN: NNA.19890315.0010

Pruess, K., J.S.Y. Wang, Y.W. Tsang. On the thermohydrologic conditions near high-level nuclear wastes emplaced in partially saturated fractured tuff, part 2. Effective continuum approximation, Water Resources Research., 26, 6, 1249-1261, 1990.
ACCN: NNA.19891026.0084

Pruess, K. TOUGH2 - A general-purpose numerical simulator for multiphase fluid and heat flow, Lawrence Berkeley National Laboratory report LBL-29400, Berkeley, CA, 1991.
ACCN: NNA.1992116.0073

Pruess, K., Y.W. Tsang. Thermal modeling for a potential high-level nuclear waste repository at Yucca Mountain, Nevada, Lawrence Berkeley National Laboratory report LBL-35381, Berkeley, CA, 1994.
ACCN: NNA.19940427.0248

Pruess, K., A. Simmons, Y.S. Wu, G. Moridis. TOUGH2 software qualification, Lawrence Berkeley National Laboratory report LBL-38383, Berkeley, CA, 1996.

Sobolik, S.R., N.D. Francis, J. Pott, Pre-experiment thermal-hydrological-mechanical analyses for the ESF Single Heater Test, Sandia National Laboratories Letter Report SLTR96-0004, 1996.

Tokunaga, T., J. Wan. Water film flow along surfaces of porous rock, submitted to Water Resources Research., 1996.

Tsang, Y.W., K. Pruess. Further modeling studies of gas movement and moisture migration at Yucca Mountain, Nevada, Lawrence Berkeley Laboratory report LBL-29127, Berkeley, CA, 1990.

Tsang, Y.W., J. Wang, B. Freifeld, P. Cook, R. Suarez-Rivera, T. Tokunaga, Letter report on hydrological characterization of the single heater test area in the ESF, Level 4 Milestone for WBS 1.2.3.14.2, August 1996.
DTN: LB960500834244.001

Vargaftik, N.B. Tables on the thermophysical properties of liquids and gases, 2nd ed., John Wiley, NY, 1975.
ACCN: NNA.19940428.0016

Walker, W.R., J.D. Sabey, D.R. Hampton. Studies of heat transfer and water migration in soils, final report, Department of Agricultural and Chemical Engineering, Colorado University, Fort Collins, CO, 1981.

Figures

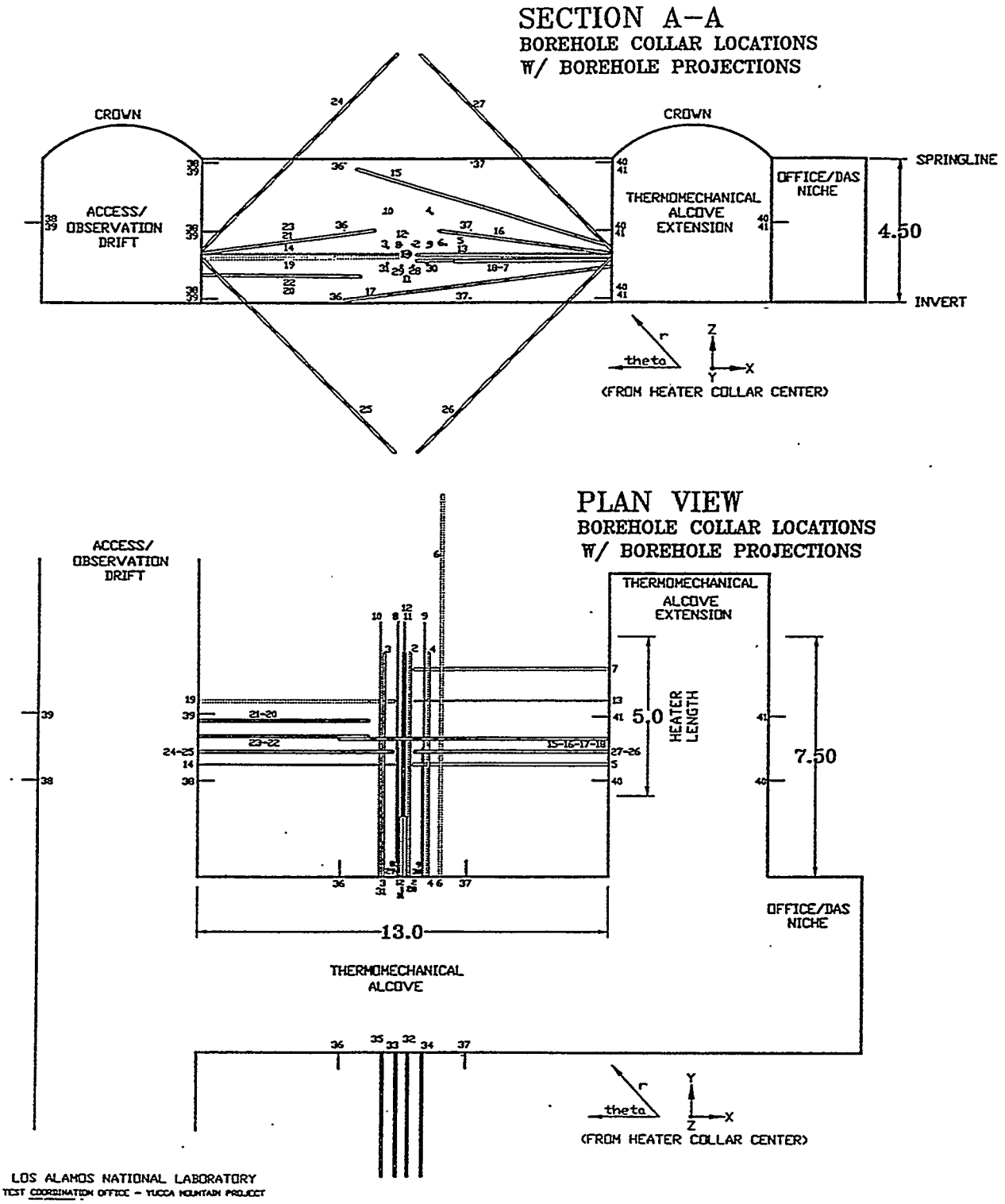

Figure 3.1-1 Layout and borehole arrangement in the Single Heater Test.

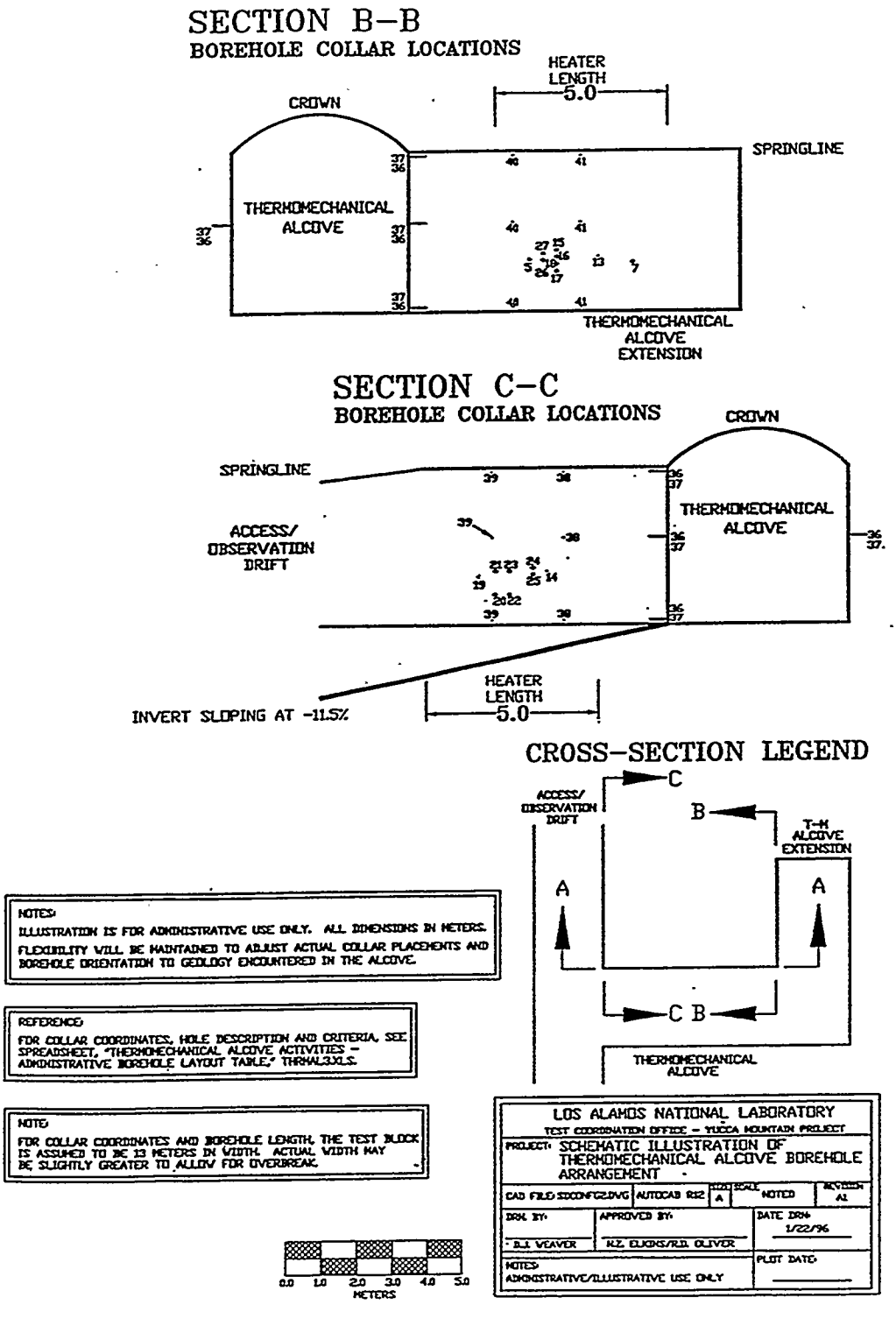

Figure 3.1-1 (cont.) *Layout and borehole arrangement in the Single Heater Test.*

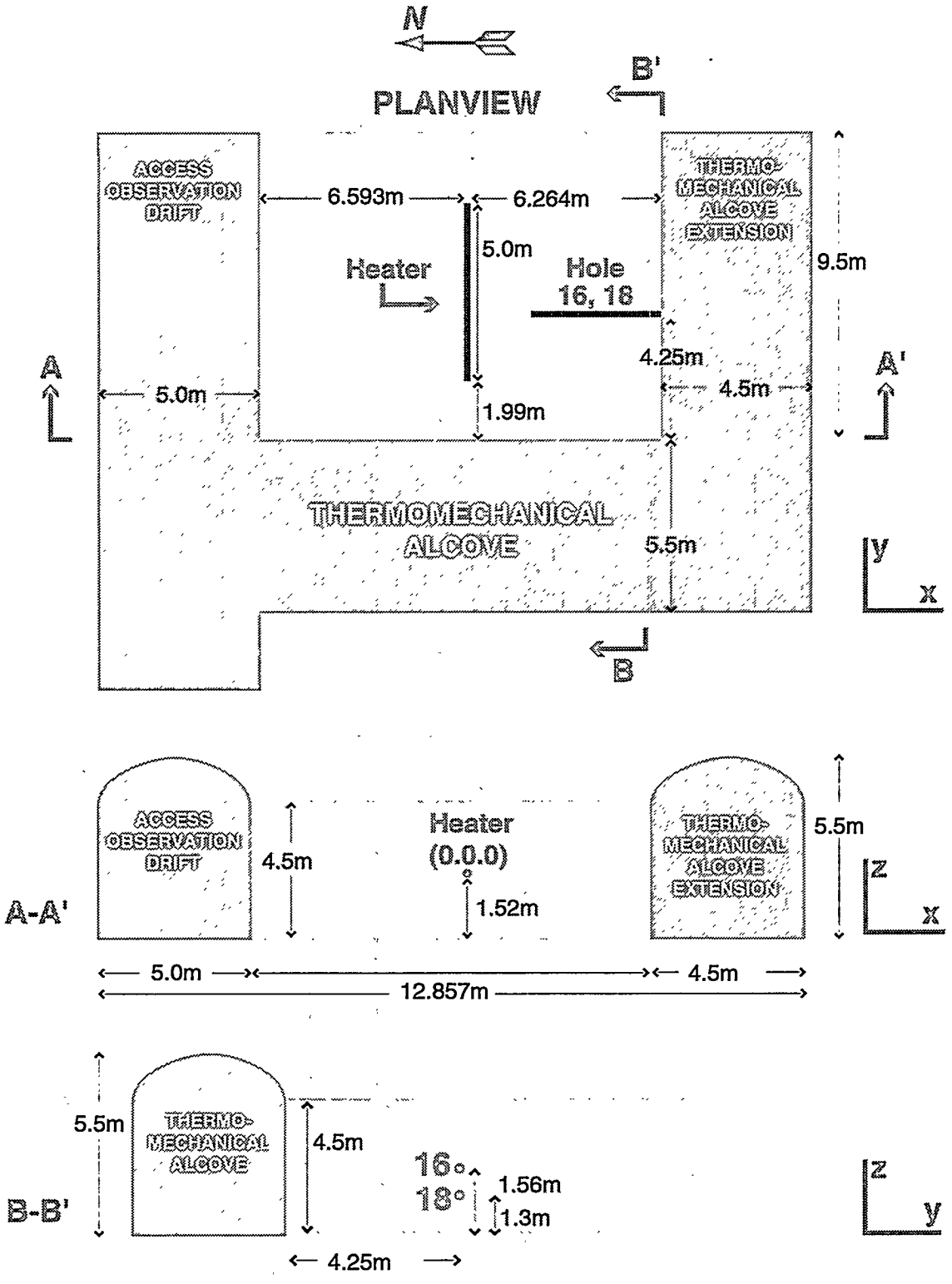

Figure 3.1-2 *Layout and configuration of the Single Heater Test with dimensions.*

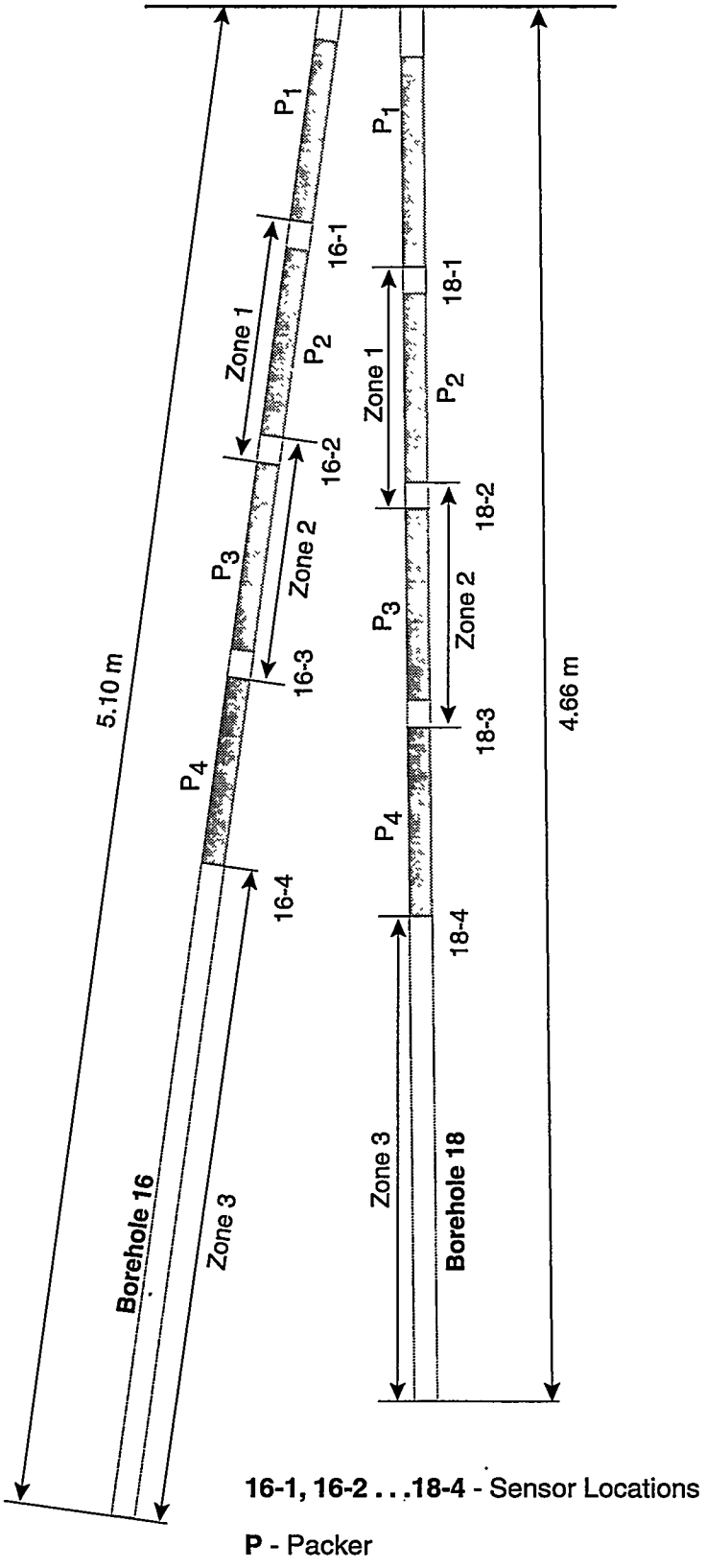

Figure 3.1-3 Geometry of the air injection test boreholes and instrumentation.

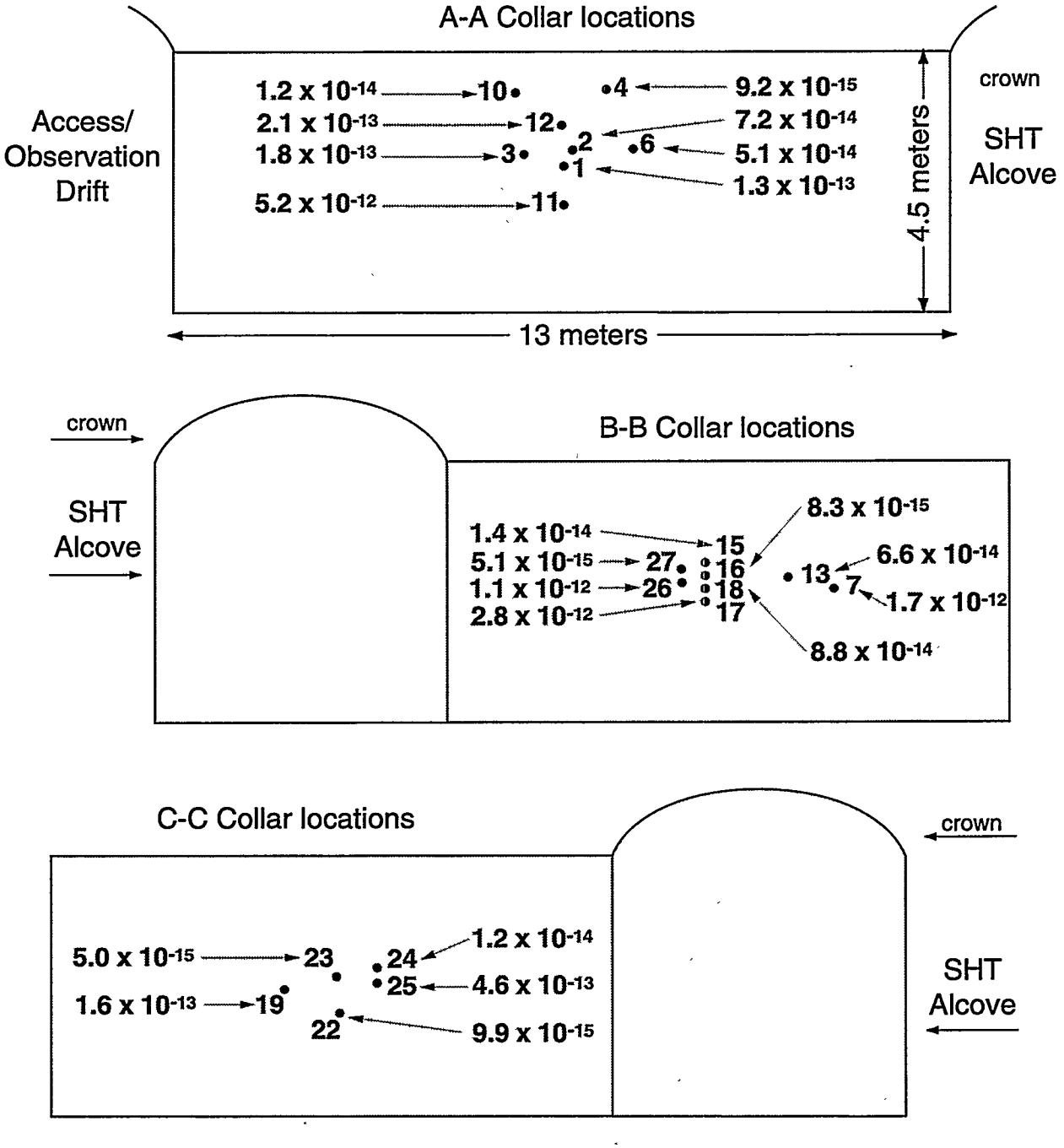

Figure 3.2-1 *Estimated permeability values for boreholes in the Single Heater Test from air injection tests in May 1996.*

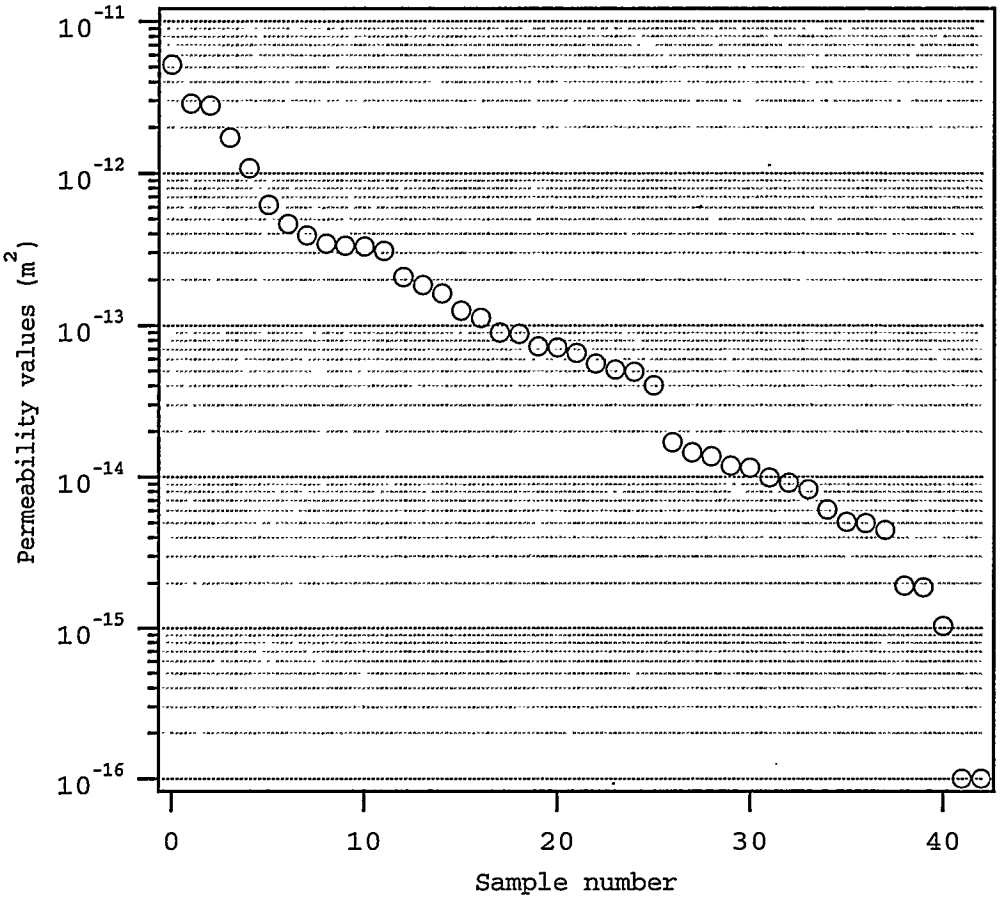

Figure 3.2-2 *Estimated air permeability values for all boreholes and straddled sections tested in May 1996.*

(This page intentionally left blank.)

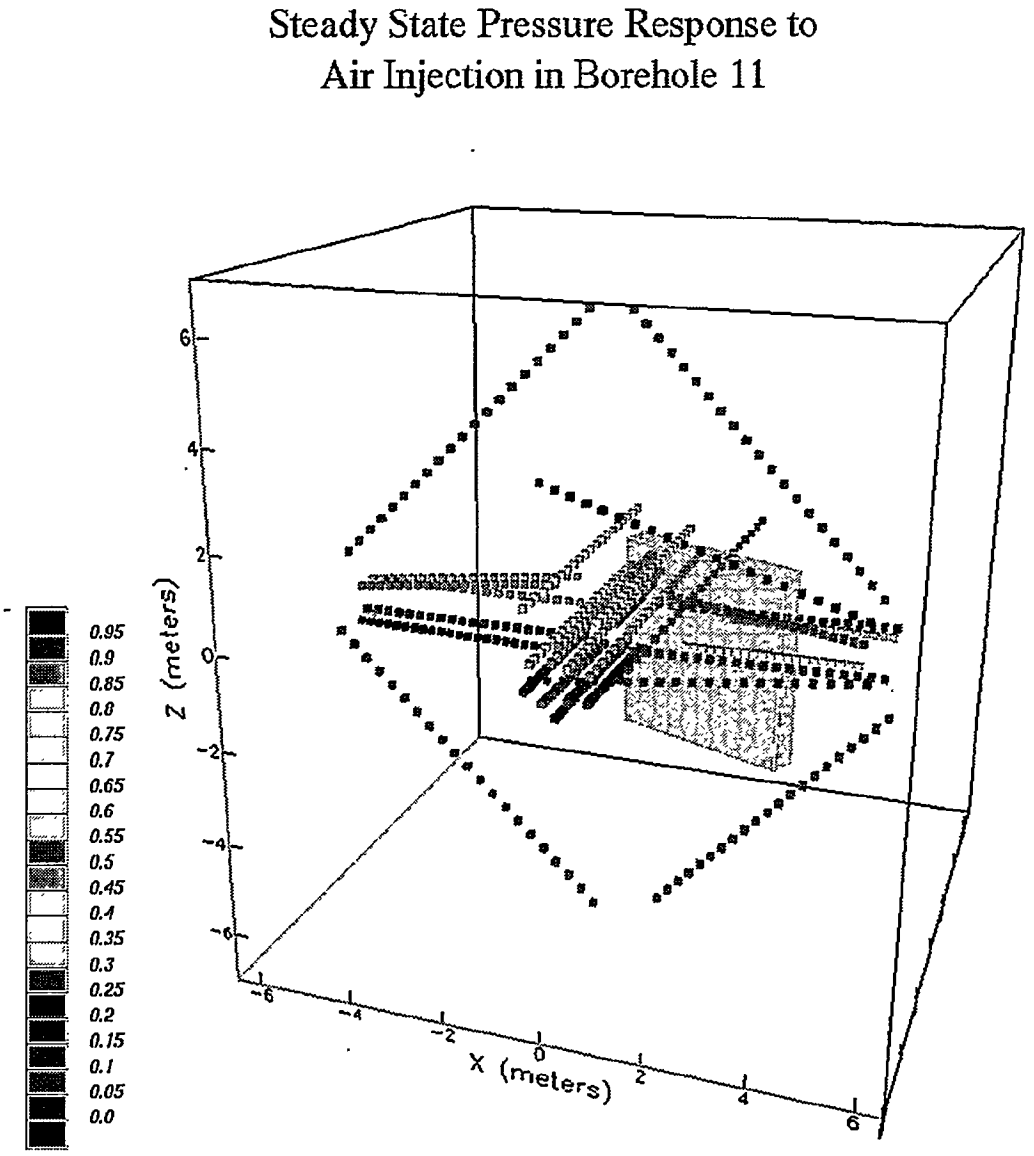

Figure 3.2-3 Steady state pressure response of instrumented boreholes to air injection in borehole 11. Also indicated is the approximate location of the high-permeability fracture zone.

(This page intentionally left blank.)

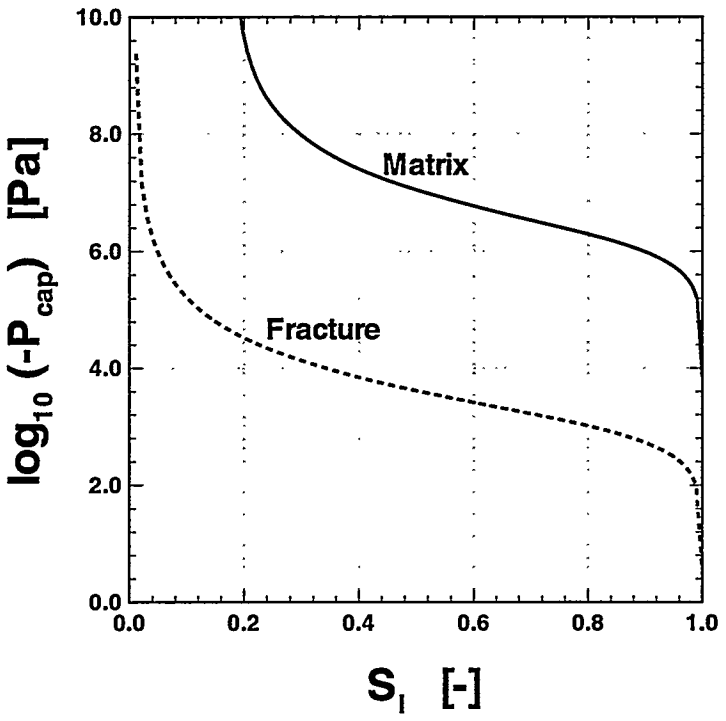

Figure 3.3-1 *Capillary pressure function for matrix and fractures with ECM model using Base Case parameters.*

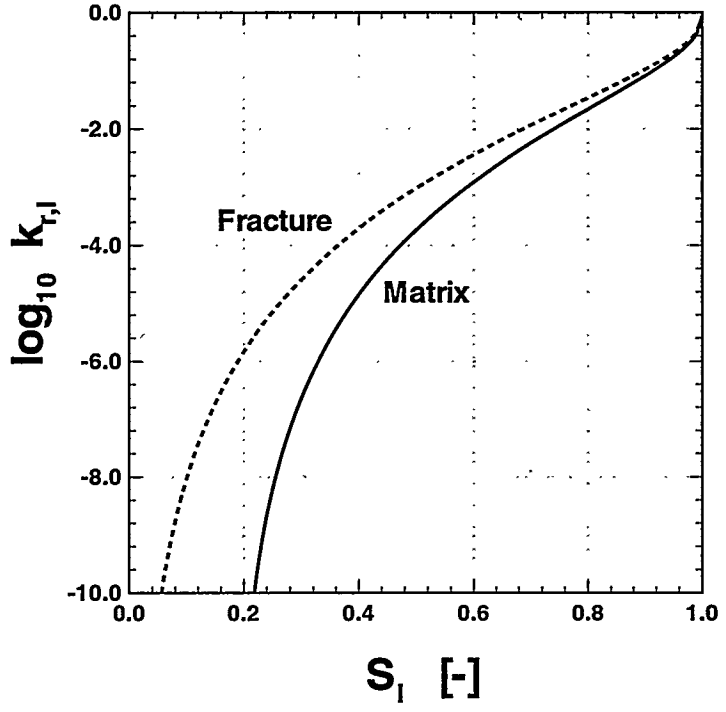

Figure 3.3-2 *Liquid relative permeability function for matrix and fractures with ECM model using Base Case parameters.*

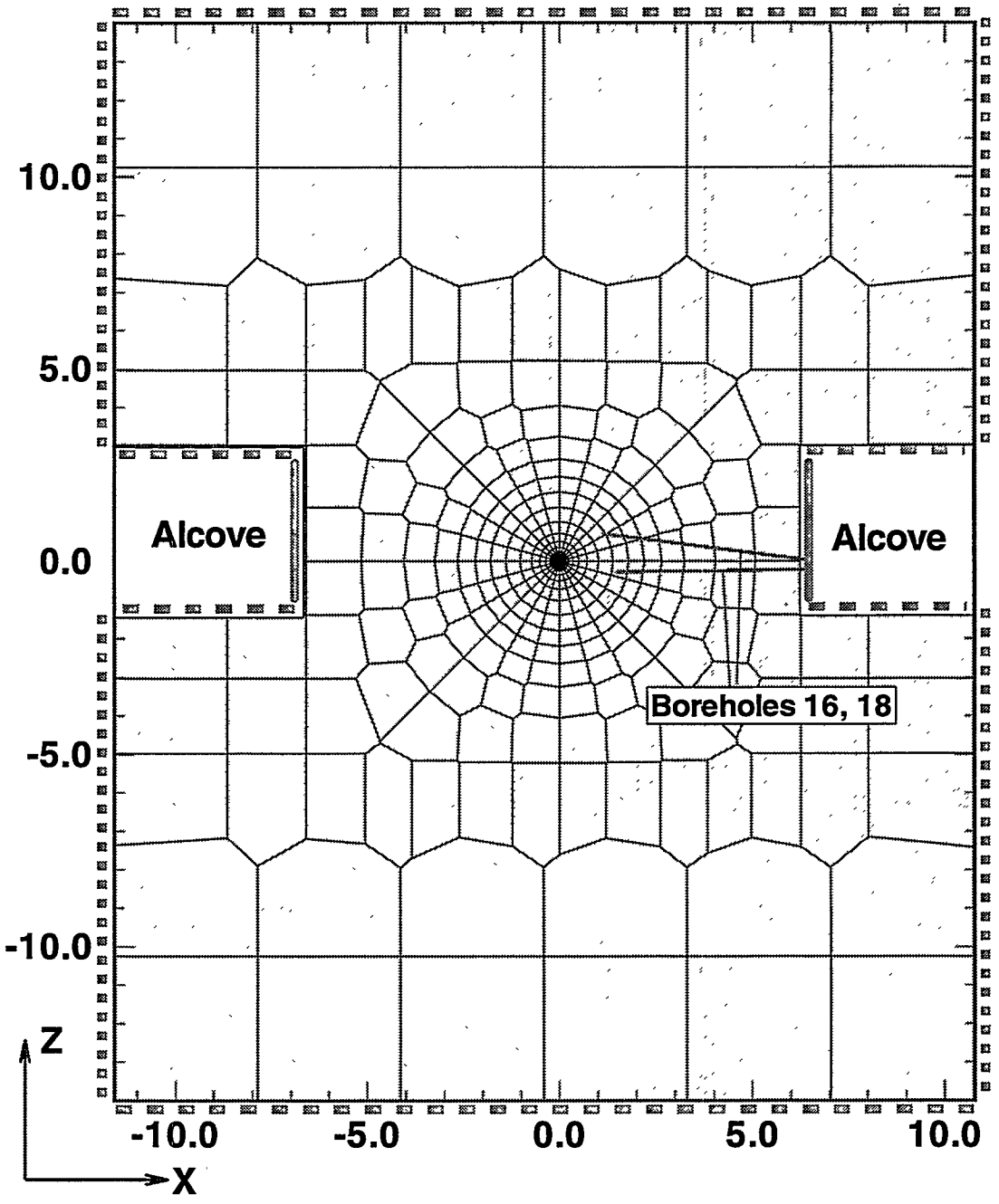

Figure 4.1-1 *XZ - cross section of the discretization grid. Dashed lines indicate a constant primary variable boundary, dotted lines represent a closed boundary, and the solid lines along the vertical alcove walls represent the thermal insulation. Also indicated is the location of the air permeability test holes 16 and 18.*

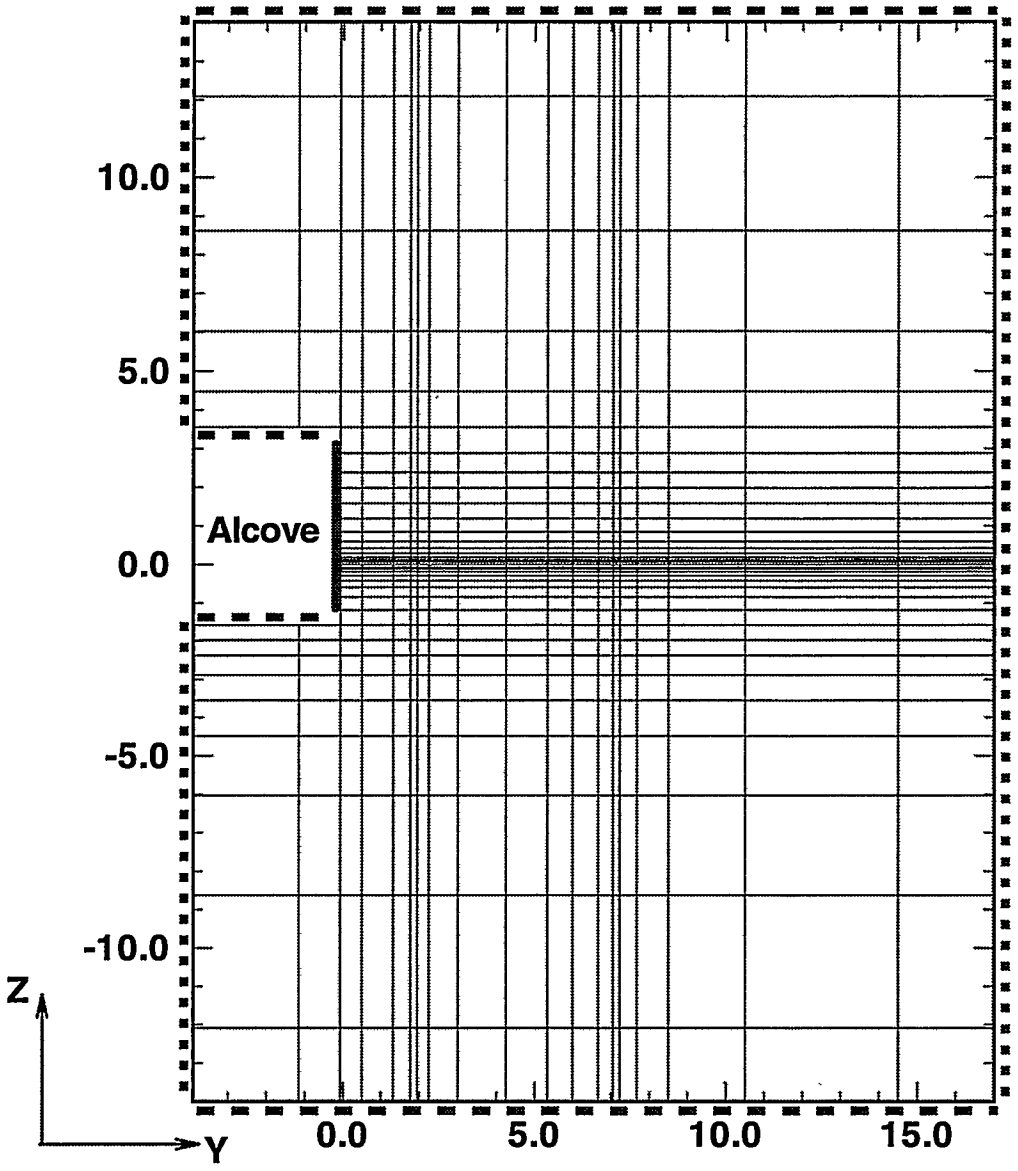

Figure 4.1-2 YZ - cross section of the discretization grid. Dashed lines indicate a constant primary variable boundary, dotted lines represent a closed boundary, and the solid line along the vertical alcove wall represents the thermal insulation.

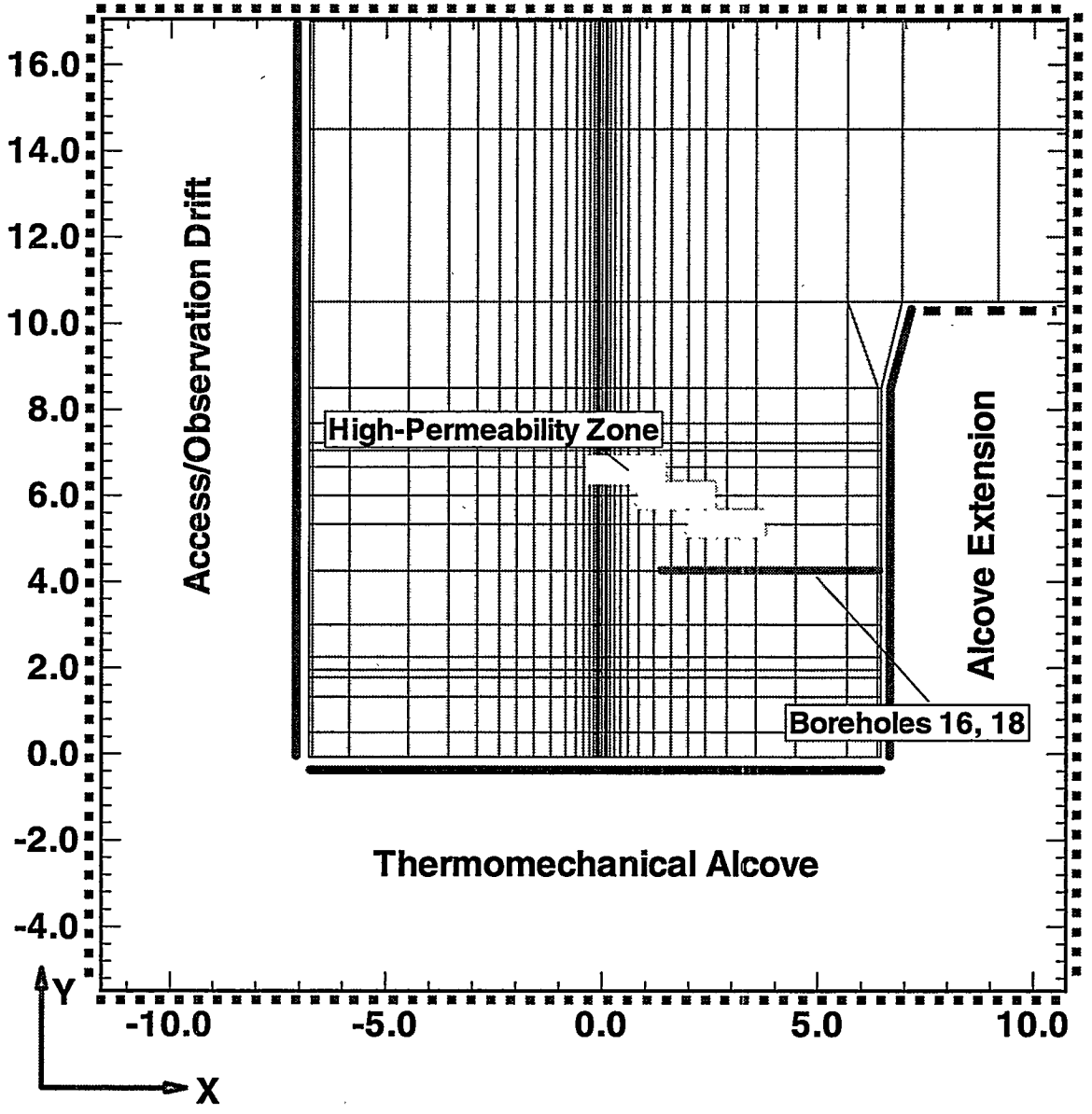

Figure 4.1-3 XY - cross section of the discretization grid. Dotted lines represent a closed boundary, and the solid lines along the alcove walls represent the thermal insulation. Also indicated is the location of the air permeability test holes 16 and 18, and the horizontal extension of the high-permeability fracture zone.

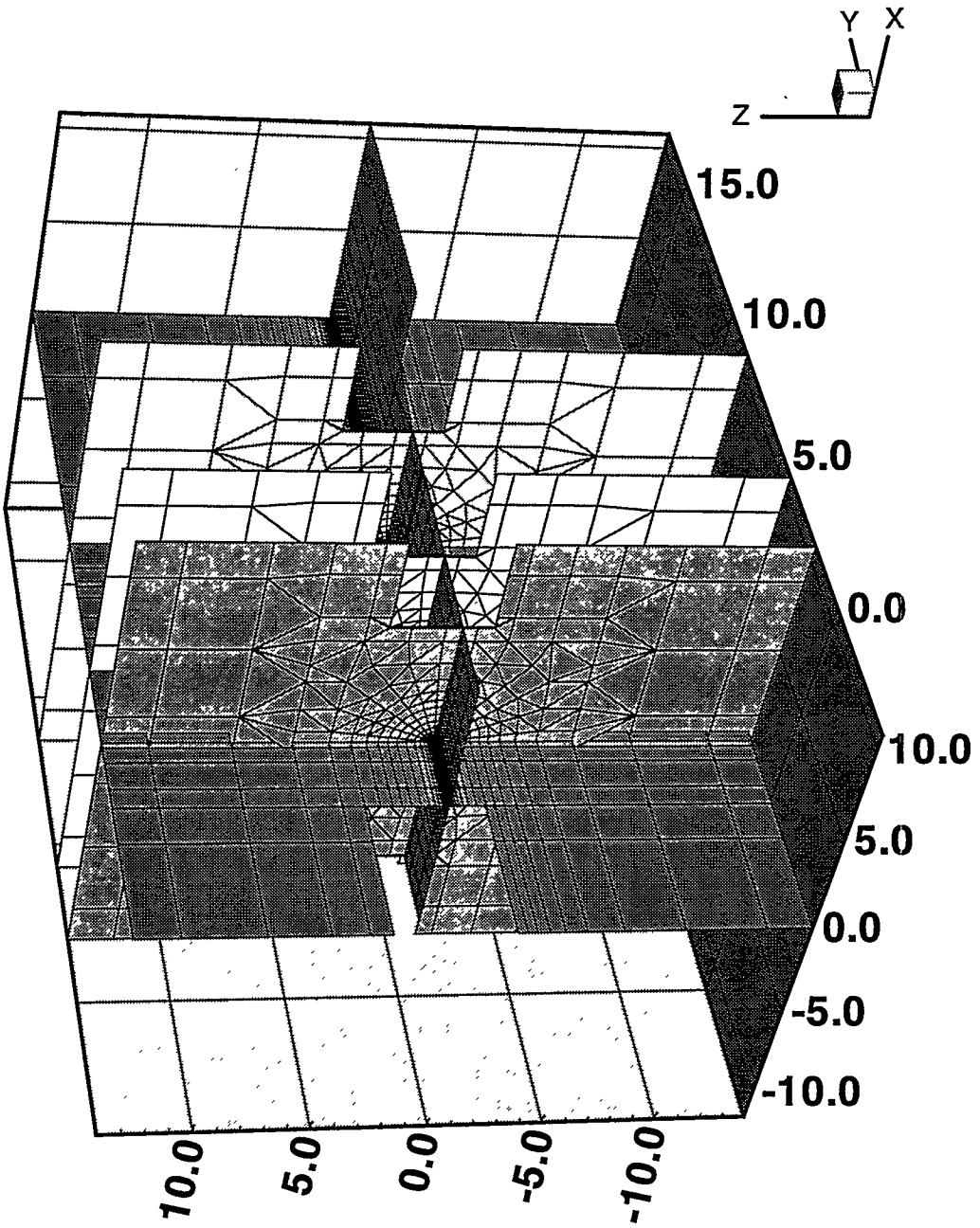

Figure 4.1-4 *Three-dimensional view of the discretization grid.*

(This page intentionally left blank.)

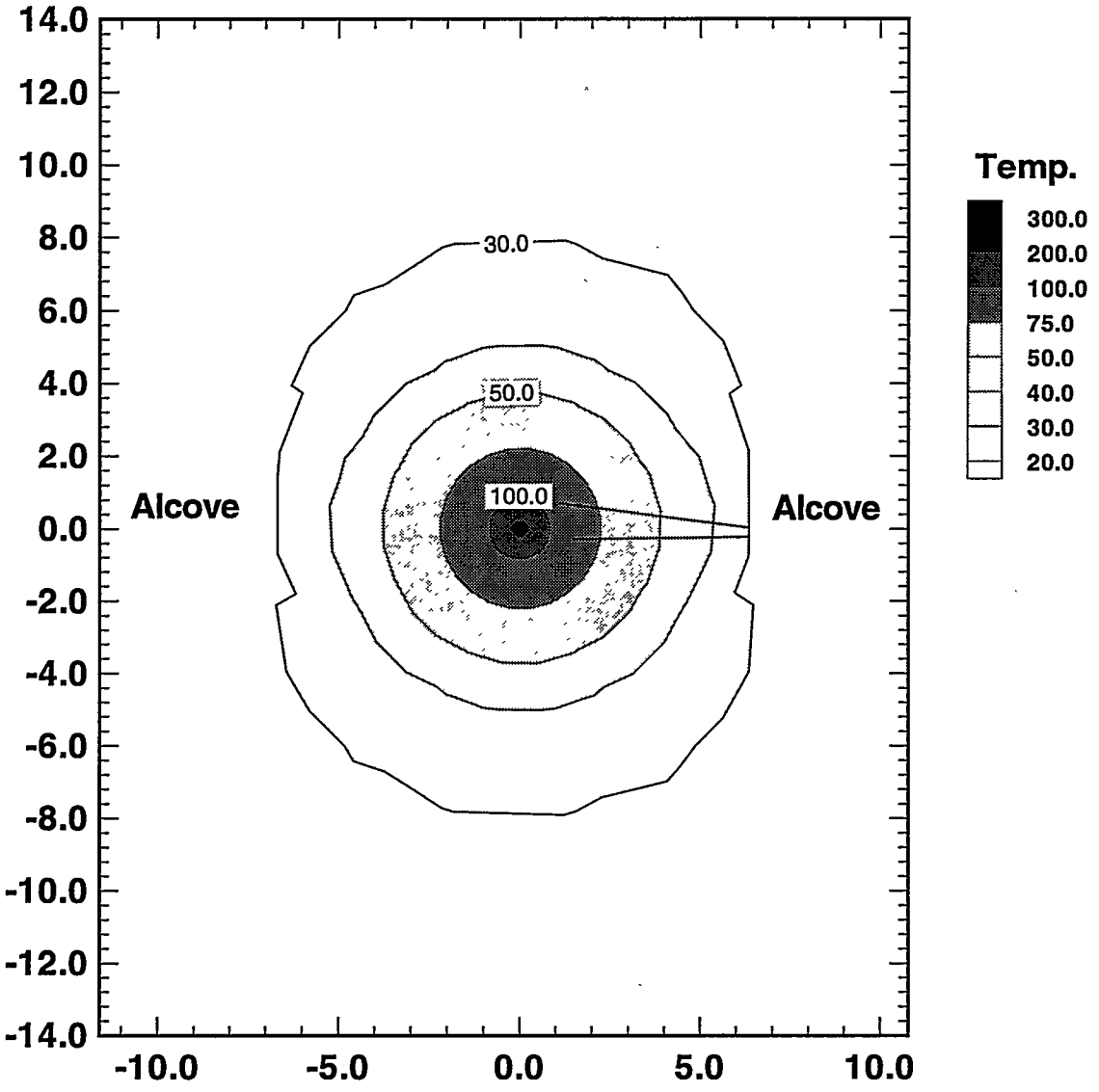

Figure 4.2-1 *Temperature response for Base Case at 1 year in XZ - cross section at Y = 4.25 m.*

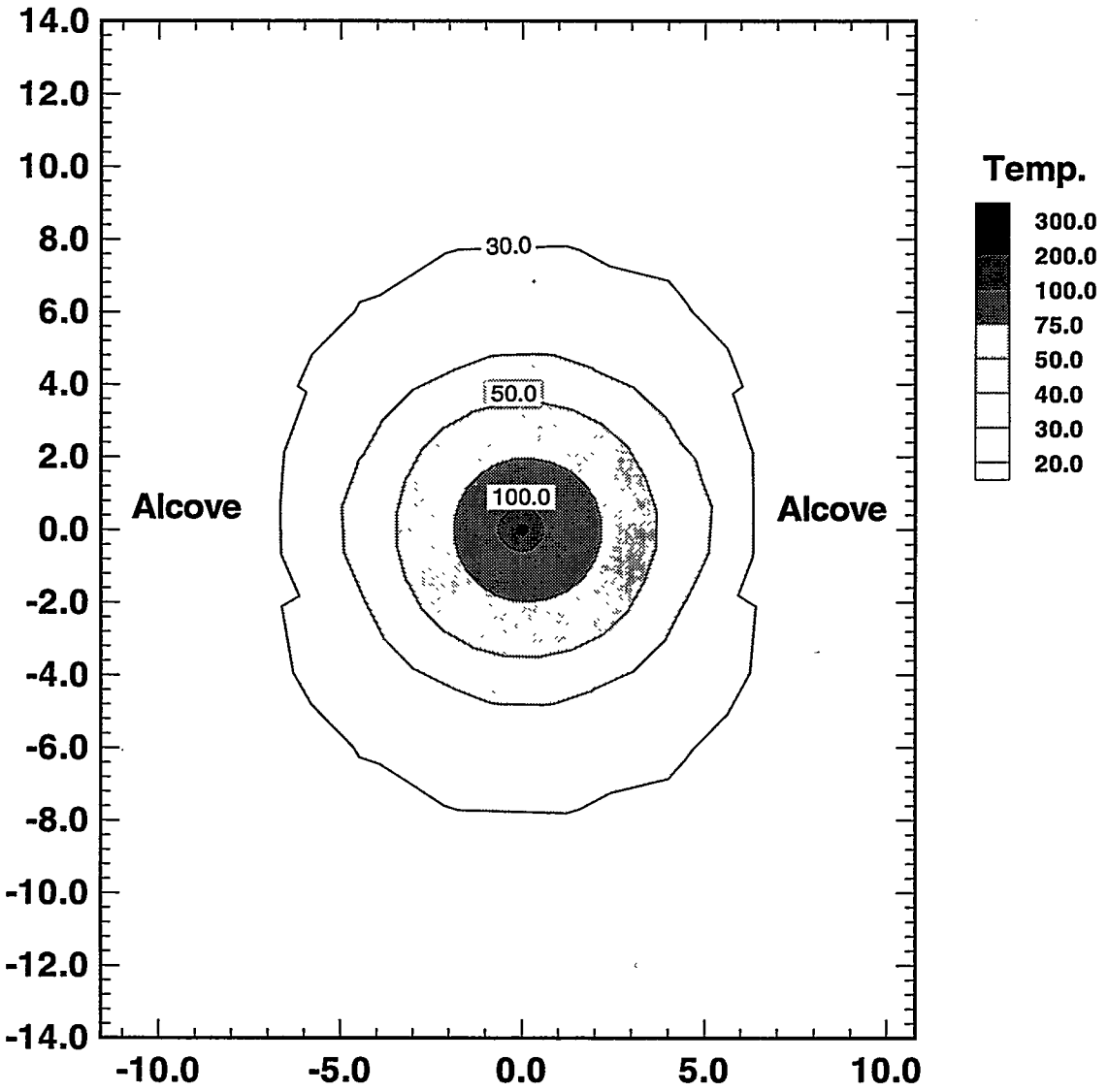

Figure 4.2-2 *Temperature response for Base Case at 1 year in XZ - cross section at Y = 6.00 m.*

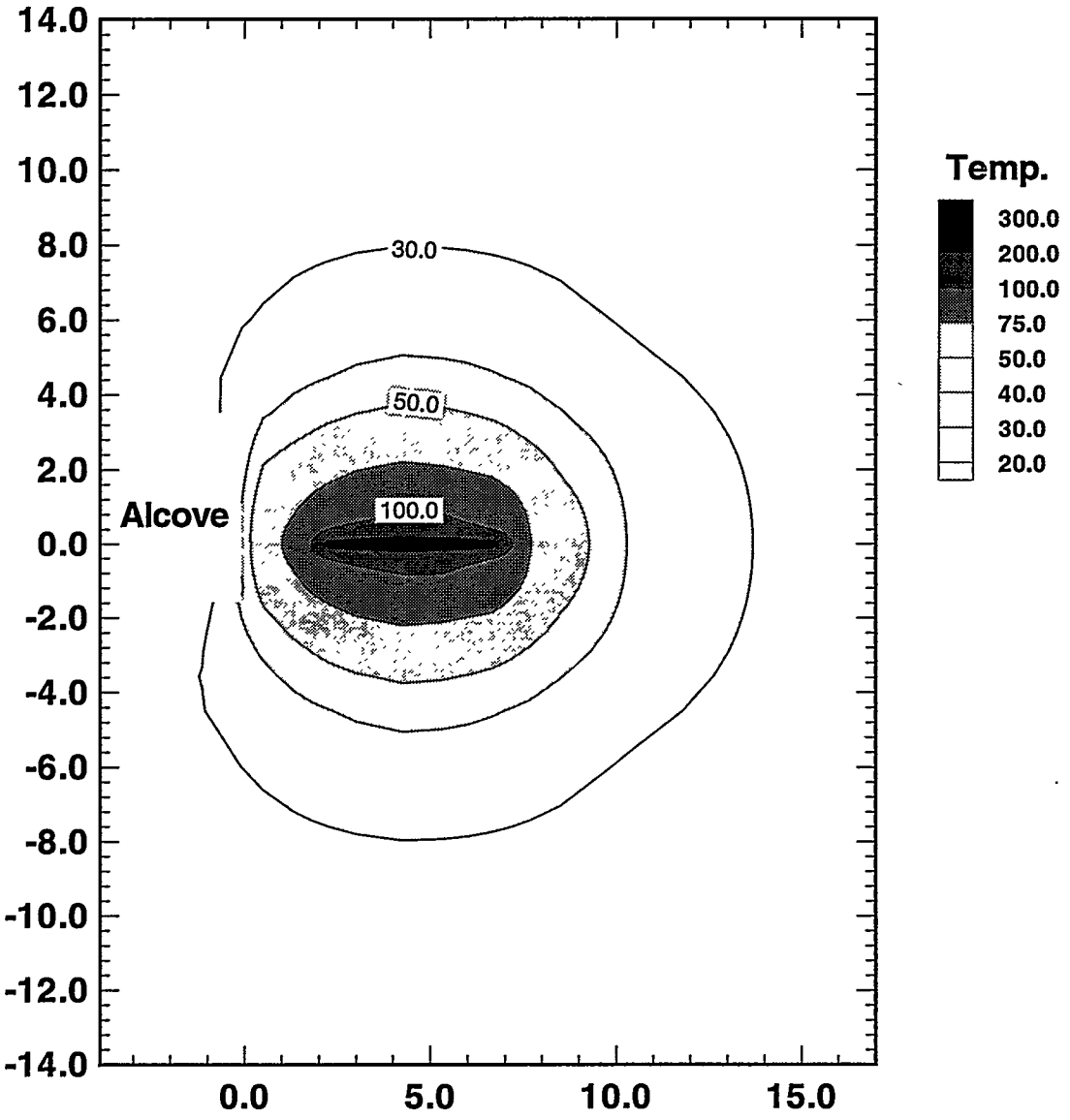

Figure 4.2-3 *Temperature response for Base Case at 1 year in YZ - cross section at X = 0.00 m.*

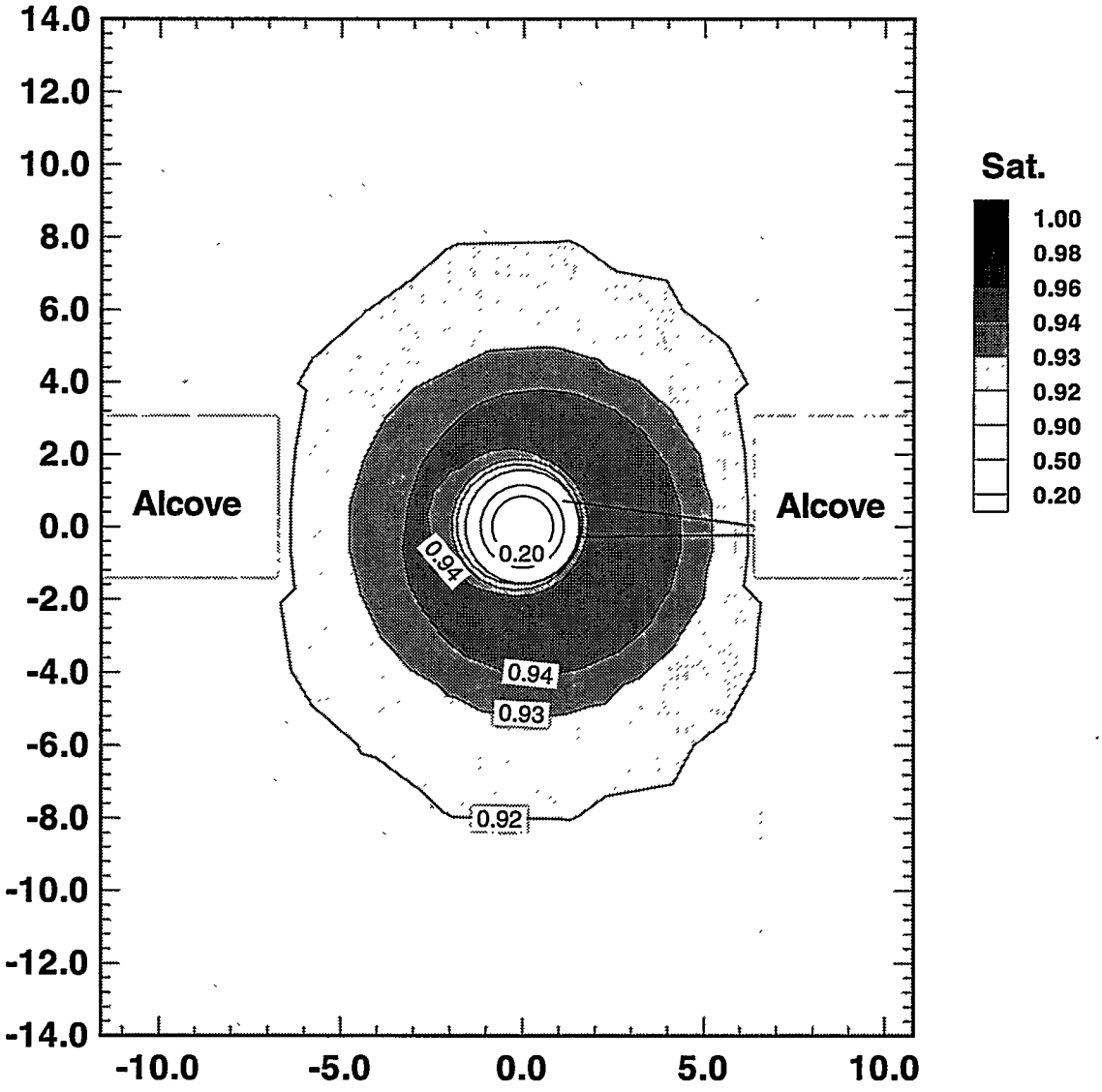

Figure 4.2-4 Equivalent continuum liquid saturation for Base Case at 1 year in XZ - cross section at Y = 4.25 m.

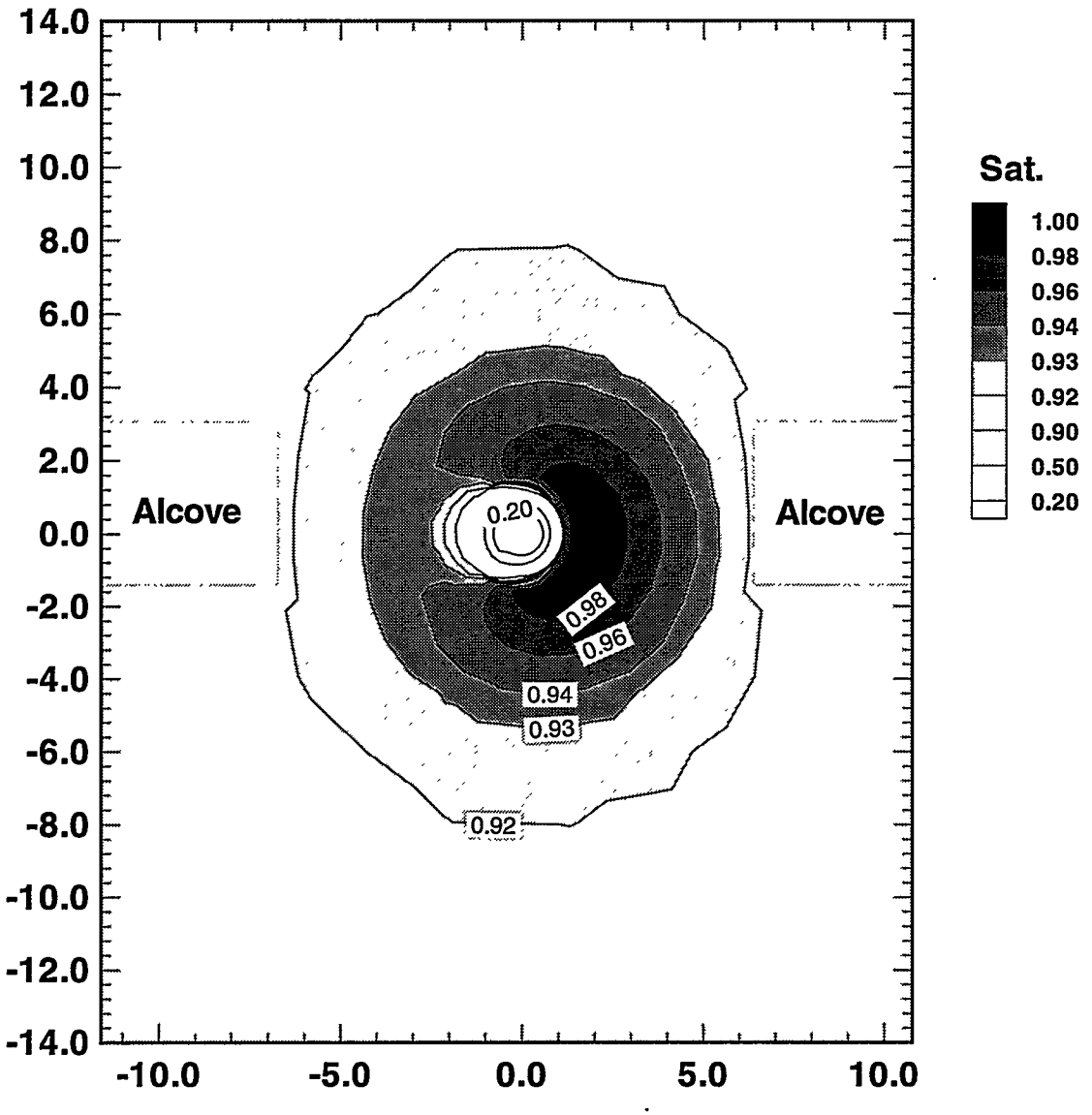

Figure 4.2-5 Equivalent continuum liquid saturation for Base Case at 1 year in XZ - cross section at Y = 6.00 m.

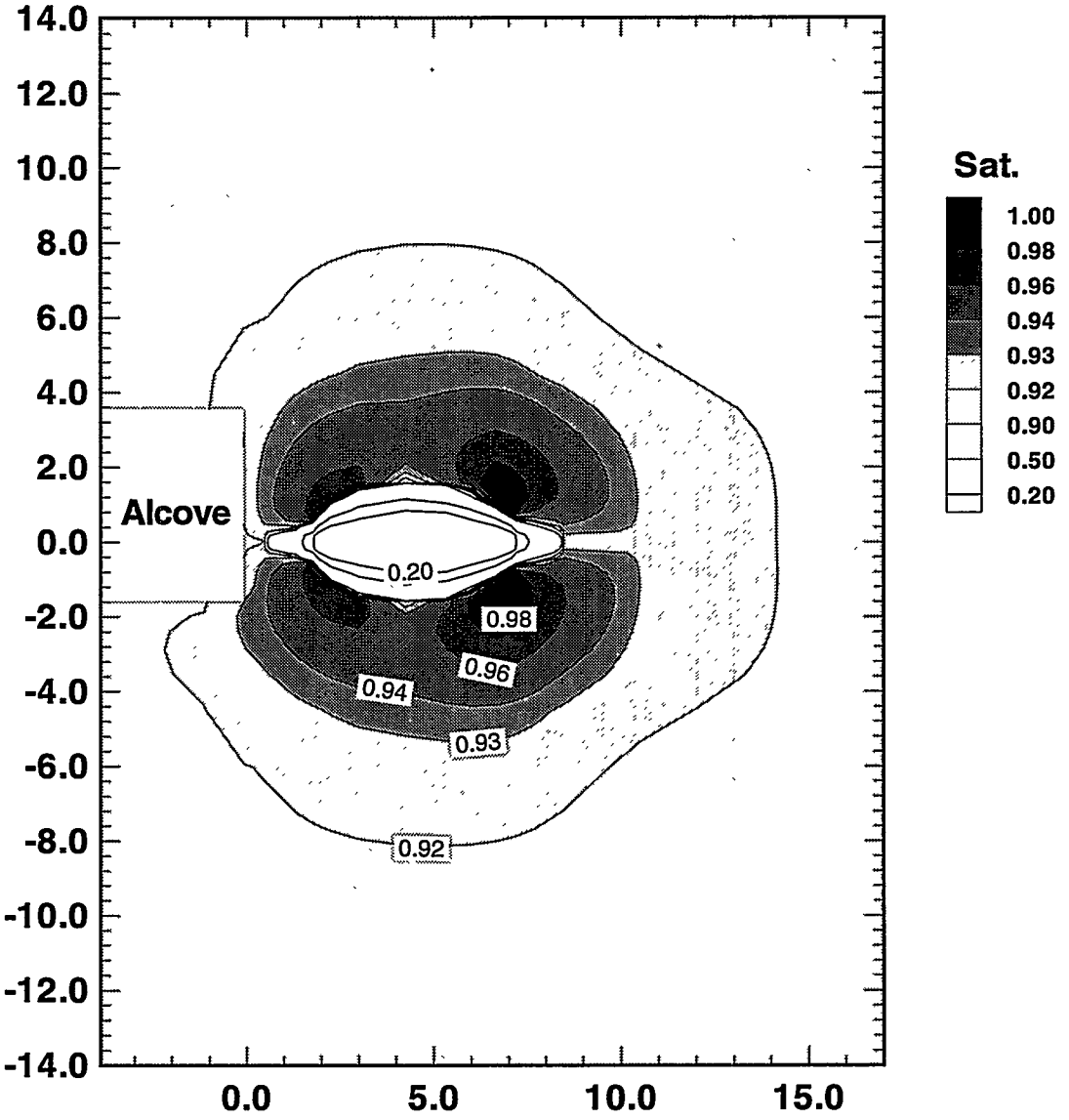

Figure 4.2-6 Equivalent continuum liquid saturation for Base Case at 1 year in YZ - cross section at X = 0.00 m.

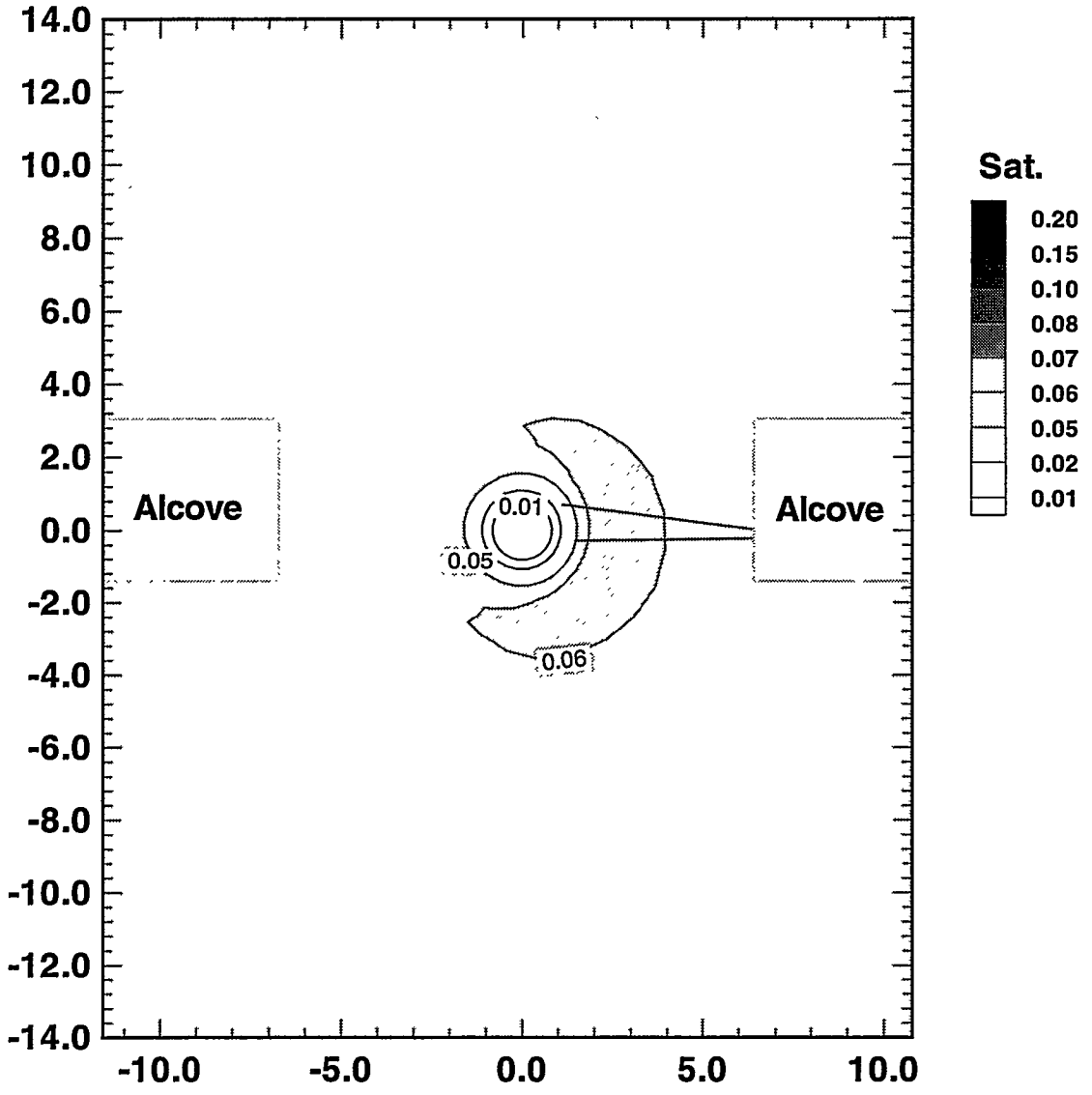

Figure 4.2-7 Fracture liquid saturation for Base Case at 1 year in XZ - cross cection at Y = 4.25 m.

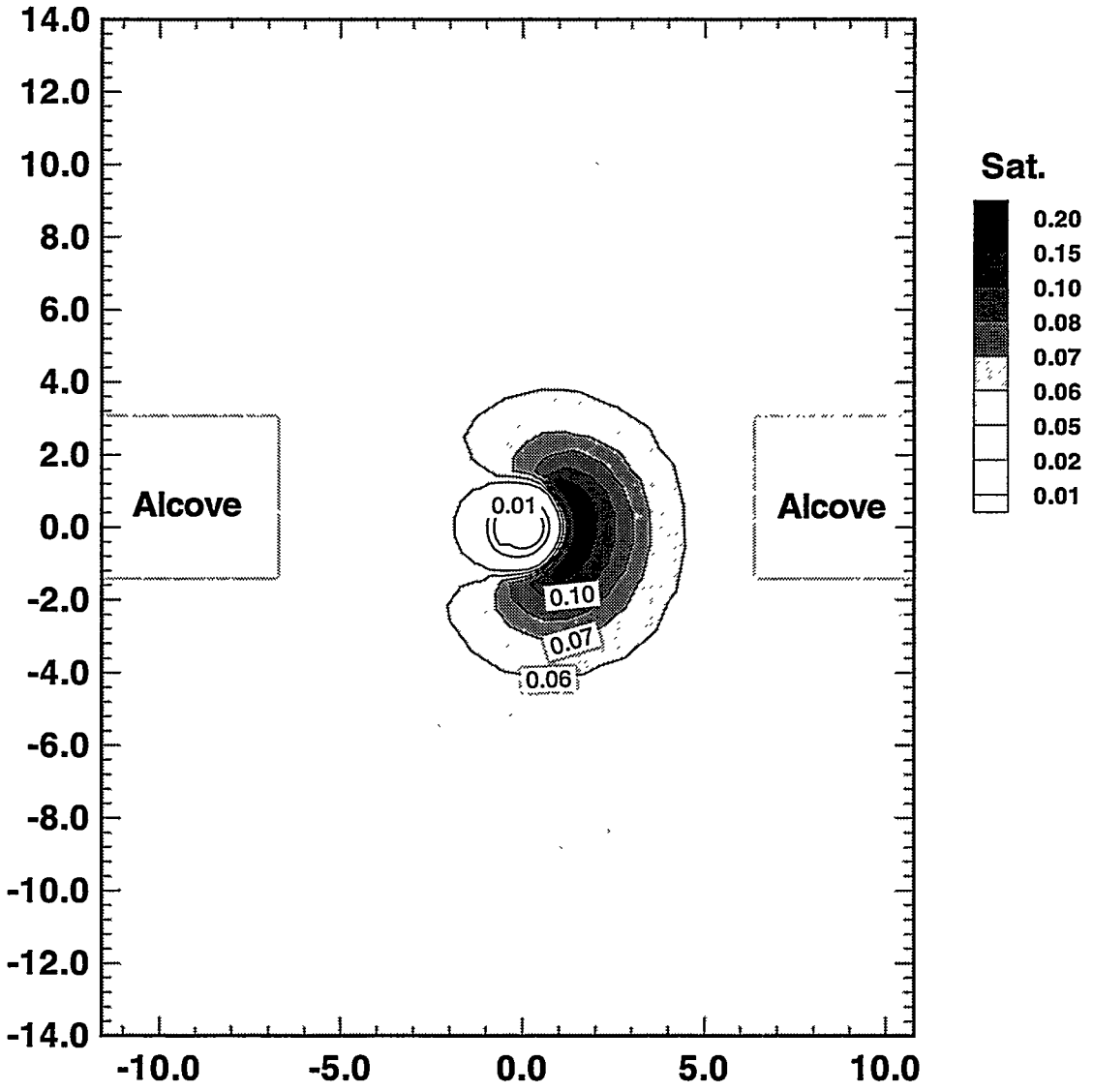

Figure 4.2-8 *Fracture liquid saturation for Base Case at 1 year in XZ - cross section at Y = 6.00 m.*

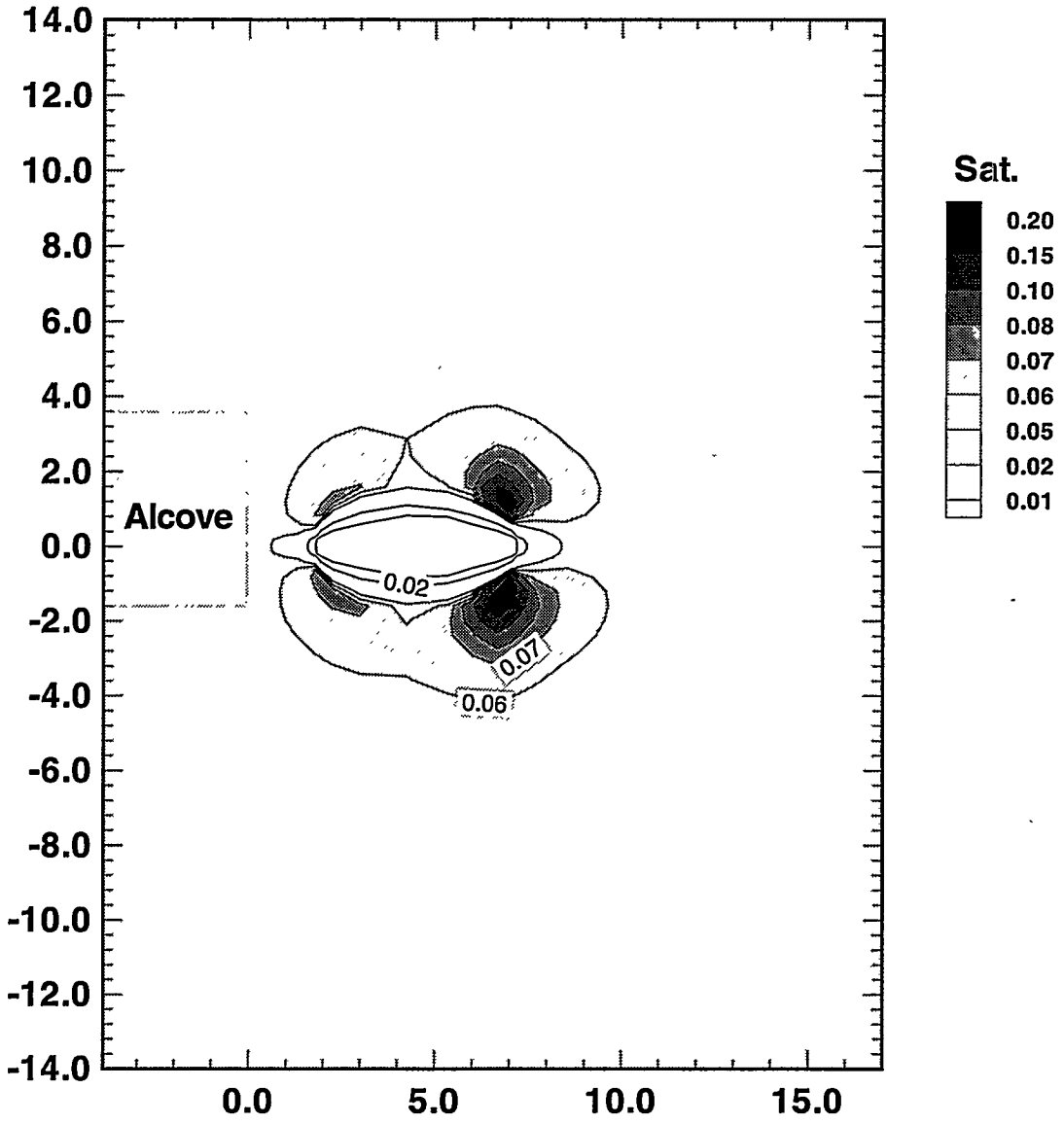

Figure 4.2-9 Fracture liquid saturation for Base Case at 1 year in YZ - cross section at X = 0.00 m.

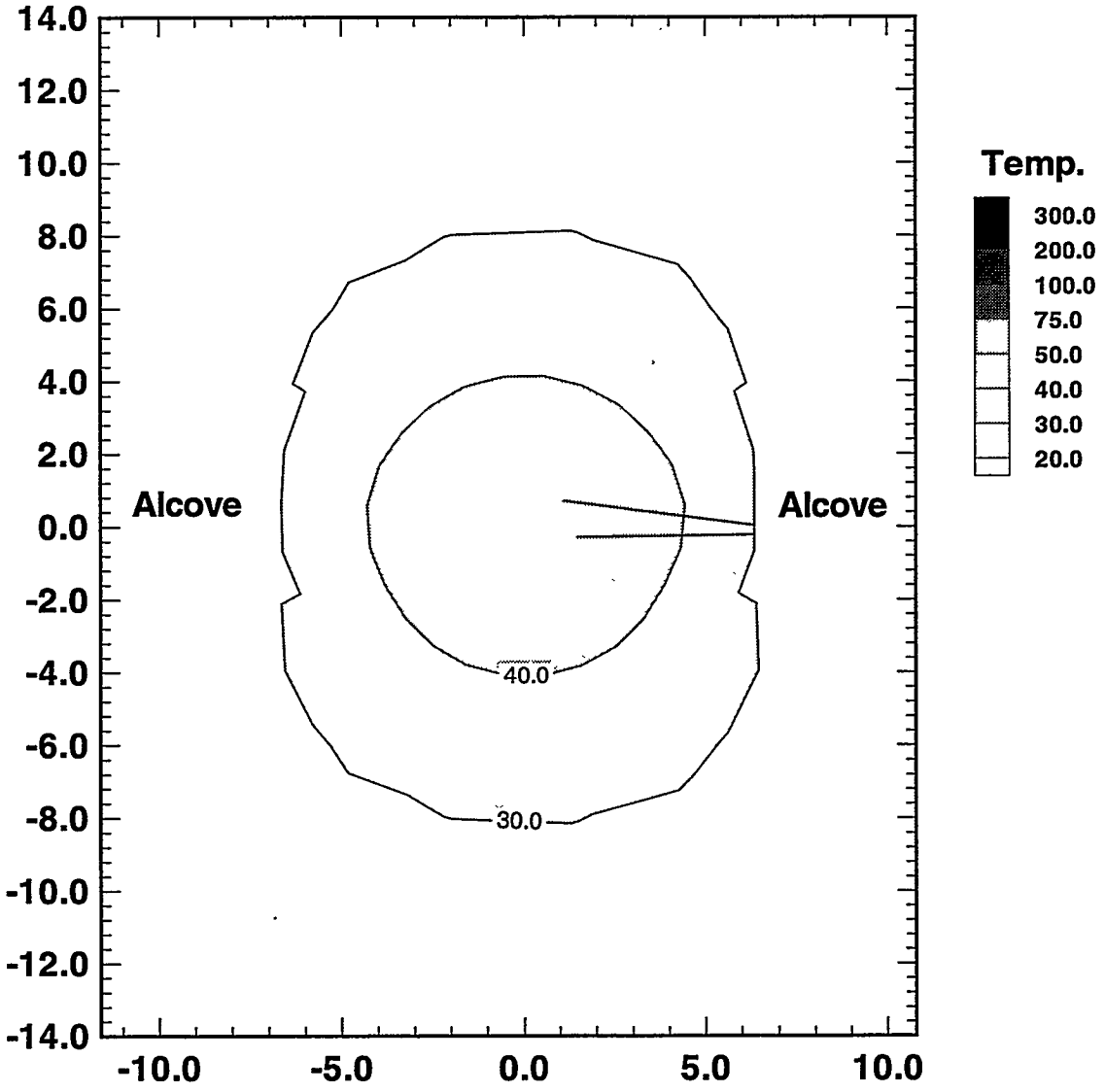

Figure 4.2-10 Temperature response for Base Case at 15 months after 1 year heating period in XZ - cross section at Y = 4.25 m.

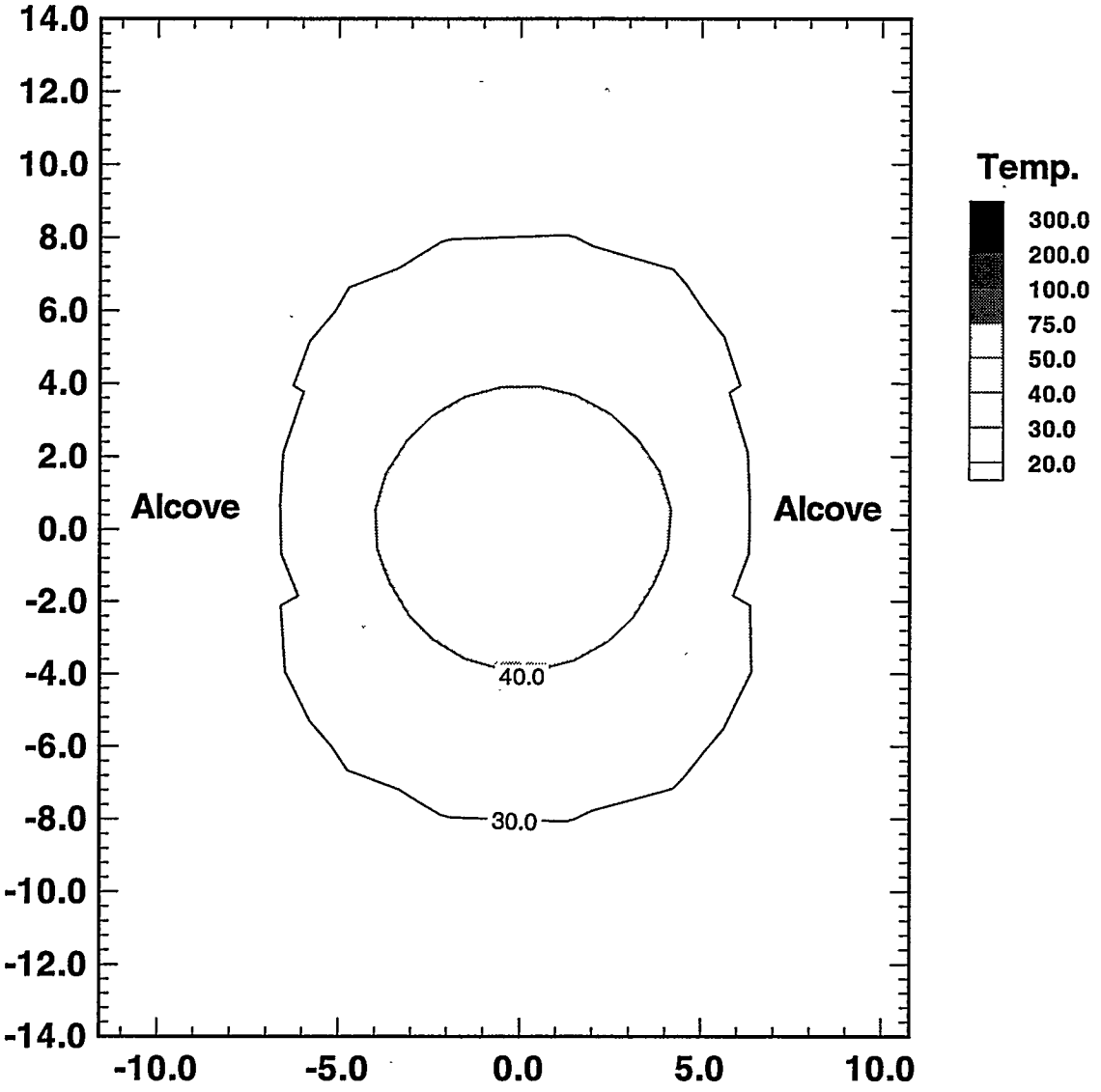

Figure 4.2-11 Temperature response for Base Case at 15 months after 1 year heating period in XZ - cross section at Y = 6.00 m.

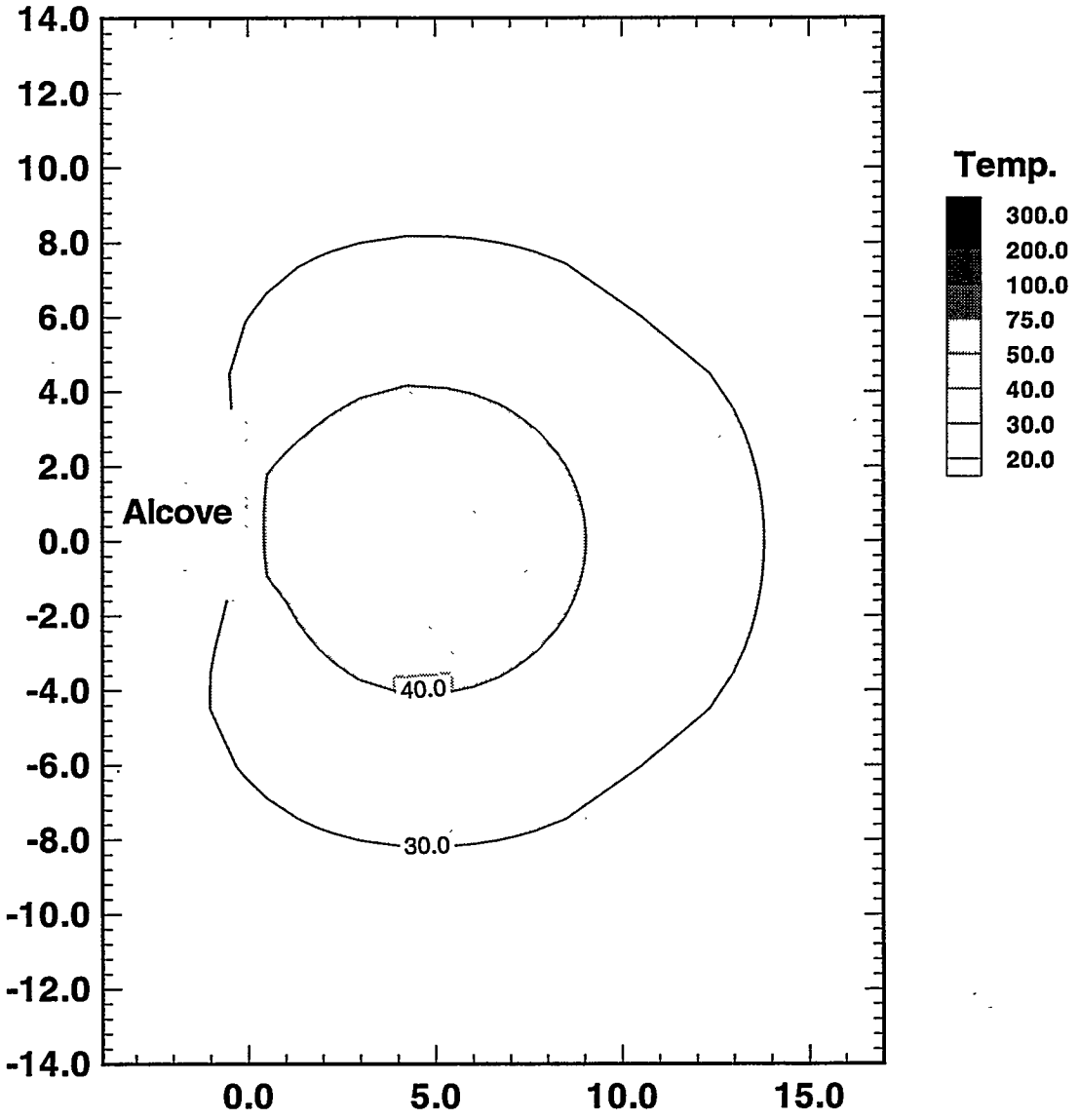

Figure 4.2-12 Temperature response for Base Case at 15 months after 1 year heating period in YZ - cross section at X = 0.00 m.

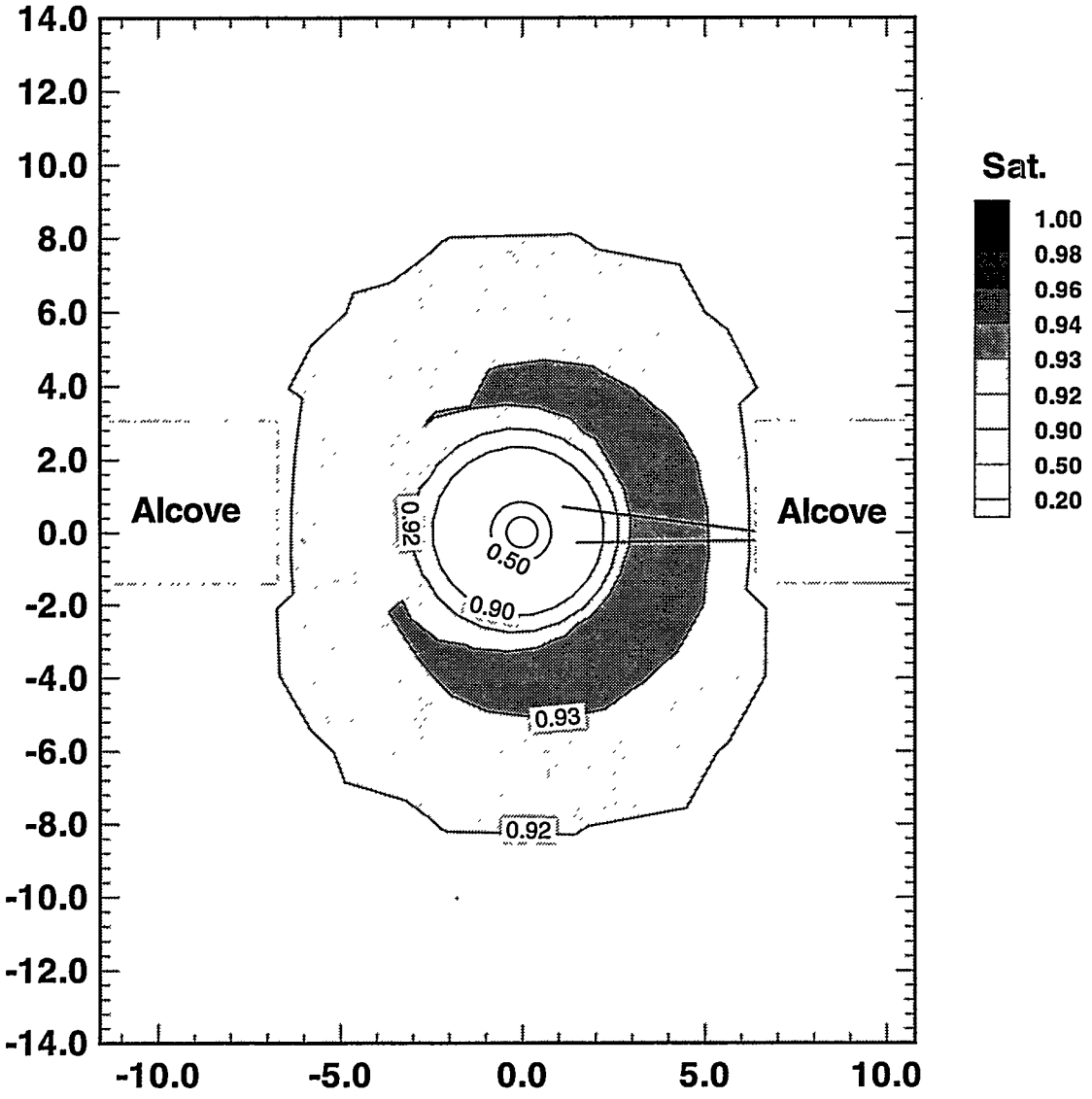

Figure 4.2-13 Equivalent continuum liquid saturation for Base Case at 15 months after 1 year heating period in XZ - cross section at Y = 4.25 m.

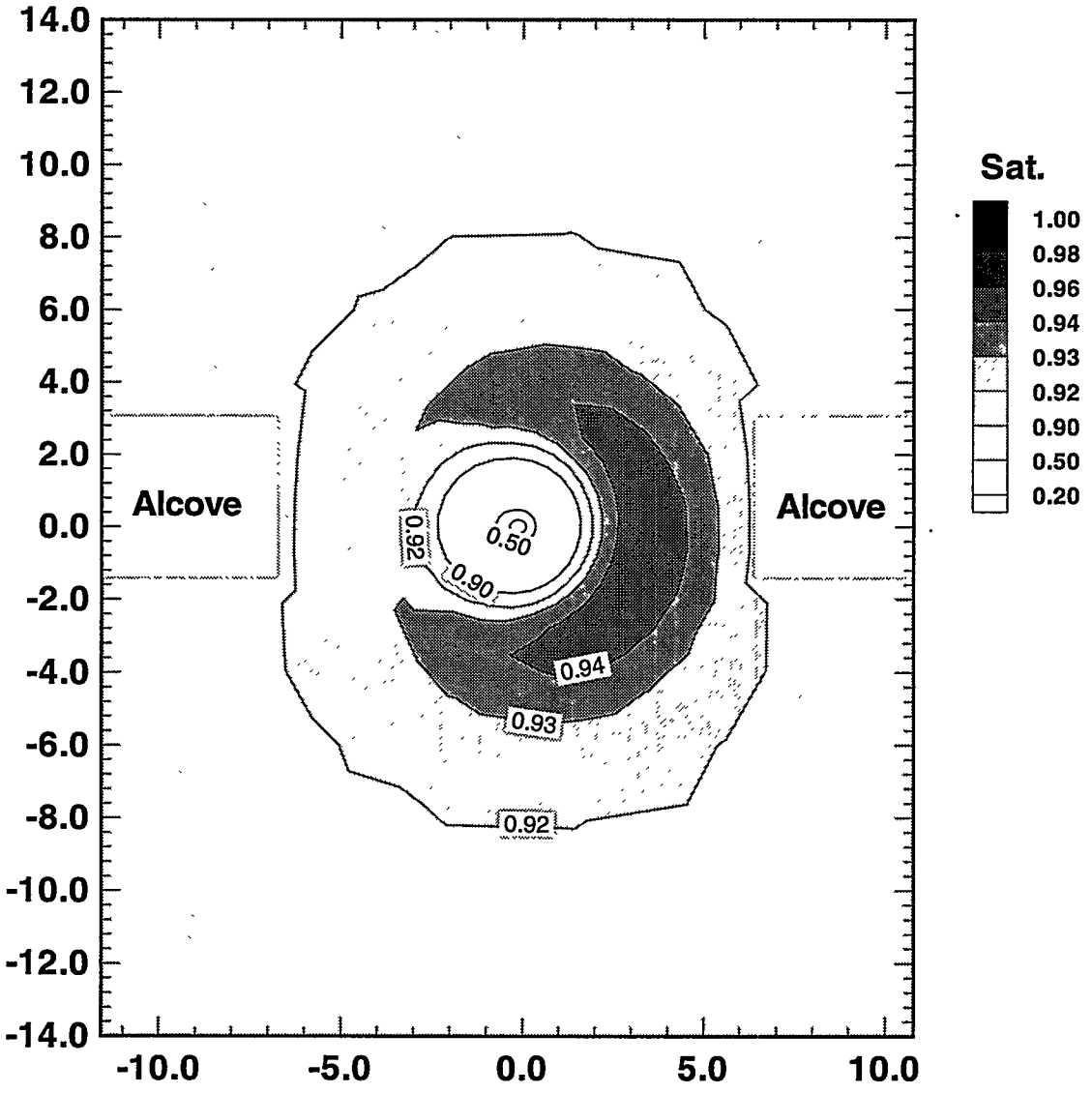

Figure 4.2-14 Equivalent continuum liquid saturation for Base Case at 15 months after 1 year heating period in XZ - cross section at Y = 6.00 m.

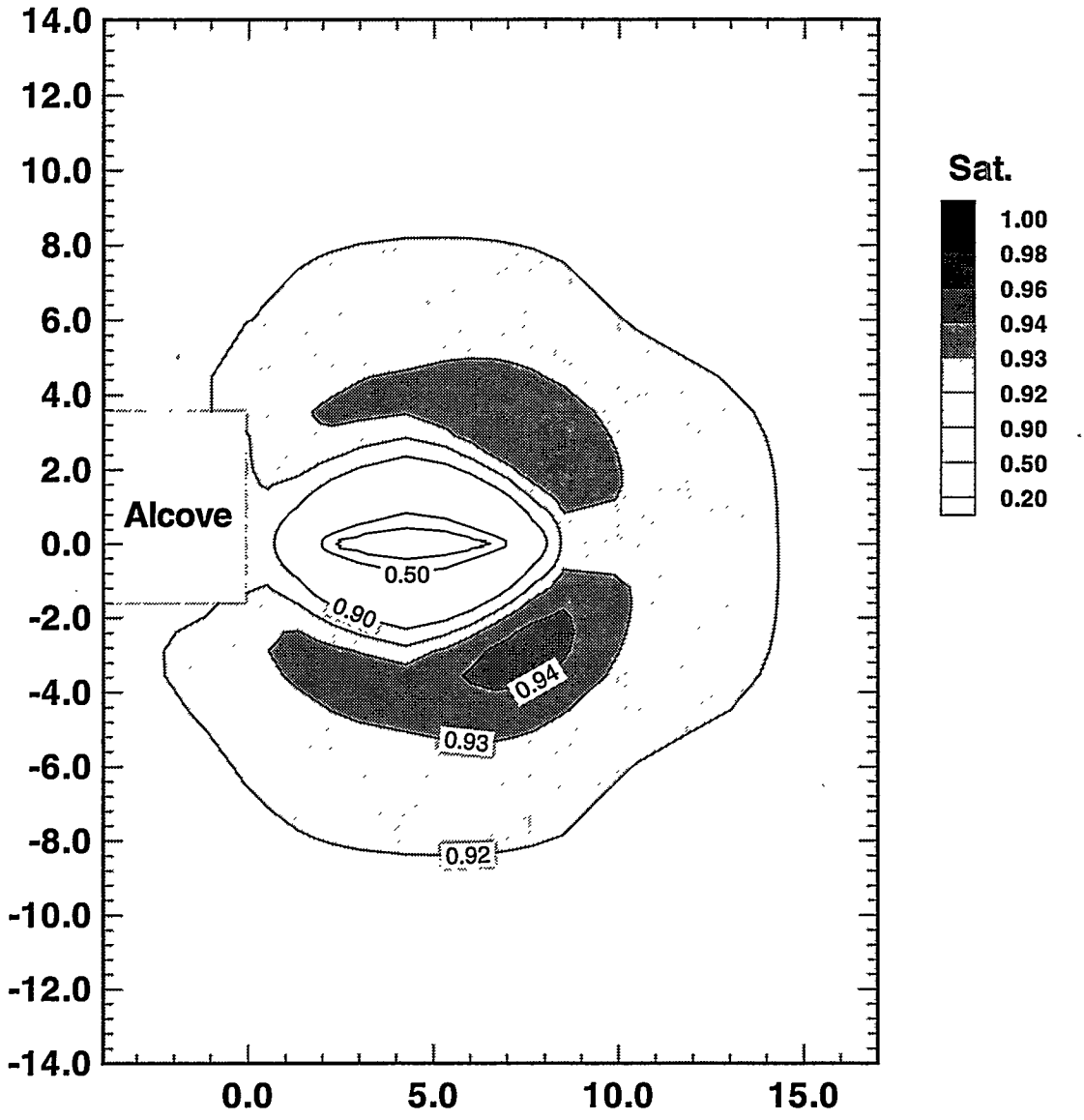

Figure 4.2-15 Equivalent continuum liquid saturation for Base Case at 15 months after 1 year heating period in YZ - cross section at X = 0.00 m.

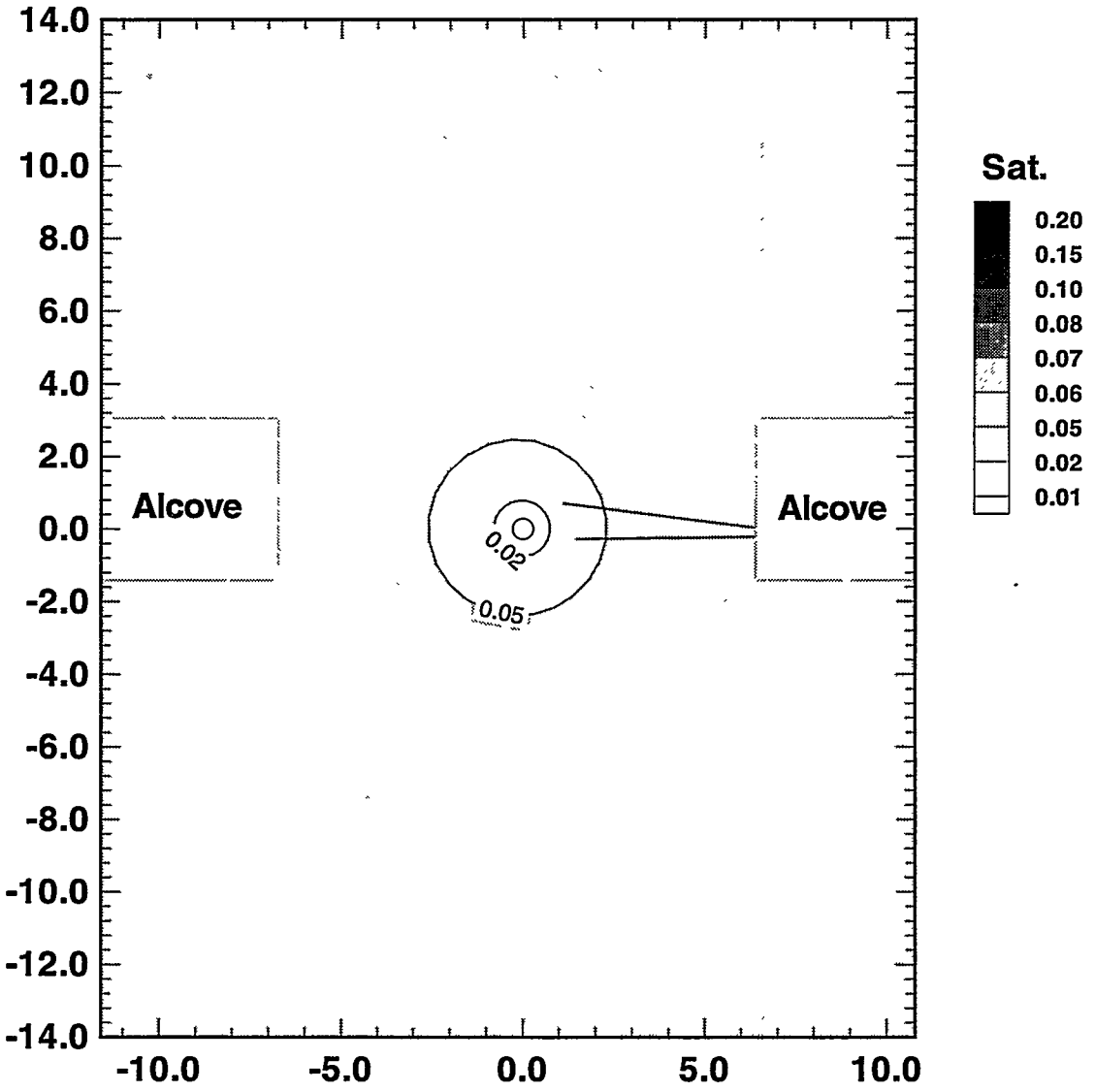

Figure 4.2-16 *Fracture liquid saturation for Base Case at 15 months after 1 year heating period in XZ - cross section at Y = 4.25 m.*

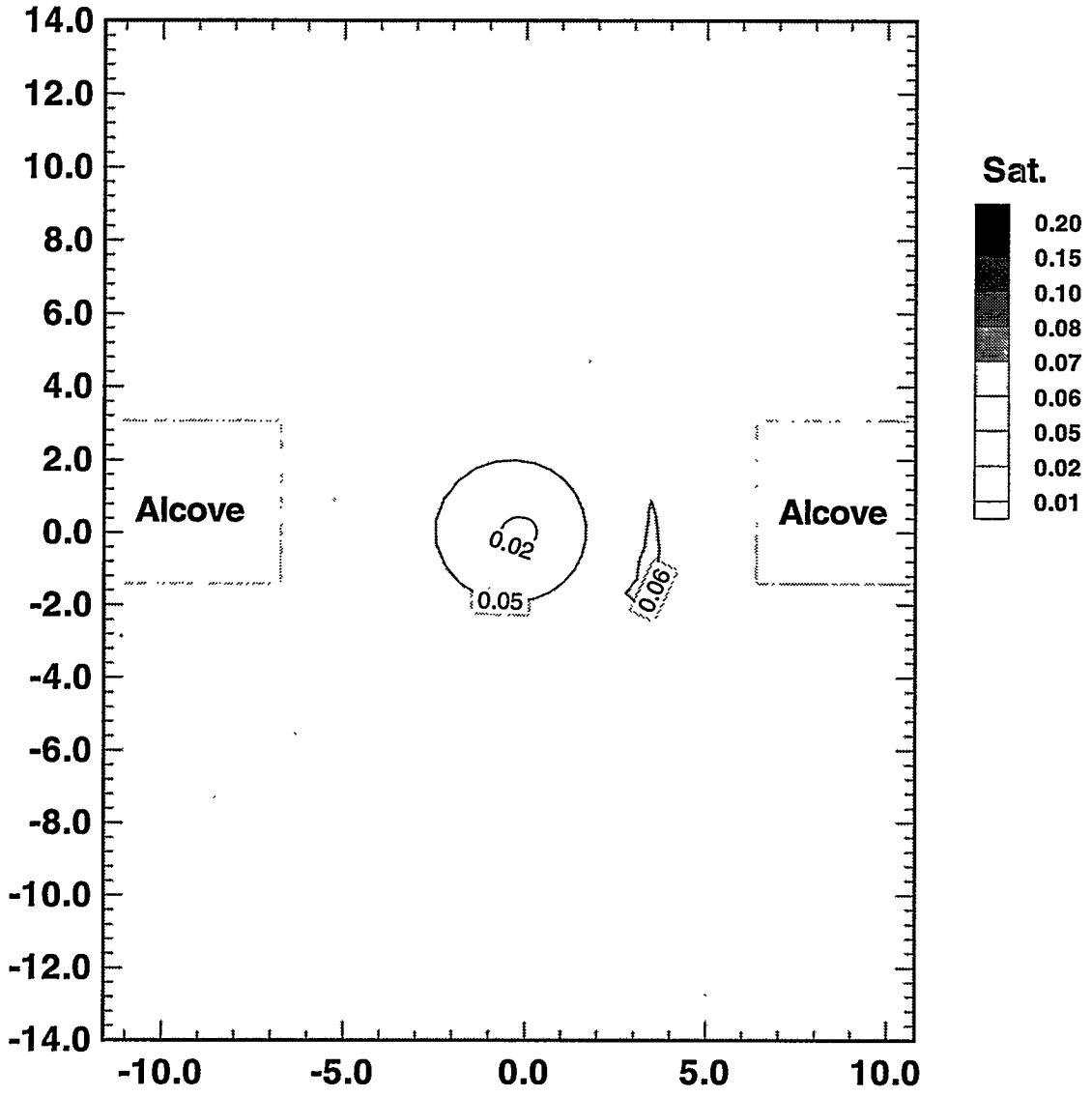

Figure 4.2-17 Fracture liquid saturation for Base Case at 15 months after 1 year heating period in XZ - cross section at Y = 6.00 m.

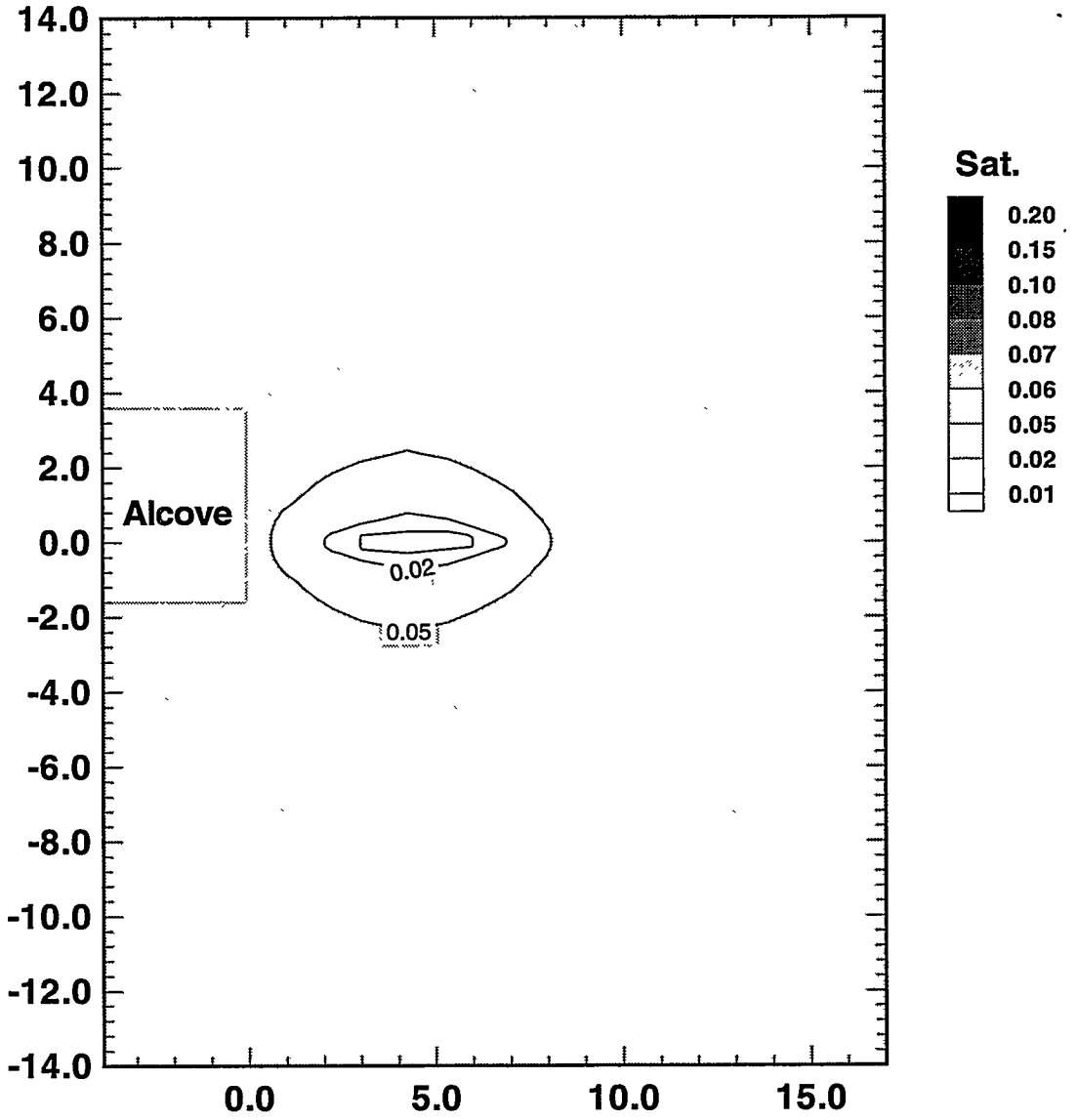

Figure 4.2-18 Fracture liquid saturation for Base Case at 15 months after 1 year heating period in YZ - cross section at X = 0.00 m.

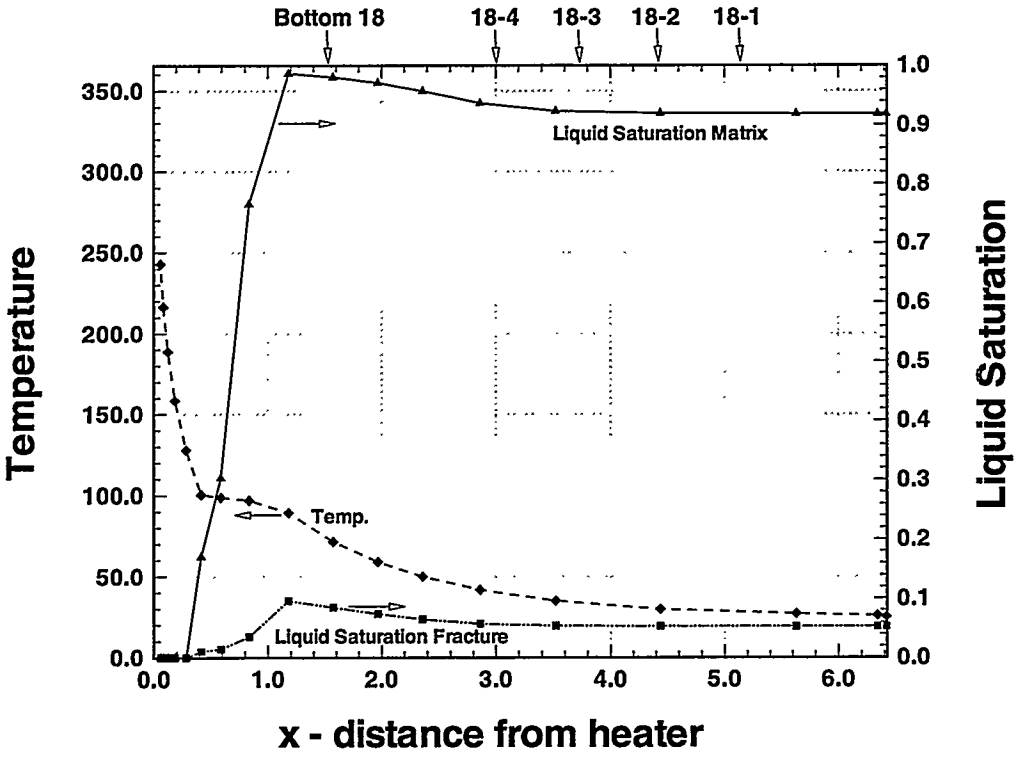

Figure 4.2-19 *Temperature / liquid saturation for Base Case at 77 days along X - axis at Y = 4.25 m and Z = 0.0 m.*

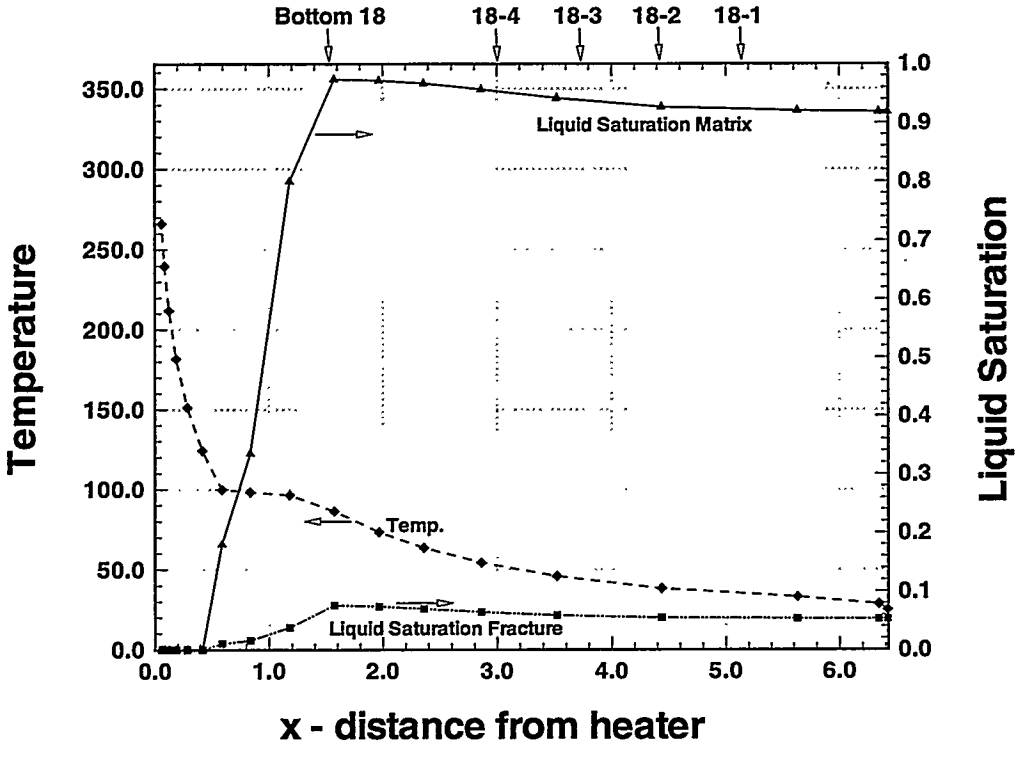

Figure 4.2-20 *Temperature / liquid saturation for Base Case at 6 months along X - axis at Y = 4.25 m and Z = 0.0 m.*

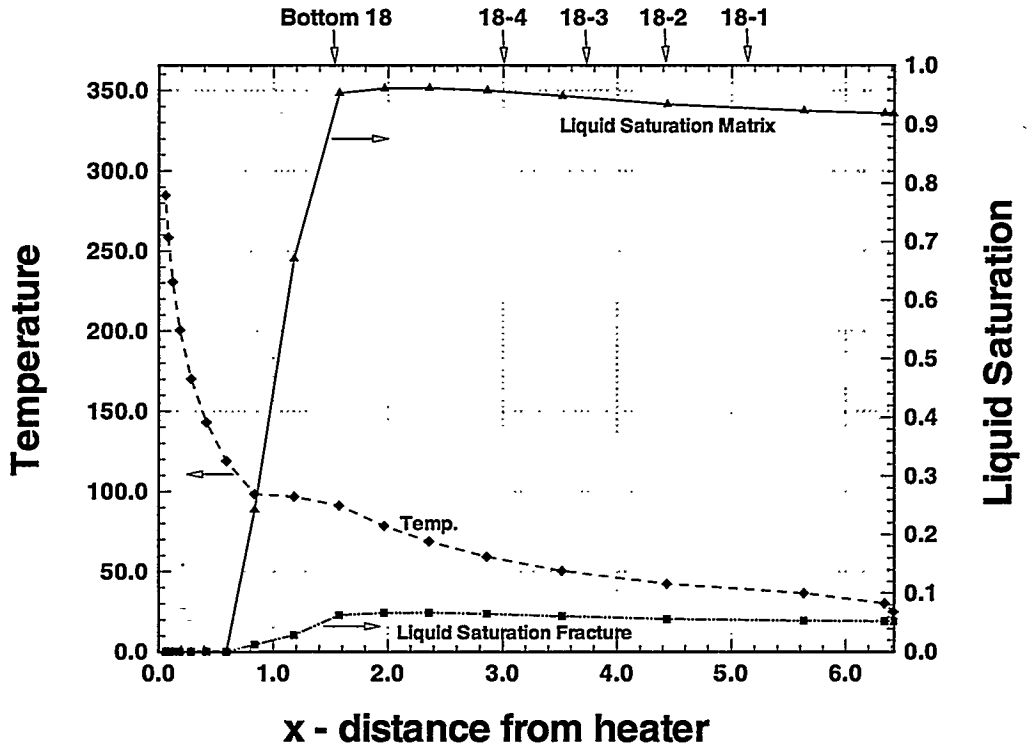

Figure 4.2-21 *Temperature / liquid saturation for Base Case at 9 months along X - axis at Y = 4.25 m and Z = 0.0 m.*

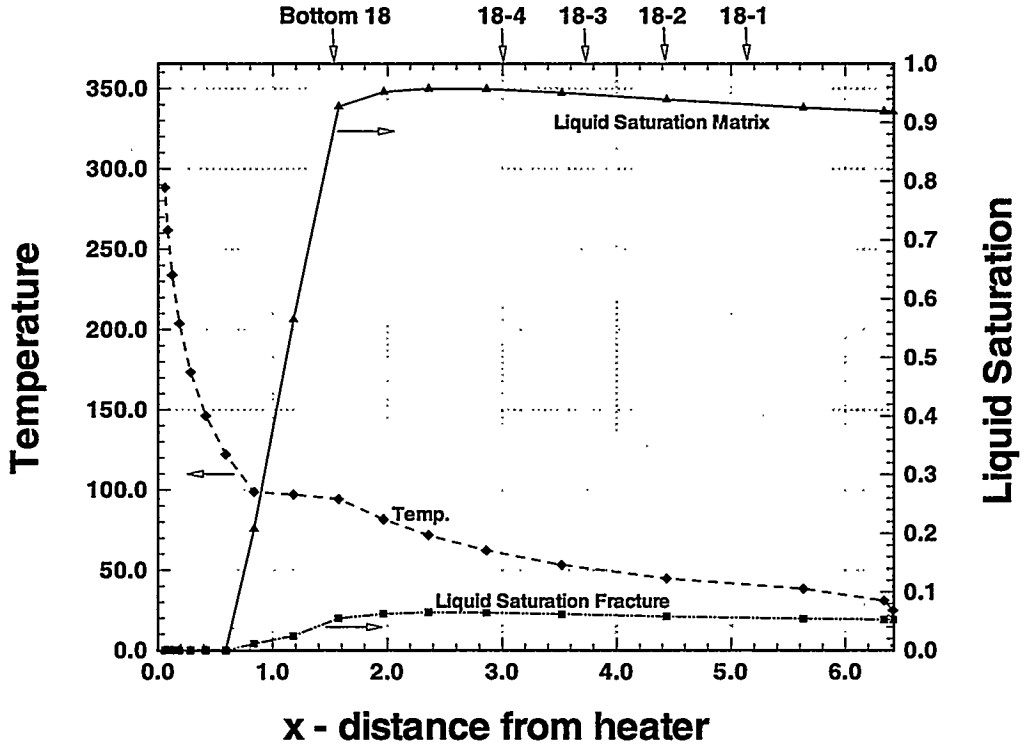

Figure 4.2-22 *Temperature / liquid saturation for Base Case at 1 year along X - axis at Y = 4.25 m and Z = 0.0 m.*

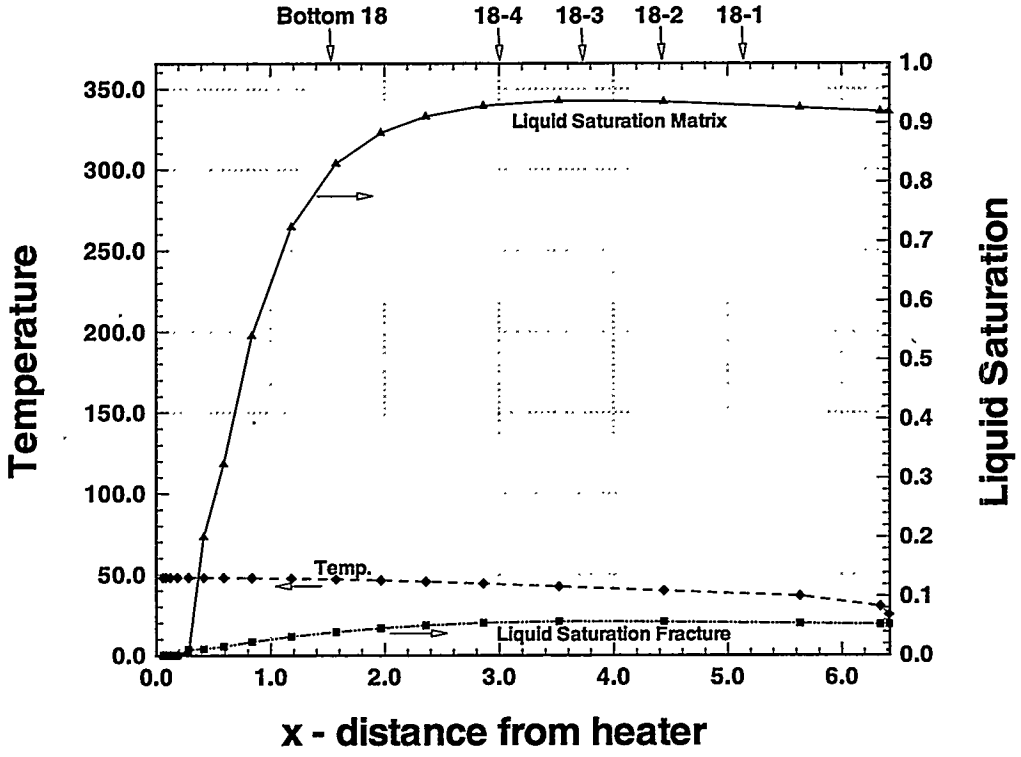

Figure 4.2-23 Temperature / liquid saturation for Base Case at 15 months after 1 year heating period along X - axis at Y = 4.25 m and Z = 0.0 m.

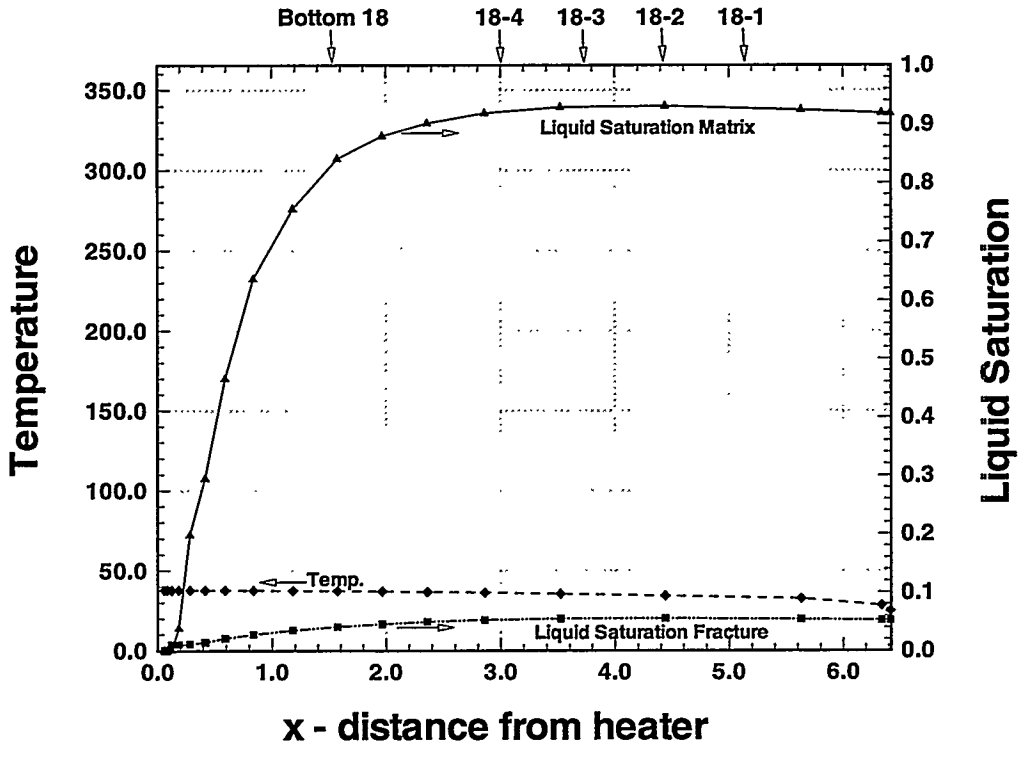

Figure 4.2-24 Temperature / liquid saturation for Base Case at 18 months after 1 year heating period along X - axis at Y = 4.25 m and Z = 0.0 m.

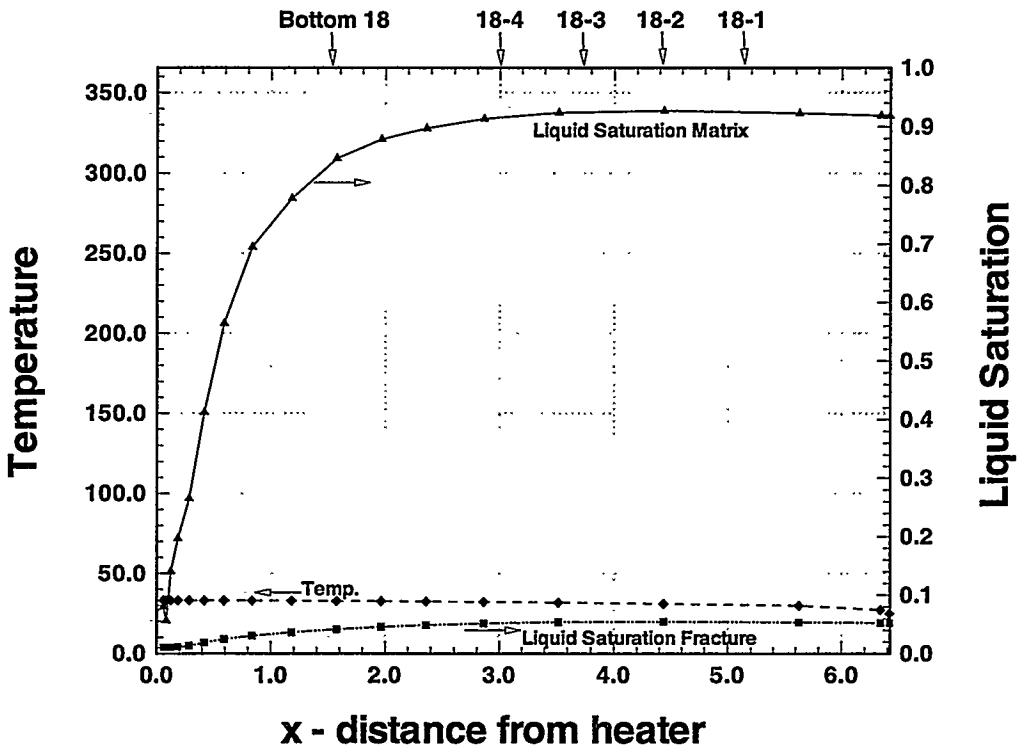

Figure 4.2-25 *Temperature / liquid saturation for Base Case at 21 months after 1 year heating period along X - axis at Y = 4.25 m and Z = 0.0 m.*

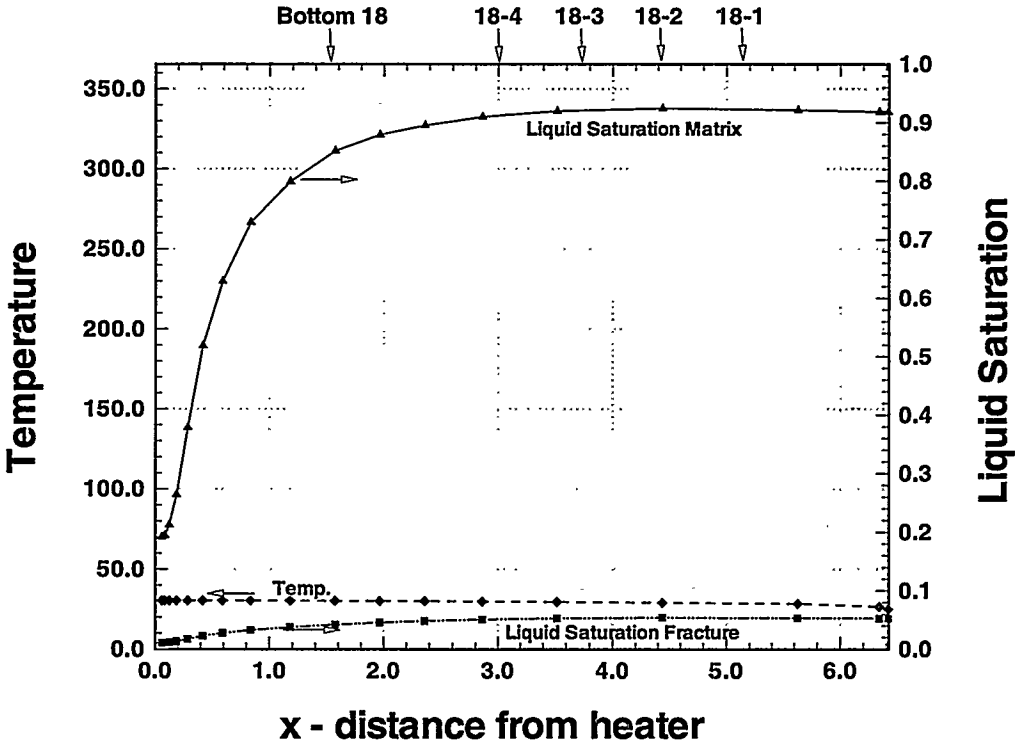

Figure 4.2-26 *Temperature / liquid saturation for Base Case at 2 years after 1 year heating period along X - axis at Y = 4.25 m and Z = 0.0 m.*

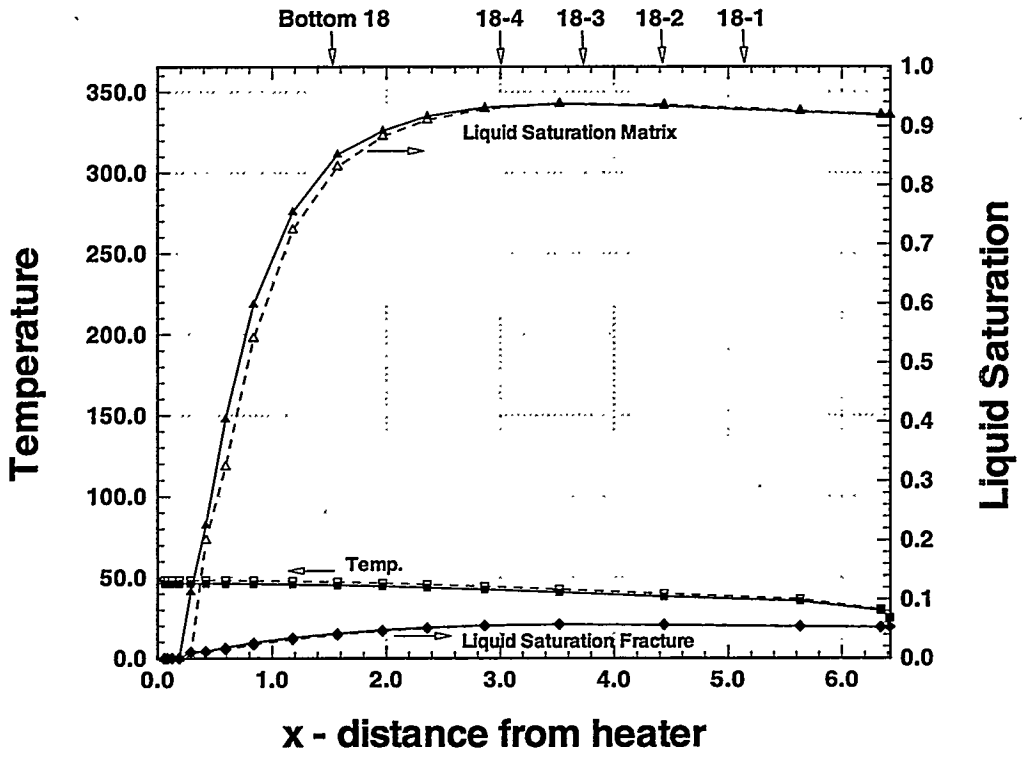

Figure 4.2-27 Comparison of temperature / liquid saturation along X - axis at Y = 4.25 m and Z = 0.0 m for two different heating periods. Results represent Base Case after a 3 month cooling period. Solid symbols / lines denote a 1 year heating period, hollow symbols and dashed lines denote a 9 month heating period.

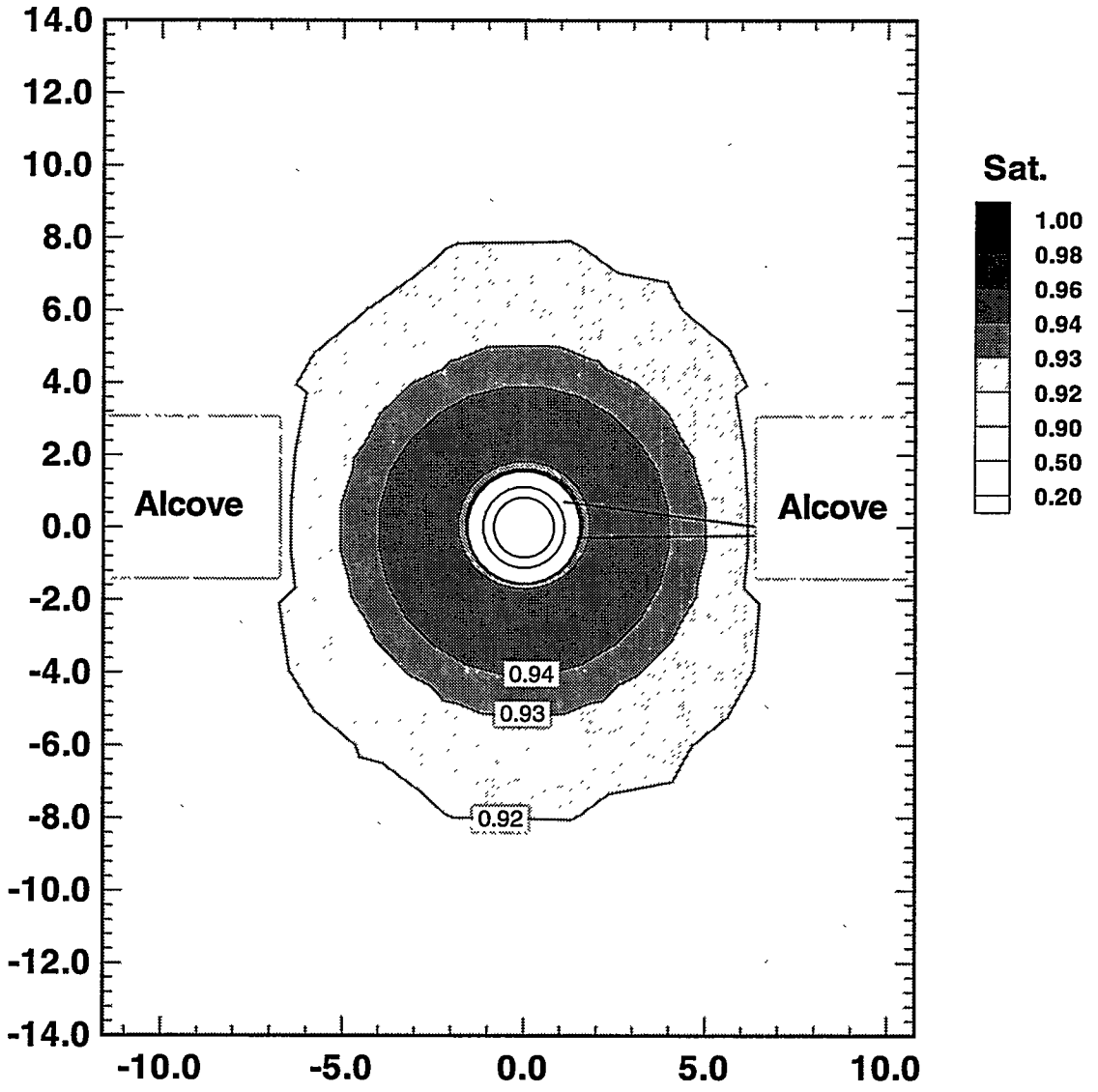

Figure 4.3-1 *Equivalent continuum liquid saturation for fully homogeneous model domain at 1 year in XZ - cross section at Y = 4.25 m.*

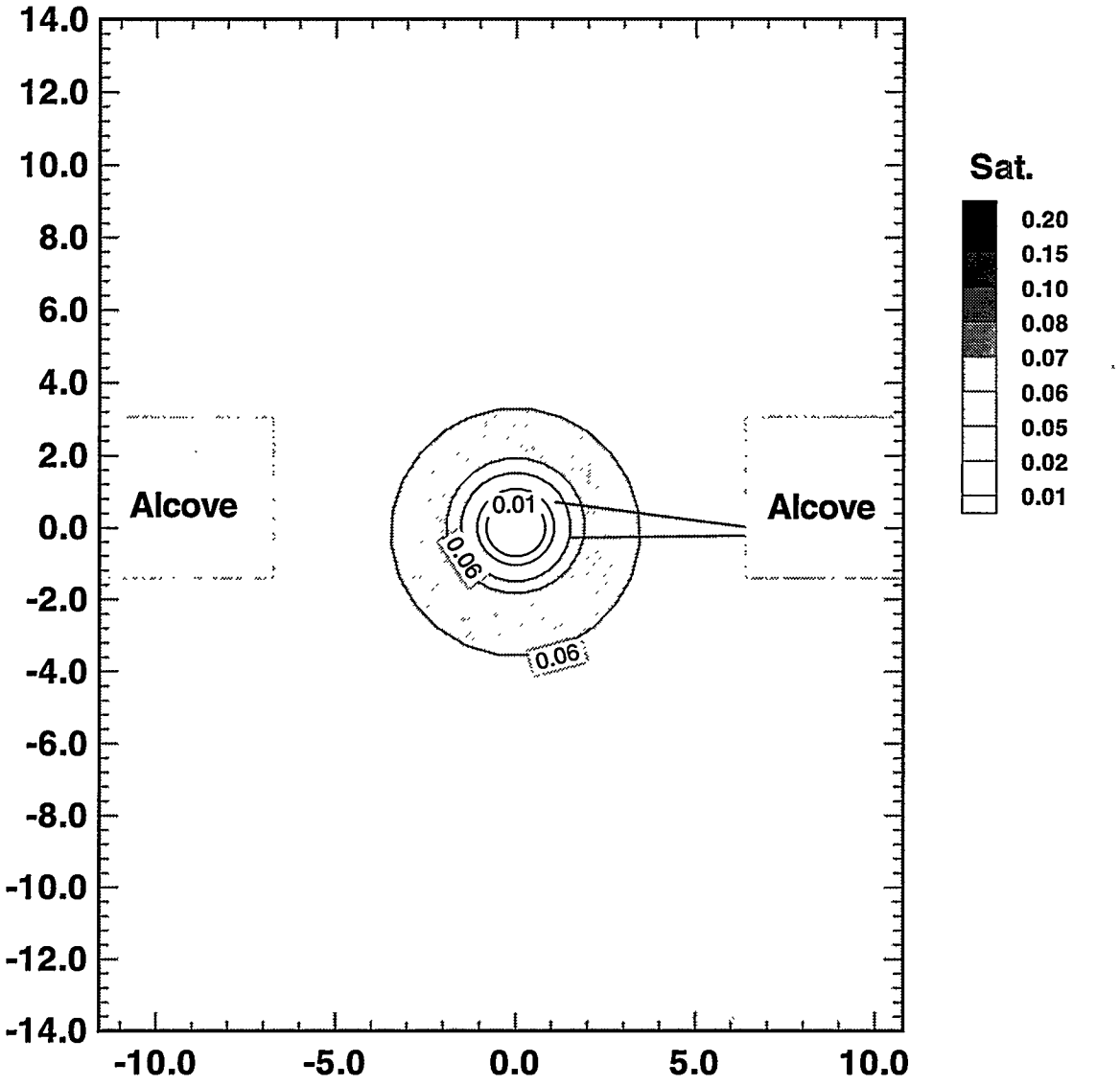

Figure 4.3-2 Fracture liquid saturation for fully homogeneous model domain at 1 year in XZ - cross section at Y = 4.25 m.

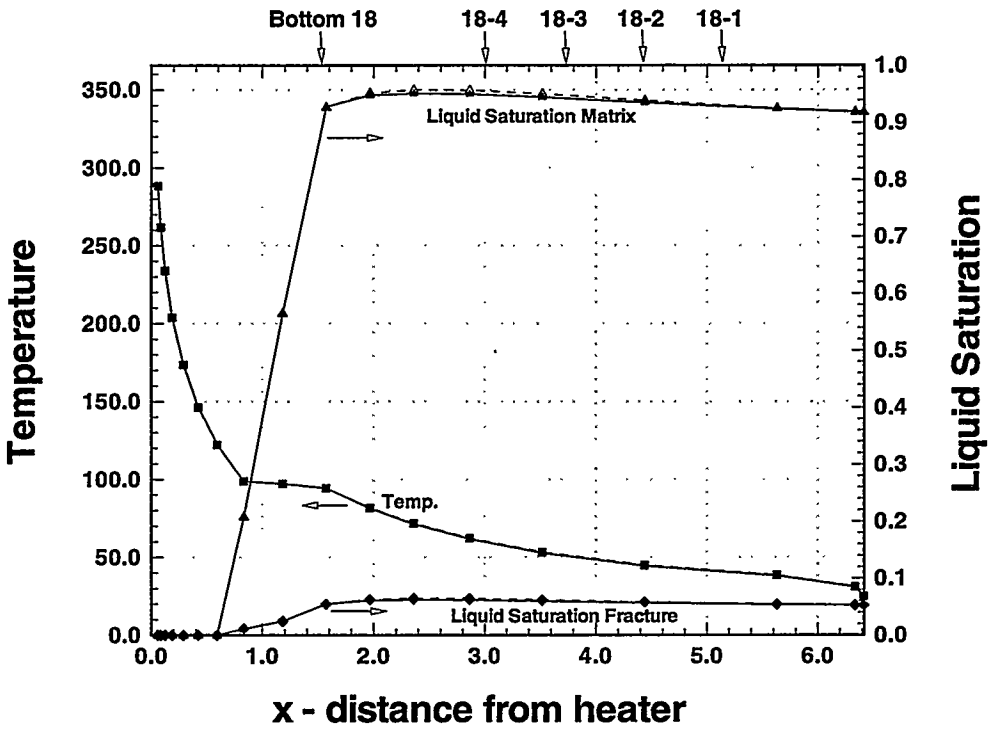

Figure 4.3-3 Comparison of temperature / liquid saturation at 1 year along X - axis at Y = 4.25 m and Z = 0.0 m for two different fracture continuum conceptualizations. Solid symbols / lines denote a homogenous domain, hollow symbols and dashed lines denote Base Case.

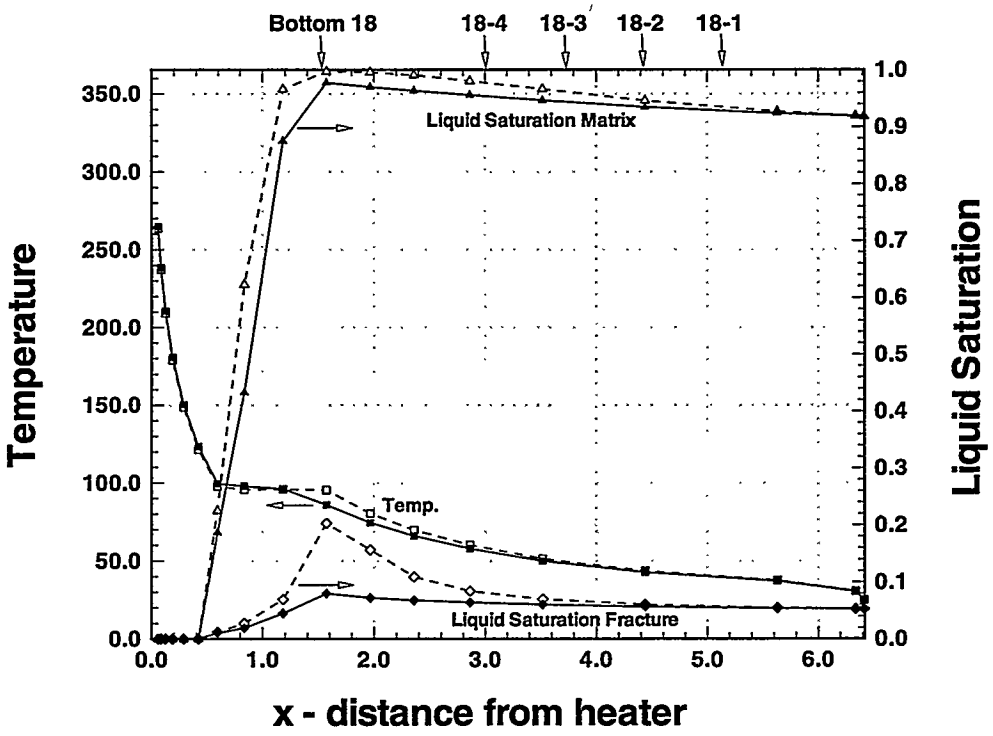

Figure 4.3-4 Comparison of temperature / liquid saturation at 1 year along X - axis at Y = 6.00 m and Z = 0.0 m for two different fracture continuum conceptualizations. Solid symbols / lines denote a homogenous domain, hollow symbols and dashed lines denote Base Case.

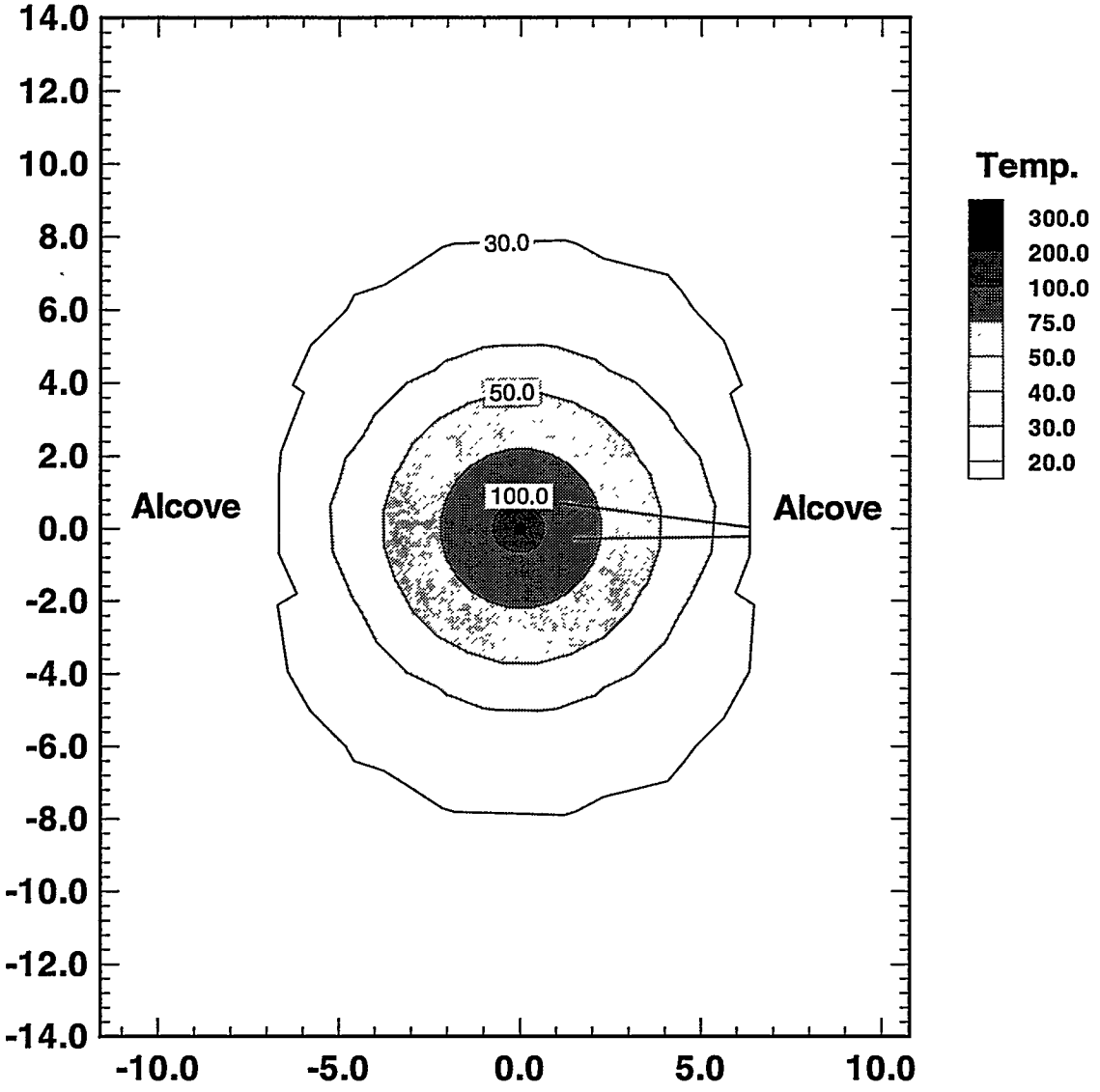

Figure 4.4-1 *Temperature response for case with high initial saturation at 1 year in XZ - cross section at Y = 4.25 m.*

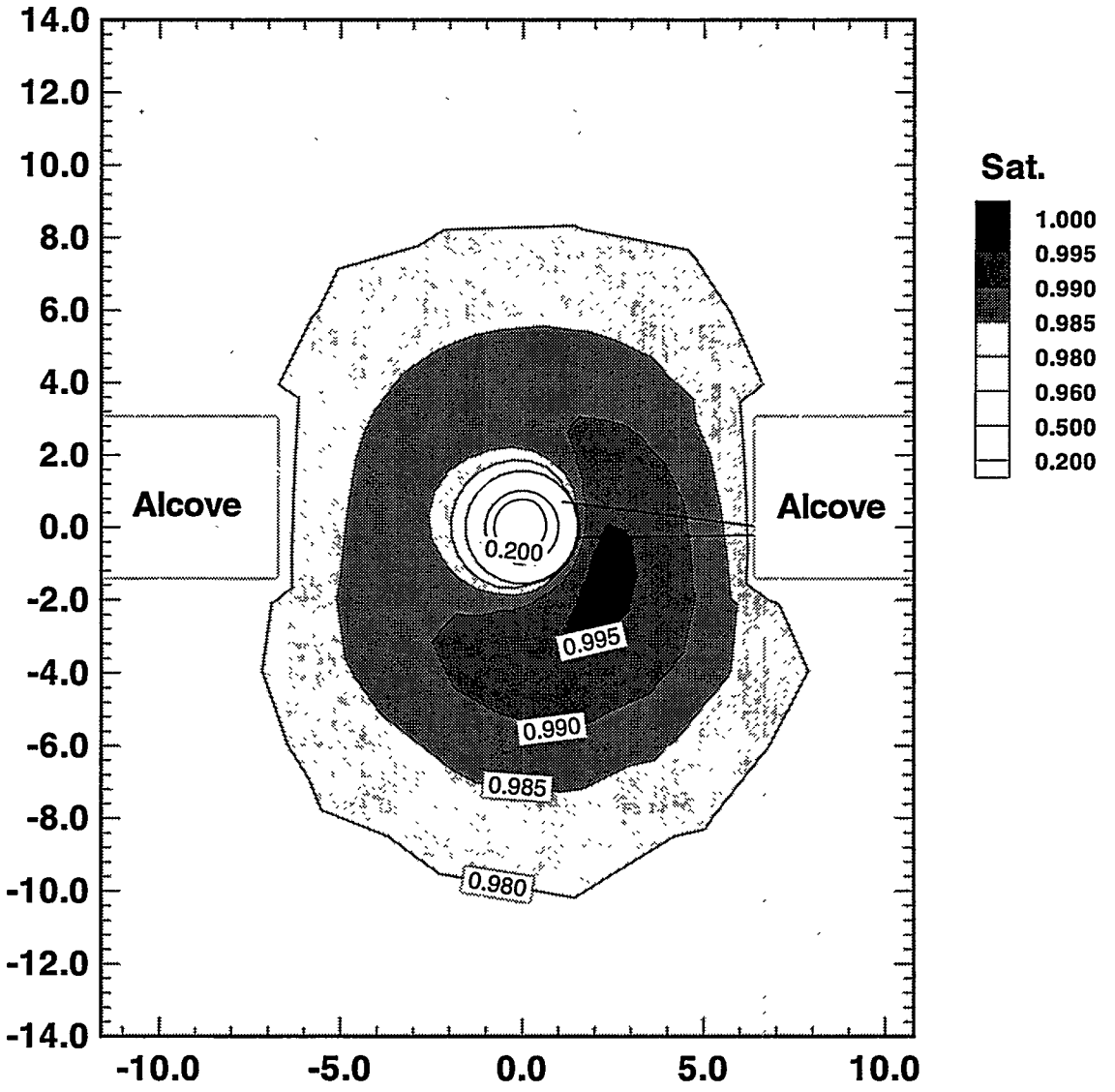

Figure 4.4-2 Equivalent continuum liquid saturation for case with high initial saturation at 1 year in XZ - cross section at Y = 4.25 m.

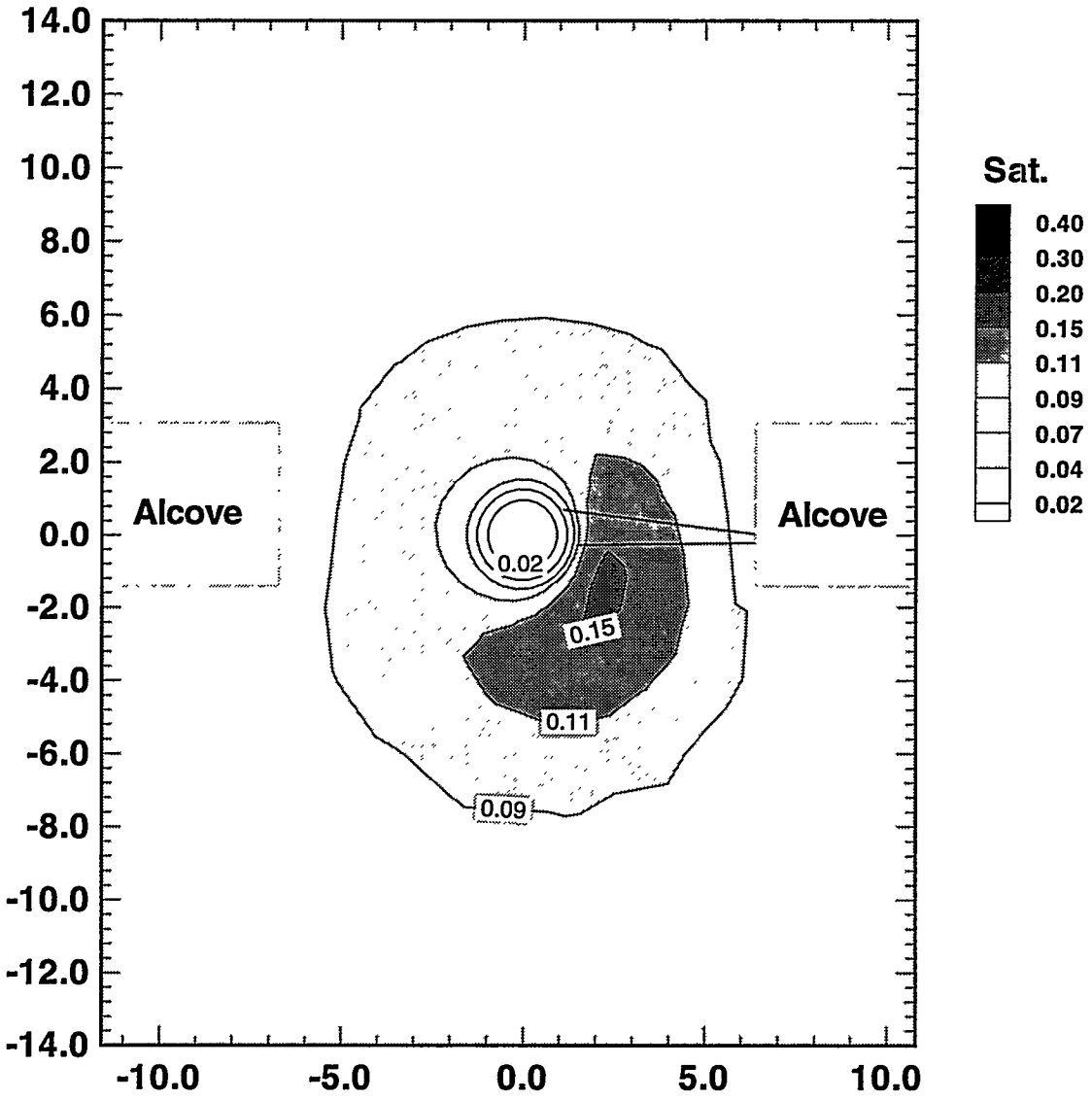

Figure 4.4-3 Fracture liquid saturation for case with high initial saturation at 1 year in XZ - cross section at Y = 4.25 m.

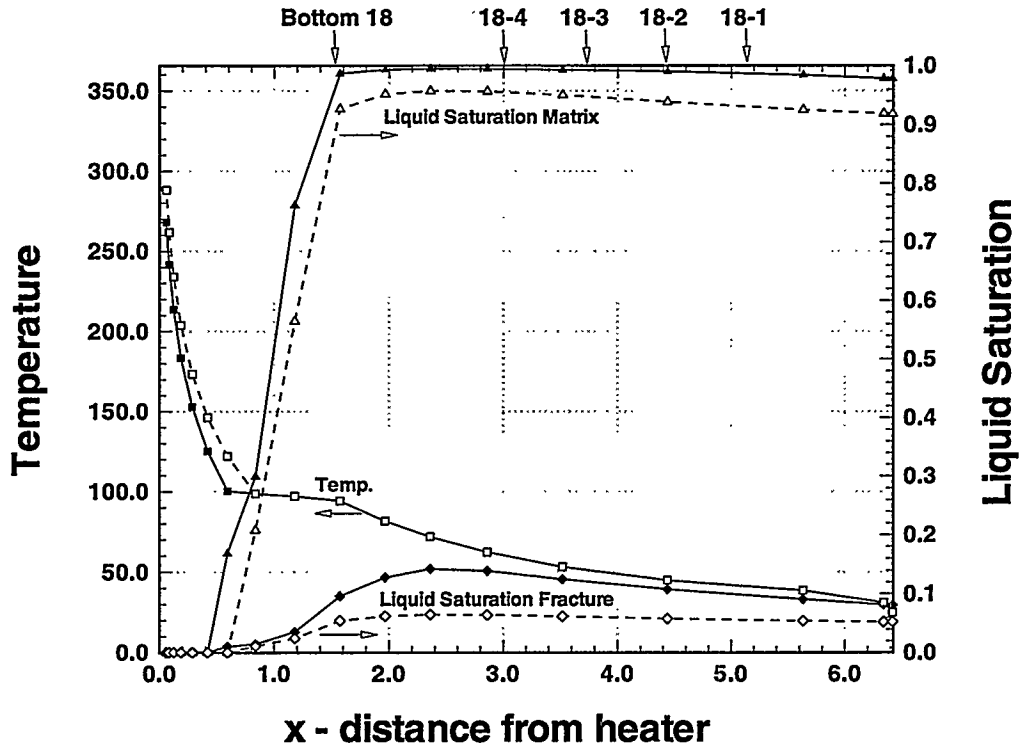

Figure 4.4-4 *Comparison of temperature / liquid saturation at 1 year along X - axis at Y = 4.25 m and Z = 0.0 m for two different initial saturation values. Solid symbols / lines denote a high initial matrix saturation of 98 %, hollow symbols and dashed lines denote Base Case with an initial matrix saturation of 92 %.*

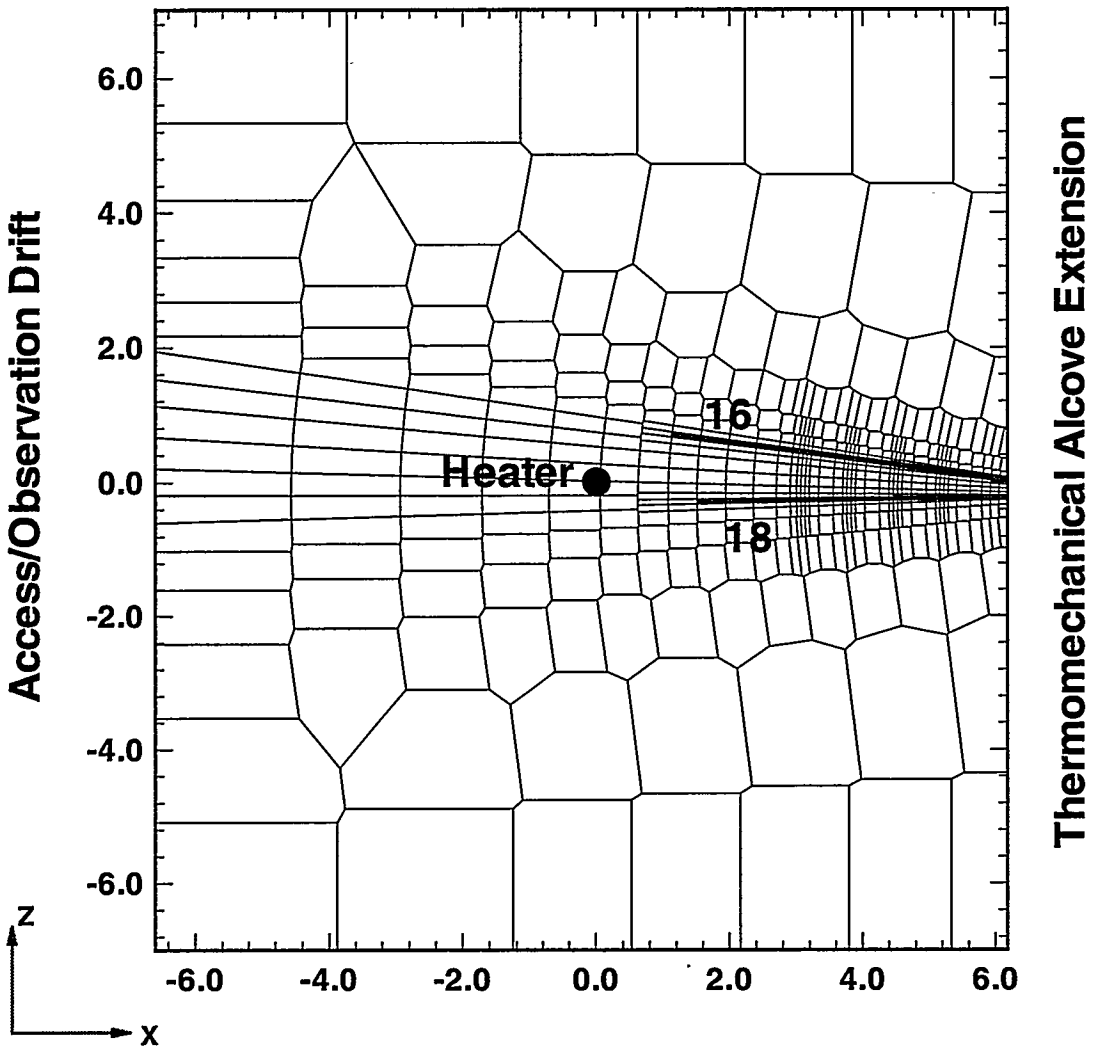

Figure 5.1-1 Grid design in XZ - cross section for air injection runs.

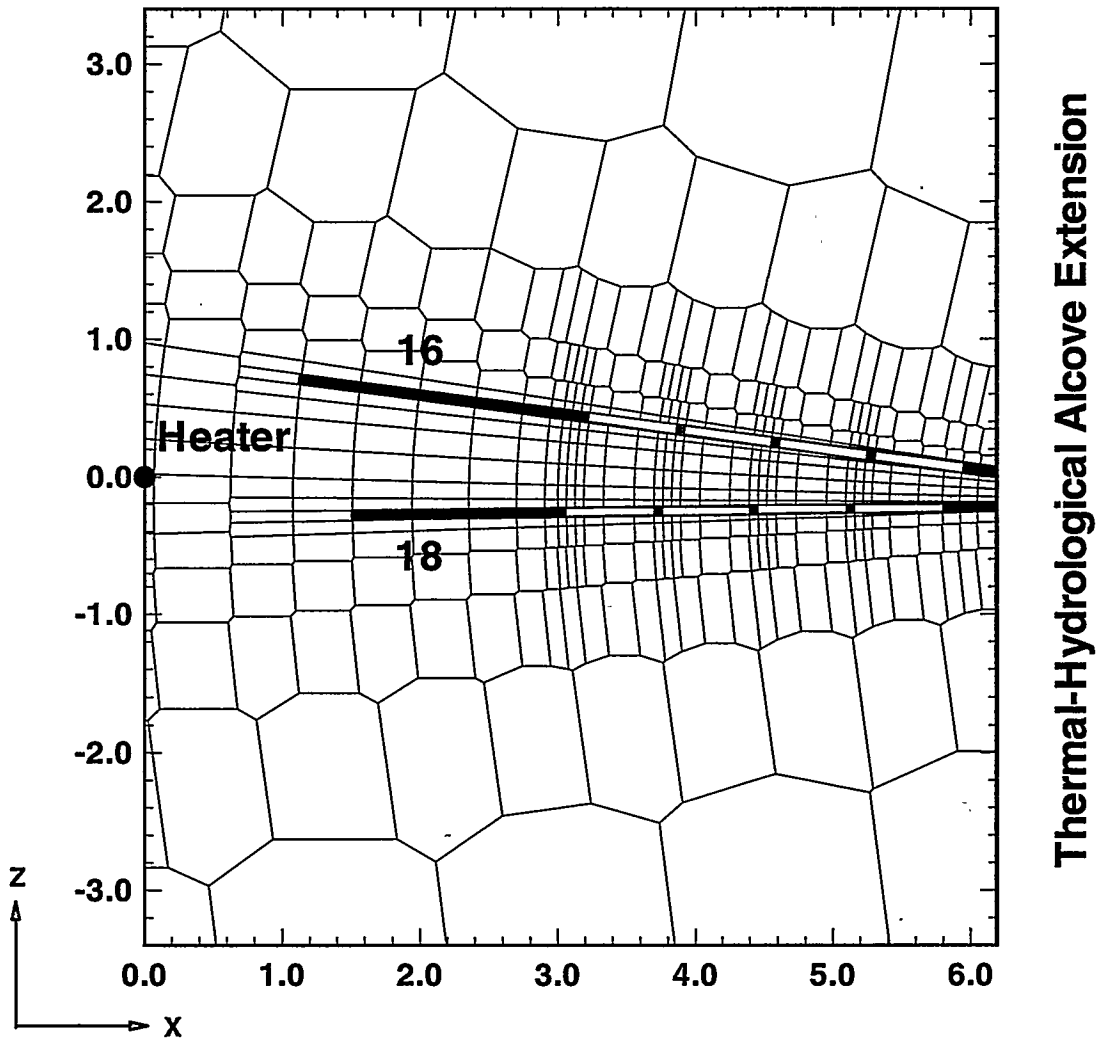

Figure 5.1-2 *Details of grid design in XZ - cross section for air injection runs showing packer and sensor arrangement in Boreholes 16 and 18.*

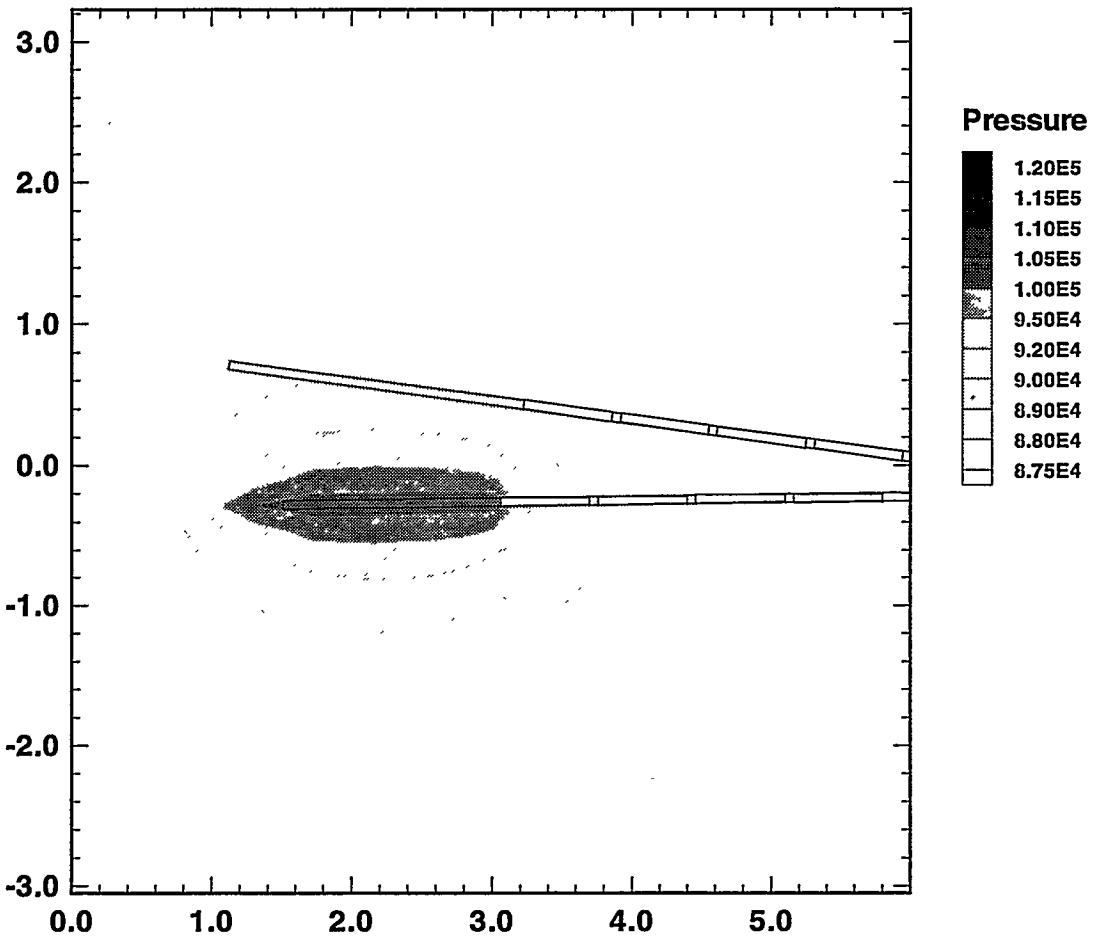

Figure 5.2-1 *Steady state pressure (in Pa) for constant flow air injection in Zone 3 of Borehole 18 for pre-heat situation. Results are shown in test hole plane (i.e. XZ - cross section at Y = 4.25 m).*

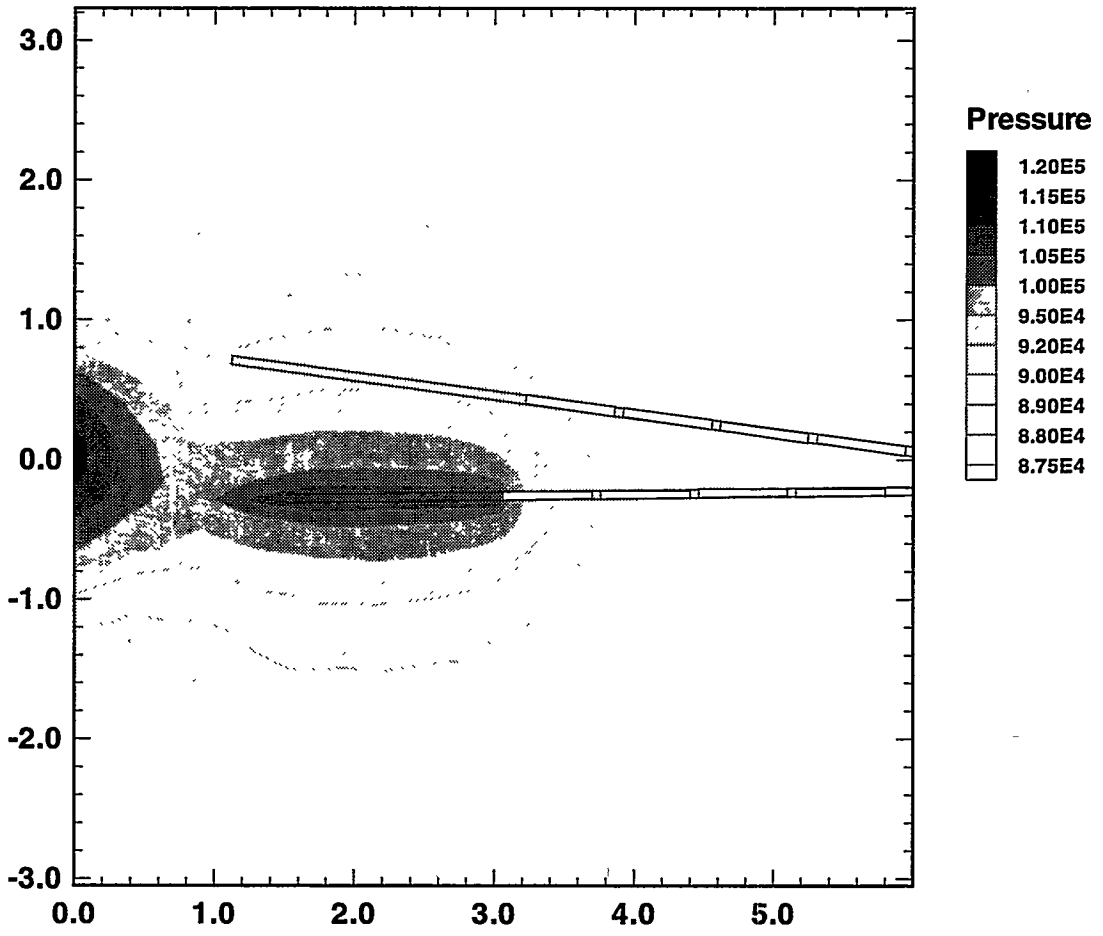

Figure 5.2-2 *Steady state pressure (in Pa) for constant flow air injection in Zone 3 of Borehole 18 for injection test performed at 77 days. Results are shown in test hole plane (i.e. XZ - cross section at Y = 4.25 m).*

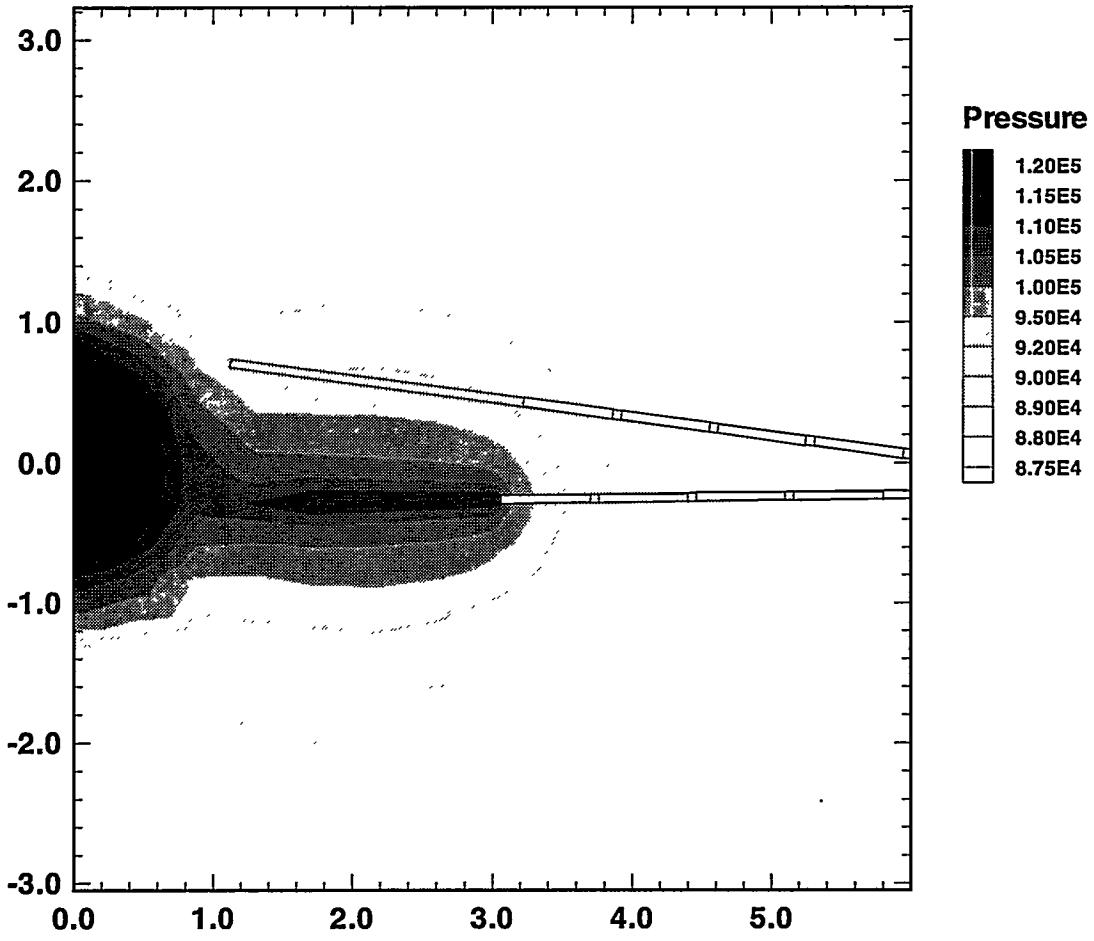

Figure 5.2-3 Steady state pressure (in Pa) for constant flow air injection in Zone 3 of Borehole 18 for injection test performed at 6 months. Results are shown in test hole plane (i.e. XZ - cross section at Y = 4.25 m).

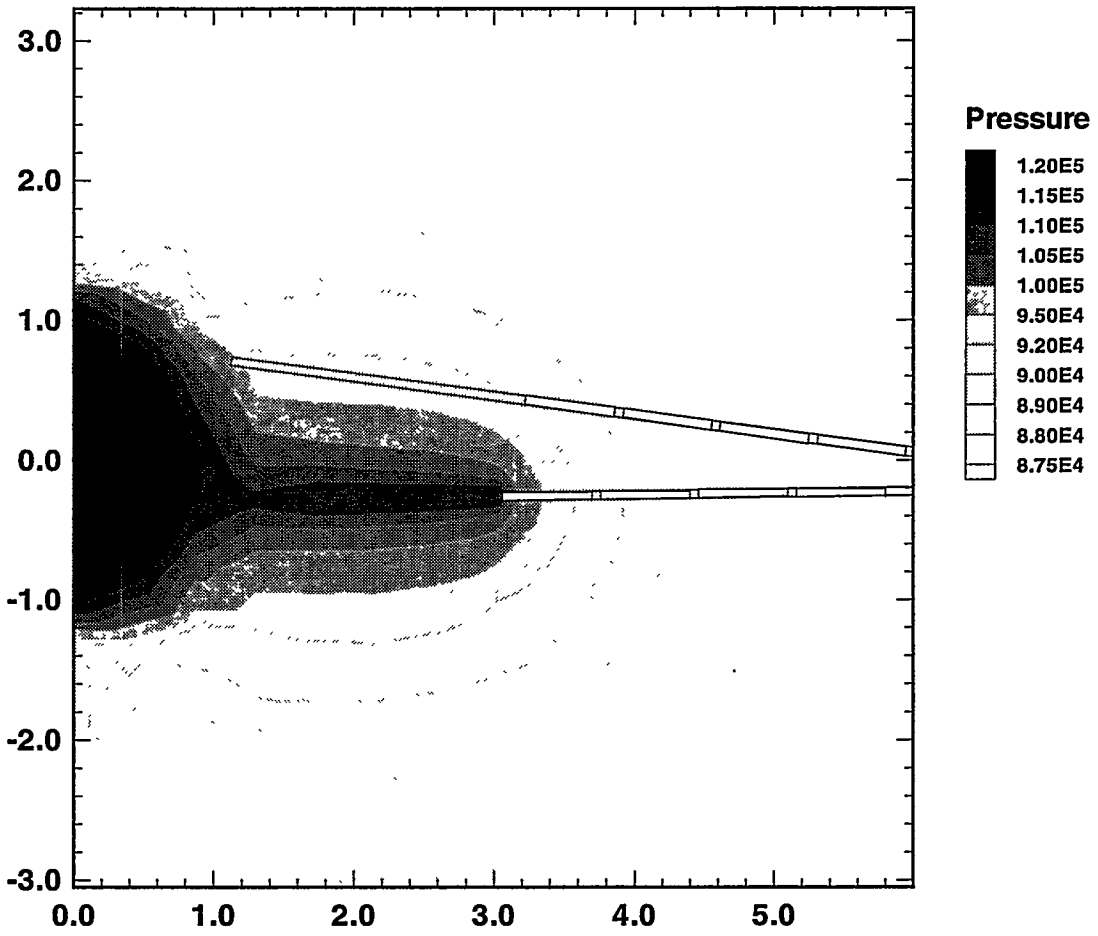

Figure 5.2-4 Steady state pressure (in Pa) for constant flow air injection in Zone 3 of Borehole 18 for injection test performed at 9 months. Results are shown in test hole plane (i.e. XZ - cross section at Y = 4.25 m).

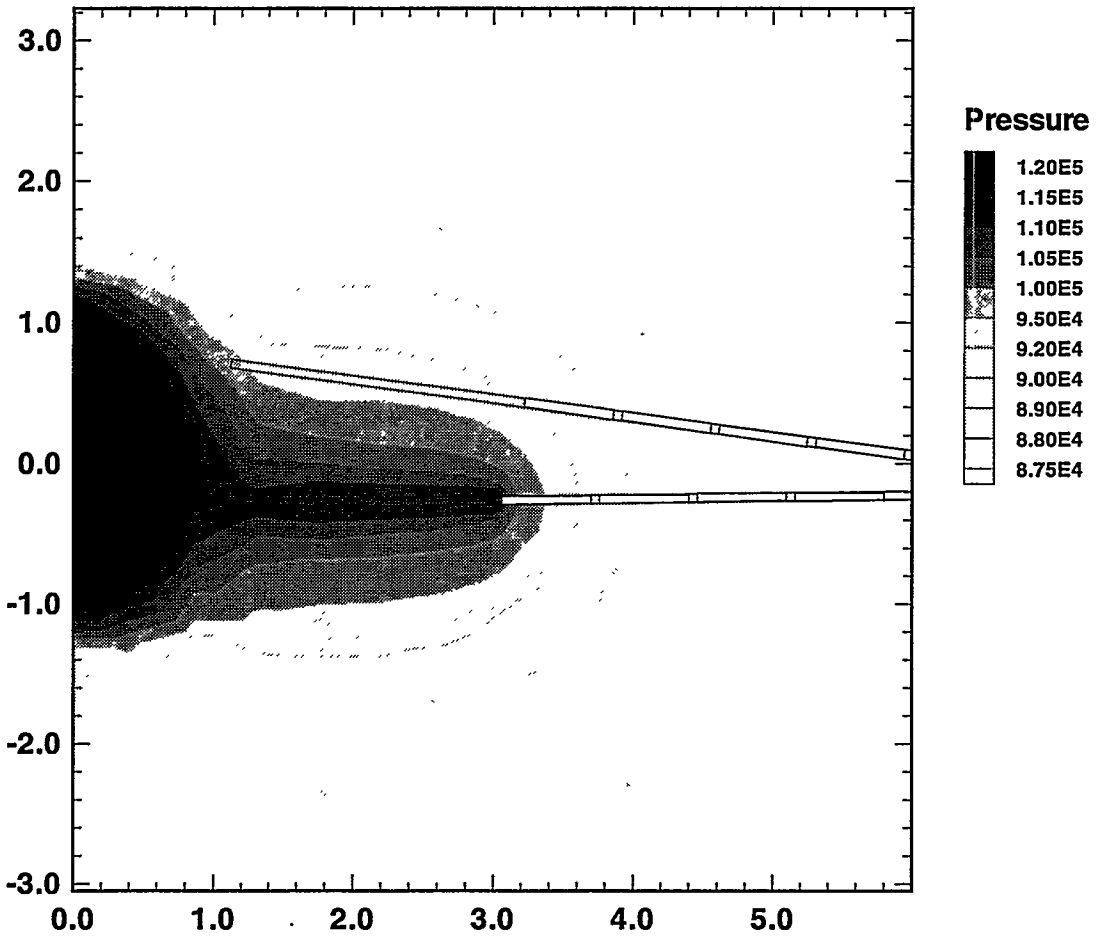

Figure 5.2-5 *Steady state pressure (in Pa) for constant flow air injection in Zone 3 of Borehole 18 for injection test performed at 1 year. Results are shown in test hole plane (i.e. XZ - cross section at Y = 4.25 m).*

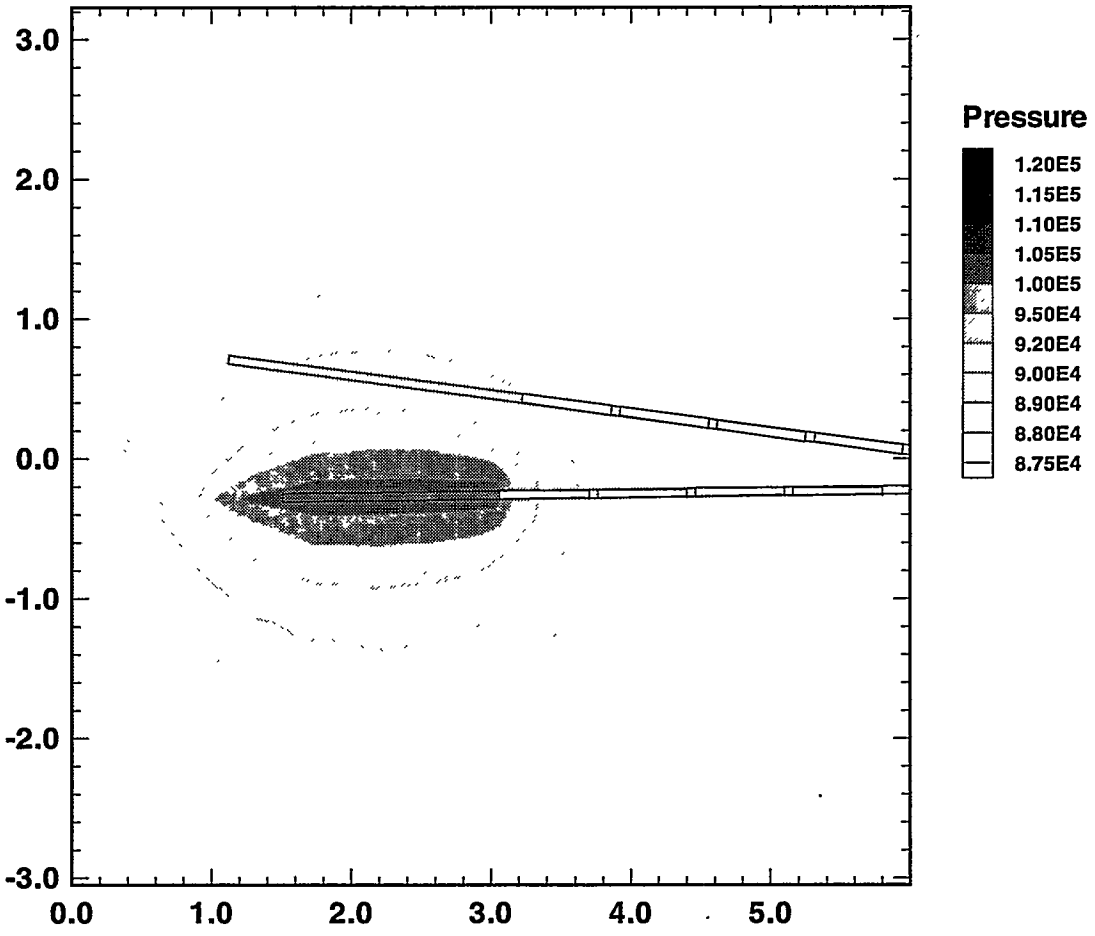

Figure 5.2-6 *Steady state pressure (in Pa) for constant flow air injection in Zone 3 of Borehole 18 for injection test performed at 15 months for a 1 year heating period. Results are shown in test hole plane (i.e. XZ - cross section at Y = 4.25 m).*

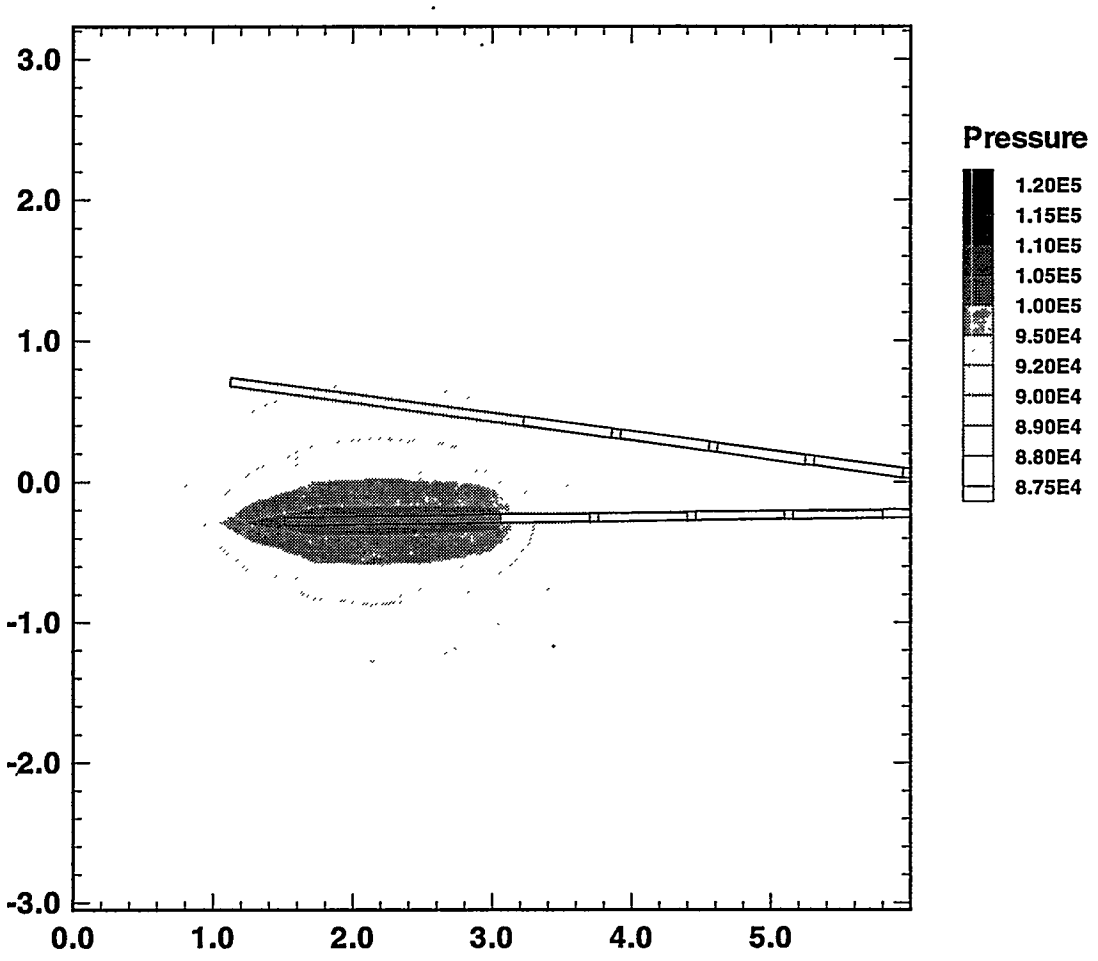

Figure 5.2-7 *Steady state pressure (in Pa) for constant flow air injection in Zone 3 of Borehole 18 for injection test performed at 18 months for a 1 year heating period. Results are shown in test hole plane (i.e. XZ - cross section at Y = 4.25 m).*

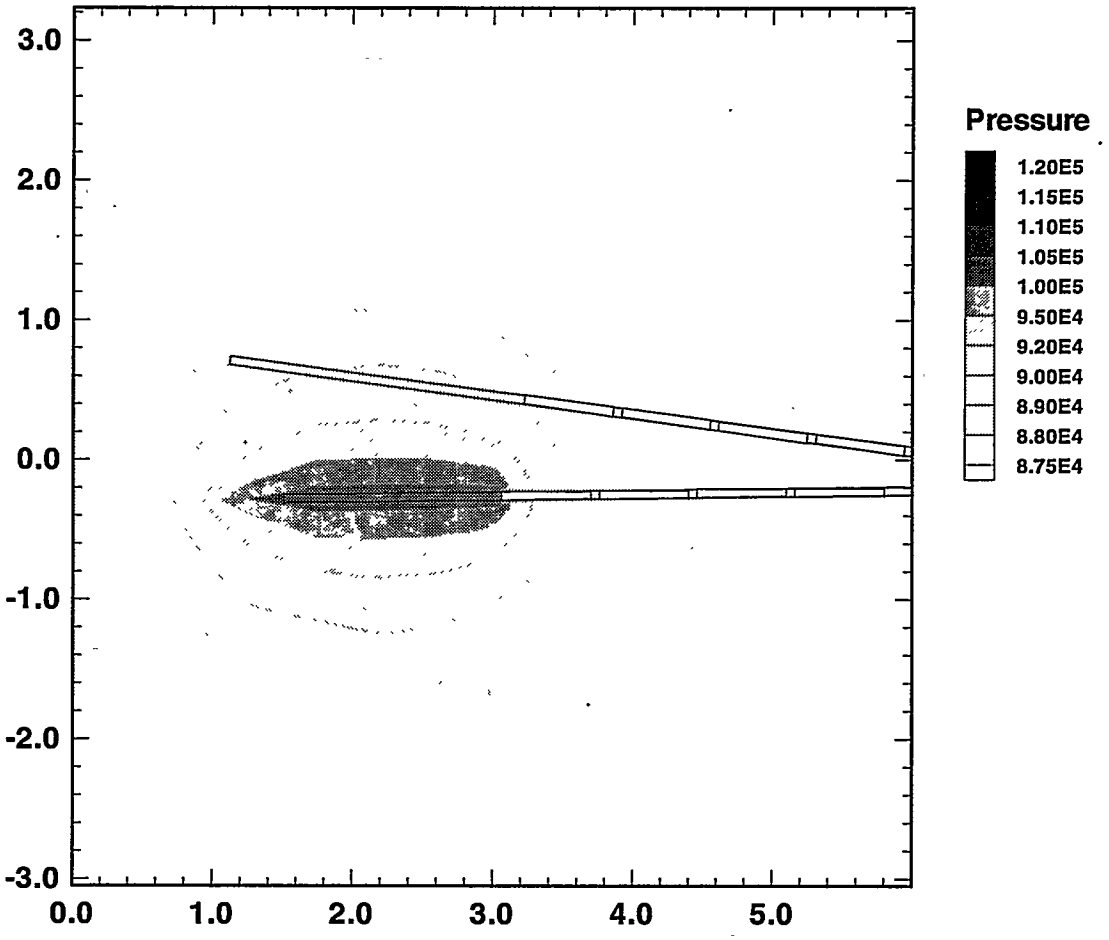

Figure 5.2-8 *Steady state pressure (in Pa) for constant flow air injection in Zone 3 of Borehole 18 for injection test performed at 21 months for a 1 year heating period. Results are shown in test hole plane (i.e. XZ - cross section at Y = 4.25 m).*

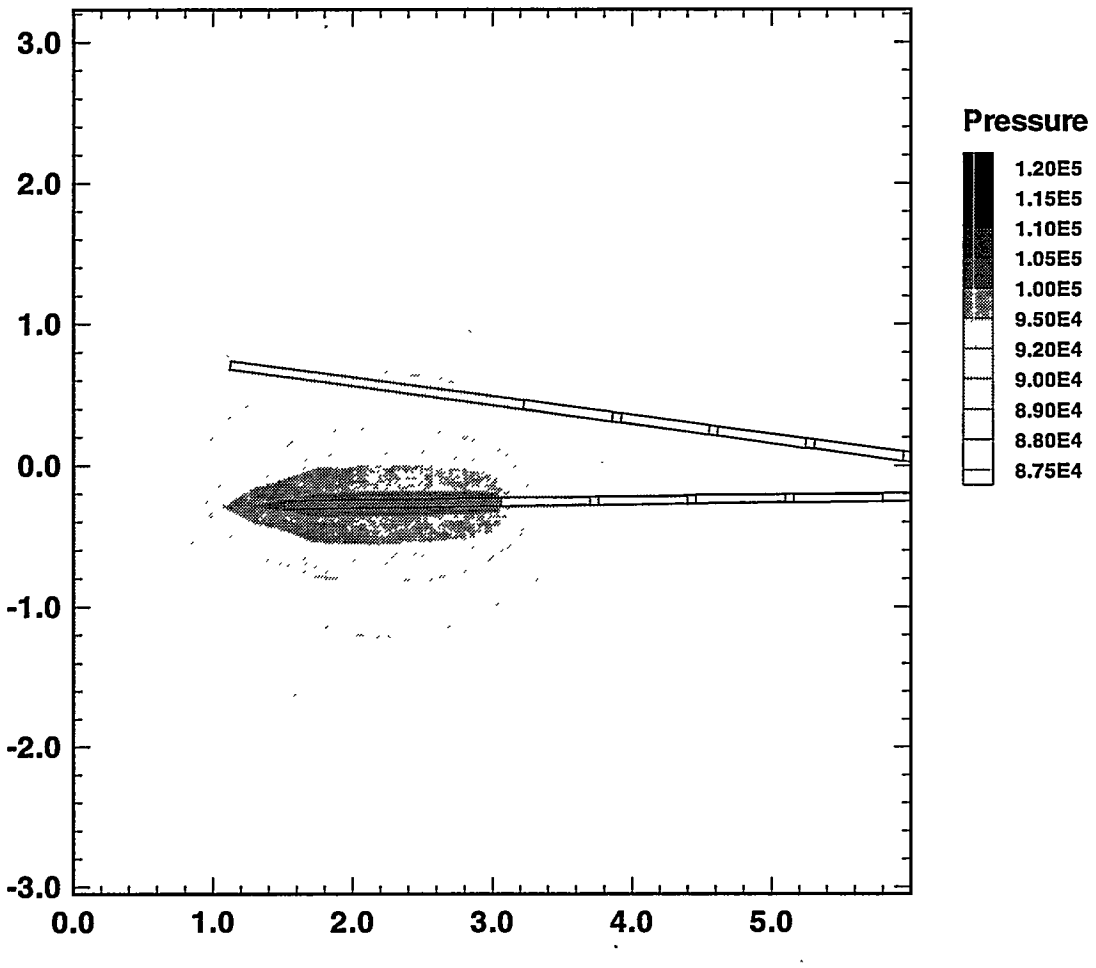

Figure 5.2-9 *Steady state pressure (in Pa) for constant flow air injection in Zone 3 of Borehole 18 for injection test performed at 24 months for a 1 year heating period. Results are shown in test hole plane (i.e. XZ - cross section at Y = 4.25 m).*

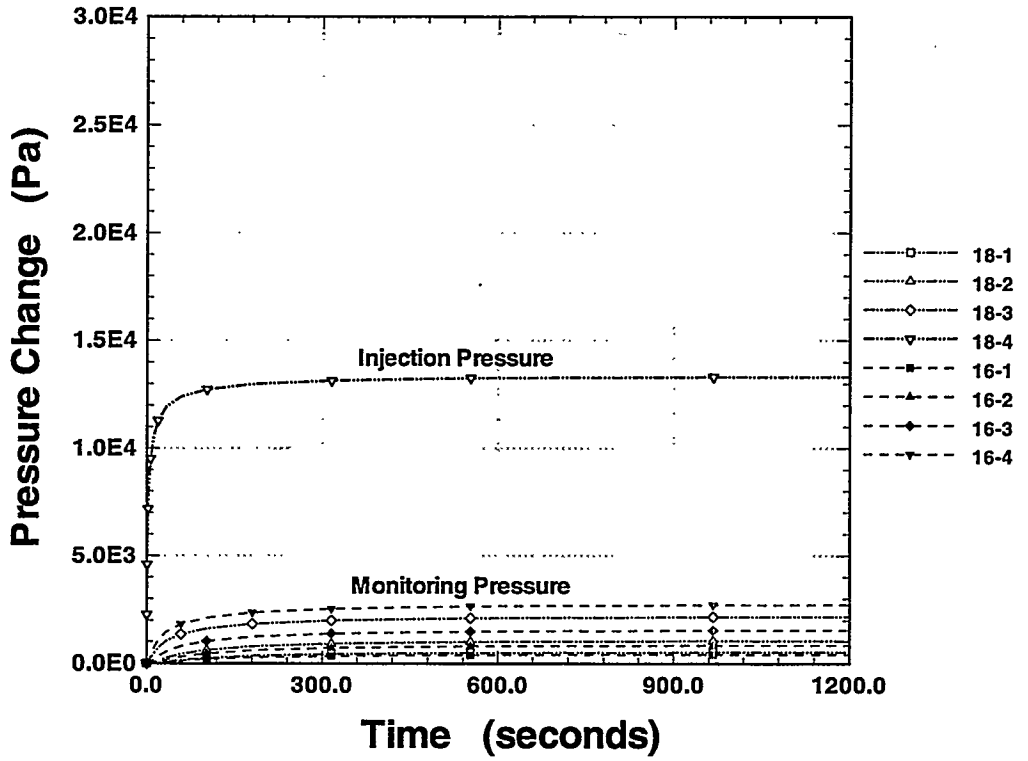

Figure 5.2-10 Pressure Response to constant flow air injection in Zone 3 of Borehole 18 for pre-heat situation.

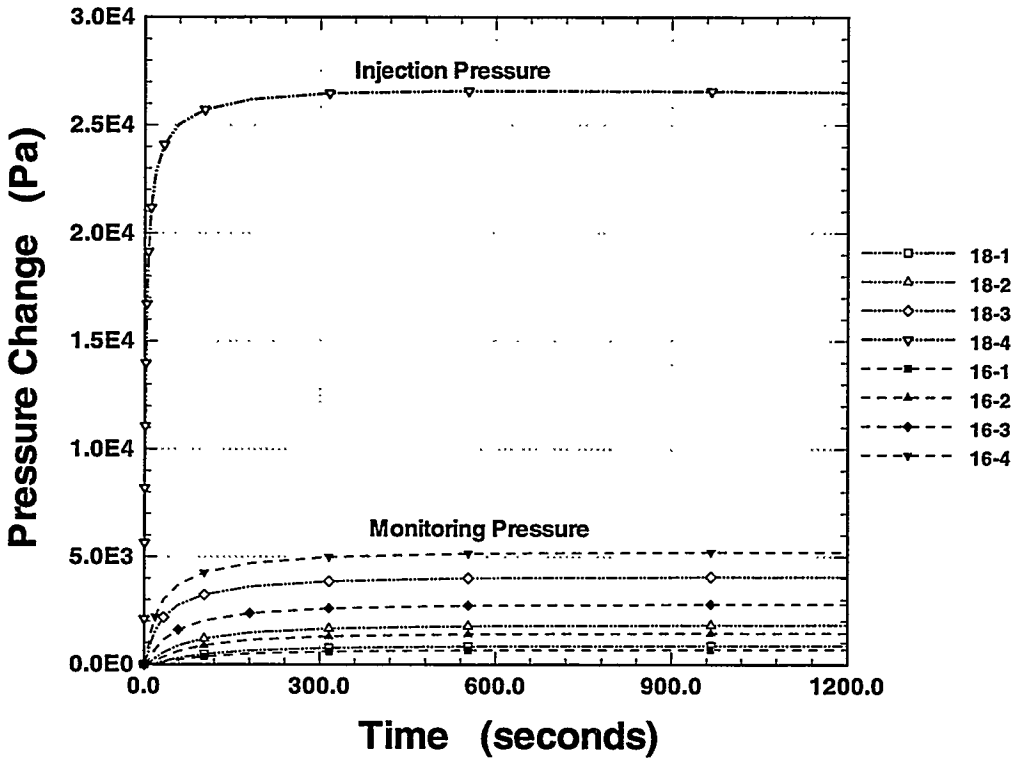

Figure 5.2-11 Pressure Response (in Pa) to constant flow air injection in Zone 3 of Borehole 18 for injection test performed at 1 year.

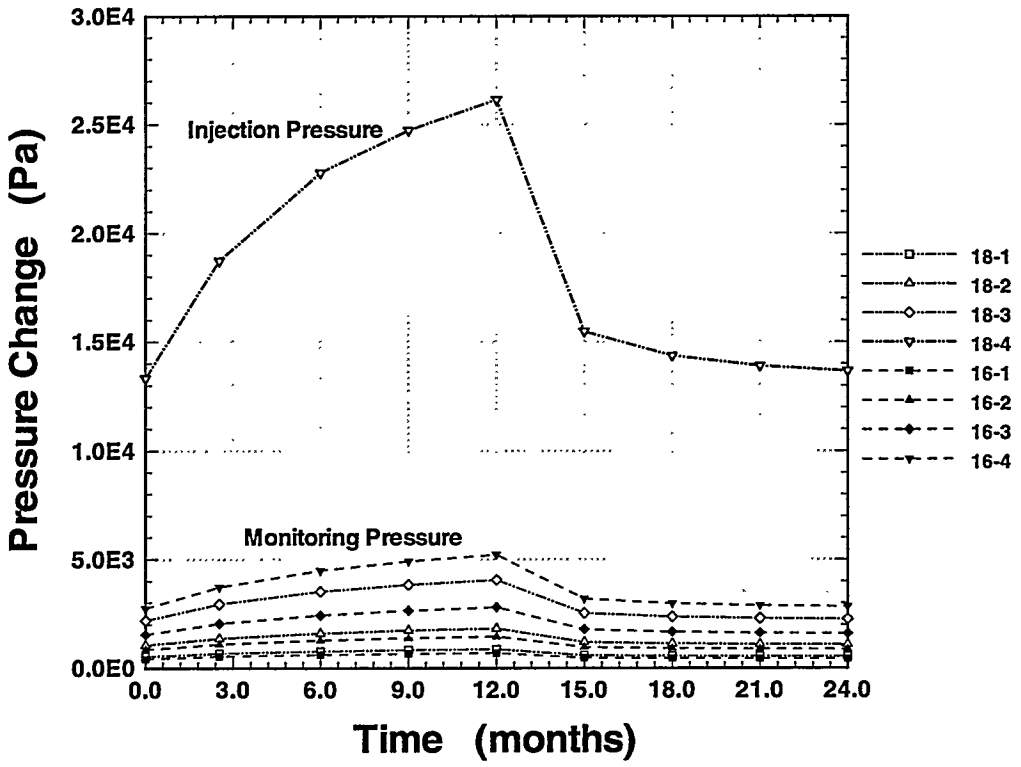

Figure 5.2-12 Steady State Pressure Response (in Pa) to constant flow air injection in Zone 3 of Borehole 18 at different test times.

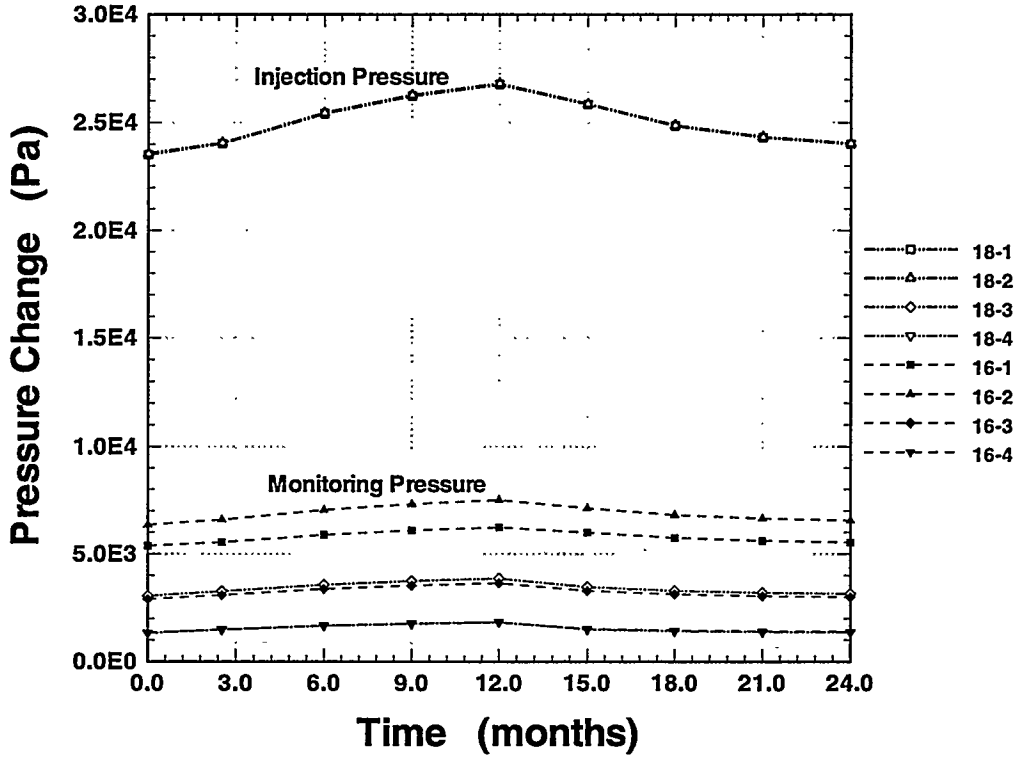

Figure 5.2-13 Steady State Pressure Response (in Pa) to constant flow air injection in Zone 1 of Borehole 18 at different test times.

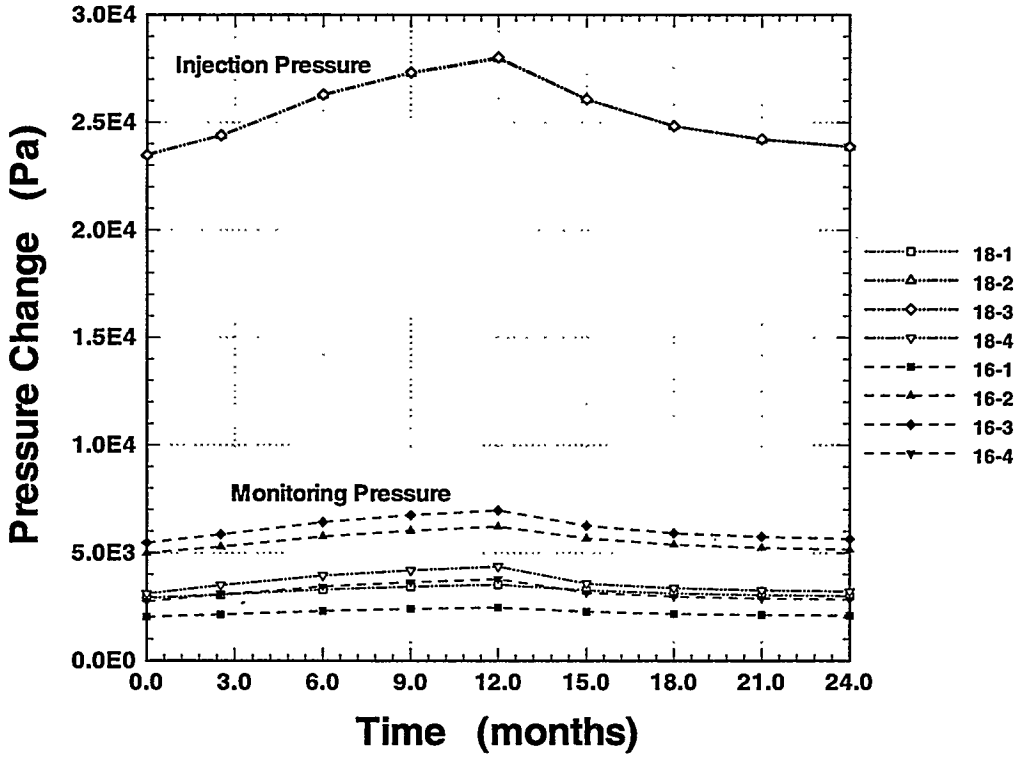

Figure 5.2-14 Steady State Pressure Response (in Pa) to constant flow air injection in Zone 2 of Borehole 18 at different test times.

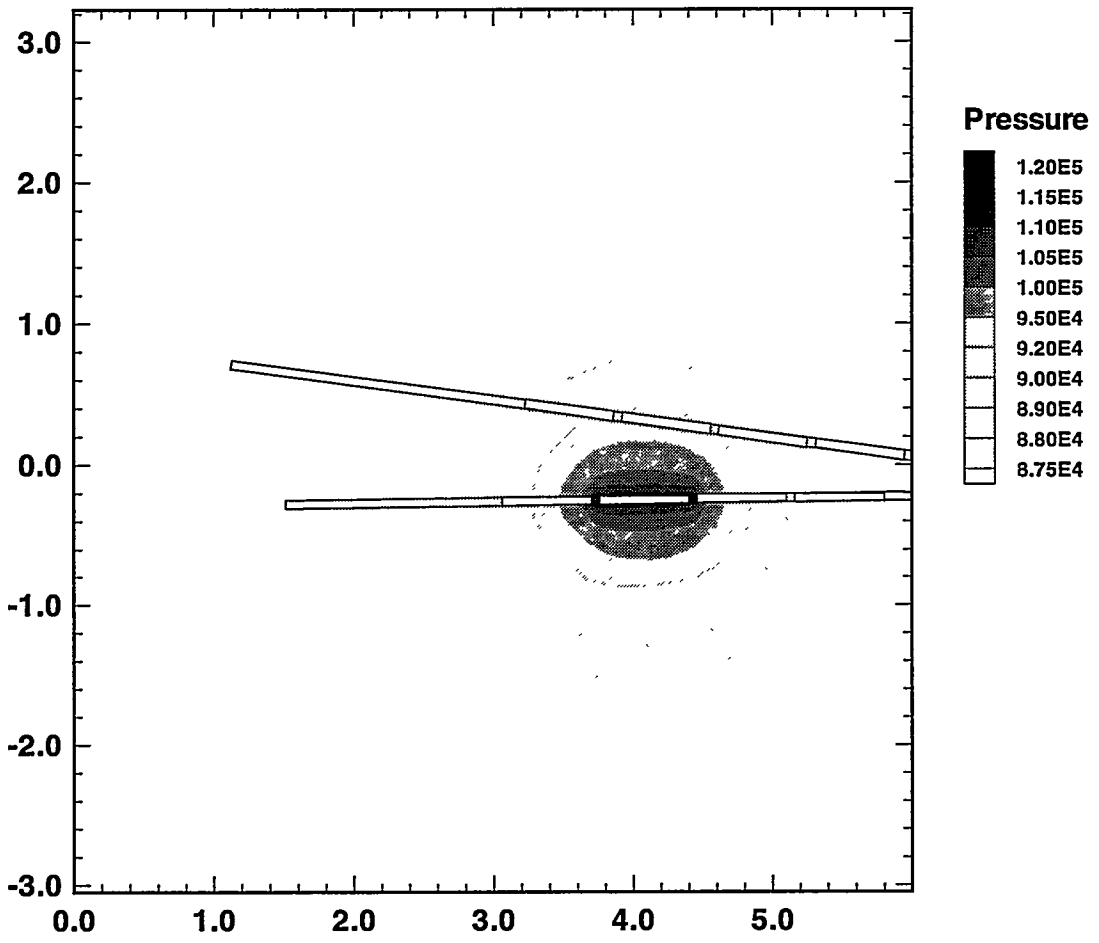

Figure 5.2-15 Steady state pressure (in Pa) for constant flow air injection in Zone 2 of Borehole 18 for pre-heat situation. Results are shown in test hole plane (i.e. XZ - cross section at Y = 4.25 m).

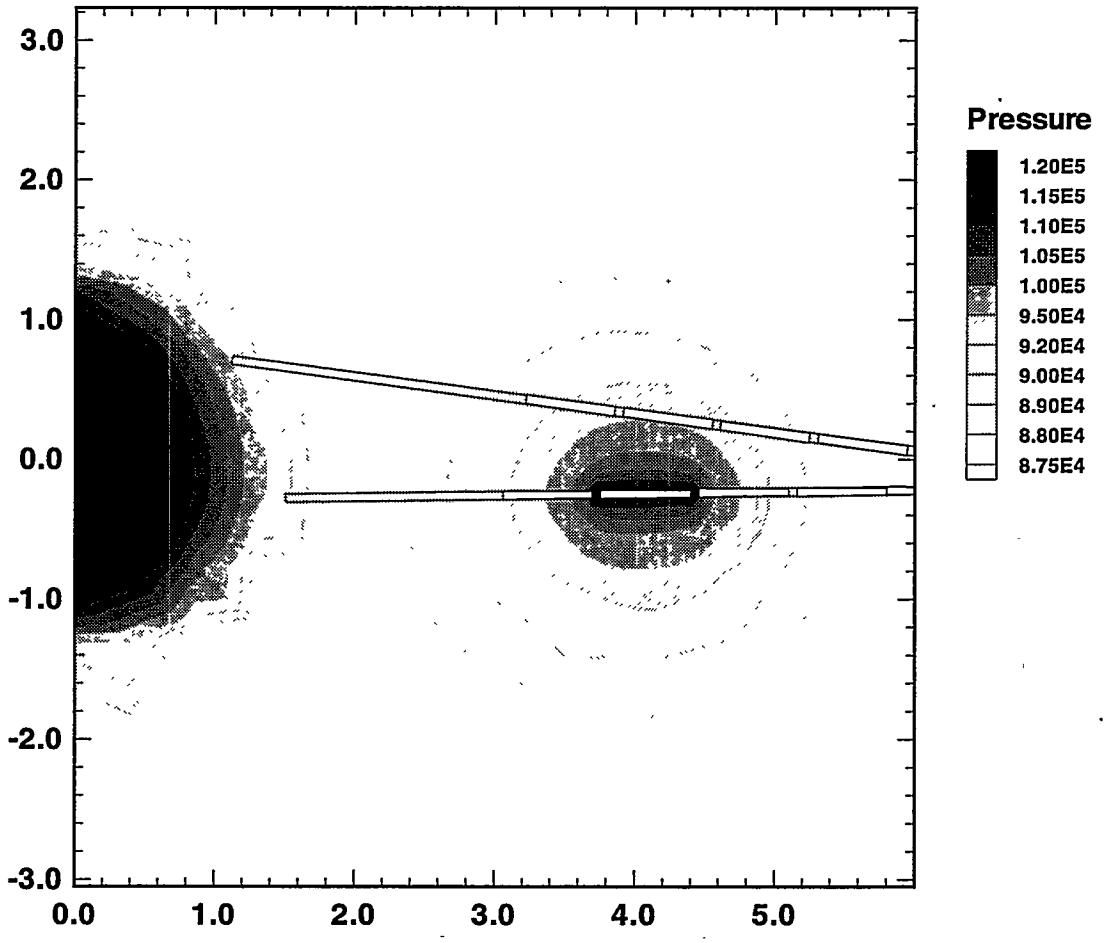

Figure 5.2-16 *Steady state pressure (in Pa) for constant flow air injection in Zone 2 of Borehole 18 for injection test performed at 1 year. Results are shown in test hole plane (i.e. XZ - cross section at Y = 4.25 m).*

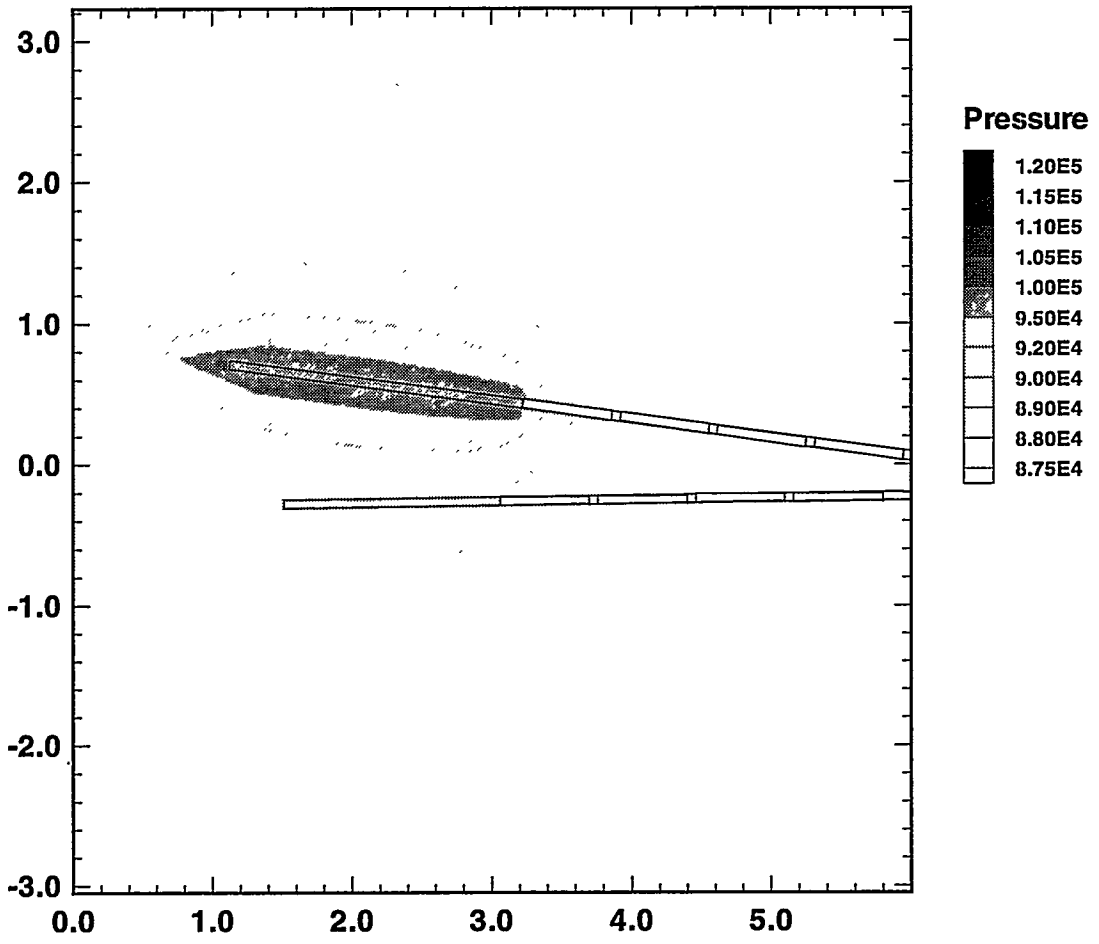

Figure 5.2-17 Steady state pressure (in Pa) for constant flow air injection in Zone 3 of Borehole 16 for pre-heat situation. Results are shown in test hole plane (i.e. XZ - cross section at Y = 4.25 m).

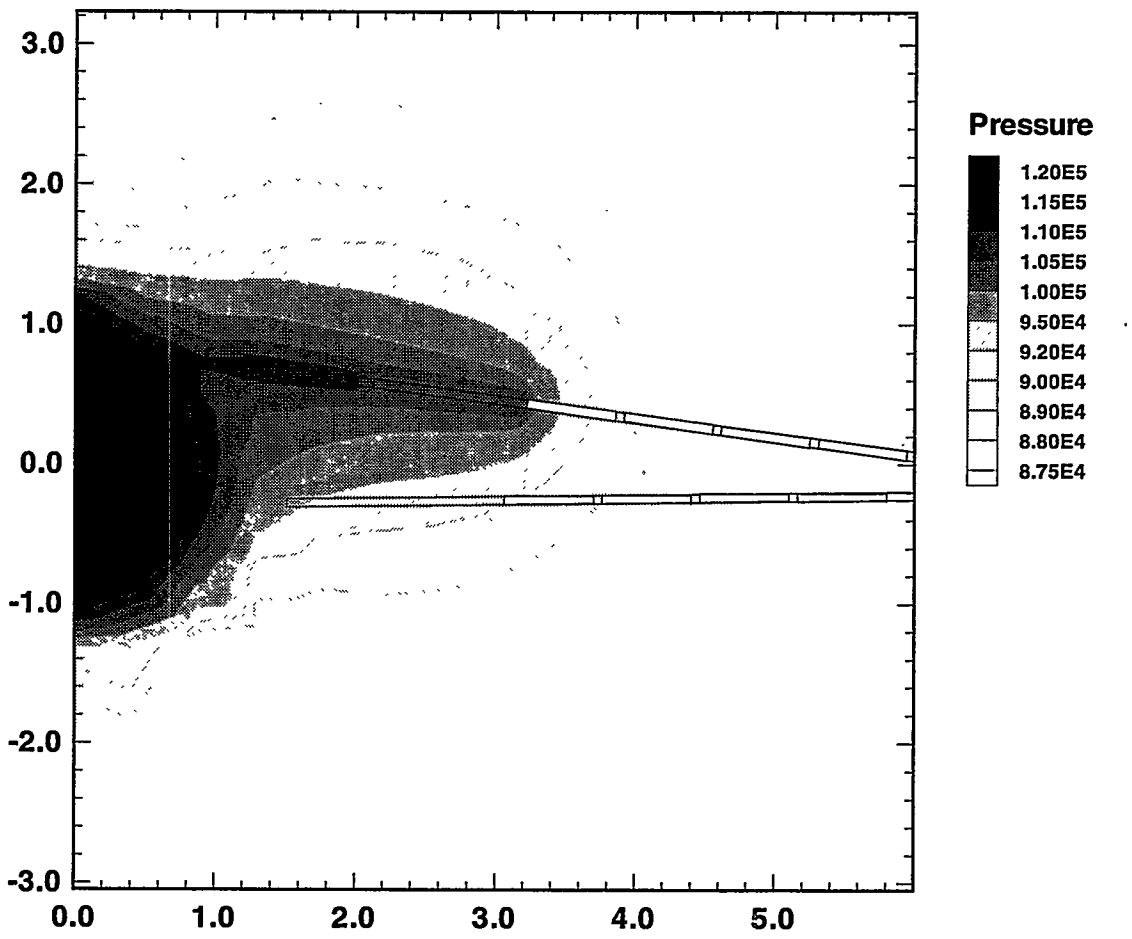

Figure 5.2-18 *Steady state pressure (in Pa) for constant flow air injection in Zone 3 of Borehole 16 for injection test performed at 1 year. Results are shown in test hole plane (i.e. XZ - cross section at Y = 4.25 m).*

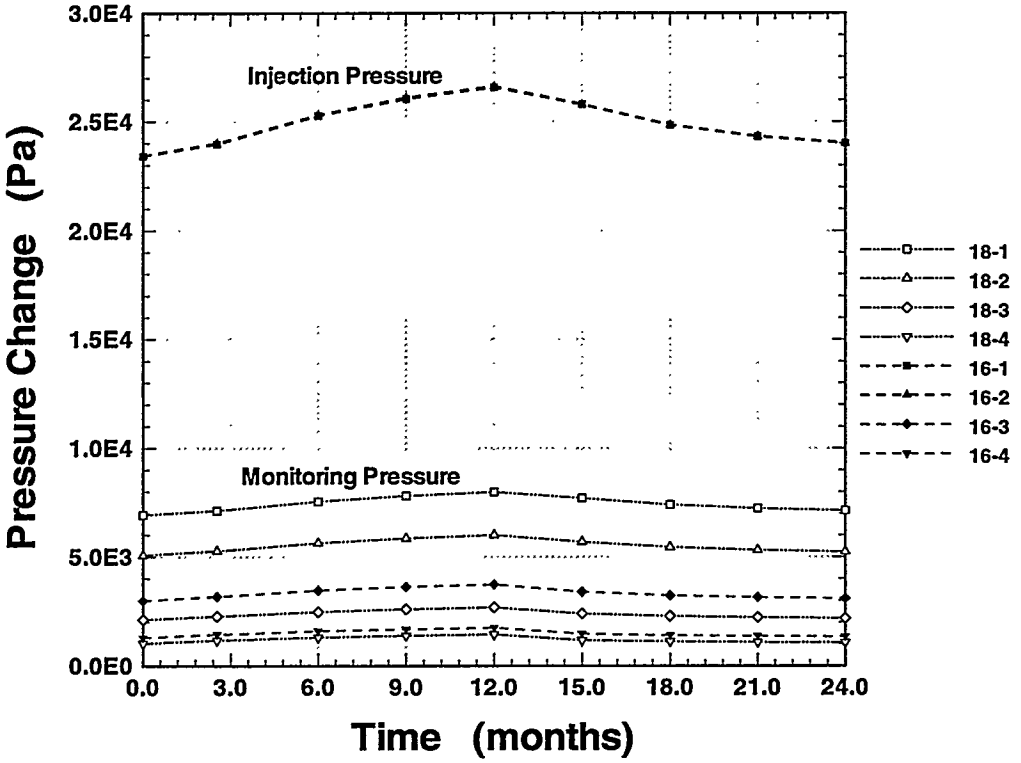

Figure 5.2-19 Steady State Pressure Response (in Pa) to constant flow air injection in Zone 1 of Borehole 16 at different test times.

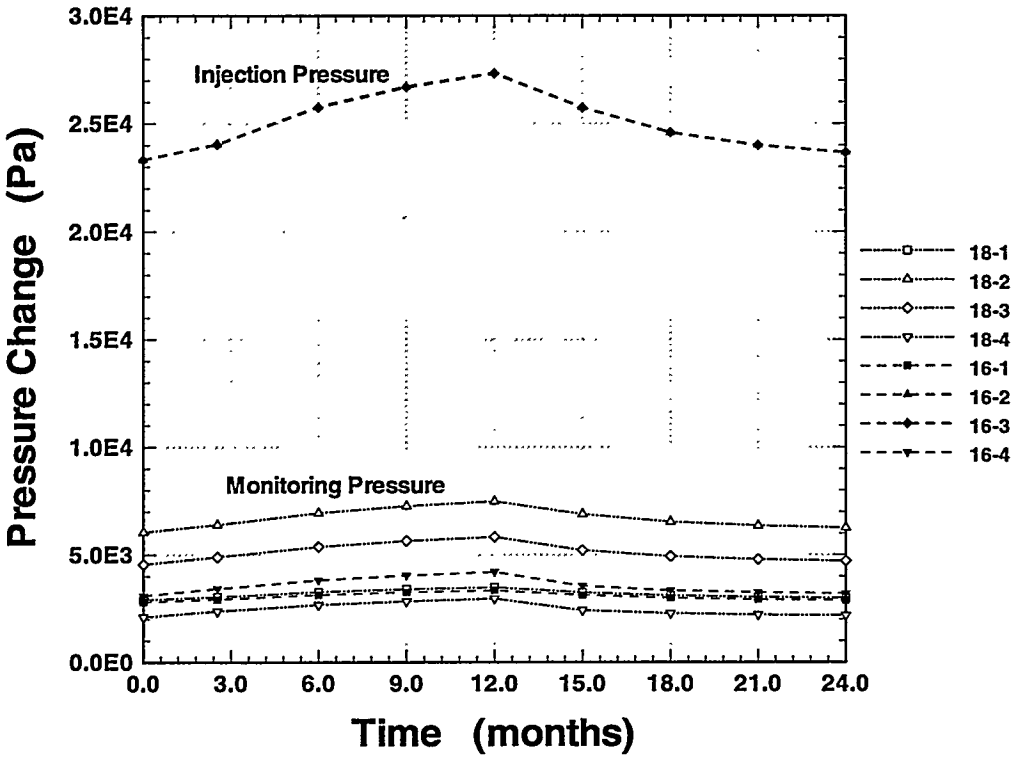

Figure 5.2-20 Steady State Pressure Response (in Pa) to constant flow air injection in Zone 2 of Borehole 16 at different test times.

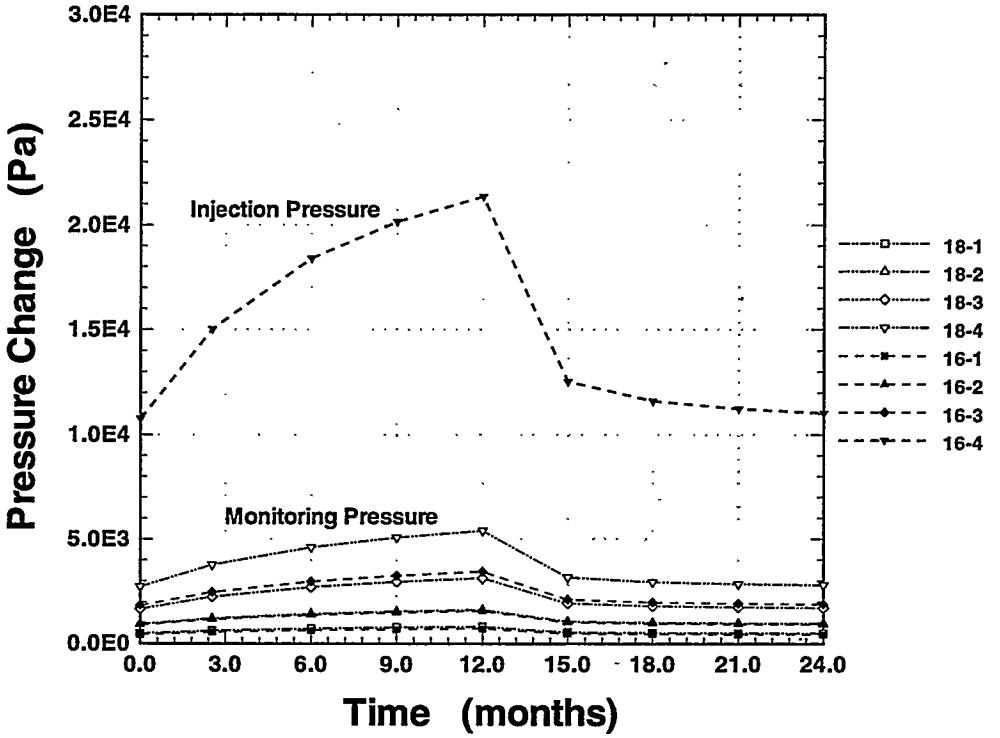

Figure 5.2-21 Steady State Pressure Response (in Pa) to constant flow air injection in Zone 3 of Borehole 16 at different test times.

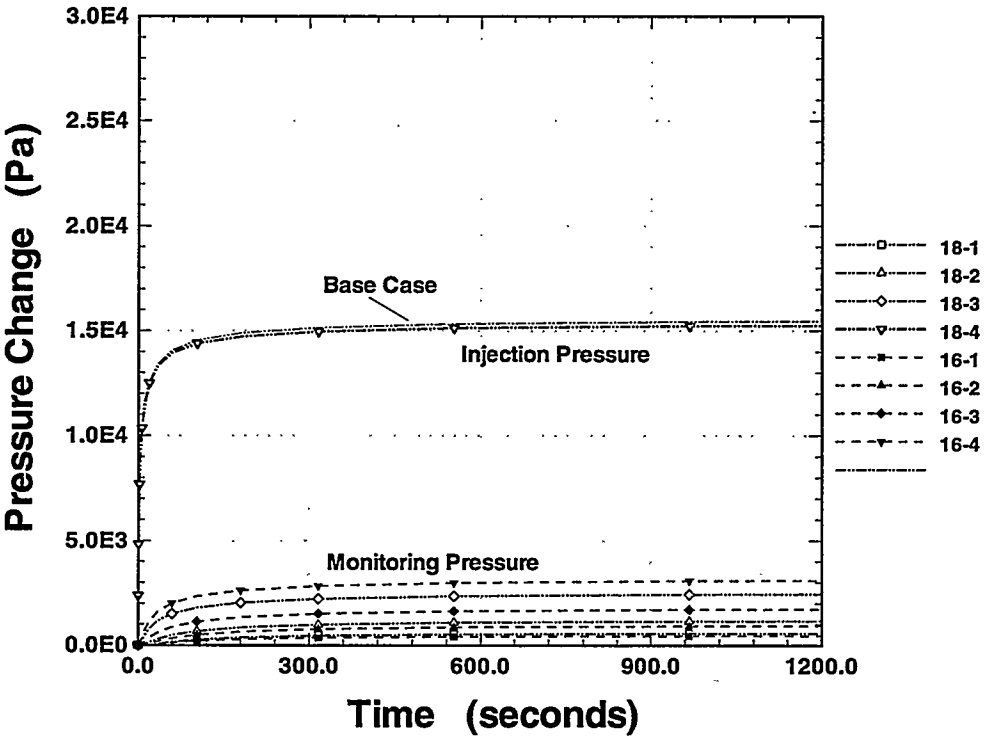

Figure 5.2-22 Pressure Response (in Pa) to constant flow air injection in Zone 3 of Borehole 18 for injection test performed at 1 year after a 9 month heating period. Injection pressure for test performed at 15 months after a 1 year heating period is also given, indicated as Base Case.

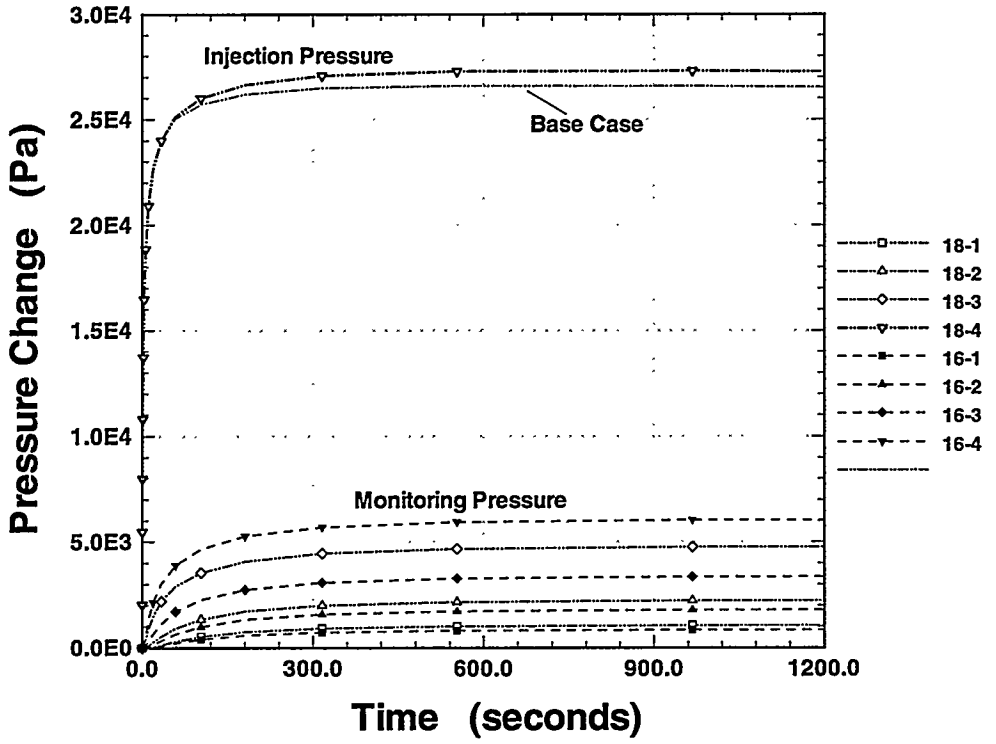

Figure 5.3-1 Pressure Response (in Pa) to constant flow air injection in Zone 3 of Borehole 18 for injection test performed at 1 year in a fully homogeneous domain. Injection pressure for Base Case is also given.

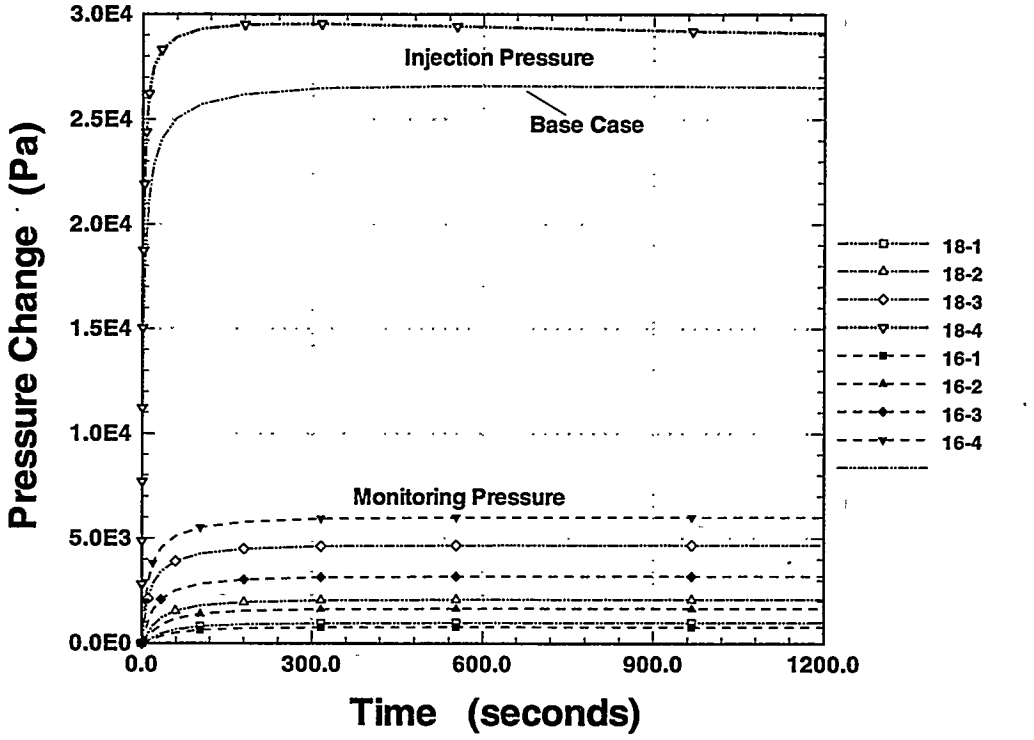

Figure 5.4-1 Pressure Response (in Pa) to constant flow air injection in Zone 3 of Borehole 18 at for injection test performed at 1 year for case with high initial saturation. Injection pressure for Base Case is also given.

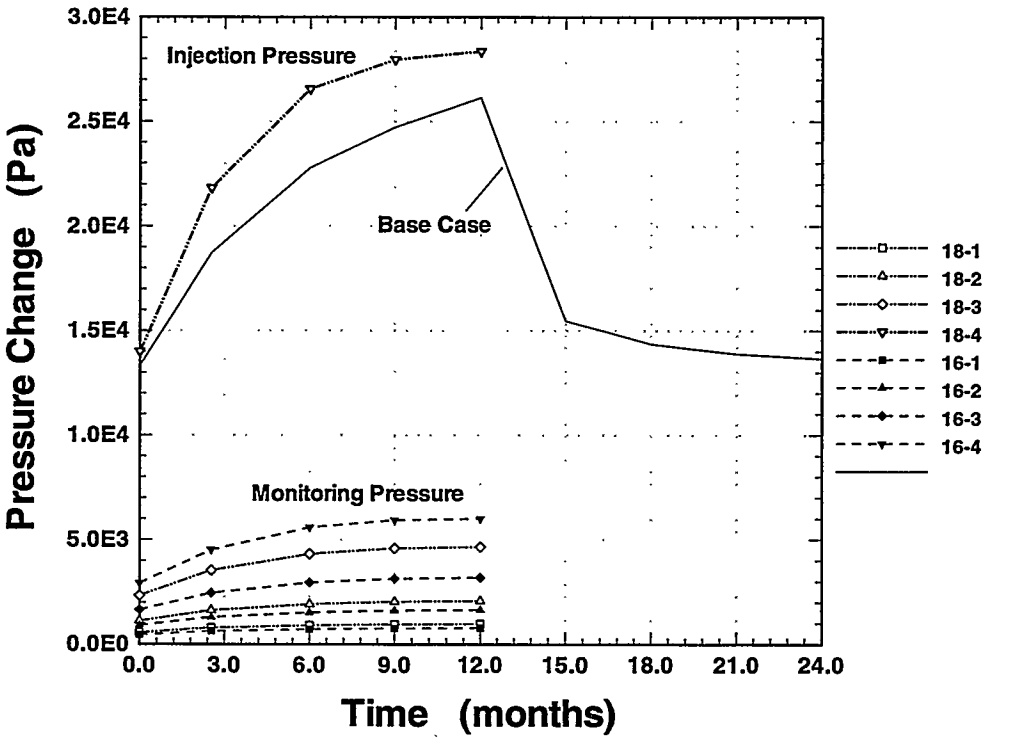

Figure 5.4-2 Steady State Pressure Response (in Pa) to constant flow air injection in Zone 3 of Borehole 16 at different test times for case with high initial saturation. Injection pressure for Base Case is also given.

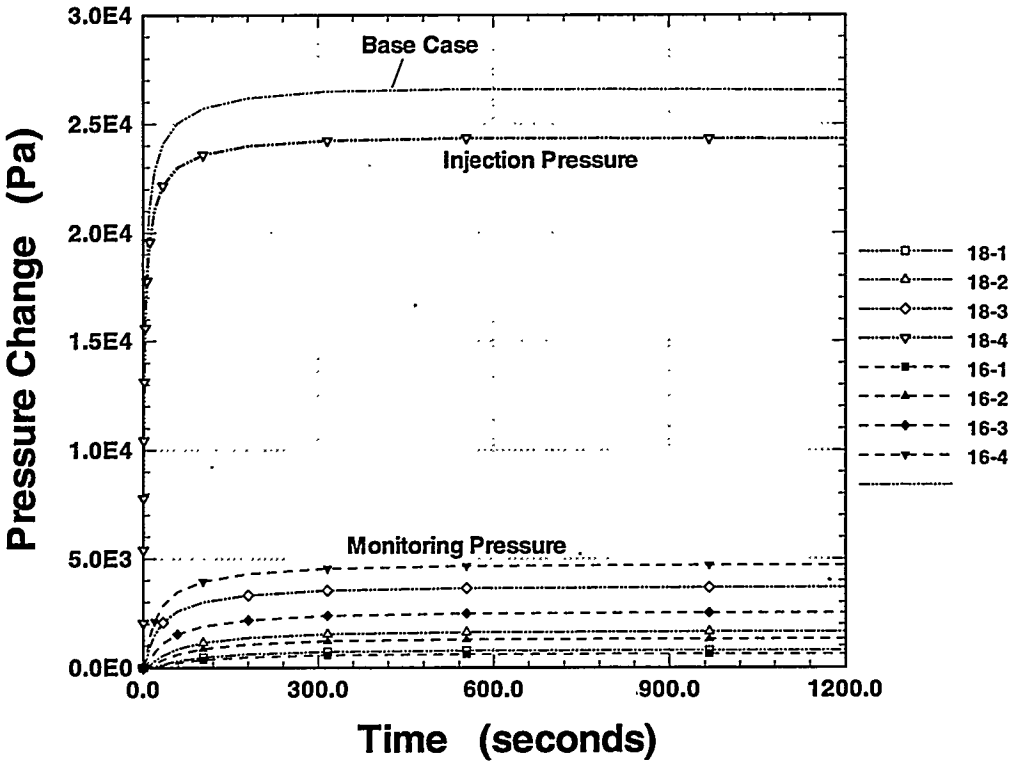

Figure 5.5-1 Pressure Response (in Pa) to constant flow air injection in Zone 3 of Borehole 18 for injection test performed at 1 year for case with different gas relative permeability formulation. Injection pressure for Base Case is also given.

(This page intentionally left blank.)

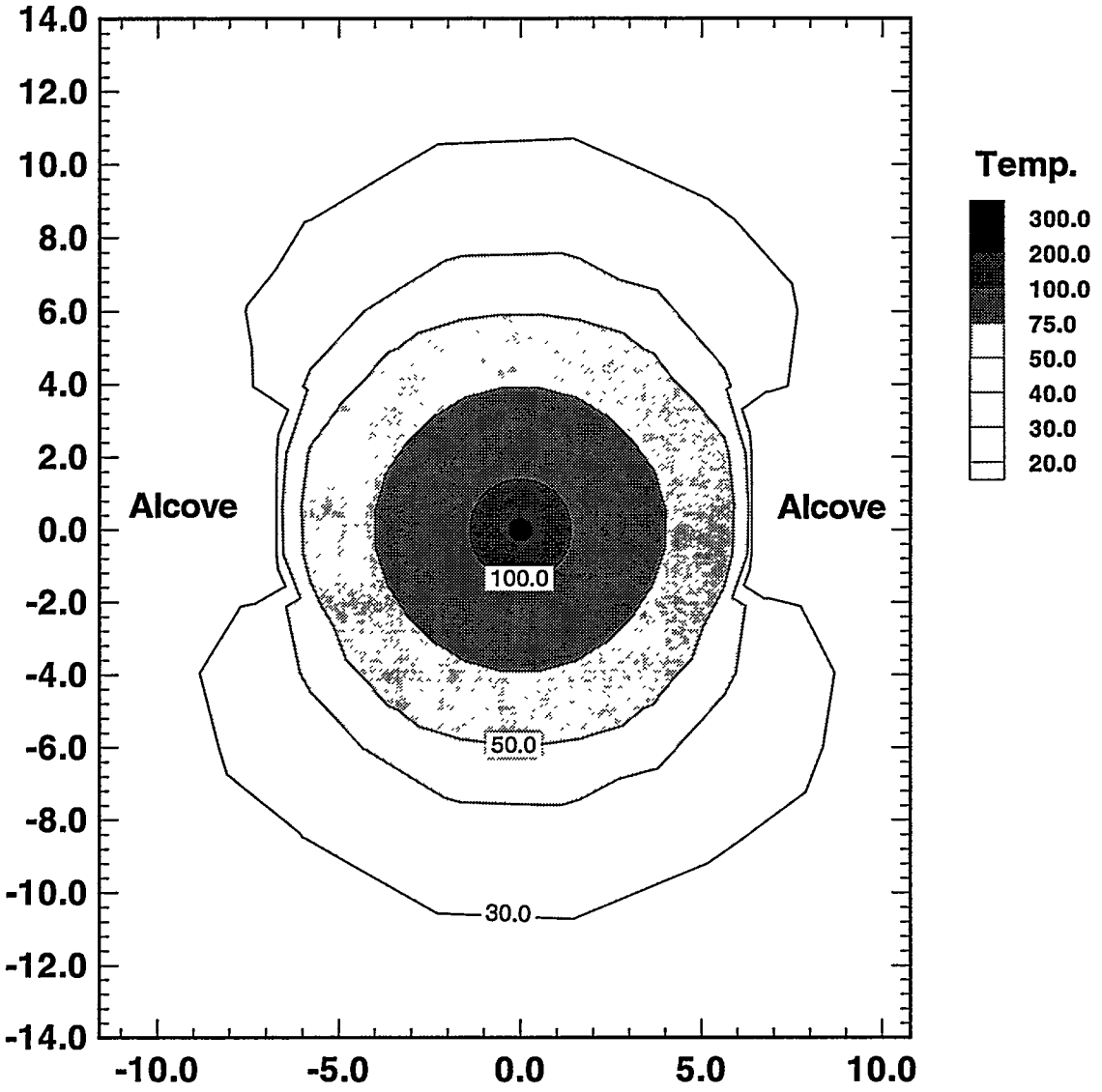

Figure 6.1-1 Temperature response for Base Case at 1 year in 2D - simulation.

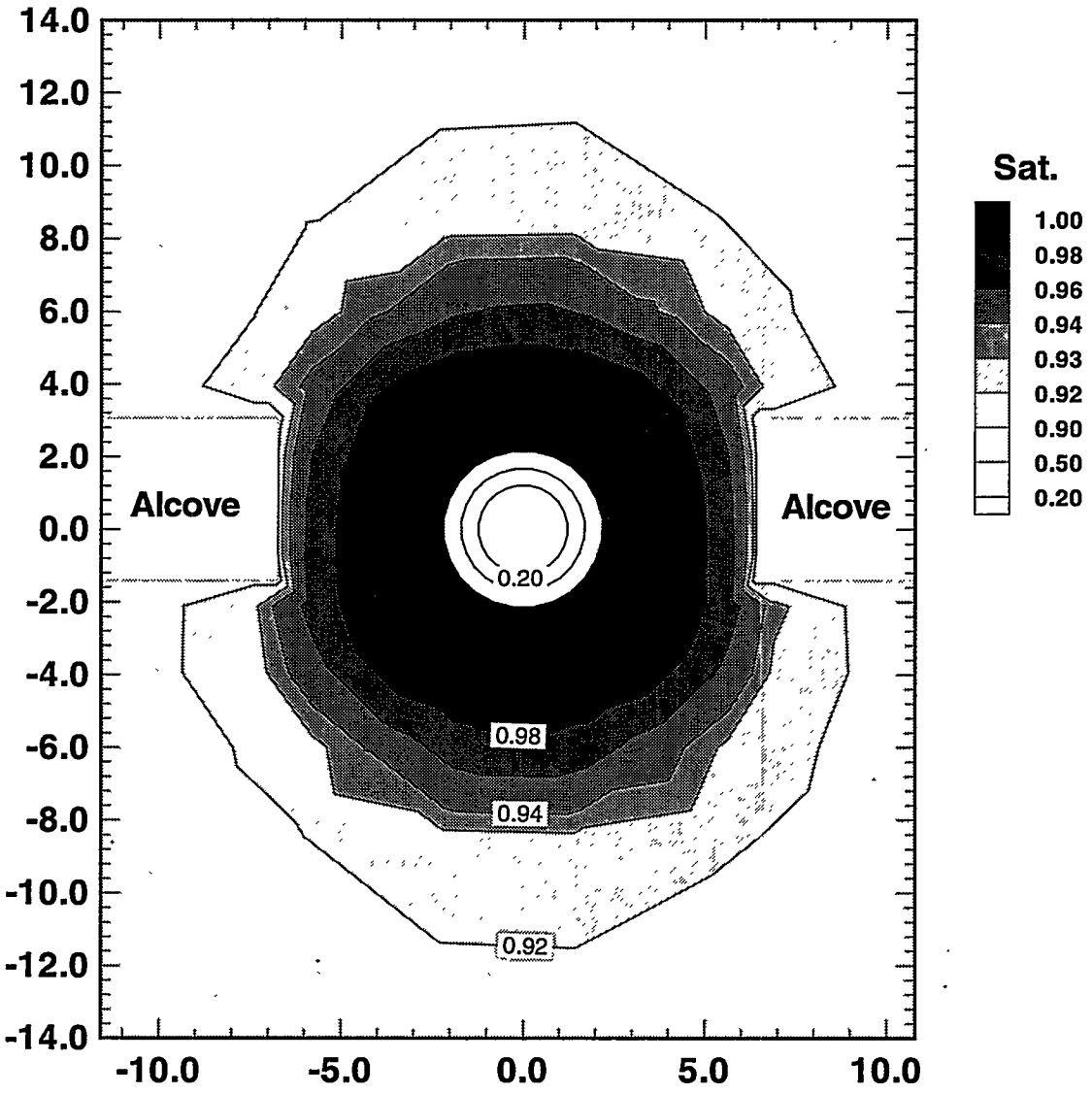

Figure 6.1-2 Equivalent continuum liquid saturation for Base Case at 1 year in 2D - simulation.

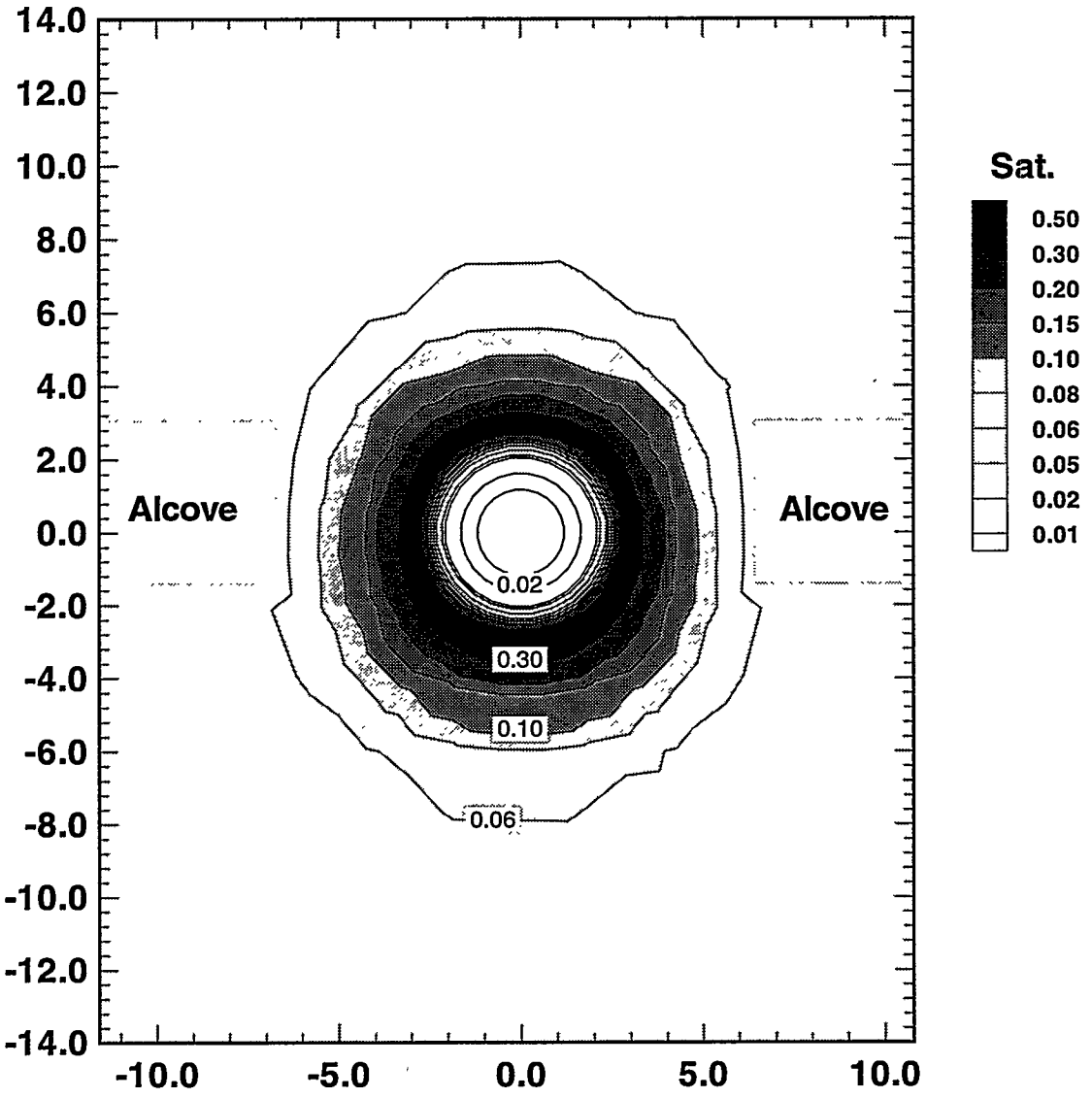

Figure 6.1-3 Fracture liquid saturation for Base Case at 1 year in 2D - simulation.

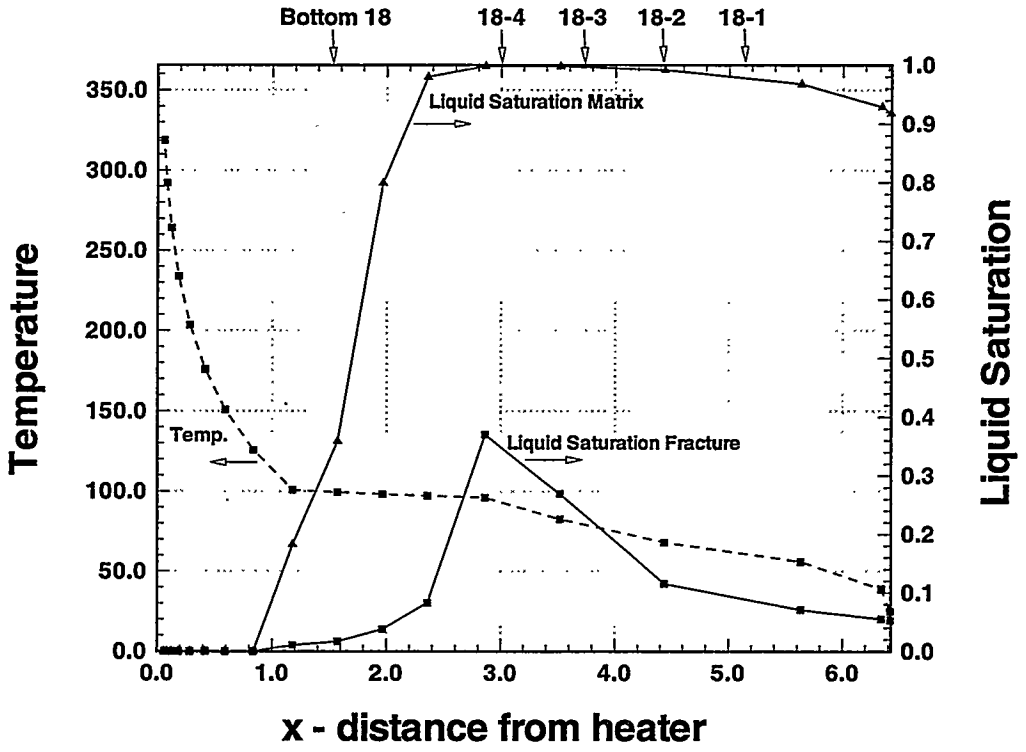

Figure 6.1-4 *Temperature / liquid saturation for Base Case in 2D - simulation at 1 year along X - axis at Z = 0.0 m.*

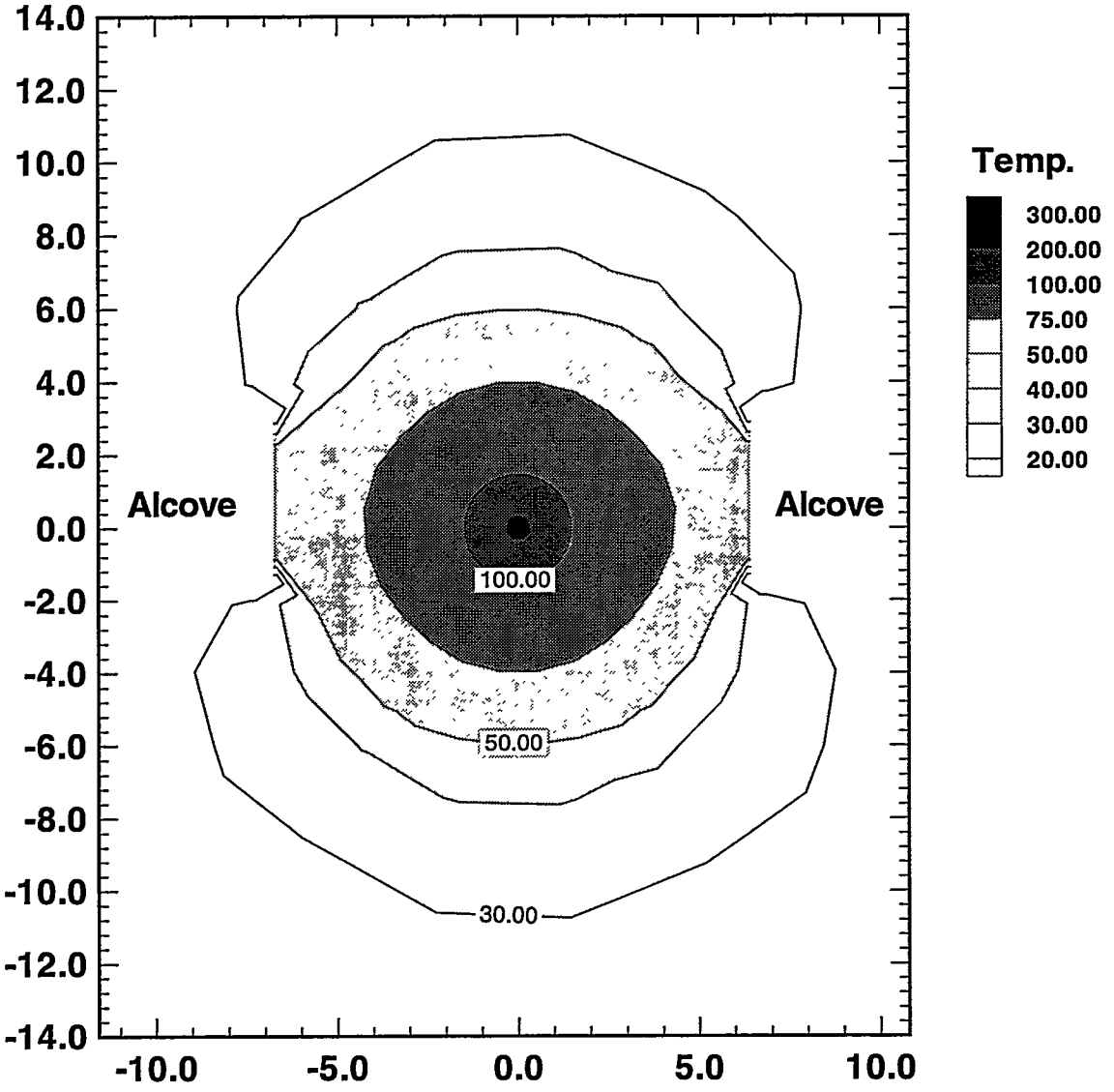

Figure 6.2-1 *Temperature response for case with perfect insulation at alcove walls at 1 year in 2D - simulation.*

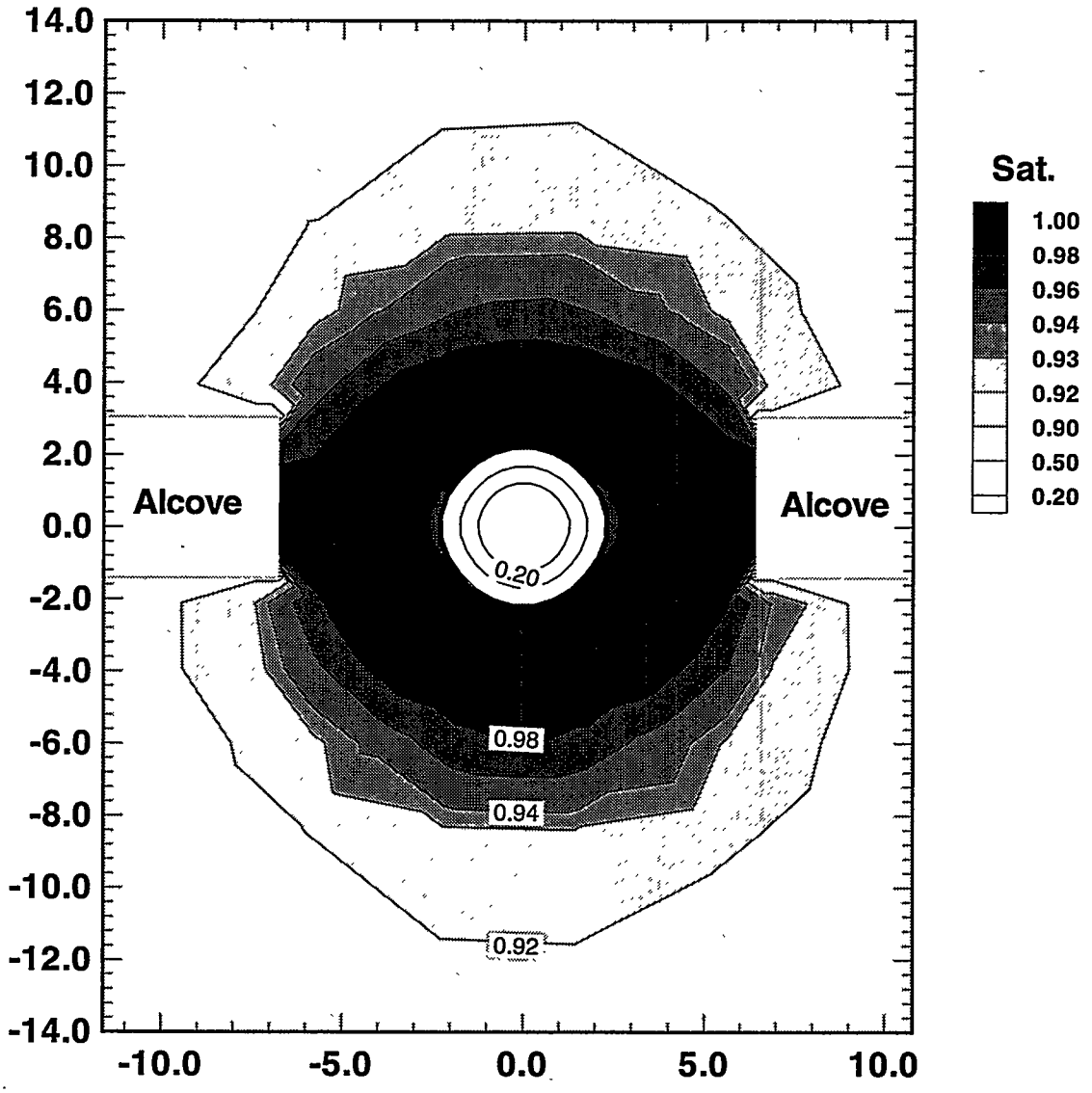

Figure 6.2-2 *Equivalent continuum liquid saturation for case with perfect insulation at alcove walls at 1 year in 2D - simulation.*

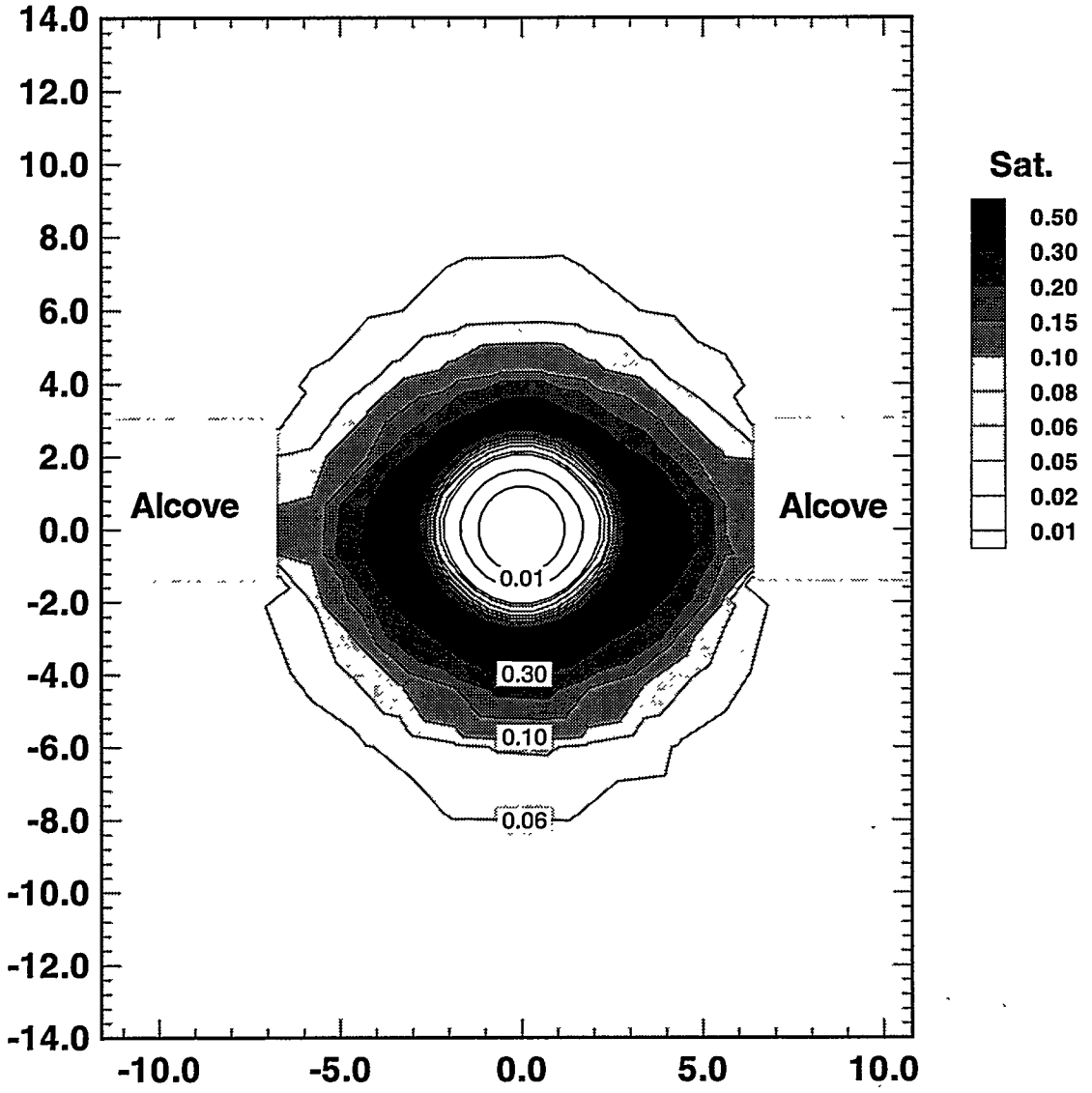

Figure 6.2-3 *Fracture liquid saturation for case with perfect insulation at alcove walls at 1 year in 2D - simulation.*

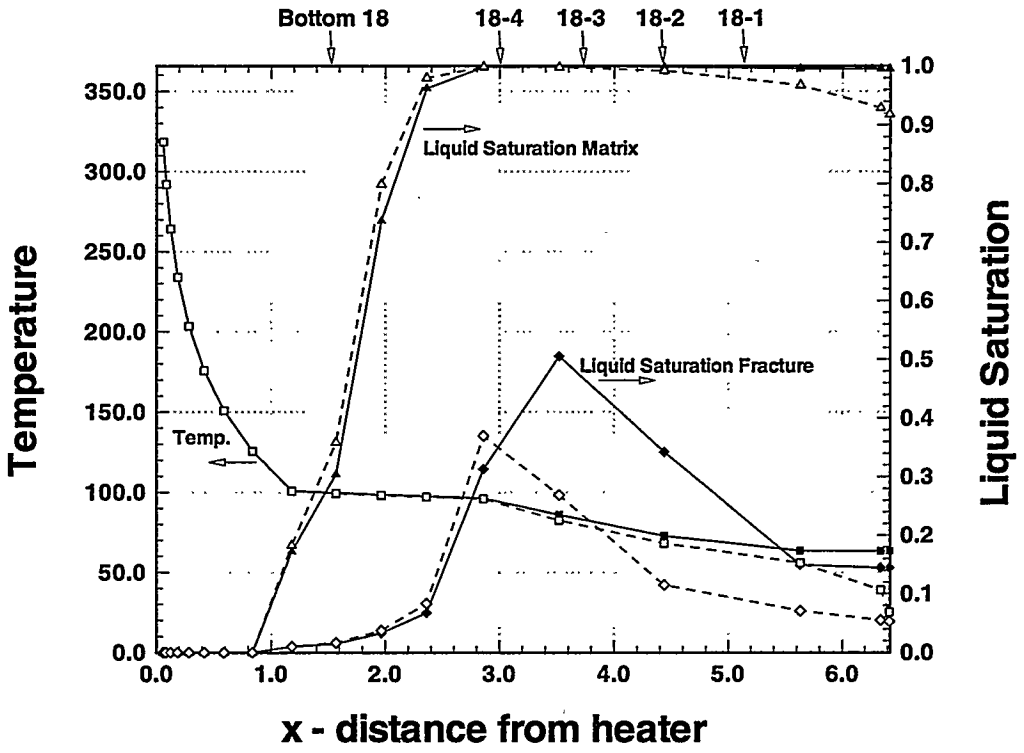

Figure 6.2-4 *Comparison of temperature / liquid saturation at 1 year along X - axis at Z = 0.0 m for two different alcove boundary conditions in 2D - simulation. Solid symbols / lines denote a perfect insulation for heat, liquid and gas; hollow symbols and dashed lines denote insulation for heat only, as used in the Base Case.*

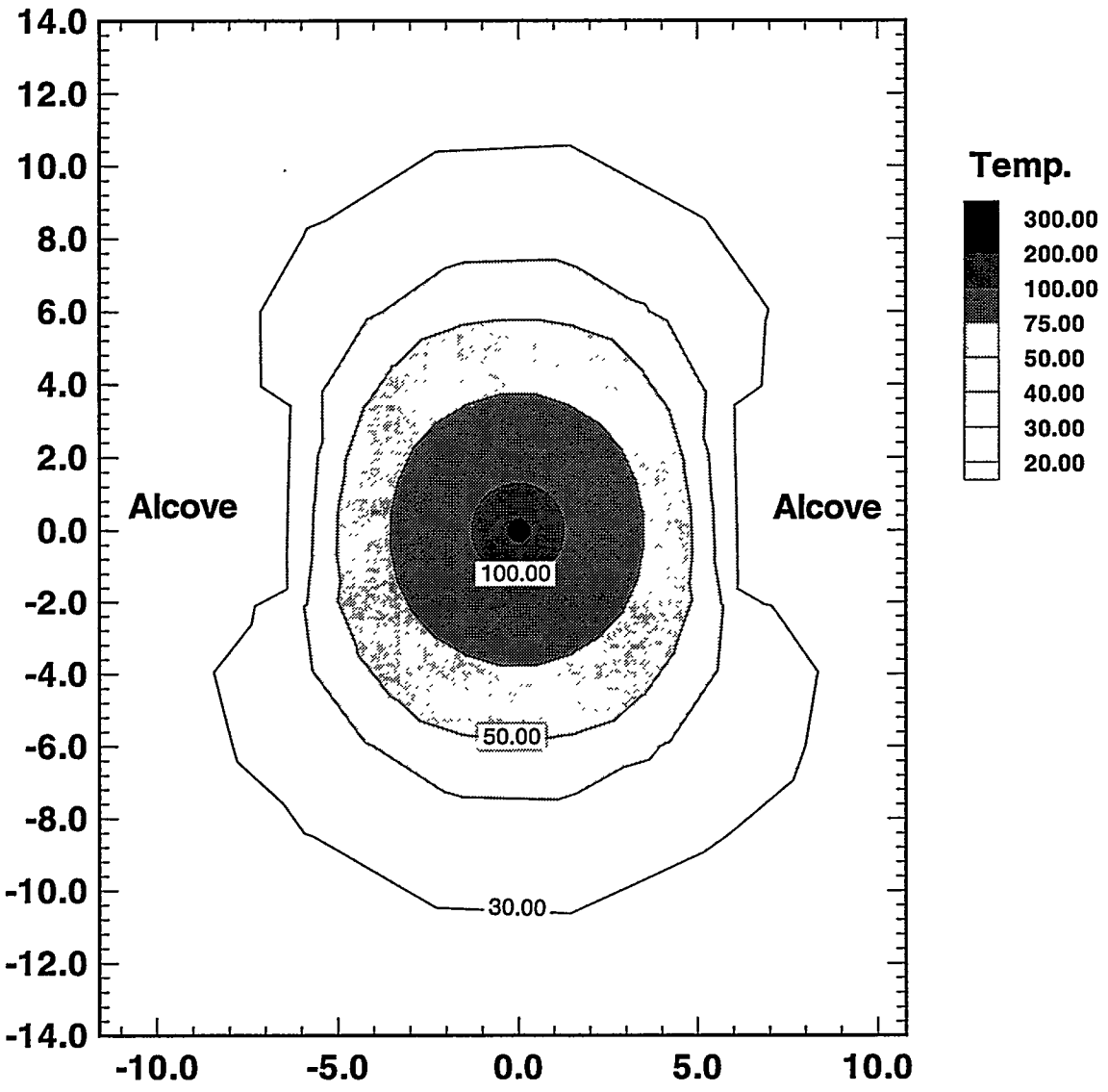

Figure 6.2-5 Temperature response for case with non-insulated alcove walls at 1 year in 2D - simulation.

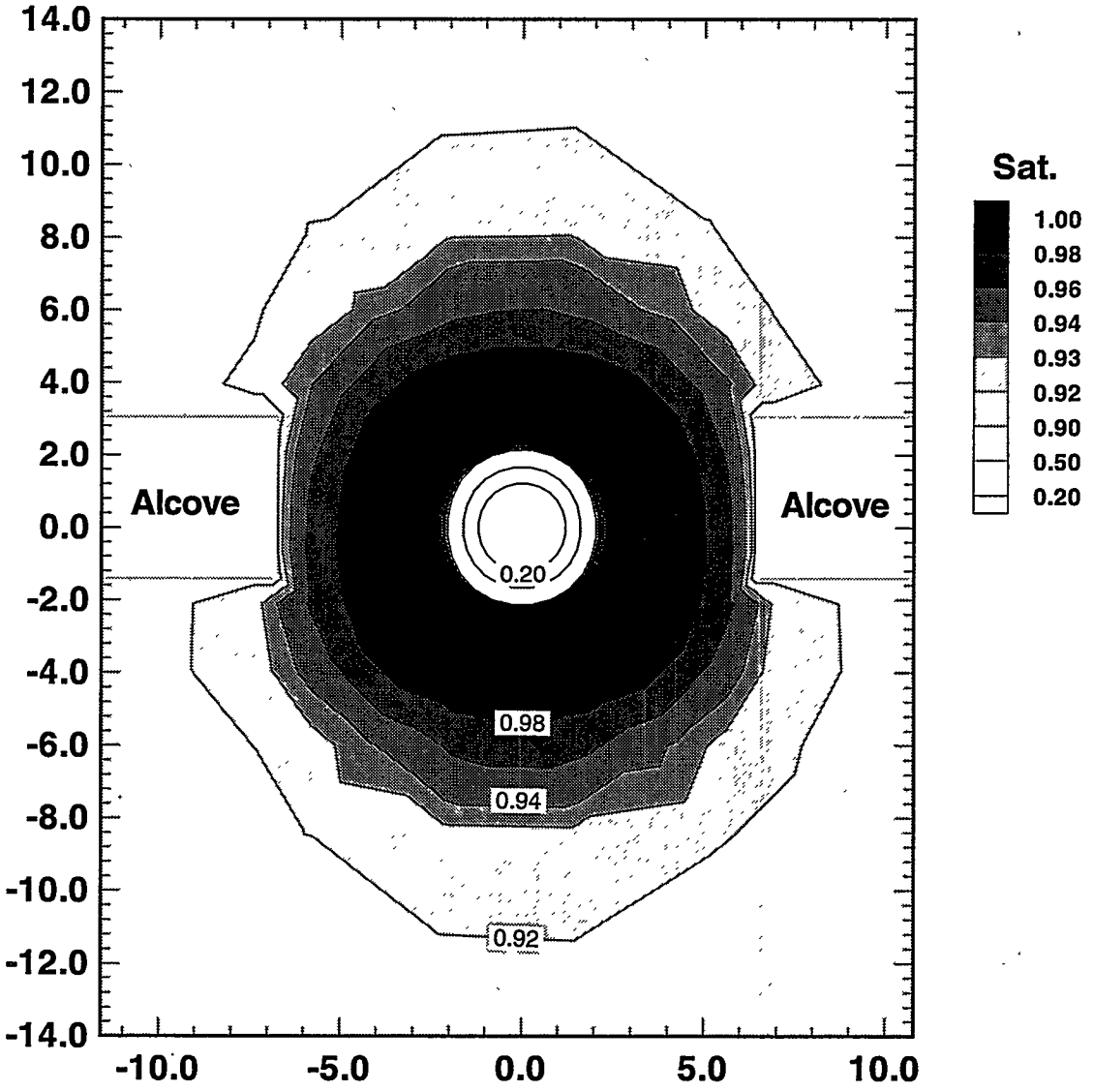

Figure 6.2-6 *Equivalent continuum liquid saturation for case with non-insulated alcove walls at 1 year in 2D - simulation.*

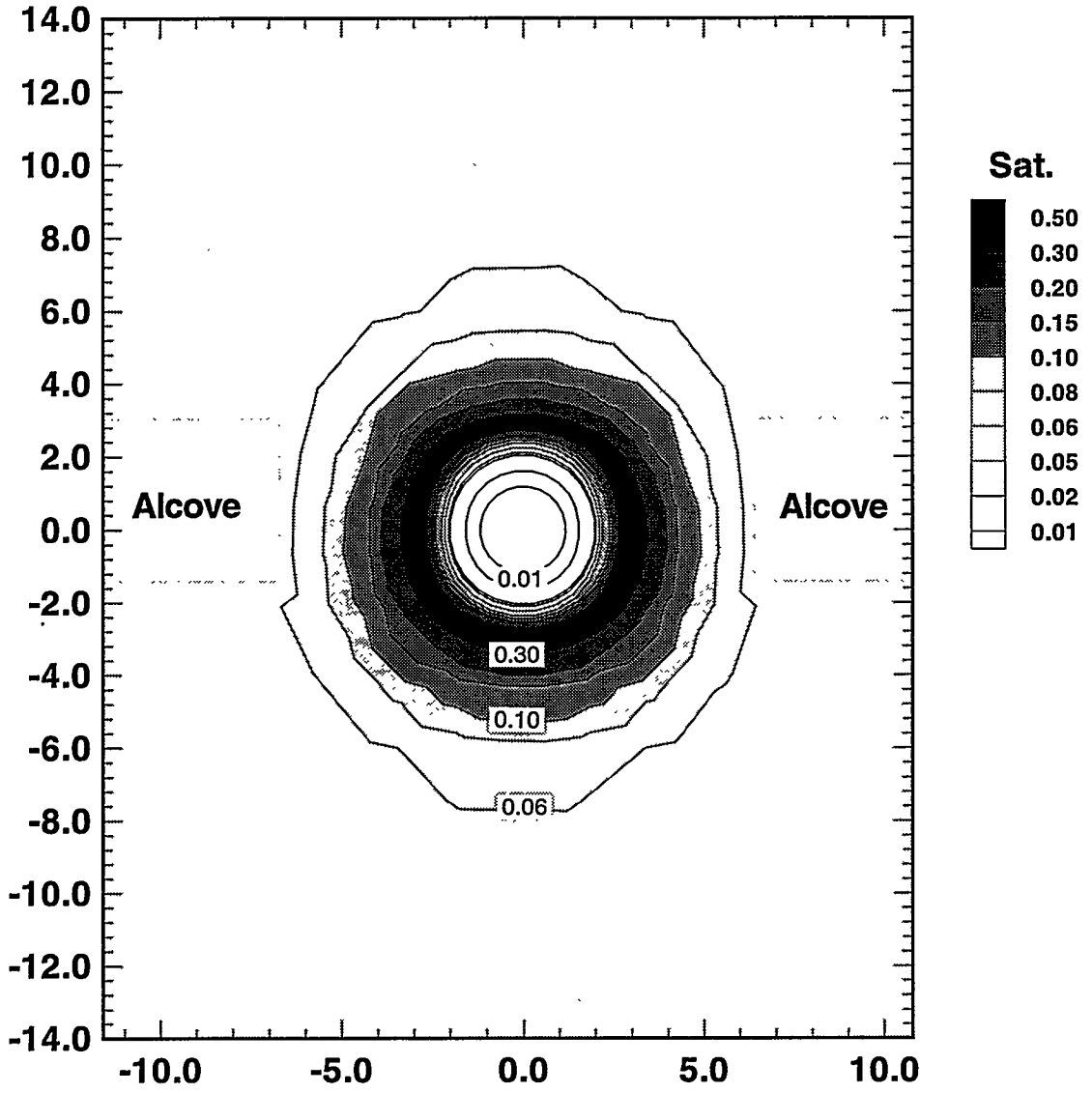

Figure 6.2-7 *Fracture liquid saturation for case with non-insulated alcove walls at 1 year in 2D - simulation.*

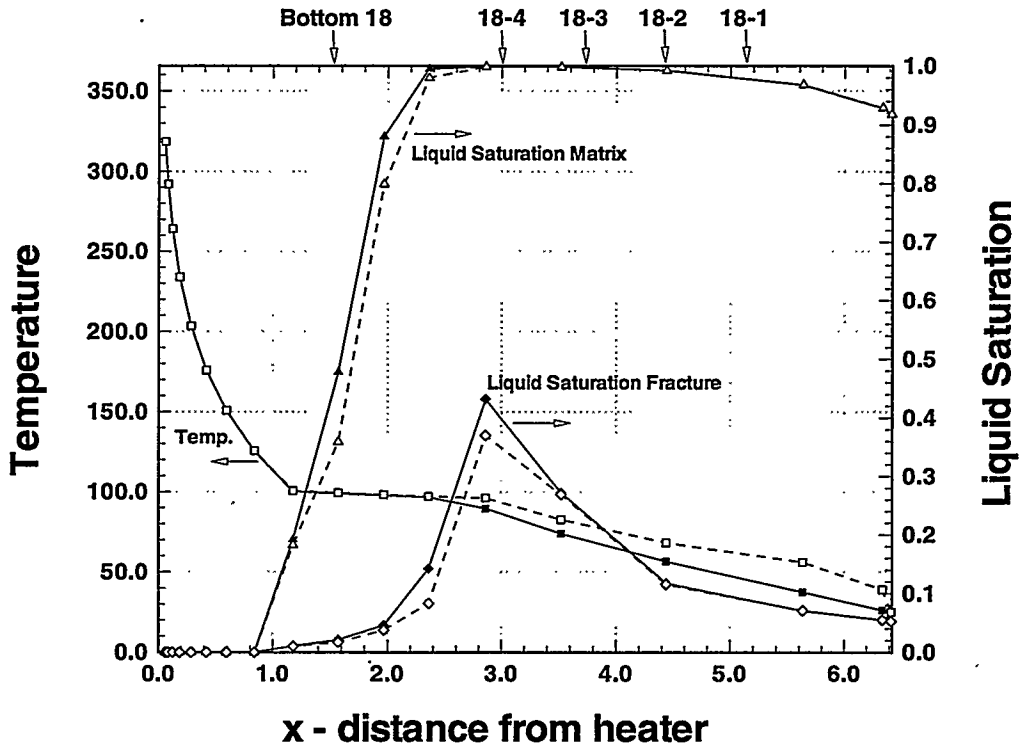

Figure 6.2-8 Comparison of temperature / liquid saturation at 1 year along X - axis at Z = 0.0 m for two different alcove boundary conditions in 2D - simulation. Solid symbols / lines denote no insulation, hollow symbols and dashed lines denote insulation for heat only, as used in the Base Case.

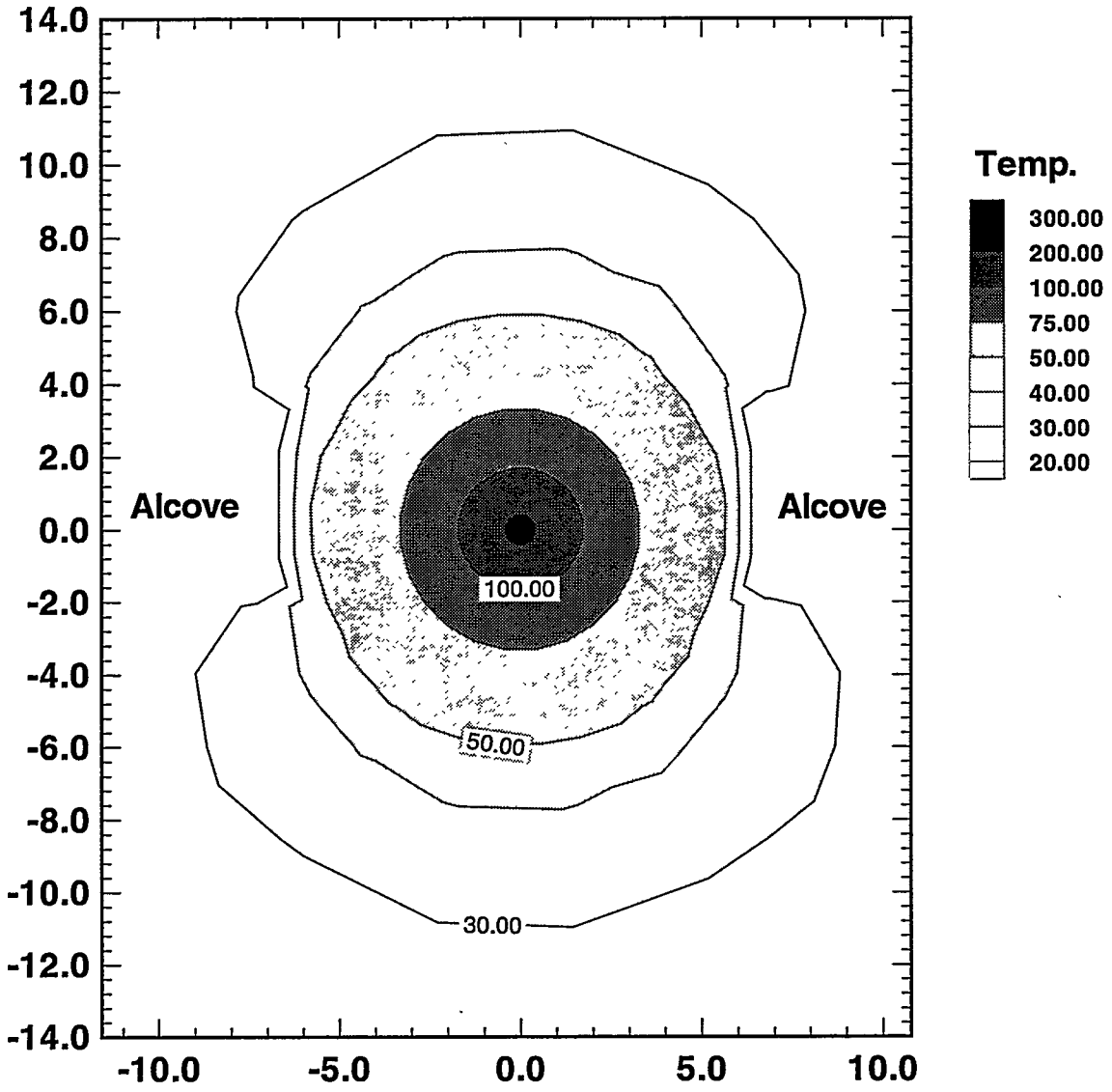

Figure 6.3-1 *Temperature response for case with enhanced vapor diffusion at 1 year in 2D - simulation.*

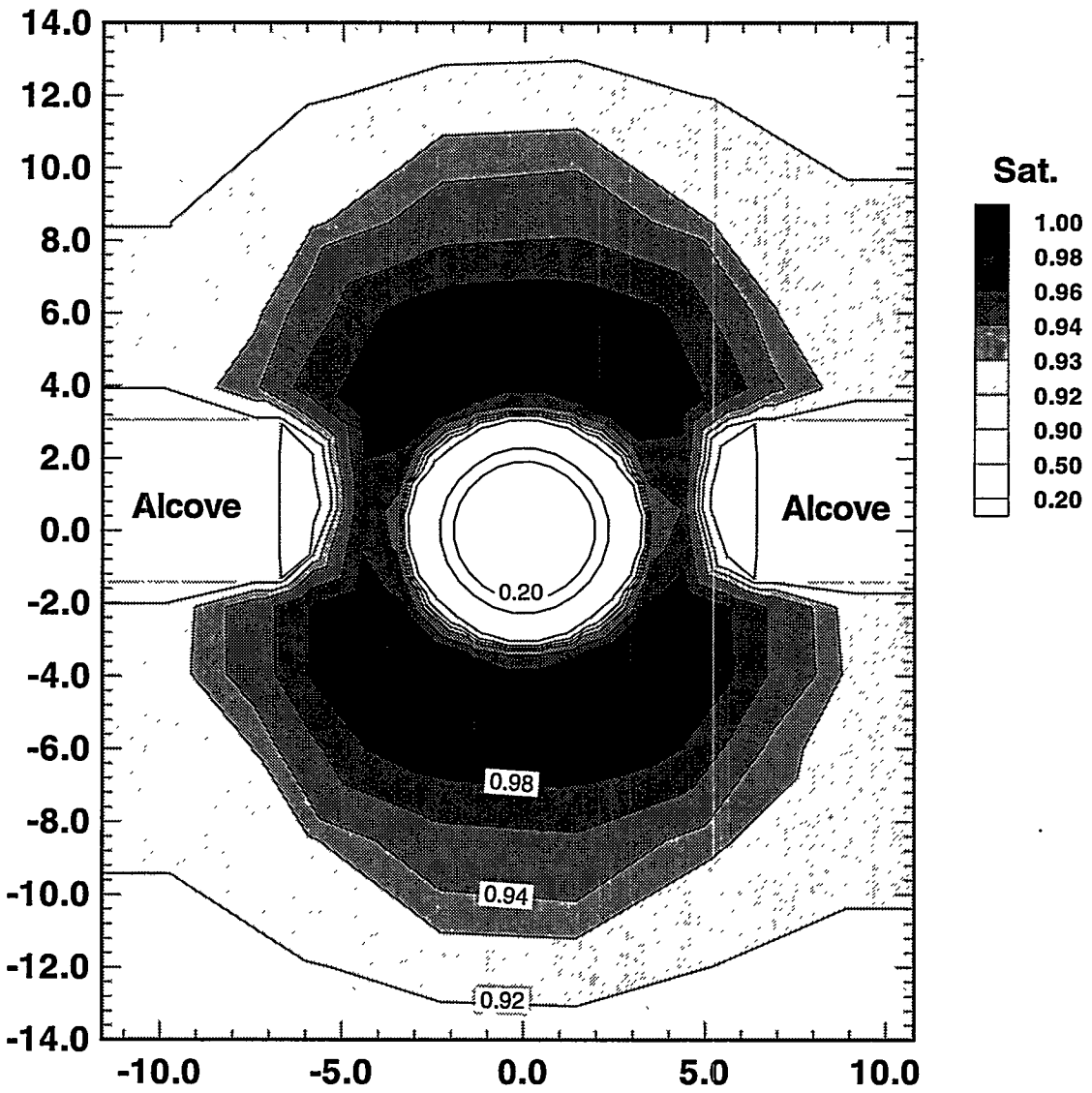

Figure 6.3-2 *Equivalent continuum liquid saturation for case with enhanced vapor diffusion at 1 year in 2D - simulation.*

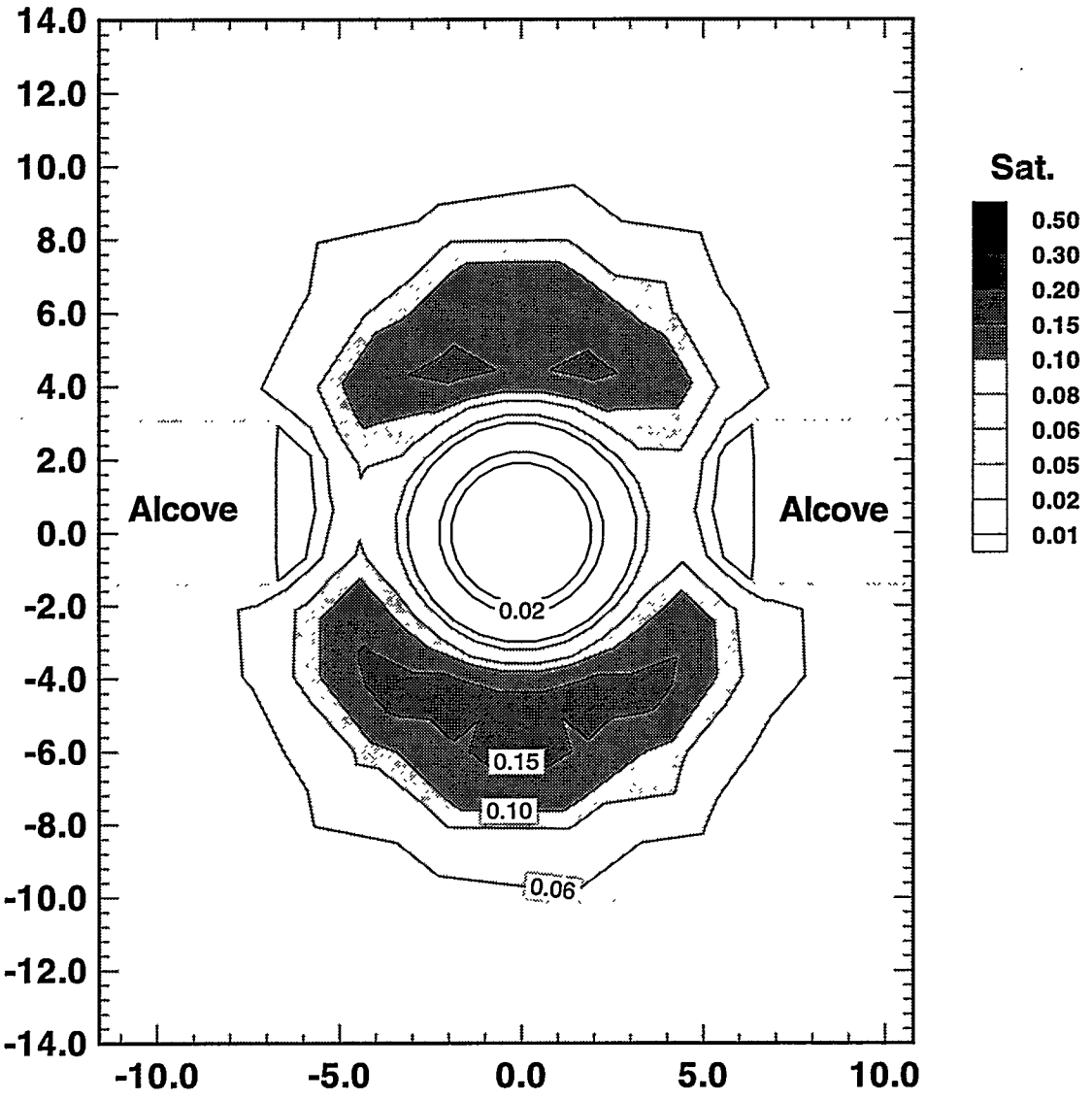

Figure 6.3-3 *Fracture liquid saturation for case with enhanced vapor diffusion at 1 year in 2D - simulation.*

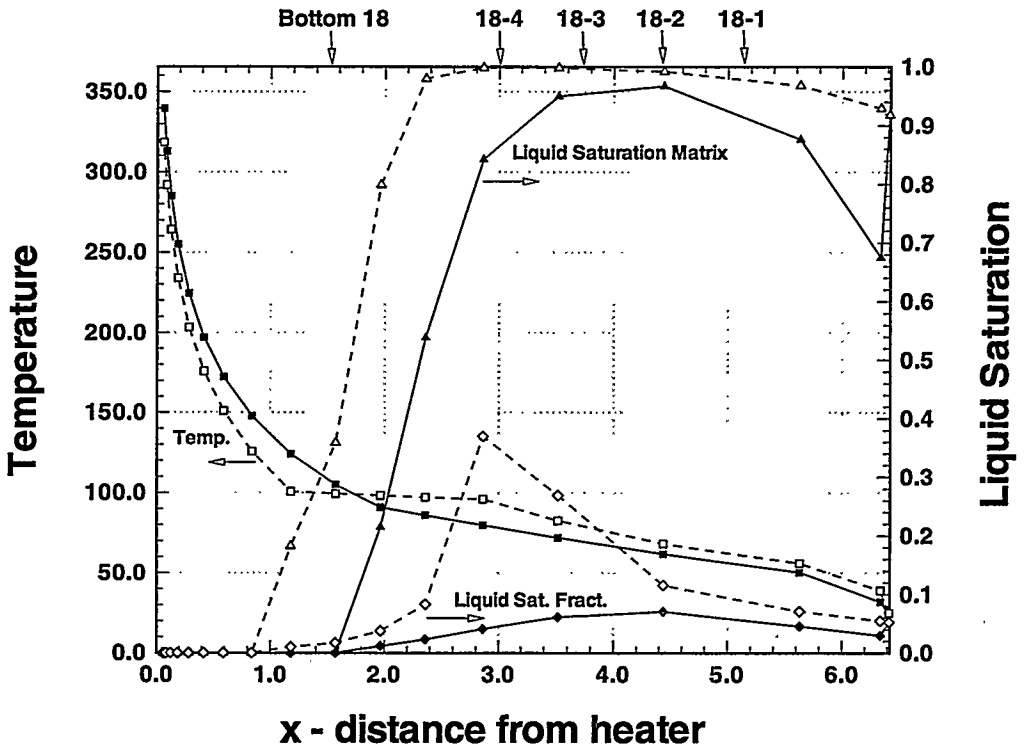

Figure 6.3-4 *Comparison of temperature / liquid saturation at 1 year along X - axis at Z = 0.0 m for ordinary and enhanced vapor diffusion in 2D - simulation. Solid symbols / lines denote enhanced vapor diffusion, hollow symbols and dashed lines denote ordinary vapor diffusion, as used in the Base Case.*

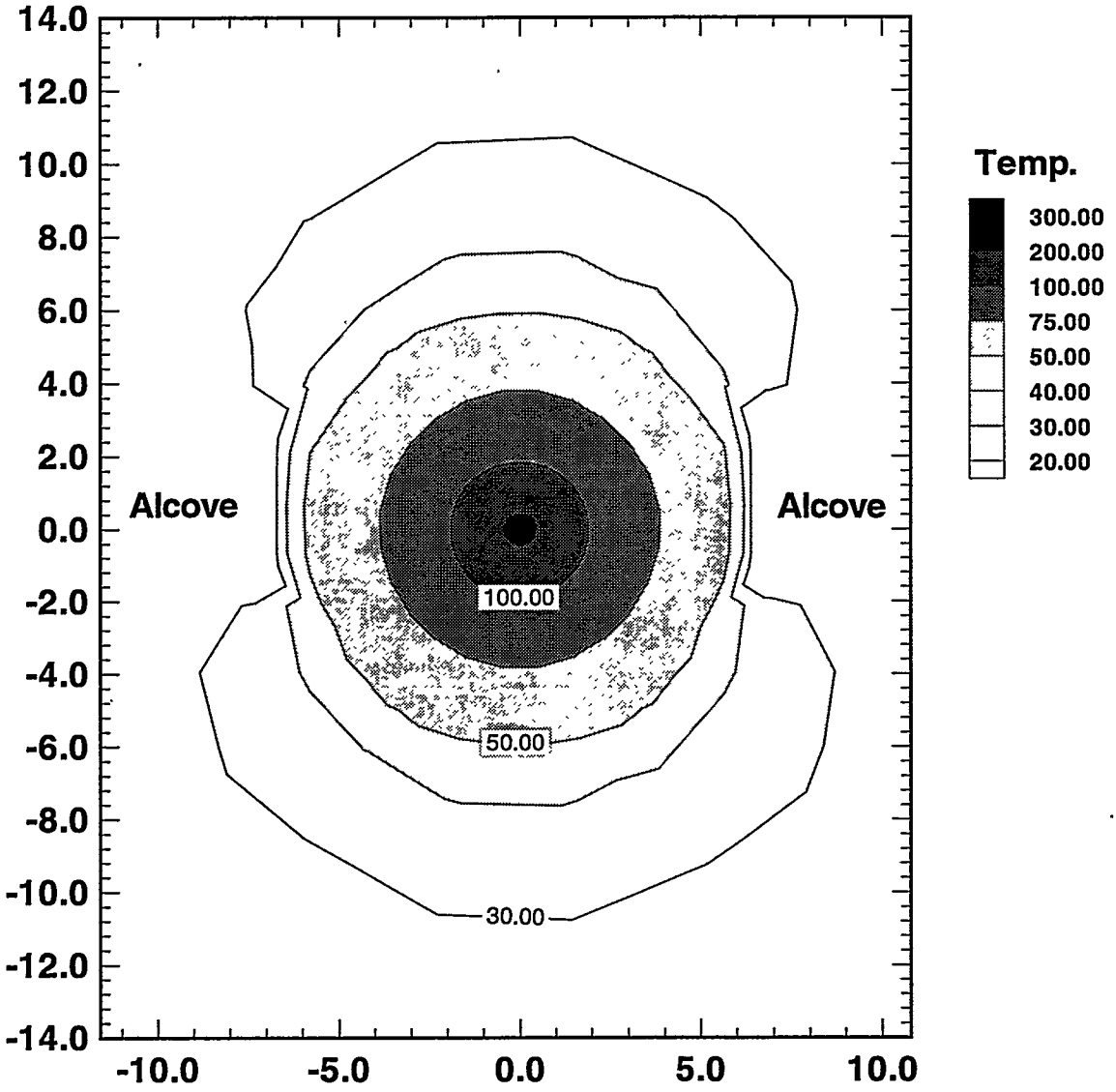

Figure 6.4-1 *Temperature response in the matrix at 1 year in 2D - simulation using dual-permeability approach.*

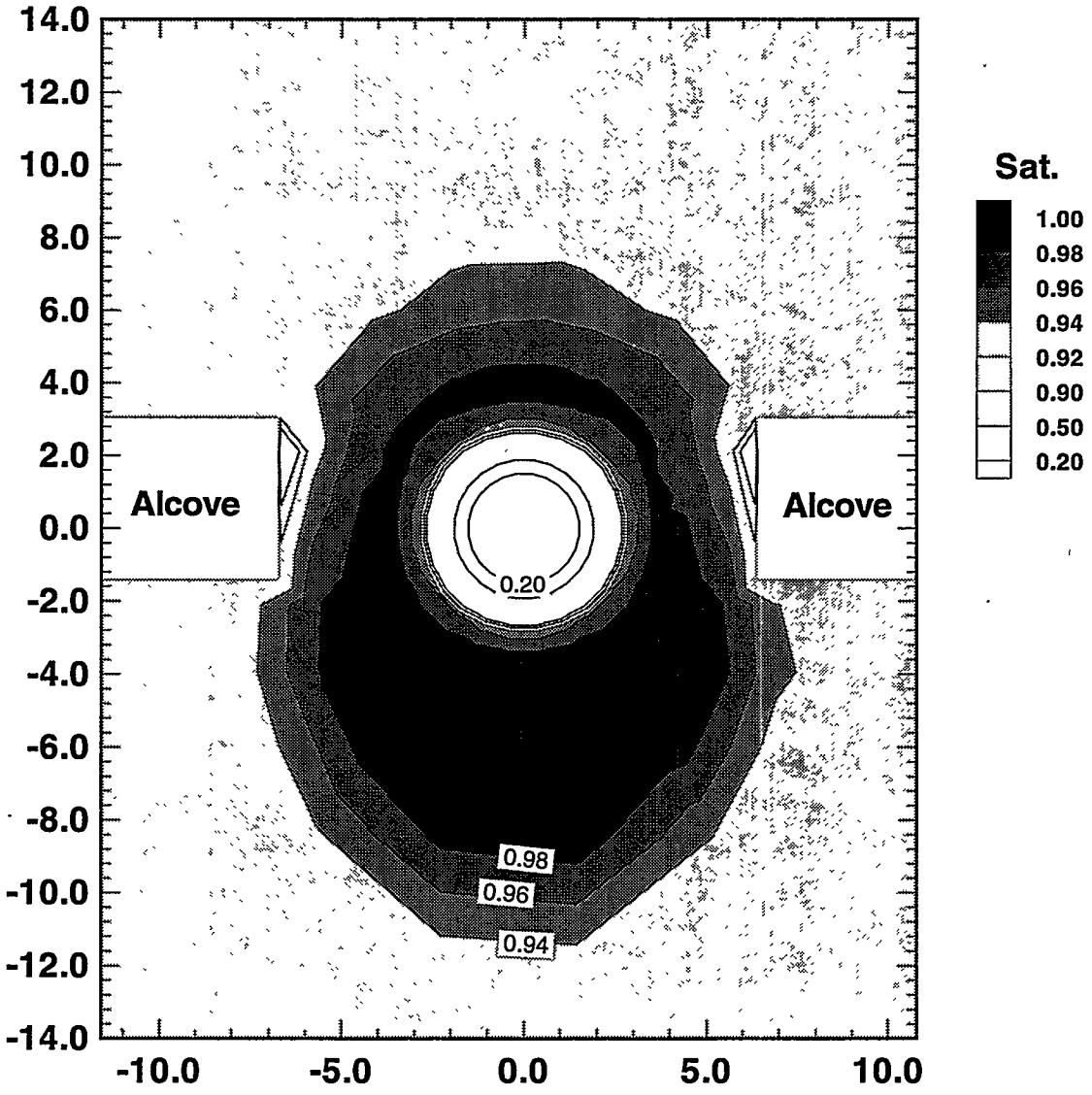

Figure 6.4-2 *Matrix liquid saturation at 1 year in 2D - simulation using dual-permeability approach.*

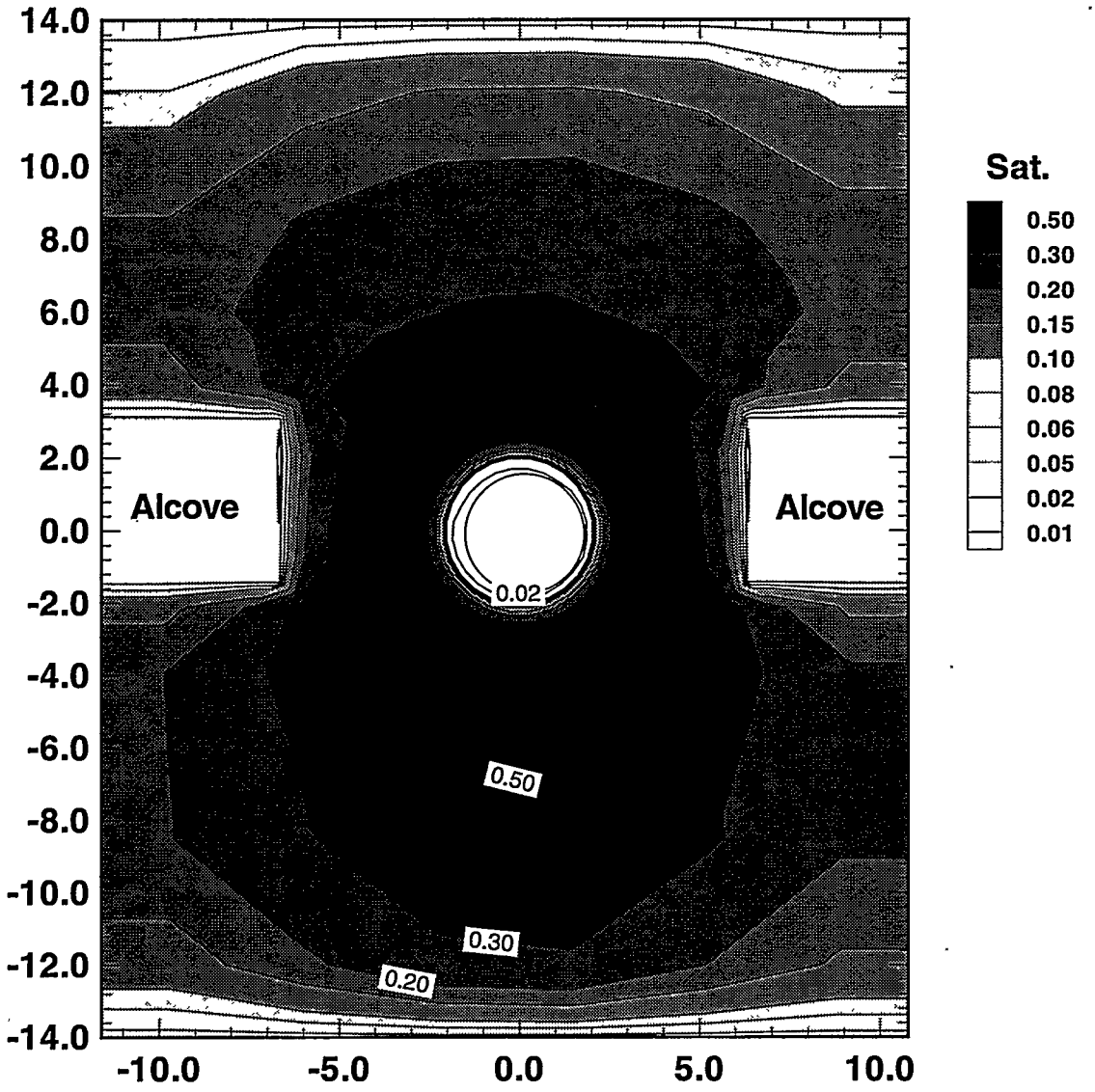

Figure 6.4-3 *Fracture liquid saturation at 1 year in 2D - simulation using dual-permeability approach.*

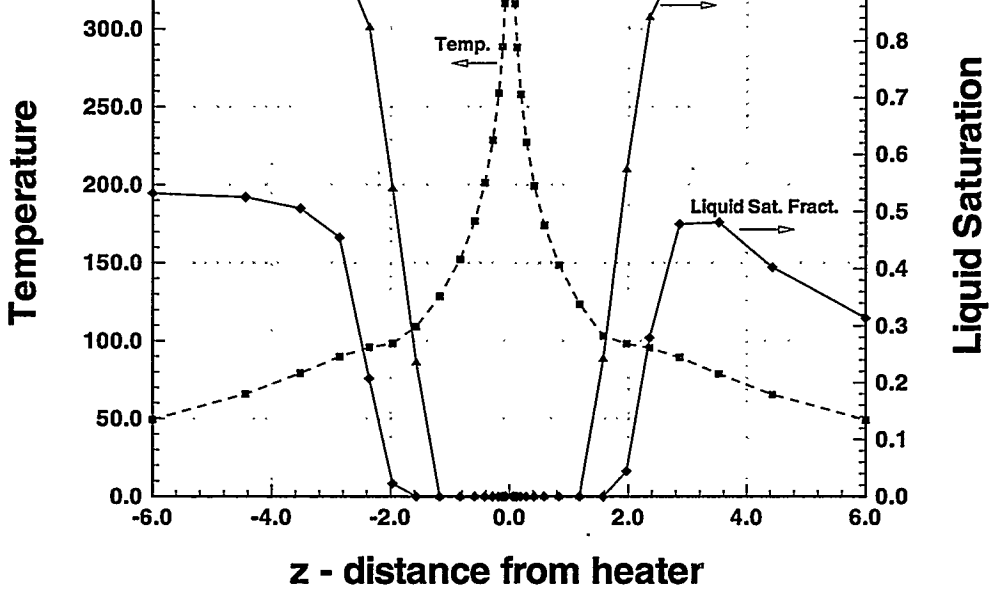

Figure 6.4-4 *Temperature / liquid saturation for dual-permeability model in 2D - simulation at 1 year along Z - axis at X = 0.0 m.*

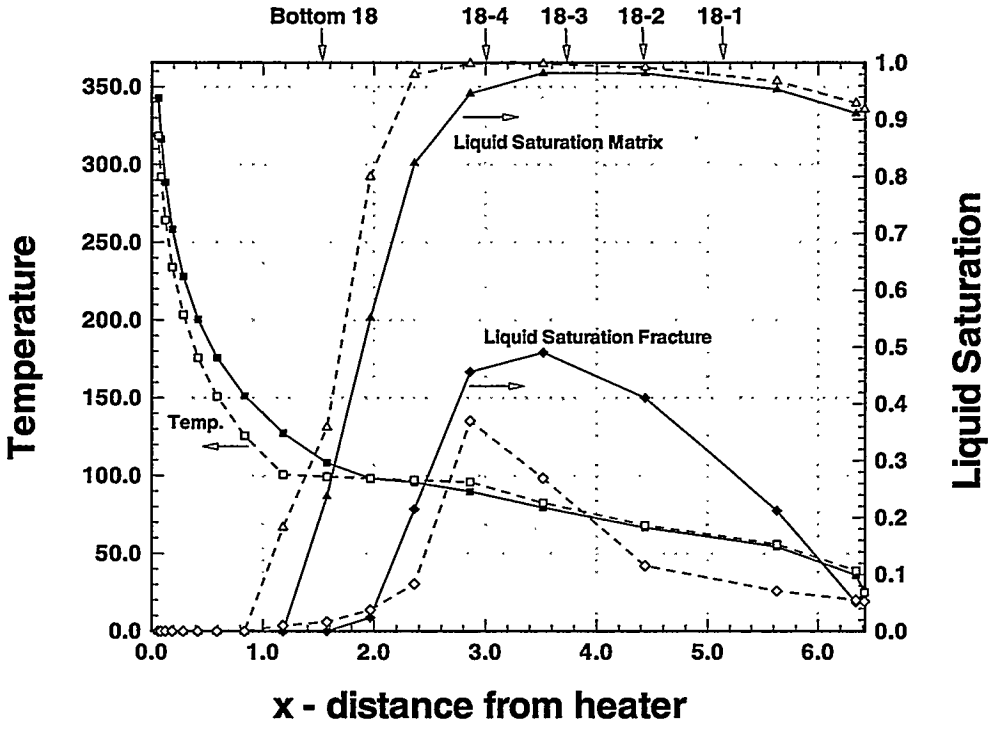

Figure 6.4-5 *Comparison of temperature / liquid saturation at 1 year along X - axis at Z = 0.0 m for different model concepts in 2D - simulation. Solid symbols / lines denote dual-permeability modeling, hollow symbols and dashed lines denote ECM - modeling.*

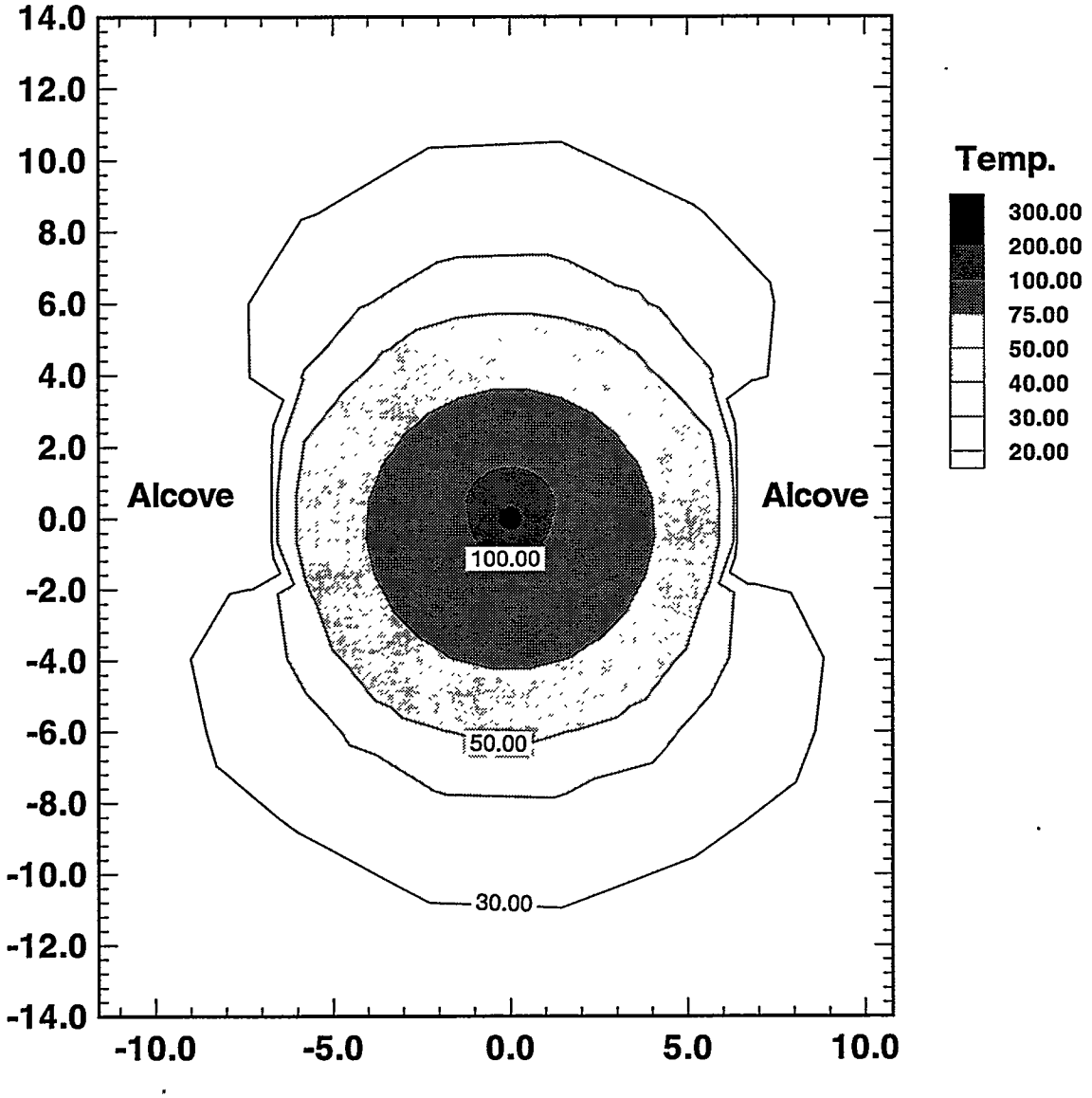

Figure 6.5-1 Temperature response for case with high fracture permeability at 1 year in 2D - simulation.

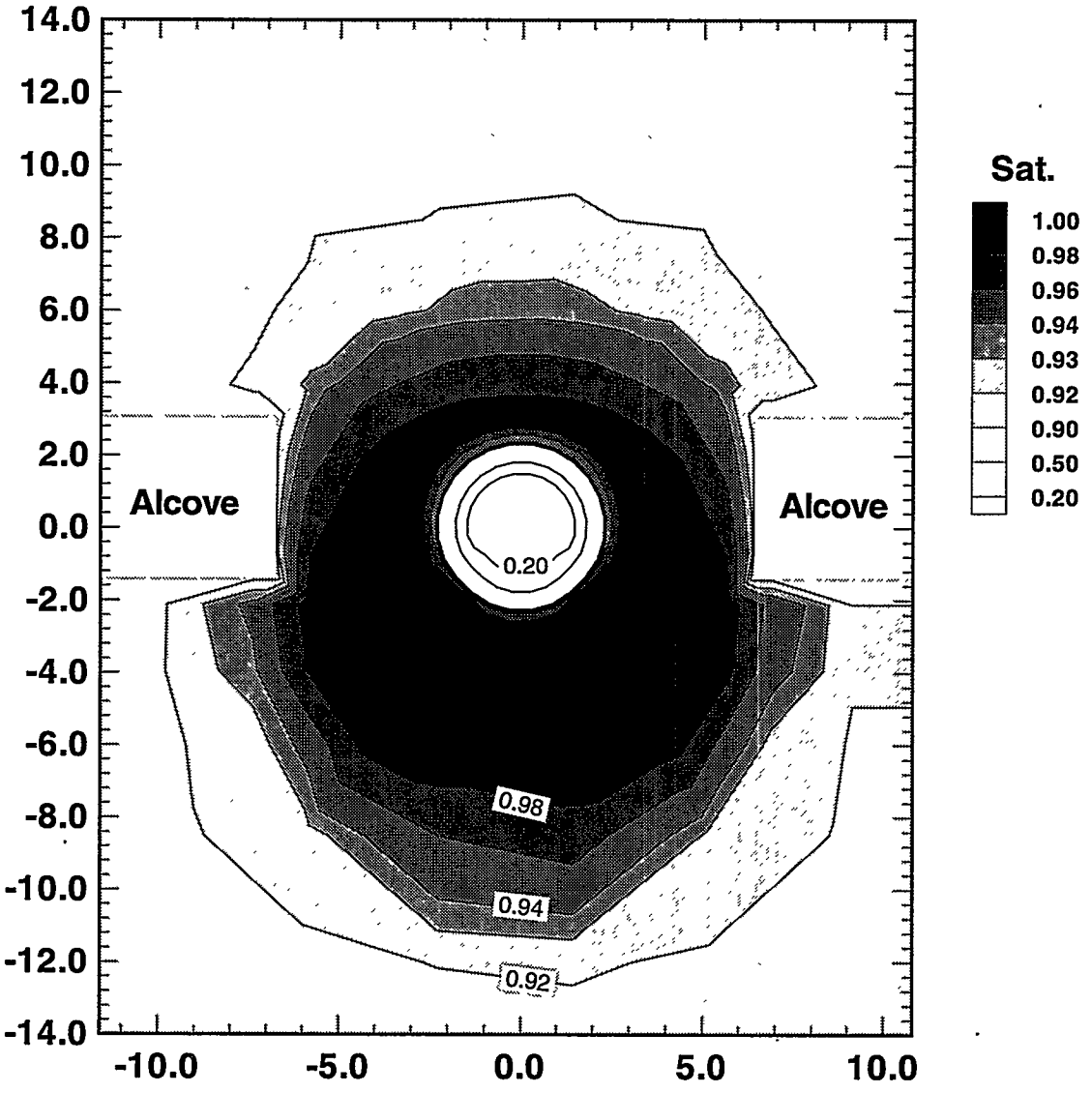

Figure 6.5-2 *Equivalent continuum liquid saturation for case with high fracture permeability at 1 year in 2D - simulation.*

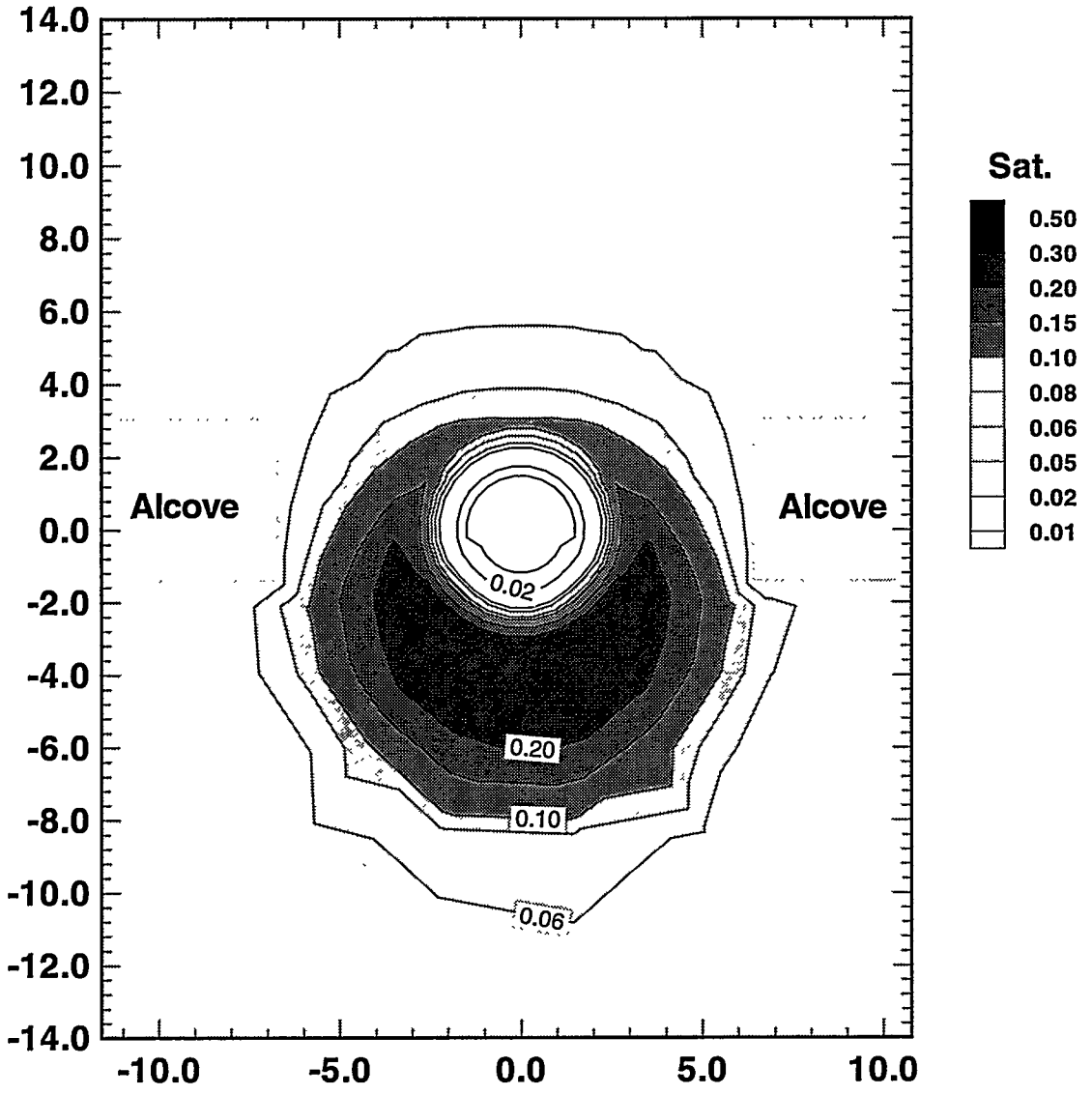

Figure 6.5-3 Fracture liquid saturation for case with high fracture permeability at 1 year in 2D - simulation.

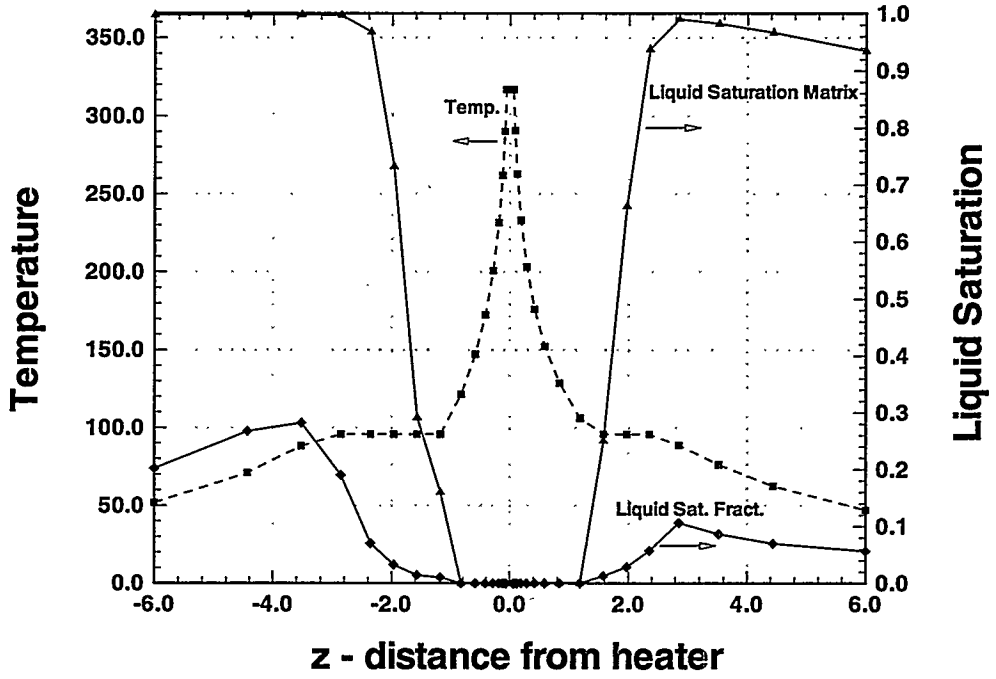

Figure 6.5-4 *Temperature / liquid saturation for case with high fracture permeability in 2D - simulation at 1 year along Z - axis at X = 0.0 m.*

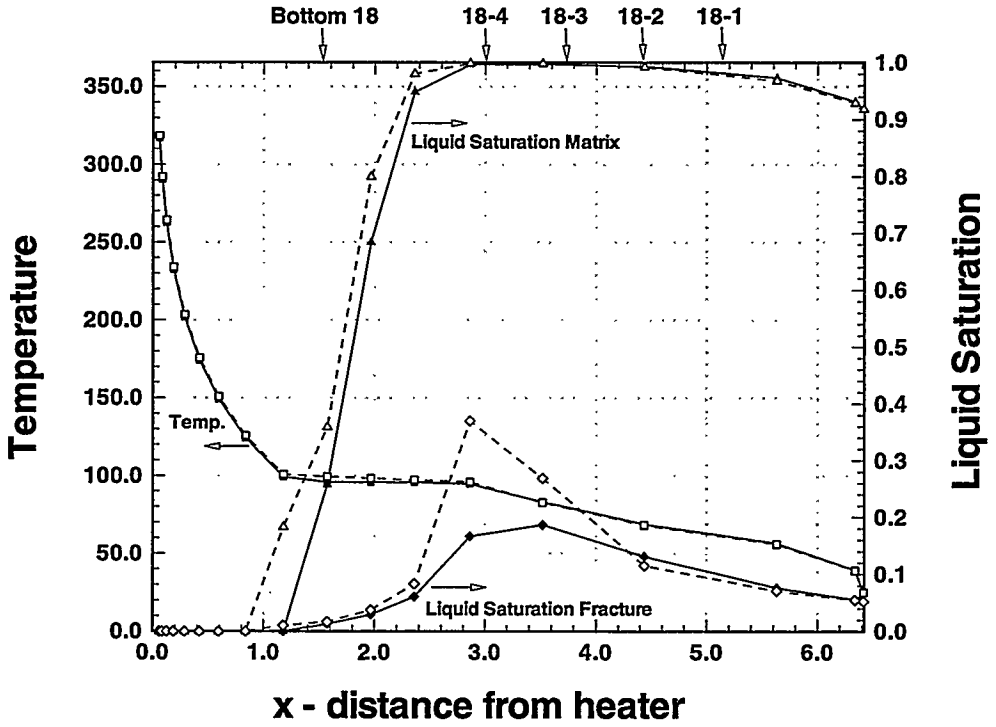

Figure 6.5-5 *Comparison of temperature / liquid saturation at 1 year along X - axis at Z = 0.0 m for different fracture permeabilities in 2D - simulation. Solid symbols / lines denote case with high fracture permeability, hollow symbols and dashed lines denote Base Case.*

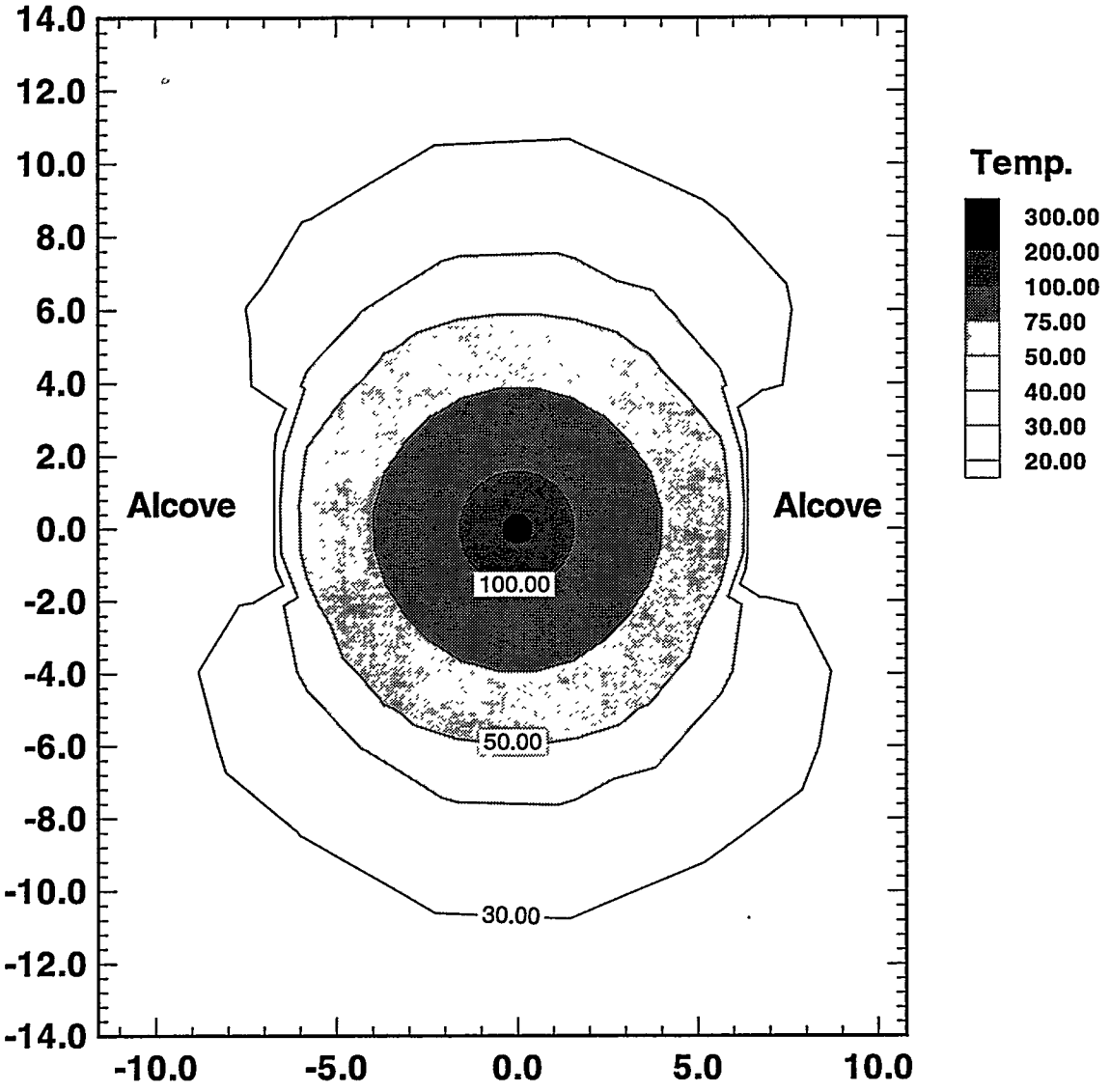

Figure 6.6-1 *Temperature response for case with low matrix permeability at 1 year in 2D - simulation.*

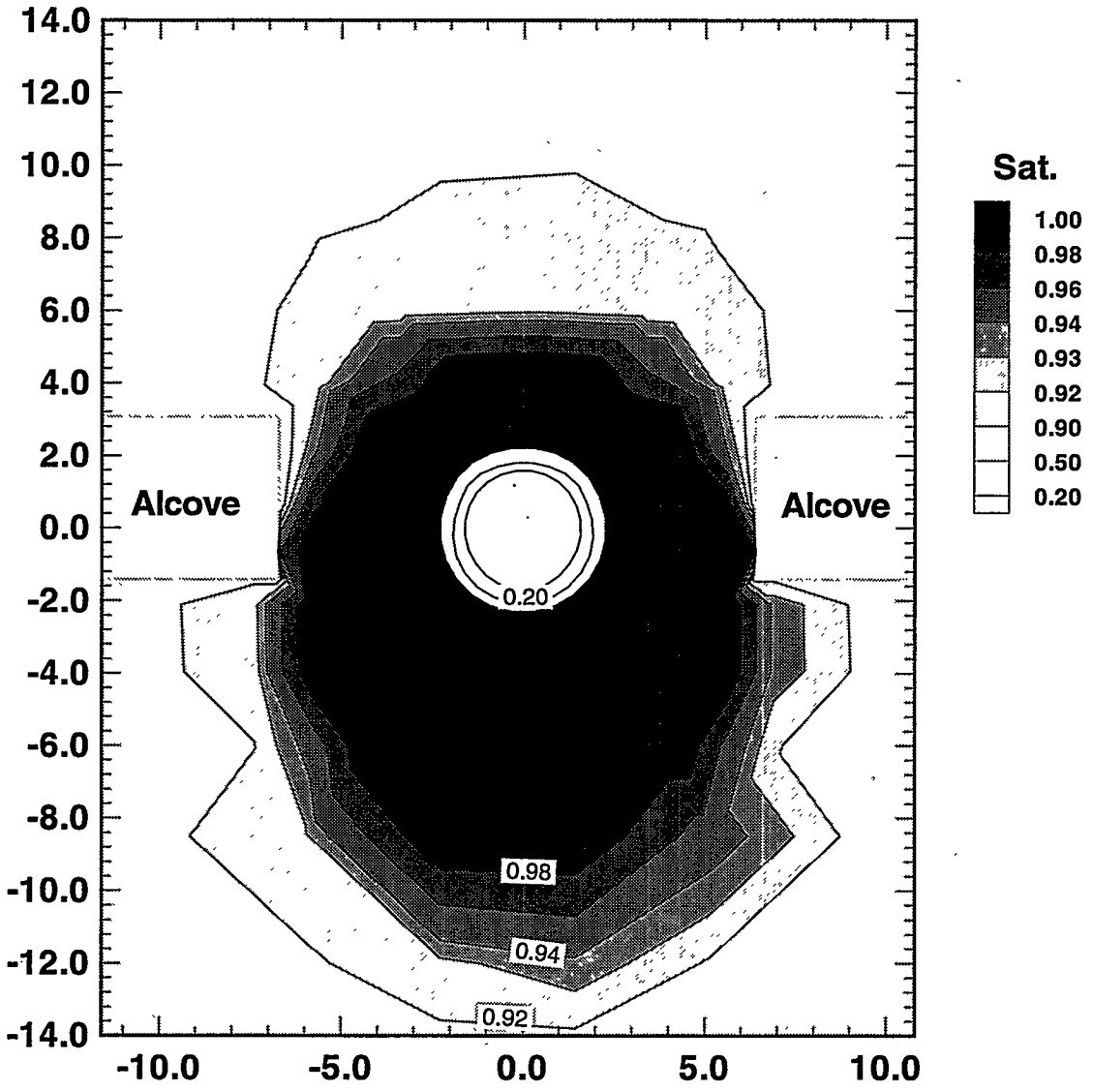

Figure 6.6-2 *Equivalent continuum liquid saturation for case with low matrix permeability at 1 year in 2D - simulation.*

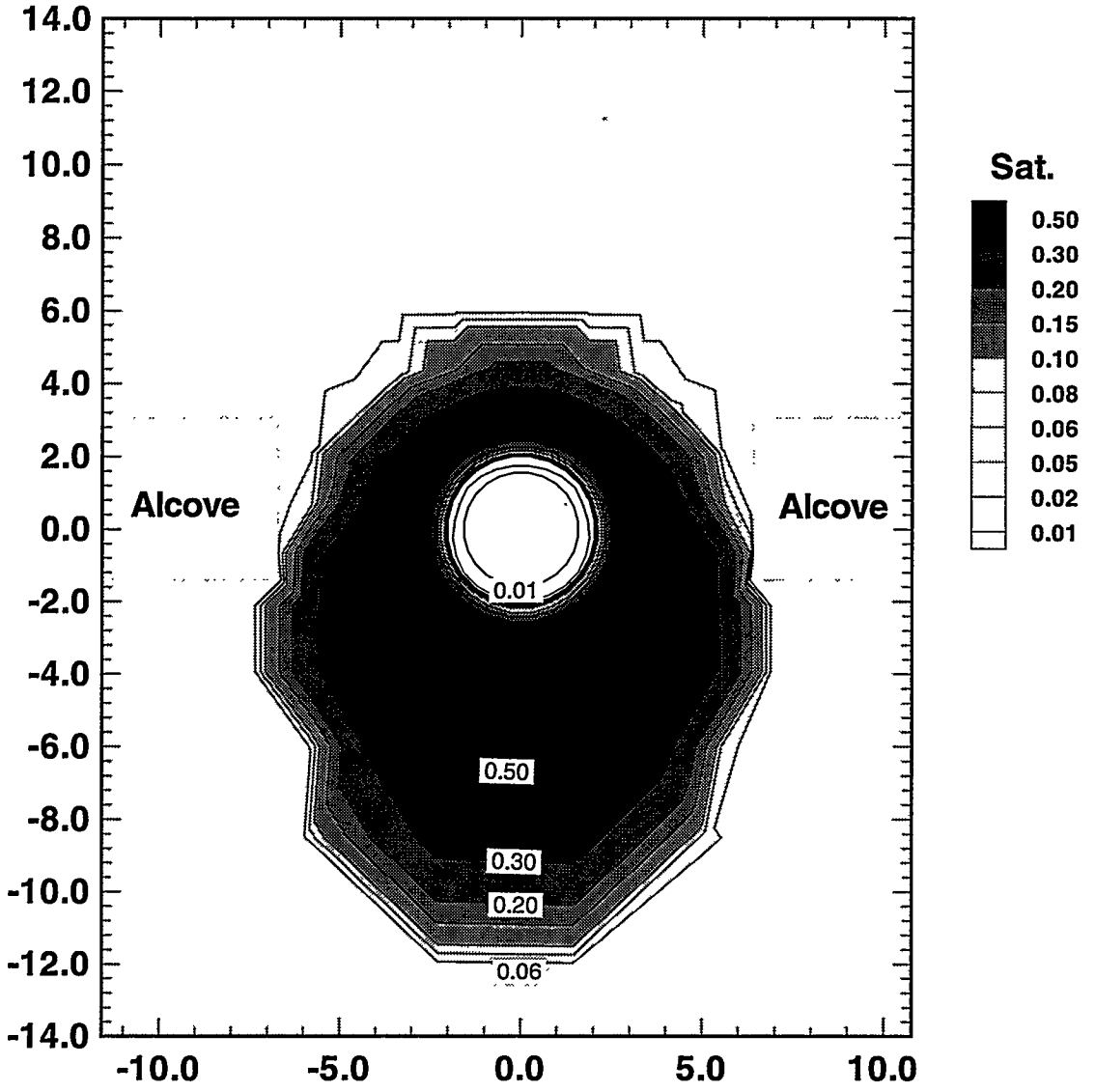

Figure 6.6-3 Fracture liquid saturation for case with low matrix permeability at 1 year in 2D - simulation.

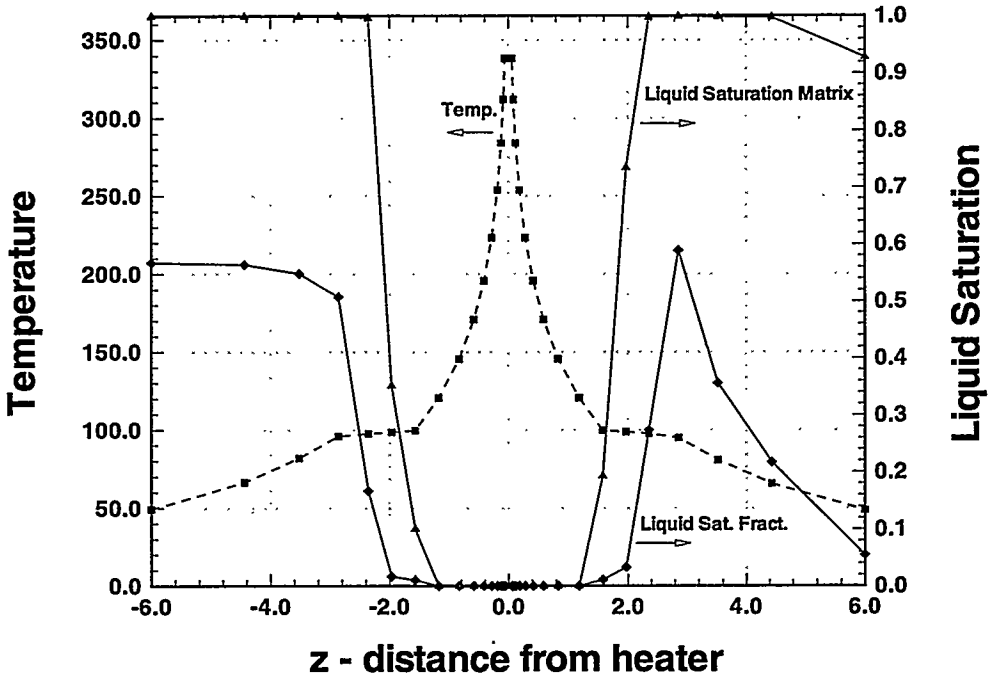

Figure 6.6-4 *Temperature / liquid saturation for case with low matrix permeability in 2D - simulation at 1 year along Z - axis at X = 0.0 m.*

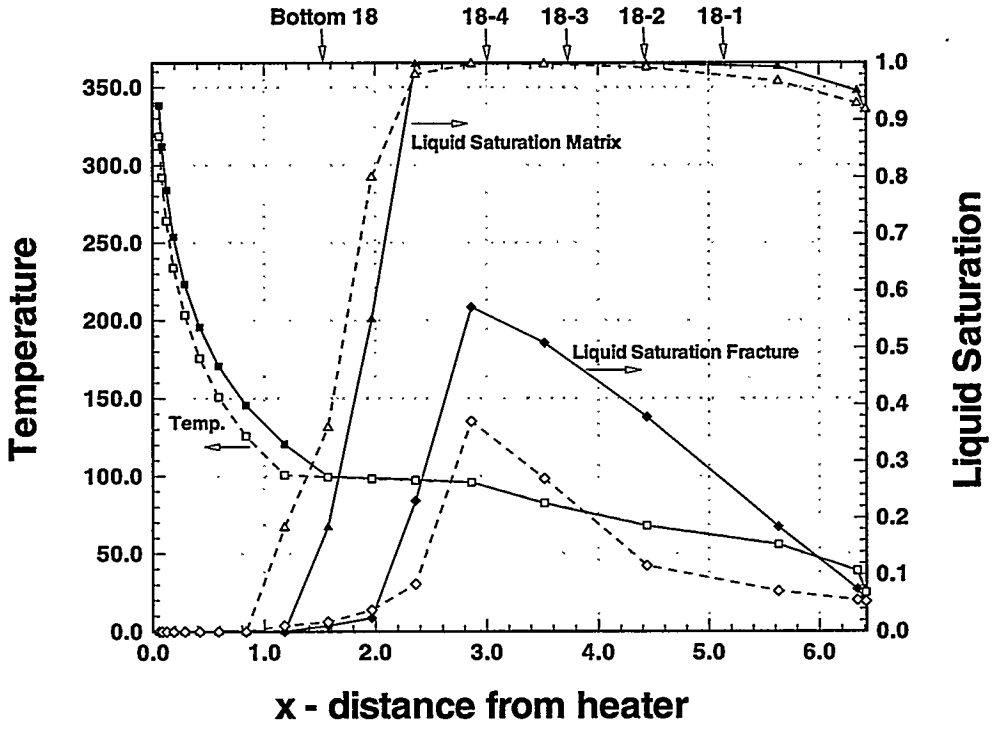

Figure 6.6-5 *Comparison of temperature / liquid saturation at 1 year along X - axis at Z = 0.0 m for different matrix permeabilities in 2D - simulation. Solid symbols / lines denote case with low matrix permeability, hollow symbols and dashed lines denote Base Case.*